Computational Studies of Oxygen Transport in Arterio-Venous Fistulae

by

Francesco Iori

Department of Aeronautics

Imperial College London, South Kensington Campus, London

SW7 2AZ, United Kingdom

This thesis is submitted for the degree of

Doctor of Philosophy of Imperial College London

Abstract

Arterio-venous-fistulae (AVF) are surgically-formed connections between an artery and a vein and are regarded as the "gold standard" method of vascular access, for haemodialysis. Nonetheless, up to 60% fail within three months of creation. Their principal failure mechanism is intimal hyperplasia (IH), an adverse inflammatory process causing AVF to block and fail. Evidence suggests that IH is a multifactorial process, attributable to an altered vascular environment, including increased metabolic stress, flow disturbances, mechanical stress, and wall hypoxia (low oxygen levels). The present work focuses on studying wall hypoxia in idealised AVF. Vascular walls are oxygenated by transport from both luminal oxygenated blood and adventitial vasa vasorum (VV), the microvascular network supplying large vessels. Luminal oxygen supply is affected by the altered AVF haemodynamics, while altered wall-mechanics can prevent adequate VV perfusion. The aim of this thesis is to ascertain what is most important in determining wall-oxygen levels: (i) modified luminal flow field; (ii) mechanically-modified VV perfusion. Hence, a model of oxygen transport, capable of accounting for VV damage/hypoperfusion, was developed. Geometries and VV perfusion fields obtained from mechanical simulations were used to provide the oxygen transport model with a VV oxygen source. Results suggest that for a given set of wall parameters, the local wall-oxygen levels are governed by the flow field, while spatial distributions of mechanically-modified VV perfusion are shown to have negligible effects on the local wall-oxygen levels. However, overall wall-oxygen levels are highly sensitive

to changes in bulk wall parameters, particularly oxygen consumption rates.

Finally, these results were used to develop a simplified oxygen transport model, that is combined with a mesh-adaptive-direct-search approach to identify an optimal AVF configuration with reduced hypoxia levels. The configuration features a non-planar anastomosis and a helical shaped vein.

Acknowledgements

Undertaking this Ph.D has been a truly life-changing experience and it would not have been possible without the assistance and guidance that I received from many individuals.

Firstly, I would like to express my sincere gratitude to my supervisor Dr. Peter Vincent, for the continuous support, his patience, enthusiastic encouragement, and insightful conversations. I would also like to offer my special thanks to my co-supervisor and mentor, Prof. Colin Caro for his mentorship and invaluable input throughout my entire stay at Imperial College. Their guidance helped me in all the stages of research and writing of this thesis. I could not have imagined having better supervisors for my Ph.D.

A special thanks goes to all the members of the Caro Renal Group, in particular Richard Corbett, Neill Duncan, Dr. Mengxing Tang, Chee Hau Leow, and Dr. Virginie Papadopoulou, for the endless Thursday afternoon meetings. They made me feel part of a lively research environment and inspired me to pursue my Ph.D.

I also gratefully acknowledge the support from the National Institute for Health Research Imperial Biomedical Research Centre, CD-adapco, the Aldama Foundation, the Engineering and Physical Sciences Research Council and funding received from the British Heart Foundation (grant number FS/14/19/30609) towards my Ph.D.

I am indebted to all my friends and colleagues in London, who made me feel

part of an enlarged family, during my time at Imperial College. Special thanks go to Stefano, Luigi, Ruben and Rosa, George, Arwind and Chan-Hui.

I would also like to express a heartfelt thank you to my family: my parents, Serena and Simone for their continuous and unparalleled love, help and support. Without you, I would not be the person I am today.

Above all, I would like to thank Lorenza, for her love, constant support, and for keeping me sane over the past few months. Thank you for being my inspiration, editor, proof-reader, and sounding board. But most of all, thank you for being my best friend. To you I dedicate this thesis.

Declaration of Originality

The work presented in this thesis comprises only my original work and does not contain material which to a substantial extent has been accepted for the award of any other degree or diploma of the university or other institute of higher learning, except where due acknowledgement has been made in the text.

Copyright Declaration

Nomenclature

Abbreviations

AVF	Arterio-Venous Fistula
AVG	Arterio-Venous Graft
BA	Brachial Artery
CABG	Coronary Artery Bypass Graft
CFD	Computational Fluid Dynamics
CS	Compartment Syndrome
CV	Cephalic Vein
CVC	Central Venous Catheter
DAO	Distal Arterial Outlet
DVO	Distal Venous Outlet
EC	Endothelial Cells
ESRD	End-Stage Renal Disease
FEA	Finite Element Analysis
FSI	Fluid-Structure Interaction
HWP	Haemodynamic Wall Parameter
IFP	Interstitial Fluid Pressure
IH	Intimal Hyperplasia
LHS	Latin Hypercube Sampling
NFK-K/DOQI	National Kidney Foundation - Kidney Disease Outcomes Quality Initiative
PAI	Proximal Arterial Inlet
POD	Proper Orthogonal Decomposition
RRT	Renal Replacement Therapies
SMC	Smooth Muscle Cells
SPI	Spectral Power Index
SV	Saphenous Vein
VA	Vascular Access
VMTK	Vascular Modelling Tool Kit

VV	Vasa Vasorum	
WSS	Wall Shear Stress	

Constants

κ	Modulating exponent for the Stretch-Based Perfusion Model	-
$D_{\square}$	Diameter of $\square$	m
μ	Dynamic Viscosity	$Pa \cdot s$
ρ	Density	kg/m^3
a	Elliptical Arteriotomy semi-major axis	m
b	Elliptical Arteriotomy semi-minor axis	m
$d_{a\text{-}v}$	Distance between BA and CV centrelines	m
$L_{\square}$	Length of $\square$	m
L_m	Length of mobilised vein	m
P_{thres}	Perfusion threshold for the Stress-Based Perfusion Model	mmHg
$R_{\square}$	Radius of $\square$	m
$T_{\square}$	Thickness of $\square$	m
$T_{v\text{-}\square}$	Thickness of the vascular layer of $\square$	m

Structural Model

γ	Collagen fibres mean angle measured from the circumferential direction	rad
$\mathbf{A_{i\text{-}th}}$	Tissue Structure of the i-th collagen fibre family	-
$\mathbf{a_{i\text{-}th}}$	Direction of the i-th collagen fibre family	-
$\mathbf{B}$	Left Cauchy-Green stretch tensor	-
$\mathbf{C}$	Right Cauchy-Green stretch tensor	-
$\mathbf{E}$	Lagrangian Finite Strain tensor	-
$\mathbf{F}$	Deformation gradient	-
$\mathbf{P}$	First Piola-Kirchhoff stress tensor	Pa
$\mathbf{R}$	Orthogonal rotation tensor	-
$\mathbf{S}$	Second Piola-Kirchhoff stress tensor	Pa
$\mathbf{U}$	Right stretch tensor	-
$\mathbf{X}$	Material point	m
$\mathbf{x}$	Deformed configuration	m
$\overline{\Psi}$	Isochoric Strain Energy Function	$Joule/m^3$
$\overline{I_{i-th}}$	I-th deformation invariant	-
$\boldsymbol{\chi}$	Deformation field	m
$\boldsymbol{\sigma}$	Cauchy stress	Pa
$\boldsymbol{\tau}$	Kirchhoff stress	Pa

Ψ	Strain Energy Function	Joule/m^3
$\sigma_{\theta\theta}$	Cauchy stress in the circumferential direction	Pa
σ_{rr}	Cauchy stress in the radial direction	Pa
σ_{zz}	Cauchy stress in the axial direction	Pa
B	Material bulk modulus	Pa
C_{10}	HGO constitutive model stress-like parameter	Pa
J	Jacobian determinant	-
k	HGO constitutive model stress-like parameter	-
k_1	HGO constitutive model stress-like parameter	Pa
k_2	HGO constitutive model stress-like parameter	-

Dimensionless Numbers

Da	Damkhöler Number	-
Pe	Peclet Number	-
Re	Reynolds Number	-
Sc	Schmidt Number	-
Sh	Sherwood Number	-

Oxygen Transport Model

$[Hb]$	Oxygen carrying capacity of haemoglobin	ml O_2/ml blood
α	Oxygen solubility in plasma	ml O_2/ml blood mmHg
α_T	Oxygen solubility in tissue	ml O_2/ml tissue mmHg
$\dot{q}$	Oxygen consumption rate	ml O_2/ml tissue s
$\dot{q}_{max}$	Maximum oxygen consumption rate	ml O_2/ml tissue s
D_b	Free oxygen diffusivity in blood	m^2/s
D_c	Haemoglobin diffusivity in blood	m^2/s
D_F	Modified oxygen diffusivity in blood	m^2/s
D_T	Free-oxygen diffusivity in tissue	m^2/s
n	Hill parameter	-
P_m	Microvessel wall oxygen permeability	m/s
$PO_{2\text{-}50}$	Half-maximum haemoglobin saturation	mmHg
$PO_{2\text{-}M}$	Half-maximum oxygen consumption tension	mmHg
S	Haemoglobin saturation	%
S_F	Modified luminal oxygen source	mmHg/s
S_w	Vasa vasorum oxygen source	mmHg/s

Subscripts

A	Artery
$aniso$	Anisotropic
art	Arterioles
cap	Capillaries
$deoxy$	Deoxygenated
fi	i-th family of embedded collagen fibers
iso	Isotropic
oxy	Oxygenated
V	Vein
ven	Venules
vol	Volumetric

Symbols

$\dot{\gamma}$	Shear rate	1/s
$\mathbf{D}$	Strain-rate Tensor	1/s
$\mathbf{m}_\square$	Tangent vector in $\square$	-
$\mathbf{O}$	Origin	
$\mathbf{p}_\square$	Centreline point in $\square$	m
$\mathbf{s}$	Parameter Set	-
$\mathbf{S}_k$	Set of tried parameter sets at step k	-
$\mathbf{t}$	Viscous stress vector	Pa
$\mathbf{v}$	Velocity Vector	m/s
$\mathbf{w}$	WSS vector	Pa
$\mathbf{x}_\square$	Centreline of $\square$	m
$\overline{PO}_2$	Time-averaged PO_2	mmHg
$\overline{V}_f$	Depth-integrated VV perfusion	-
$\overline{V}_f$	Normalized volume fraction of microvessel per volume of tissue	-
ϕ	Azimuthal angle of the venous tangent	rad
$\boldsymbol{\mathcal{T}}$	Viscous stress tensor	Pa
Ψ	Cost Function	-
$\rho_\square$	Spearman rank correlation coefficients of $\square$	-
θ	Elevation angle of the venous tangent	rad
$\tilde{\mathbf{S}}_k$	Set of feasible tried parameter sets at step k	-
$\widehat{PO}_2$	Depth-averaged $\overline{PO}_2$	mmHg
ξ	Parameter for the position of $\mathbf{p}_3$	rad

$C_\square$	Windkessel Capacitance at $\square$	mmHg/ml
p	Pressure	Pa
$P_\square$	Average pressure at $\square$	mmHg
PO_2	Oxygen tension in plasma	mmHg
$Q_\square$	Flow rate at $\square$	ml/s
r	Radial coordinate	m
$R_{1\square}$	Proximal Windkessel Resistance at $\square$	mmHg s/ml
$R_{2\square}$	Peripheral Windkessel Resistance at $\square$	mmHg s/ml
$S_\square$	Main effect Sobol Sensitivity index of $\square$	-
$S_{\square,\square}$	First-order Sobol Sensitivity index of $\square$ and $\square$	-
$S_{T\square}$	Total Sobol Sensitivity index of $\square$	-
V_f	Volume fraction of microvessel per volume of tissue	ml VV/ml tissue
x_{p1}	x coordinate of $\mathbf{p}_1$	m
y_{p1}	y coordinate of $\mathbf{p}_1$	m
z_{p1}	z coordinate of $\mathbf{p}_1$	m
DI	Distortion Index	-
LNH	Local Normalized Helicity	-

Contents

List of Figures

List of Tables

Chapter 1

Introduction

1.1 Background

Arterio-venous-fistulae (AVF) are surgical connections formed between an artery and a vein in the upper arm or wrist of patients, affected by end-stage-renal disease (ESRD), a permanent reduction or loss of renal function. Due to their higher reliability in terms of lower risk of infections, thrombosis, and greater patency, AVF are regarded as the "gold standard" method of vascular access for haemodialysis [1]. However, up to 60% of AVF fail within three months of creation, reducing patient's quality of life, and leading to significant additional costs for healthcare systems [1]. The principal failure mechanism for AVF, as well as for a number of vascular interventions, including bypass grafts and arterial stents, is intimal hyperplasia (IH). IH is an acute inflammatory disease that appears as an abnormal expansion in the cellularity of the intimal layer, causing the obstruction of the vessel lumen where it occurs [2]. Evidence suggests that IH is a strongly multifactorial process, attributable to changes in the biochemical and biomechanical vascular environment, which include increased metabolic stress, *i.e.* the accumulation of metabolites such as lactate, phosphate inorganic (Pi)

and hydrogen ions, due to an increased metabolism, flow disturbances, abnormal shear stress, mechanical stress and wall hypoxia, *i.e.* low oxygen levels [2].

This study focuses on investigating the occurrence of hypoxia in AVF, via numerical modelling. Evidence from *in-vivo* and *in-vitro* studies shows a well-established link between the insurgence of wall hypoxia and the formation of IH [3, 4]. However, despite an initial interest in the biomechanical and fluid mechanics community [5, 6, 7, 8, 9, 10, 11], the majority of recent efforts have focused on studying the effect of fluid shear-stress on vascular disease. Notwithstanding the abundant clinical and experimental studies supporting the low-oxygen theory [12, 3, 4, 13, 14], the role of hypoxia in the initiation of IH has yet to be clarified. A deeper understanding of oxygen transport can be crucial to elucidate the role of hypoxia in the IH initiation process, and would allow to design a more reliable vascular access with higher patency rate.

1.2 Research Question

The vascular walls of healthy vessels are oxygenated through transport from both luminal oxygenated blood and adventitial vasa vasorum (VV), the microvascular network that supplies medium and large vessels. Forming an AVF exposes the local circulation to altered haemodynamics, that may negatively affect the local flow field and luminal oxygen supply [2, 15, 16]; in addition, recent *in-vivo* studies have demonstrated that altered wall biomechanics, *i.e.* increased levels of solid stress/deformation in the wall, can prevent adequate VV perfusion and hinder adventitial oxygen supply, thus leading to wall hypoxia [17, 18, 19].

The main aim of this study is to ascertain what is most important in determining wall oxygen levels: (i) modified luminal flow field; (ii) mechanically modified VV perfusion. To answer this question, a model of oxygen transport, capable of accounting for potential VV damage/hypoperfusion, is developed and used to quantify the effect of varying flow conditions and wall parameters.

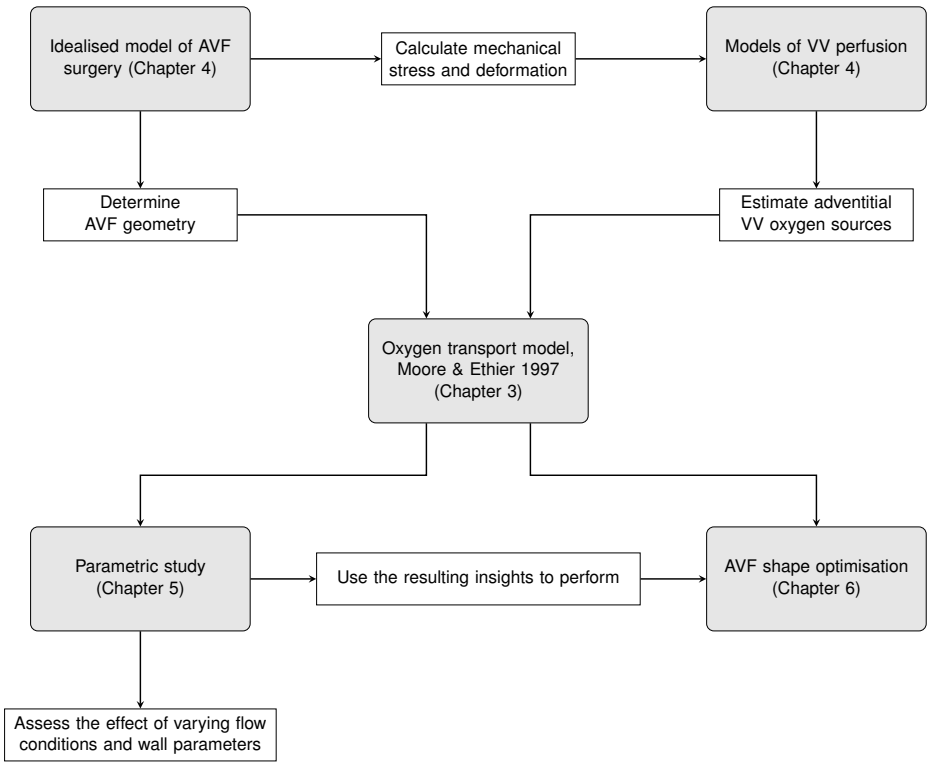

Figure 1.1: Block diagram outlining the workflow of the thesis.

The work in this thesis is organized according to the following steps:

- Initially, an idealised model of AVF surgery is developed, to estimate wall stress and deformation.
- Simple models of VV perfusion are proposed to investigate the effect of wall biomechanics.
- A model of oxygen transport is developed; geometries and VV perfusion fields obtained from the mechanical simulations are used to provide the oxygen transport model with a VV oxygen source.
- A parametric study is devised to assess the effect of varying flow conditions and wall parameters, and the relative importance of the fluid-side and wall-side oxygen transport;

- Finally, using the insights produced so far, an optimisation framework is used to identify an optimal AVF configuration, with reduced hypoxia levels.

1.3 Thesis Overview

The dissertation is divided in 7 chapters:

- Chapter 1, Introduction.
- Chapter 2, Literature Review. The purpose of this chapter is to provide the reader with a broad introduction to the problem, explaining thoroughly the concepts of IH, AVF maturation and failure. In addition, a critical literature review on the state-of-the-art numerical models of AVF and grafts and oxygen transport.
- Chapter 3, Developing a Model of Oxygen Transport in Arterio-Venous Fistulae. In this chapter, the model of oxygen transport used throughout the study is introduced. The model used is based on the recent extension of Murphy [11] of Moore and Ethier's work [5] and features a coupled fluid-wall oxygen transport.
- Chapter 4, Developing a Model of Arterio-Venous Fistulae Surgery. An idealised Finite Element (FE) model of AVF surgery is developed, to quantify wall stress and deformation. Simple models of VV perfusion are proposed to study the effect of the wall biomechanics.
- Chapter 5, Simulating Oxygen Transport in Arterio-Venous Fistulae. In this chapter, geometry and VV perfusion fields obtained from FE simulations in Chapter 4, are used to provide the oxygen transpor model introduced in Chapter 3, with VV oxygen source. A parametric study is undertaken, to assess the effect of varying flow conditions and bulk wall param-

eters and determine the relative importance of the fluid-side and wall-side oxygen transport.

- Chapter 6, Reducing Hypoxia in Arterio-Venous Fistulae. Mesh-adaptive-direct-search optimisation and Kriging surrogate models were used an identify an optimal AVF configuration with reduced hypoxia levels.
- Chapter 7, Conclusions. A critical summary of the results and future work.
- Appendix. The numerical methods adopted in the thesis are reported and commented upon.

1.4 Resulting Publications

Part of the work produced during the PhD has been presented in the following journals, oral and poster presentations.

Journal Papers

- F. Iori, L. Grechy, R. Corbett, W. Gedroyc, N. Duncan, C. G. Caro, P. E. Vincent, The Effect of in Plane Arterial Curvature on Blood Flow and Oxygen Transport in Arterio-Venous Fistulae, Physics of Fluids, Volume 27, 2015.
- C. H. Leow, F. Iori, R. Corbett, N. Duncan, C. G. Caro, P. E. Vincent, M. Tang, Microbubble Void Imaging - A Non-Invasive Technique for Flow Visualisation and Quantification of Mixing in Large Vessels using Plane Wave Ultrasound and Controlled Microbubble Contrast Agent Destruction, Ultrasound in Medicine and Biology, Volume 41, Pages 2926-2937, 2015.

Oral Presentations

- World Congress on Computational Mechanics, 24-29 July 2016, Seoul, South Korea, Coupled Fluid-Wall Oxygen Transport In Arterio-Venous Fistulae: Impact of Mechanical Stresses.

Poster Presentations

- UK Kidney Week, 7-10 June 2016, Birmingham, UK, Coupled Fluid-Wall Oxygen Transport in Arteriovenous Fistulae: Impact of Mechanical Stresses.
- Summer Biomechanics Bioengineering and Biotransport Conference, 17-20 June 2015, Snowbird, Utah, USA, The Effect of Vascular Curvature on Blood Flow and Oxygen Transport in Arterio-Venous Fistulae.
- Summer Biomechanics Bioengineering and Biotransport Conference, 17-20 June 2015, Snowbird, Utah, USA, Microbubble Void Imaging - A Novel Technique For Flow Visualisation and Quantitative Assessment of Intravascular Mixing in Larger Vessels Using Ultrasound.

Chapter 2

Literature Review

2.1 Arterio-Venous Fistulae

2.1.1 Treatment of End Stage Renal Disease

Patients with End-Stage Renal Disease (ESRD) suffer from an irreversible reduction in kidney function. Before the introduction of Renal Replacement Therapies (RRT), such as haemodialysis, ESRD was a terminal illness. RRT are used to compensate the loss of kidney function by removing toxic metabolic waste, controlling the concentration of solutes and removing excess water. In 2004, Grassman *et al.* estimated that worldwide, more than 1,700,000 people suffered from ESRD and 1,300,000 needed RRT, corresponding to prevalence values of 280 and 215 per million population (pmp) respectively. Among these, in the European Union alone, 252,000 patient with RRT were treated (550 p.m.p.) [20]. Specifically, two main types of RRTs exist: haemodialysis (HD), and peritoneal dialysis (PD) [21]. According to Grassman *et al.*, HD is the most commonly used type of RRT, as in 2004 more than 89% of the world ESRD population was treated with HD [20].

2.1.2 Vascular Access

First examples of working dialysers have existed since 1943, when Kolff developed the first clinically usable device [22]. However, chronic haemodialysis started to be a viable treatment only in 1966, when Brescia and Cimino realised the first example of internal arterio-venous shunts [23, 24], which were used to effectively connect the dialyser machine to the patient.

Since the introduction of the Brescia-Cimino fistula, the original design has substantially evolved and types of vascular access have been developed. The National Kidney Foundation - Kidney Disease Outcomes Quality Initiative (NFK-K/DOQI) Clinical Practice Guidelines identify the features of a good vascular access for haemodialysis. According to the K/DOQI guidelines, an effective vascular access should "provide high flow rate to the dialyzer when used, should be reliable, durable, easy-to-use, and should minimize the risk of infections for patients" [25]. The main forms of vascular access adopted in clinical practice are:

- **Arterio-Venous Fistula (AVF):** connection between an artery and a vein formed by vascular surgeons either in the upper or lower arm of patients. When AVFs are formed in the upper arm, they usually involve the brachial artery and the cephalic vein (brachio-cephalic fistula, see Fig. 2.1). If the cephalic vein is not available or too small, the basilic vein is used (brachio-basilic fistula), which, because of its greater depth and position with respect to the brachial artery, has to be "transposed". The term basilic vein transposition refers to the dissection and mobilisation of the basilic vein, up to the axillary vein, to allow connection to the brachial artery. This is a much more invasive procedure, compared to normal brachio-cephalic AVF, and only a shorter section of vein is available for cannulation.

  When AVFs are created in the lower arm, radial artery and cephalic vein are used (radio-cephalic fistula) [26].

According to the K/DOQI Guidelines, the formation of an AVF represents the "gold-standard" method for creating a vascular access, for its superior patency and lower complication rates, compared with other access options [25].

The connection between the artery and the vein can be formed via three different methods:

- **end-to-side** anastomosis: when the vein is cut and connected to the side of the artery. Currently, it represents the most commonly used form of AVF [27].
- **side-to-side** anastomosis: when the side of the artery is directly connected to the side of the vein. This type of connection is also known as the Brescia-Cimino fistula [24, 28].
- **end-to-end** anastomosis: when terminal parts of both vein and artery are cut and connected together, forming a loop. This anastomosis is available only if the vessels have matching diameters [27].

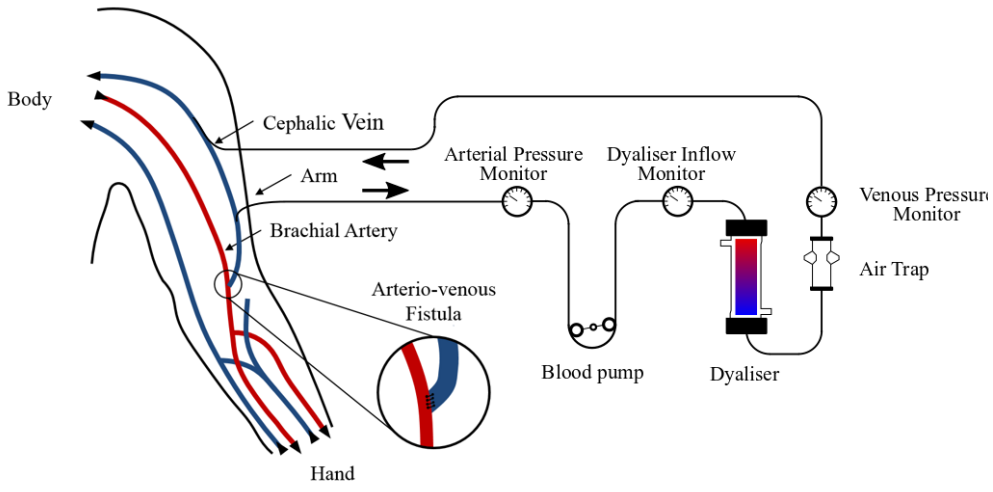

Figure 2.1: End-to-side brachio-cephalic fistula and connection to the dialyser. Black arrows indicate direction of the blood flow.

- **Arterio-Venous Graft (AVG):** connection between the arterial and the venous systems through a synthetic prosthetic segment, commonly made of polytetrafluro-ethylene (PTFE) [26]. AVGs can be connected with a great variety of configurations. The K/DOQI Guidelines suggest that an AVG should only be formed when an AVF is not available [25]. Similarly, the European Best Practice Guidelines for haemodialysis recommend the use of autologous AVF as first choice for vascular access and AVG only as a second choice. However, the debate is still open [29, 30, 27, 31, 32], and as Riella and Roy-Chaudhury observed that, surprisingly, no randomized controlled trial has compared access types [33].

- **Central Venous Catheter (CVC):** a catheter connected to the central venous system, normally via jugular, subclavian or femoral veins. CVC does not require access to arterial blood flow, as high flow rate is directly provided by central veins. CVC are prone to higher risks of infection and associated with high morbidity [34]. For this reason, K/DOQI Guidelines recommend the use of CVC only when no other option is available [25].

2.2 AVF Maturation

The term maturation refers to a series of physiogical and histological changes in the vessels involved in an AVF, which lead to the fistula being suitable for cannulation and thus dialysis. Common agreement exists on the macroscopic changes that occur after AVF formation, whereas the exact remodelling mechanism by which an AVF matures, has not been established yet [2, 33, 1, 35, 27, 32]. In his review of 2006, Dixon provides a detailed description of the maturation process. When an AVF is formed, the large pressure difference existing between the arterial and venous systems leads to increased blood flow through the vein, which in turn will (ideally) cause the vein walls to strengthen and the vein itself to enlarge.

The result - an enlarged 'arterialised' vein, with strengthened walls, and a high blood flow rate (at least 300 ml/min) - can accommodate a large gauge needle, and provide excellent access for haemodialysis over a period of several years [1].

2.3 Complications And Failure

The AVF represents the gold-standard method for creating a vascular access for haemodialysis, as indicated by the K/DOQI. However, up to 50% of newly formed AVF does not reach maturation [33, 35, 2]. Aneurysms, stenosis, thrombosis and steal syndrome, *i.e.* hand and/or forearm ischemia due to insufficient blood flow to the distal artery, have all been reported among the major causes of AVF failure.

In addition, several groups have shown an increased interest in assessing whether the increased levels of oxidative stress and inflammation present in uraemic patients can influence the magnitude of the remodelling response [1, 33].

Riella and Roy-Chaudhury identified an inflammatory process, known as Intimal Hyperplasia (IH) or Neointimal Hyperplasia, as the principal cause of primary failure or maturation failure [33, 2]. IH causes an abnormal thickening of the intimal layer of the artery and/or vein, followed by a narrowing of the lumen and a dramatic blood flow reduction through the AVF. In native vascular accesses, stenoses occur mostly in the venous segment. In particular, the most predominant site for IH development is the juxta-anastomotic vein for radio-cephalic AVF, the cephalic arch for brachio-cephalic AVF and the proximal vein segment for brachio-basilic AVF [36, 37].

In AVG, 80% of stenoses are on the venous side of the anastomosis, whereas only 4% are found on the arterial side. IH also appears in coronary artery bypass grafts and stented arteries restenosis [38, 39]. A deeper understanding of how IH develops is needed to identify possible strategies to avoid it. The next section provides a brief review on IH and its potential causes.

2.3.1 Intimal Hyperplasia

The term IH refers to an increase of the intimal layer cellularity, normally accompained by an increased extracellular connective matrix production and recruitment of leukocytes, macrophages and other immunity cells [2]. Spaet *et al.* suggests that IH has medial orgin, being mainly caused by Smooth Muscle Cells (SMC) that migrate from the medial layer to the intima where they proliferate and form the lesion [40]. More recent studies on coronary angioplasty and saphenous vein grafting, have shown the migration of fibroblasts from the adventitia to the intima, where they acquire the phenotype of myofibroblasts [41, 42]. Finally, recent data have also suggested a role for bone marrow derived multipotent cells that subsequent to migration to the media and intima, acquired a smooth muscle phenotype, in the pathogenesis of IH [2].

Whilst the exact mechanisms underlying development of IH are unknown, multiple risk factors have been identified in previous publications, such as inflammation, hypoxic stress, shear stress, mechanical stress and uremia, *i.e.* the high plasma concentration of urea and creatinine resulting from renal failure [2].

IH is a strongly multifactorial process attributable to a broad spectrum of risk factors. Evidence suggests that the paradigm of one single factor that drives a range of responses rarely applies and appears as an oversimplification of this complex pathological process [2].

In their review, Brahmbhatt *et al.* summarise the effect of inflammation in newly formed anastomosis. An inflammatory response can be caused by local effects, i.e. surgical trauma, hypoxia or shear stress-induced wall damage and by chronic/systemic effects, i.e. elevated uremia in ESRD patients [43]. It is hypothesized that a local inflammatory response can be caused by the release of macrophage migration inhibitory factor (MIF). MIF has been shown to enhance neointimal thickening by driving macrophages and inflammatory cells toward the neointima and leading to the proliferation of medial and intimal cells [43].

Moreover, the situation is worsened by the presence of chronic kidney disease and consequent elevated uremia; a significant increase in the mean concentration of cytokines implicated in IH formation (IL-6, TGF-b1, and TNF-a) was found as well as altered cellular calcium extrusion, fibrosis and deposition of calcium phosphates that ultimately leads to vascular calcifications [43, 2].

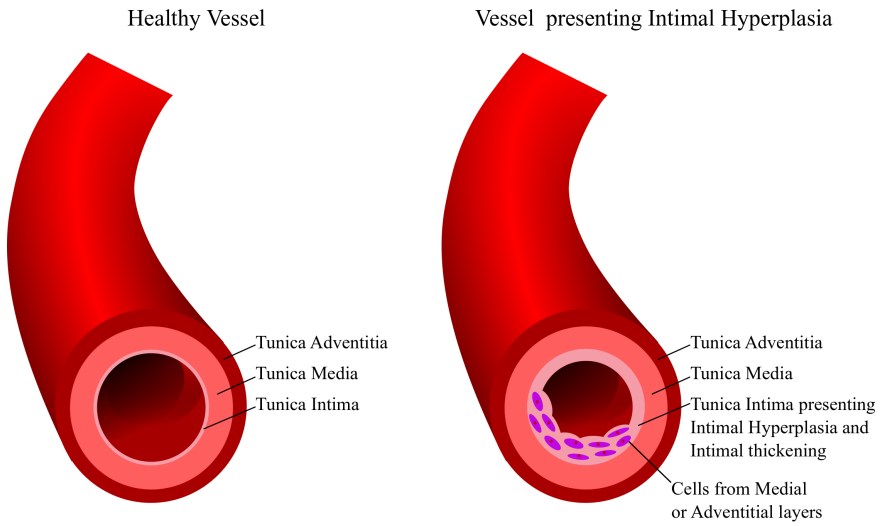

Figure 2.2: Schematic representation of a healthy vessel, and a vessel presenting intimal hyperplasia, courtesy of Lorenza Grechy [44].

2.3.1.1 Wall Shear Stress and Flow Disturbances

The prevalence of vascular pathologies varies spatially within the mammalian vasculature. However, abundant evidence has led to the hypothesis that particular "disturbed" flow patterns, which are normally found in regions presenting curvature and branching, are involved in the development of vascular disease. Conversely, the laminar flow normally found in straight sections of the arterial tree is believed to be atheroprotective [45]. Despite it is now widely accepted that blood flow may play an important role in the development of vascular pathologies, there is still confusion about which particular blood flow feature may induce vascular remodelling. Also the term "disturbed flow", although frequently used, is vague and has often assumed multiple connotations in different settings [16]

This relation was proposed for the first time in 1968 by Fry, who showed that acutely increased shear stress affects the morphology and orientation of ECs, causing increased tran-endothelial transport of lipids and proteins, and at very high levels leads to endothelial denudation [46]. Although this study suggested the possibility that lesions developed preferentially in regions of high Wall Shear Stress (WSS) , studies by Caro *et al.* in human cadavers showed that early lesions appeared around arterial branches of the abdominal aorta, where, due to flow separation, WSS was expected to be low [47, 48]. Today, the low WSS theory has become the consensus mechanism for the initiation of vascular disease and is widely accepted in the atherosclerosis community. Since then, a large number of *in-vivo*, *in-vitro* and *in-silico* studies have found correlation between IH and low WSS. Intima and media thickening was observed in conjunction with regions of low wall shear stress [49] and demonstrated *in-vivo* in pigs [50, 51], canines [52] and mice [53] animal models.

Extremely low WSS (< 0.2 Pa) stimulates high rates of smooth muscle cellular proliferation in arterialized vein patches and IH appear to be accelerated in these regions [54]. This theory also finds support in the observation that elevated blood flow rates can induce regression of IH [55]. Low WSS is normally found in regions presenting branching, curvature and cross-sectional expansion, which are sites known to disturb the laminar flow and make it non-uniform and irregular, causing flow separation and reattachment as well as recirculation.

Over the course of many years, other authors have proposed different failure mechanisms. Ku *et al.* suggest a potential correlation between low/oscillatory shear stress and atherosclerotic plaques formation [56]. This theory relies on the observations that particular geometries can induce recirculation eddies and changes in direction of the WSS vector over time. Laminar flows normally found *in-vivo* oscillate at frequencies contained in the normal physiological cardiac range (0-25 Hz) and are thought to modulate endothelial cell function and vascular

biology [56]. More recent studies suggest a correlation between multidirectional WSS and atherosclerotic lesions [57]. Others propose that high values of WSS spatial gradient can be linked with IH initiation [58, 59, 60].

IH lesions have also been correlated with the occurrence of transitional unsteady flows. This type of flow regime typically has a very high frequency content and differs substantially from the reciprocating flow described above, whose spectrum possesses a much lower frequency content. Transitional flows are characterised by highly oscillating, multi-directional shear stress, and pressure fluctuations, giving rise to audible bruits. Fillinger *et al.* observed a statistically relevant correlation between the development of intimal thickening and wall vibration caused by unsteady, disrupted flows, that are typical of end-to-end and end-to-side venous anastomosis [61]. Huynh *et al.* reported a significant *in-vitro* reduction in nitric oxide production, an strong inhibitor of SMC proliferation and inflammation, in compliant tubes cultured with EC [62]. suggesting that the occurrence of transitional flow can disrupt ECs normal function. These unphysiological flows are not usually found in healthy autologous vessels but are particularly common in AVF and AVG and Coronary Artery Bypass Graft (CABG), that is, vascular connections that share the following features: elevated flow rates and consequently Reynolds numbers and non-anatomical geometries. Several CFD studies have described this class of disturbed flows in a range of vascular connections having unnatural bifurcation angles and flow divisions [63, 15, 64].

In conclusion, overall no general agreement can be found about the causes leading to vascular disease. In their systematic review, Peiffer *et al.* pointed out how, even though the low/oscillatory WSS theory is now widely accepted, the exact mechanism leading to vascular disease has not been clearly identified yet [65]. These findings emphasize the need for further experimental and numerical models, as well as for a unified hypothesis and standardised numerical techniques.

2.3.1.2 Hypoxia

Oxygen delivery is crucial to maintaining normal aerobic metabolism in mammals. Medium and large size blood vessels in the circulatory system receive oxygen from the blood passing through the Vasa Vasorum (VV) within the adventitia, which supply most of the oxygen needed to the media, while the intima is predominantly supplied from the blood that flows within the central vessel lumen.

Hypoxia is defined as the presence of lower than normal oxygen content in living tissues. Heuper first hypothesised that wall hypoxia may contribute to atherosclerosis development in 1944 [12]. Since then, a number of *in-vivo* and *in-vitro* studies have established the same link. Barker *et al.* observed IH formation in pigs and rabbits, in which hypoxia was induced by removing the VV [3]. Correlation between hypoxic regions and intimal lesions was also found by Lee *et al.* in rabbit aorta [4]; the same authors were then able to decrease the cellular proliferation by administration of supplemental oxygen [66, 13].

Hypoxia signalling pathways are some of the most well known of all the different risk factors. Hypoxia exerts its effect on molecular signaling by activation of hypoxia-inducible factors. Hypoxia-inducible factor 1a (HIF-1a) expression is involved in a positive feedback loop, influencing molecular pathways, that ultimately induce angiogenesis, inflammation, cell proliferation. One of its most important downstream mediators is VEGF. The arterialization of venous vessels, with consequent increased VV count, medial thickening and EC proliferation, is thought to be mediated by VEGF through the transcriptor factor mediating angiogenic response, Ets-1 [43]. While this is necessary for the proper maturation of AVF, however, it is suspected that overexpression of VEGF can induce negative wall remodeling and IH [14].

Santilli *et al.* and Cheema *et al.* studied the effect of intra-arterial stenting on the normal artery wall physiology, and hypothesized that, the deployment of intra-arterial stents could lead to increased wall stress and deformation which

could potentially compromise the optimal VV perfusion. Diminished flow through the VV following deployment of an intra-arterial stent could therefore contribute to wall hypoxia and in turn IH [17, 18].

2.3.1.3 Mechanical Factors

Despite the large interest shown by the fluid-mechanics community on the correlation between hypoxia and fluid shear and vascular pathologies, few studies focused their attention on the effect of an altered wall-mechanics on the regulation of IH. Bassiouny *et al.* proposed that anastomotic intimal hyperplasia might be induced by different underlying mechanisms. They first investigated the location of intimal thickening in relation to mechanical and haemodynamic factors and concluded that there are at least two different types of intimal thickening. Arterial floor intimal thickening developed in regions of flow oscillation and low shear, whereas suture line intimal thickening had greater prominence in prosthetic grafts, as the compliance mismatch between the vascular tissue and the prosthetic material is greater [67]. While the compliance mismatch could explain IH formation near the anastomosis, it does not explain distal venous IH formation.

Conversely, Dobrin observed that autogenous veins exposed to arterial pressure, undergo histological changes, that are similar to those experienced by arteries exposed to hypertension. Particularly, it was demonstrated that while intimal thickening was correlated with low flow velocity (which is directly related to WSS), medial thickening was best correlated with mechanical factors [68]. Together, the studies seems to suggest that arterial and venous tissue reacts differently to fluid and mechanical induced stimuli, due to their different structure and function. Therefore more research is required to establish the different causes leading to IH.

In addition, recent studies by Chang *et al.*, Song *et al.* and Lim *et al.* have suc-

cessfully linked mechanical stretch with the expression of the Hypoxia-Inducible Factor-1 (HIF-1), a key regulator of gene expression, that responds to changes in oxygen tension, particularly hypoxia [69, 39, 70]. If confirmed, this theory would suggest that mechanical factors are not a primary cause of IH, which is, instead, induced by hypoxia.

2.4 Numerical Studies

Over the last two decades, Computational Fluid Dynamics (CFD) and Finite Element Analysis (FEA) have been increasingly used to investigate the blood flow dynamics and mechanical stress in vascular anastomosis. A large number of studies have undertaken simulations of blood flow, oxygen transport, mechanical deformation within anastomotic connections, such as AVF, AVG and bypass grafts. The following sections will provide a brief overview of the main publications, compare different modelling approaches and issues.

2.4.1 Computational Fluid Dynamics in Vascular Access

In recent years, CFD simulations have been extensively employed in the study of blood flow within AVF and AVG. CFD simulations allow one to estimate, non-invasively and at a relatively low cost, important quantities that are otherwise difficult to measure, such as pressure, velocity and shear stress. Furthermore, VA exhibit a complex mix of fluid-dynamic phenomena and can potentially aid the quest for causal linkages between disease localization and fluid-dynamic details for arteries in general [63]. However, Ene-Iordache and Remuzzi in their literature review on idealised vascular accesses, highlighted a strong inhomogeneity between computational studies, which differ for modelling assumptions, grid resolutions, boundary conditions and disturbed flow metrics [16]. In the next sections we provide an overview of the most relevant publications and analyse the different

approaches.

2.4.1.1 Disturbed Flow Metrics

As introduced in Section 2.3.1.1, strong evidence suggests that initiation and progression of vascular disease is influenced by disturbed flow. Regions of the endothelium affected by disturbed flow may be localized by means of haemodynamic wall parameters (HWP). Some of these HWP are based on the magnitude of WSS, like the time-averaged wall shear stress (TAWSS), the oscillatory shear index (OSI) and the relative residence time (RRT). The use of WSS-magnitude based metrics is motivated by the tendency of ECs to align with the time-averaged flow direction [71]. The OSI, originally introduced by Ku *et al.*, is a dimensionless metric that measures the degree of WSS reversal in a pulsatile flow [56]. The RRT, introduced by Himburg *et al.*, is also a dimensionless metric, proportional to a combination of TAWSS and OSI, and measures the residence time of particles near the wall [72] - larger values of RRT could correspond to increased uptake of immunity cells and macro-molecules. In addition, recent findings suggest that oscillatory flow may have pro-inflammatory effects when acting perpendicularly to the cell axis [73, 71]. In this context, a new metric proposed by Peiffer *et al.*, the transversal WSS (transWSS), could be useful to characterise multidirectional flows [74].

Other HWP are based on the gradient of WSS, like the spatial gradient (WSSG), temporal gradient (WSSTG) or angle gradient (WSSAG). The WSSG, originally proposed by Lei *et al.*, may be considered as a marker of EC traction [60], while WSSAG introduced by Longest and Kleinstreuer [75], and WSSTG introduced by Ojha [76], respectively measure angular and temporal changes of WSS and both have been linked to IH.

Finally, one last class of HWP is based on the harmonic content of the WSS field. Transitional and turbulent-like flows, having high-frequency content have

been linked, both *in-vivo* and *in-vitro* to adverse vascular remodeling [46, 61, 77]. Himburg and Friedman observed regions of porcine iliac arteries with increased endothelial permeability are exposed to higher frequency oscillations in shear stress [78]. However, there appears to be no consensus on how to robustly quantify such unsteady flows. In addition, conventional WSS-based markers, such as TAWSS and OSI, while may be appropriate for unsteady laminar flow regimes, are not necessarily adequate descriptors of these turbulent-like stimuli [79]. To analyse spectrum arising from pulsatile flow components, Gelfand *et al.* proposed the harmonic index (HI), defined as the relative fraction of the unsteady signal intensity to the overall signal intensity [80]. Subsequently, Khan *et al.* proposed a new mectric, the spectral power index (SPI), defined as the relative fraction of the power of the signal, processed through a high-pass filter, to the overall signal power. To better highlight flow instabilities, the cut-off frequency of the filter was chosen to exclude frequencies in the normal physiological range ($f = 25Hz$) [79].

2.4.1.2 Numerical issues

One of the main challenges, when using CFD, is to accurately resolve turbulent and transitional flows. In their review on the use of CFD to predict aneurysm rupture, Valen-Sendstad and Steinman speculate that it is possible that some of the present confusion regarding haemodynamic predictors of risk factors may have originated from an incomplete understanding of the haemodynamics, which is attributable to an overabundance of under-resolved CFD studies [81]. Ventikos, in a commentary on Valen-Sendstad and Steinman's article, iterates that CFD has proven to be a useful tool, that can provide valuable answers to the right questions, when it is done properly [82]. While large uncertainty is acceptable when other information, for instance imaging, is affected by even larger uncertainties, the need for accurate CFD models becomes more persistent, as the information

available is becoming more comprehensive [82].

In the circulatory system, the typical Reynolds number (Re) range varies from approximately 4000 in the aorta, to 1 in small arterioles [83]. Transition to turbulence occurs in straight pipes at Re $\approx$ 2000 [84], thus, blood flow can be considered laminar almost in every healthy blood vessel in the body, with the only exception being the aortic arch [45]. However, both the pulsatile nature of physiological flows as well as deviations from straight pipe geometry (branching, curvature and torsion, taper and stenosis) can induce transition to turbulent-like flows at Re lower than critical. AVF and AVG normally exhibit relatively low inflow Re ($\approx$1000), however, their complex geometry, unnatural branching angles, and flow-split ratio, are such to induce laminar-to-turbulent transition, making simulation of such flow regimes challenging, if high accuracy is required within a reasonable computation time.

Ene-Iordache and Remuzzi, in their review on CFD studies in VA, report different numerical approaches, including direct numerical simulation (DNS) and high resolution as well as lower resolution (often under-resolved) CFD simulations [16]. DNS is a computational technique that aims at resolving all the spatial and temporal scales of the flow, directly solving Navier-Stokes equations, without the use of any turbulence model. On the other hand of the scale we have Reynolds-averaged Navier-Stokes equations (RANS), which represent a much more economical solution method, as all the turbulent scales are modelled instead of being solved, resulting in a lower computational cost, but at the price of accuracy. DNS is often impractical due to its high computational cost, whereas the nature of the flow and the relatively low Reynolds numbers make RANS not suitable for modelling AVF haemodynamics. Other computational approaches such as large eddy simulations (LES), only solve larger, more energetic eddies and model the smaller scales, using various subgrid models, but are less used in this field and still object of research. Recent publications have shown that simulations with

appropriate spatial and temporal resolution, *i.e.* having average fine grid size and time step, set according to the viscous lenght and time scale, are able to capture flow instabilities, otherwise not captured by under-resolved studies [85].

Early pioneeering work on this topic was done in 1997 by Lei *et al.*, who undertook computational simulations of the blood flow, within idealised models of AVG to determine an optimal graft configuration capable of reducing WSS gradients and low WSS patterns [60]. However, although the mean inflow Reynolds numbers were relatively low (113 and 365), the simulations appear to be noisy and under-resolved for today's standard. A large number of CFD studies, having grids coarser than necessary, have been published on this topic [86, 87, 50]. The work of Sherwin *et al.* in 2000 [88] and Papaharilaou *et al.* [89] in 2002 on the effect of out-of-plane curvature on blood flow, represent the first examples of properly resolved blood flow simulations within AVG. Here, the need of high-resolution CFD is addressed through the use of a high polynomial order/spectral finite element solver. This necessity is emphasised also in the work of Loth *et al.* who simulated blood flow within idealised grafts and compared results with those obtained *in vivo*. High-frequency flow unsteadiness was observed in the anastomosis and then correlated with measured *in vivo* wall vibration [63]. More recently Iori *et al.* performed a preliminary study of blood flow and oxygen transport within idealised models of AVF, in presence of in-plane arterial curvature [15]. To ensure appropriate spatial and temporal resolutions, the resolution criteria set out by Valen-Sendstad was verified *a posteriori* [85]. Flow instabilities similar to those obtained by Loth *et al.* were observed, in agreement with the work of Browne *et al.*, on pressure drops in AVF [90], who also observed such structures.

2.4.1.3 Idealised vs Patient-Specific Models

Previous computational studies of blood flow in AVF and AVG can be sub-divided into two groups: those containing idealised models and those with patient-specific geometries. Studies in idealised geometries have been widely used in the field of cardiovascular biomechanics to investigate the link between hemodynamics and vascular disease. While this approach may seem over simplistic, it helps improving the understanding of basic flow characteristics, and provide a simpler framework for studying the effect of different geometrical f and flow conditions on the hemodynamics. Thus, it is normally considered a good practice before tackling more complex patient-specific simulations [16].

Ene-Iordache *et al.* used this idealised models, to study pulsatile blood flow in different end-to-end and side-to-end AVF configurations with various anastomotic angles. The authors found that the anastomotic angle affects the nature of the unsteady flow, and suggested that a more acute angle may inhibit development of IH [86, 87]. Sherwin *et al.* [88] investigated the effect of out-of-plane curvature on blood flow within simple models of AVG. Results of this study and a in-depth analysis of other geometrical features that can be observed in bypass graft, i.e. branch angles and curvatures, were summarised in 2003 in the publication by Sherwin and Doorly [91]. Particularly, it was found that the flow non-planarity notably alters the distribution of WSS at the anastomosis bed, and reduces the peak WSS. Iori *et al.* studied blood flow and oxygen transport within idealised models of AVF, in presence of in-plane arterial curvature. Results suggest that forming an AVF via a vein graft onto the outer curvature of a curved artery, reduces arterial flow unsteadiness, while low WSS and low oxygen patches are reduced when the vein is connected to a straight artery or to the inner curvature of a curved artery. It can be noted how these contrasting findings highlight the importance of ascertaining the exact mechanisms underlying development of IH in AVF [15].

Patient-specific models, on the other hand, due to their more complex geometries, do not allow easy understanding of which features affect the haemodynamics and do not offer an insight into how those features can be leveraged to modify the flow. However, they can be used to correlate haemodynamic factors to the development of IH and follow the AVF maturation or failure. Sigovan *et al.* performed CFD simulations on patient-specific geometries reconstructed from MRI scan images. Evolution of haemodynamic factors were recorded over a period of ten months, with the objective of correlating them with AVF failure. The authors found that regions of the vein exposed to flow disturbances were more prone to remodelling [92]. Also Kharboutly *et al.* performed a series of patient specific CFD simulations in 2007 and subsequently in 2010 used PIV model to cross-validate CFD results. Good agreement was found between experimental and numerical data, but it was impossible to find a correlation between blood flow disturbances and plaque formations within the geometry. Perhaps, the main limitation of this approach was that geometries were acquired only after AVF maturation, thus not allowing to observe the potential causes of failure [93, 94]. McGah *et al.* simulated blood flow in four mature AVF. They hypothesised a relation between regions with elevated TAWSS and fistula failure [95]. In 2014, the same authors studied a compliant model of AVF, showing that, even though the TAWSS is lower than in the rigid case, the peri-anastomotic area still presents very high TAWSS [96]. In the publications of Krishnamoorthy *et al.* [50] and Rajabi-Jagahrgh *et al.* [51], numerical simulations were compared with *in vivo* data from pigs, studying the relationship between fistula maturation and vein curvature. Their findings showed that either the lowest or the highest WSS values are inside the straight vein, which presented eccentric intimal-media thickness [50], and therefore the curved configuration is associated with a more favourable remodelling for fistula maturation [51].

2.4.1.4 Boundary Conditions

One last modelling point that needs to be addressed in this section is whether flow in vascular connections has to be modeled as pulsatile or it is acceptable to prescribe time-averaged boundary conditions. In reality, blood flow is obviously pulsatile, hence, there are drawbacks associated with the use of steady-state simulations, as they do not allow calculation and analysis of interesting metrics such as Oscillatory Shear Index and cannot capture intrinsically unsteady flow phenomena [45]. However, steady-state simulations are less computationally intensive and can be analysed with relative ease, offering insight that will facilitate interpretation of future more complex and costly unsteady studies [97]. In the recent publication by Iori *et al.*, it was shown that a fine temporal resolution is necessary to resolve high frequency coherent structures that are present in AVF, even when time-averaged boundary conditions are prescribed. These fine temporal structures have not been reported in previous CFD studies of the blood flow within AVF, and their harmonic content appears to be in agreement with that of stethoscope recordings of the audible 'bruit', clinically observed in functioning AVFs. The presence of a palpable thrill or bruit on auscultation is thought to be caused by flow transition to a weakly turbulent state [63]. Nonetheless, while this assumption yields interesting results, prescribing time-average inflow and outflow conditions clearly represents a significant simplification of *in vivo* conditions, highlighting the potential importance of future pulsatile studies.

2.4.2 Oxygen Transport In Computational Fluid Dynamics

Oxygen transport in medium/large arteries has been investigated in a number of previous CFD studies. Existing models can be divided into *fluid-phase* [8, 9, 6], *wall-phase* [98, 99] and *coupled fluid-wall* models [5, 11, 7, 10].

The first two solve a transport only equation respectively in the lumen or in the wall, fixing the oxygen concentration at endothelium. The *wall-phase* approach is less reported in the literature [98, 99], as it does not allow direct predictions of the effect of the local fluid-dynamics on the oxygen supply. Conversely, most recent studies follow the *fluid-phase* approach introduced by Tarbell and Qiu in 2000 [6], as it allows one to correlate, with relative ease, gross features of the flow with luminal oxygen transport. In Tarbell's model, haemoglobin is neglected and oxygen is considered as a free solute in blood. In addition a spatially constant oxygen concentration is prescribed at the wall. The imposition of a constant oxygen concentration at the wall relies on the assumption that arterial walls act as oxygen sinks. Oxygen is a low-molecular-weight species that is readily consumed by the arterial wall, thus oxygen transport is most likely to be limited by the fluid-phase [6]. Hence, regions of potential hypoxia can be identified via direct comparison of the local Sherwood number (dimensionless mass transfer coefficient) at the endothelium with the Damkhöler number (dimensionless wall reaction rate coefficient) [8, 9, 6].

This model is much easier to implement than *coupled fluid-wall* models, only requiring the solution of a supplementary transport equation, and thus has been extensively employed in a number previous of studies. In 2008 and 2009 Coppola and Caro [8, 9] applied it to study oxygen transport in helically-shaped vessels. They showed that 3-D geometrical features, such as out-of-plane curvature, highly influence mass transfer and WSS [8], and that the mixing through stirring, induced by the helical shape, can lead to more favourable outcomes in stented arteries [9]. Recently, Zheng *et al.* [100] published an article on oxygen transfer in a helically shaped bypass graft under steady inflow conditions. Similar patterns to those of Coppola and Caro [8, 9], were observed. Tarbell's model was also adopted by Tada, who in 2010, undertook numerical simulations of the mass transfer in a carotid bifurcation, coupling luminal oxygen transport with

a wall model, to account for in-wall diffusion/consumption. It was shown that the results obtained with their model differed from previous experimental results, suggesting the need for a wall-side oxygen transport model [10].

Fully coupled models offer the advantage of a more realistic representation of the oxygen transport conditions [5, 11, 7, 10]. In this case, oxygen transport is solved in both the lumen and the wall without decoupling the two transport phenomena, or prescribing a concentration at the fluid-wall interface. Perhaps, the most realistic model that can be found in the literature is that developed in 1997 by Moore and Ethier [5]. Two distinct species are used to describe oxygen dissolved in plasma and bound to haemoglobin.

In reality, oxygen is carried in blood in two forms: free oxygen dissolved in the plasma and oxygen reversibly-bound to hemoglobin, contained within red blood cells (RBC), which are subjected to shear-dependent dispersion. Several studies often omit bound oxygen in their analysis. Although the predicted patterns are able to provide an indication of potentially hypoxic regions, Moore and Ethier's work shows that ignoring the haemoglobin-bound oxygen leads to substantial prediction errors [5].

Moore and Ethier applied this model to the simulation of oxygen transport in a 2D model of a stenotic artery and tested the effect of a series of simplifying assumptions. Specifically, the effect of haemoglobin, Schmidt (Sc) number, and presence of a multi-layered wall were investigated. One of the main findings was that the distribution of the Sherwood (Sh) number (dimensionless wall normal oxygen gradient) had similar patterns either considering haemoglobin or modelling the oxygen as a free solute. This is particularly important as a simplified model, such as that proposed by Tarbell, is much easier to implement in common commercial finite volume solvers, and does not present the strong non-linearity introduced by the haemoglobin [5].

From these studies, it emerges that this approach can be a useful simplification

to predict oxygen transport in physiological conditions. However, the lack of measured Damkhöler numbers only allow qualitative analysis of hypoxic regions. In addition, neglecting haemoglobin effects might represent an excessively strong approximation. Recently, Murphy *et al.* applied a modified version of Moore and Ethier's model to study oxygen transport in stented coronary arteries, and showed that simplifying the model, resulted in significant errors in predicting oxygen transport [11]. Therefore, Tarbell's model may be inappropriate if one wants to investigate the potential presence of wall hypoxia due to unphysiological conditions, as it completely neglects any wall-side oxygen transport as well as haemoglobin effects.

In conclusion, a final point needs to be addressed: oxygen transport in blood is characterised by a very high value of Schmidt number (Sc$\sim$2700), which physically relates the relative thickness of the momentum boundary layer and mass-transfer boundary layer. At Reynolds numbers normally encountered in medium-large arteries (Re $\sim$ 10^2-10^3), the corresponding Peclet (Pe) numbers (Pe=Re·Sc) assume values between Pe $\sim$ 10^5-10^6, which indicates that the transport process is strongly dominated by convection. This poses a numerical challenge, as extremely fine boundary layer grids are required to resolve the steep wall gradients [15, 8, 5].

2.4.3 Mechanical Modelling Of Vascular Anastomosis

A large number of studies exist in literature, regarding the mechanical modelling of arteries, under various physiological and unphysiological conditions. However, only a limited portion of these have focused their attention on the modelling of vascular anastomosis.

In 2002, Perktold *et al.* studied fluid dynamics and wall mechanics within anatomically realistic models of two surgical techniques used to create bypass grafts. An iterative coupling procedure was used to couple the two problems,

which were both solved using the FE method. Linear elastic material behaviour was assumed for the wall, that was modelled as a shell, by applying the thin-wall approximation. Results of the wall mechanical studies show increased intramural stresses due to compliance mismatch, which may induce suture line hyperplasia [101]. However, healthy arteries are highly deformable composite structures with a behaviour similar to rubber and a typical non-linear stress-strain response [102]. Therefore, the assumption of a linear elastic behaviour might represent a strong limitation in faithfully reproducing realistic stress and displacement.

Subsequently, Gu *et al.* simulated, using mechanical FE analysis, the slit arteriotomy procedure, which is the surgical technique used to create end-to-side vascular anastomosis. Four consecutive static equilibrium steps were used to simulate the operation procedure and assess whether the slit opens to a width sufficient for blood supply [103]. In this study, hyperelastic shell elements were used to model the donor and recipient artery. Although this represents an improvement over the use of linear elastic materials, isotropic hyperelastic materials fail to represent the typical stress stiffening of arterial tissue, that is based on the recruitment of wavy collagen fibrils, at physiological strain levels [104].

Cacho *et al.* proposed a computational methodology to simulate coronary artery bypass graft surgery with different incision lengths. This parameter was found to have a critical influence on the graft shape and stress and in particular, stresses appeared to be higher at the heel region. In addition, severe changes in mechanical stresses are present in the transition between arterial and venous wall [105]. This study presents an improved modelling approach over the study of Gu *et al.*, as arteries were modelled as a three-layer thick-walled tube and residual stresses were included in the simulation. Furthermore, the hyperelastic anisotropic material proposed by Gasser *et al.* [106] was chosen for the wall. This material represents the state of the art in vascular structural mechanics allowing to capture the typical stress stiffening due to the embedded collagen fibres, and

thus has been used extensively in many FE studies.

More recently, there have been several studies that have also undertaken fluid-structure interaction (FSI) analysis in idealised [107] and patient-specific [96, 108] models of vascular access. While FSI has become a standard modelling approach in other cardiovascular problems, *i.e.* the prediction aneurysm rupture, the presence of rigid walls still represents one of the most common limitations of traditional CFD studies on VA haemodynamics. However, some authors suggest that rigid-wall simulations can predict HWP within the same order of accuracy of the equivalent FSI simulation [96]. Moreover, the higher computational cost is not always justified, as the calculated wall displacements have limited influence on blood flow [107, 108].

Chapter 3

Developing a Model of Oxygen Transport in Arterio-Venous Fistulae

3.1 Blood Flow

3.1.1 Governing Equations

Blood is a complex mixture of cells, proteins, lipoproteins and smaller molecules. Red and white blood cells and platelets typically comprise approximately 40% of blood by volume, and are suspended in an aqueous polymer solution, the plasma, containing electrolytes and organic molecules. While plasma exhibits a nearly Newtonian behaviour, blood shows marked non-Newtonian characteristics, mainly induced by the red blood cells tendency to aggregate at low shear rates [45]. On a macroscopic scale, blood can be considered as an incompressible non-Newtonian fluid [45]. In medium and large vessels, where non-Newtonian effects are negligible, blood flow is governed by the time-dependent incompressible

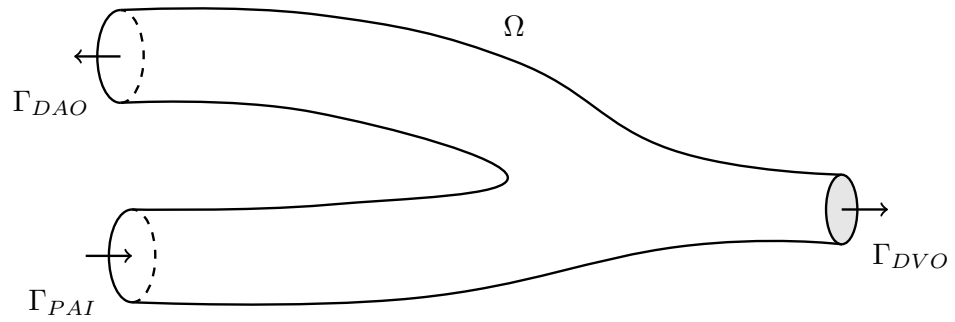

Figure 3.1: Fluid domain Ω. The arrows show the direction of the mean flow.

Navier-Stokes equations, which can be written as

$$\begin{cases} \nabla \cdot \mathbf{v} = 0 \\ \rho \left(\dfrac{\partial \mathbf{v}}{\partial t} + (\mathbf{v} \cdot \nabla)\mathbf{v} \right) = -\nabla p + \mu \nabla^2 \mathbf{v} \end{cases} \tag{3.1}$$

where μ is the viscosity of human blood, ρ is the density of human blood, $\mathbf{v}$ is the three-dimensional velocity vector field and p is the pressure field. Values of $\mu = 3.5 \times 10^{-3}\text{Pa} \cdot \text{s}$ and $\rho = 1060\text{kg} \cdot \text{m}^{-3}$ [92] were used in this study.

The assumption of Newtonian rheology ignores the well-known 'shear-thinning' property of blood [45]. However, according to Brooks *et al.* [109] shear thinning effects are significant only at shear rates below 100s^{-1}. The shear rate $\dot{\gamma}$ is defined as the square root of twice the second invariant of the strain-rate tensor $\dot{\gamma} = \sqrt{2tr\mathbf{D}^2} = \sqrt{2\mathbf{D} : \mathbf{D}}$, where the strain-rate tensor is the symmetric part of the velocity gradient tensor $\mathbf{D} = (\nabla\mathbf{v} + \nabla\mathbf{v}^T)/2$. In this study and in previous simulations the shear rates found were on an average greater than 400s^{-1} [15, 110, 111]. Exposure to high shear rate suggests widespread suppression of rouleaux aggregation, which is responsible for shear-thinning and occurs on a time-scale of order 1 s [112]. This same assumption has also been widely used in previous studies of blood flow in AVF and vascular grafts [91, 95, 63, 92, 15, 110] and therefore is considered reasonable in this study.

3.1.2 Boundary Conditions

All simulations presented here and in Chapter 5, unless otherwise stated, employ steady boundary conditions. Imposition of steady-state boundary conditions is clearly an approximation, since in reality blood flow is pulsatile. However, pulsatility has been shown to have minimal effects on transported species like oxygen and LDL [113, 114, 7].

Steady-state parabolic boundary-normal flow profiles were applied at the Proximal Arterial Inlet (PAI) and the Distal Arterial Outlet (DAO) (see Figure 3.1). At the PAI, the profile had a spatially averaged velocity V_{PAI} into the domain. At the DAO, the profile had a spatially averaged velocity V_{DAO} out from the domain. A constant (and arbitrary) reference pressure was applied at the Distal Venous Outlet (DVO). The aforementioned conditions enforce a fixed flow split between the DVO and the DAO (with antegrade flow in the distal artery).

A zero-velocity no-slip condition was applied at the endothelium and the walls were assumed to be rigid. The rigid wall assumption clearly represents a limitation, as in reality blood vessels are deformable structures. However, a recent FSI study of blood flow and wall deformation in a patient specific model of AVF, suggest that rigid-wall simulations can predict HWP within the same order of accuracy of the equivalent FSI simulation [96]. This could be attributed to the relatively small wall displacement, which has been shown to have a limited influence on blood flow [107, 108]

3.2 Oxygen Transport

As discussed in Section 2.4.2, Moore and Ethier's coupled fluid-wall model represents the state-of-the-art model to study oxygen transport in large arteries, as it includes non-linear effects due to the exchange between free and bound oxygen,

as well as a variable shear-induced RBCs dispersion coefficient [5].

Among the remaining models of oxygen transport, which exhibit various degrees of simplification, Tarbell's model [6] is definitely the most commonly used in the literature [8, 9, 6, 7]. This model only requires solution of a supplementary advection-diffusion equation, while a constant oxygen concentration is assumed at the wall.

Regions exposed to low Sherwood number (Sh), the dimensionless mass transfer coefficient, highlights potential areas of hypoxia. To establish what constitutes low Sh, Sh is compared to the Damkhöler number (Da), the dimensionless wall reaction rate coefficient, which can be estimated from wall properties. When $Sh \gg Da$, the supply exceeds the demands, thus the wall is considered to be properly oxygenated. However, when $Sh \rightarrow Da$, wall oxygen becomes strongly dependent upon the blood oxygen transport and could drop below hypoxic levels.

This model does not take into account the oxygen supplied by the vascular portion of blood vessels, which in healthy blood vessels corresponds to the adventitial layer. While this approach is appropriate for modelling oxygenation in blood vessels under normal physiological conditions, it might not be appropriate in those cases where wall oxygenation relies on aventitial supply and this might be disrupted, *e.g.* in hypertensive patients [14]. For these cases, a fully coupled wall-fluid model, such as that developed by Moore and Ethier, represents a more realistic approach to study oxygen transport in AVF. Oxygen tension is calculated in the lumen and the wall, without assuming a constant wall concentration, an assumption that according to Moore and Ethier can lead to highly misleading conclusions [5].

A more physiologically relevant characterization of oxygen transport within the wall can increase understanding of the main causes of IH development and help designing AVF configurations with a general better outcome. For this reason, it was decided to use Moore and Ethier's model for the simulations in the present

study. In the following sections, a brief overview of this model and its main features will be provided.

3.2.1 Governing Equations

3.2.1.1 Blood-side

Oxygen is carried in blood in two distinct phases: dissolved in plasma and bound to haemoglobin, a heavy molecular weight globular protein contained within RBCs. According to Moore and Ethier, oxygen transport in blood can be modelled via the solution of the following coupled transient advection-diffusion equations [5]:

$$\begin{aligned} \alpha \frac{DPO_2}{Dt} &= \alpha \nabla \cdot (D_b \nabla PO_2) + r, \\ [Hb] \frac{DS}{Dt} &= [Hb] \nabla \cdot (D_c \nabla S) - r, \end{aligned} \tag{3.2}$$

where PO_2 is the oxygen tension in plasma, D/Dt is the material derivative, α is oxygen solubility in plasma, $[Hb]$ is total oxygen carrying capacity of haemoglobin, D_b and D_c are diffusivity respectively of free oxygen and oxyhaemoglobin in blood, S is the haemoglobin saturation and r is the exchange rate between the two phases. Oxygen is dissolved in plasma, thus, according to Henry's law, oxygen tension (or partial pressure), measured in mmHg, can be used instead of concentration. The two transport equations are added and after some manipulations can be written in the following compact form:

$$\left(1 + \frac{[Hb]}{\alpha} \frac{\mathrm{d}S}{\mathrm{d}PO_2}\right) \frac{DPO_2}{Dt} = \nabla \cdot \left[D_b \left(1 + \frac{[Hb]}{\alpha} \frac{D_c}{D_b} \frac{\mathrm{d}S}{\mathrm{d}PO_2}\right) \nabla PO_2 \right]. \tag{3.3}$$

The coefficient $c_1 = (1 + ([Hb]/\alpha)(\mathrm{d}S/\mathrm{d}PO_2))$ can be interpreted as a non-constant carrying capacity, while the coefficient $c_2 = D_b(1 + ([Hb]/\alpha)(D_c/D_b)(\mathrm{d}S/\mathrm{d}PO_2))$ is a non-constant diffusivity.

Most oxygen is transported bound to the heme groups of the haemoglobin

molecules contained in RBCs. The binding of the oxygen to haemoglobin takes place in 4 successive steps, during which each oxygen molecule binds to a different heme group, determining a conformational change of the haemoglobin molecule, that influences its affinity to further oxygen molecules [115]. This behaviour can be approximated by the well-known Hill equation:

$$S = \frac{PO_2^n}{PO_2^n + PO_{2\text{-}50}^n} \tag{3.4}$$

where S is the saturation, or fractional occupancy, of a haemoglobin molecule, n is the Hill parameter and PO_{50} is the value at which the haemoglobin is 50% saturated (see Figure 3.2). Blood-side oxygen transport is coupled to wall-side oxygen transport and consumption.

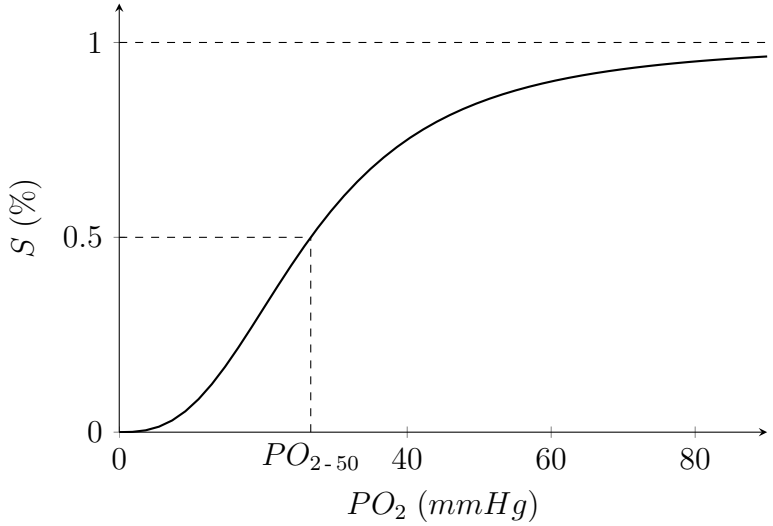

Figure 3.2: Hill's equation: oxygen saturation S for $n = 2.7$ and $PO_{2\text{-}50} = 26.6mmHg$.

3.2.1.2 Numerical Details

In order to implement Equation 3.3 in Star-CCM+, its terms need to be re-arranged appropriately. Star-CCM+, as many other commercial FV packages,

solves transport equations of the following form:

$$\frac{Dc}{Dt} = \nabla \cdot (D_F \nabla c) + S_F. \tag{3.5}$$

Equation 3.3 can be manipulated and its terms rearranged to obtain the following modified diffusivity D' and the source term S_F,

$$D_F = \frac{c_2}{c_1} \quad , \quad S_F = \frac{c_2}{{c_1}^2} \frac{[Hb]}{\alpha} \nabla PO_2 \cdot \nabla \left(\frac{\mathrm{d}S}{\mathrm{d}PO_2} \right). \tag{3.6}$$

The non-linearity of the oxygen transport problem originates from the non-linear dependence of the oxygen dissociation curve S, on plasma oxygen partial pressure [5]. Specifically, non-linearity enters the model through the term $\mathrm{d}S/\mathrm{d}PO_2$, contained in both coefficients (Figure 3.3).

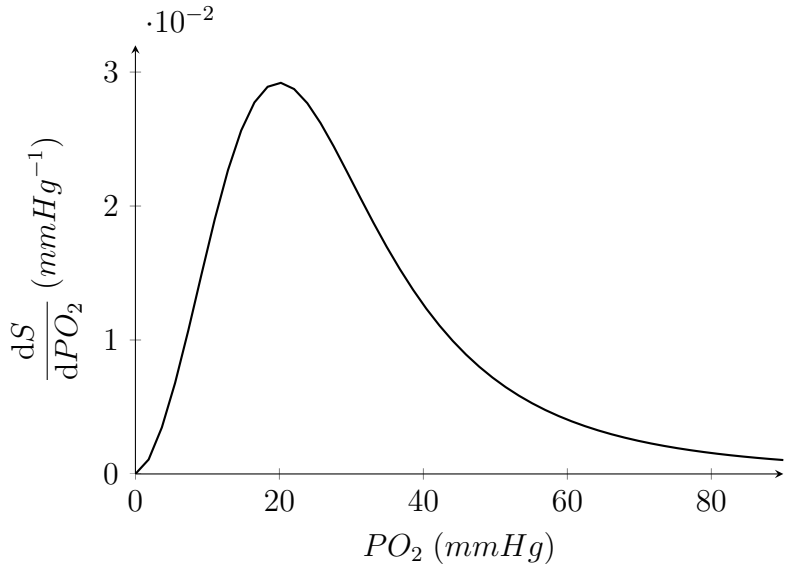

Figure 3.3: The gradient $\mathrm{d}S/\mathrm{d}PO_2$ of the oxygen saturation curve, plotted against PO_2.

3.2.1.3 Dispersion Coefficient

Oxygenated haemoglobin is carried in blood within RBCs, and D_c is usually interpreted as the diffusivity of red blood cells in blood, which is effectively zero [5].

However, it is known that red blood cells in shear flows undergo significant dispersion, thus D_c can be interpreted as the shear-augmented dispersion coefficient of RBCs.

In previous studies, its value was assumed to be the constant dispersion coefficient for red tracer cells in a straight tube at an approximate shear rate of $20s^{-1}$ [5]. However, while this is an acceptable initial approximation, at the higher shear rates that are normally encountered in large vessels, D_c is likely not to be constant [11]. To take into account this effect, Murphy *et al.* [11] extrapolated the following piece-wise linear function (Figure 3.4) to link the dispersion coefficient to the shear rate $\dot{\gamma}$:

$$D_c = \begin{cases} 5.0 \times 10^{-12} + 5.14 \times 10^{-13}\dot{\gamma} \quad for \quad 0 \leq \dot{\gamma} \leq 100s^{-1} \\ \\ 3.68 \times 10^{-11} + 1.96 \times 10^{-13}\dot{\gamma} \quad for \quad \dot{\gamma} > 100s^{-1}. \end{cases} \tag{3.7}$$

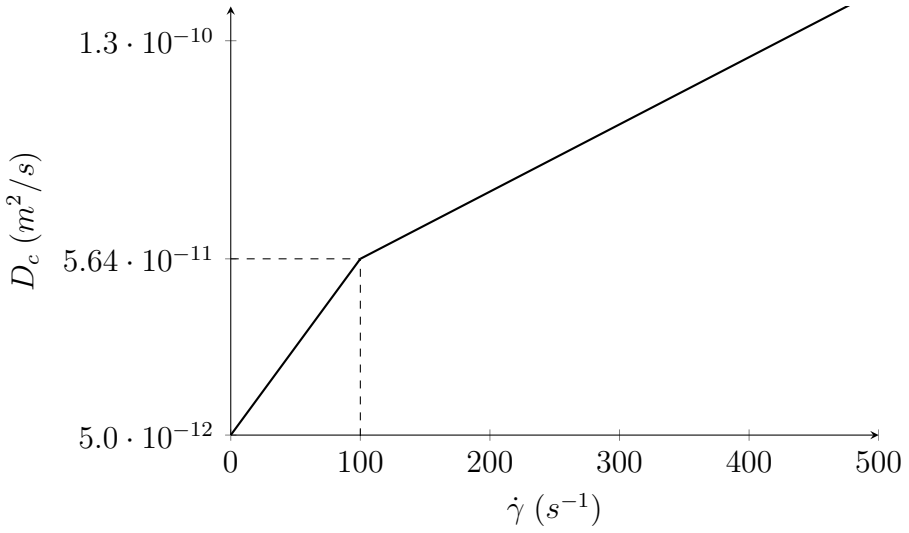

Figure 3.4: Dispersion coefficient D_c curve plotted against the shear rate $\dot{\gamma}$, from [11].

3.2.1.4 Wall Transport

Modelling transport of large molecules in living tissues, such as LDL, generally requires the solution of a convective-diffusive-reactive transport equation, which, in turn, calls for the determination of a porous media filtration velocity field [116]. However, Moore and Ethier observed that typical filtration velocities across arterial walls are $\sim 10^{-6}$ cm/s, while oxygen diffusion velocities are about two orders of magnitude greater. Hence, convection can be neglected when modelling wall oxygen transport, which results in the following much simpler reaction-diffusion equation [5]:

$$\alpha_T \frac{\partial PO_2}{\partial t} = \alpha_T \nabla \cdot (D_T \nabla PO_2) - \dot{q} \tag{3.8}$$

where α_T is the oxygen solubility in tissue, D_T is the free-oxygen diffusivity in tissue and $\dot{q}$ is the volumetric oxygen consumption rate.

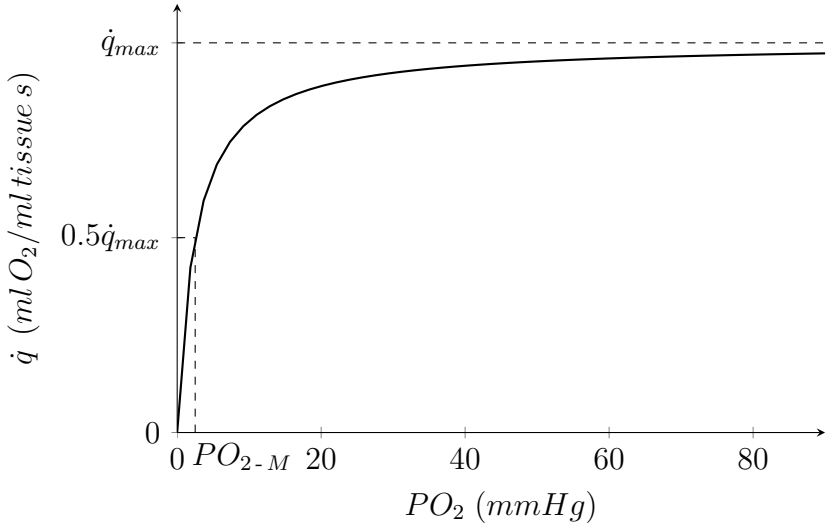

Figure 3.5: Typical oxygen consumption rate curve, following a Michaelis-Menten kinetics: $\dot{q}$ asymptotically approaches $\dot{q}_{max}$ with increasing values of PO_2; $PO_{2\text{-}M}$ is the half-maximum oxygen consumption tension.

In previous studies, it was observed that the measured oxygen consumption rate is approximately constant above a certain critical $PO_{2\text{-}M}$, and sharply drops to zero below this value. Hence, in line with previous studies, a first order

Michaelis-Menten kinetics was adopted to model this reaction ratein line with previous studies, a first order Michaelis-Menten kinetics was adopted to model this reaction rate (see Figure 3.5), which corresponds to the following equation:

$$\dot{q}(PO_2) = \dot{q}_{max} \frac{PO_2}{PO_{2\text{-}M} + PO_2} \tag{3.9}$$

where $\dot{q}_0$ is the maximum tissue consumption rate, and $PO_{2\text{-}M}$ is the half-maximum oxygen consumption tension [117]. This represents a reasonable approximation to the actual reaction rate, although the consumption is not strictly constant above the critical oxygen tension. Nonetheless, these kinetics represents a more computationally convenient approach than a zero-th order model [117].

3.2.2 Boundary Conditions

A constant oxygen tension is assumed at the flow entrance. The imposition of this boundary condition is common practice and based on the assumption that oxygen is 'well mixed' upstream of the AVF [118]. Values of about $80-100 mmHg$ and $25-40$ mmHg have been reported in the literature, respectively for arterial and venous blood [119, 120].

At the outlets, the following Neumann boundary condition is applied, $\partial PO_2 / \partial \mathbf{n} = 0$. The imposition of zero boundary-normal oxygen concentration gradients at the outlets is also standard practice [121, 7, 10, 8, 9], and minimizes the impact on the evolution of the oxygen boundary layer as it exits the domain. At the blood-wall interface, continuity of both PO_2 and oxygen flux, $\partial PO_2 / \partial \mathbf{n}$ are required. The continuity of oxygen tension relies on the assumption that the endothelium offers no resistance to the oxygen transport. Stangeby and Ethier calculated that overall, the greatest resistance to oxygen transport is exerted in the wall, while the endothelium has a negligible resistance [122].

Blood-side			
Parameter	Value	Units	Reference
$[Hb]$	0.2	$\left[\frac{\text{ml O}_2}{\text{ml blood}}\right]$	[123]
D_b	1.2×10^{-9}	$\left[\frac{\text{m}^2}{\text{s}}\right]$	[123]
α	2.5×10^{-5}	$\left[\frac{\text{ml O}_2}{\text{ml blood mmHg}}\right]$	[123]
$PO_{2\text{-}50}$	26.6	[mmHg]	[124]
n	2.7	[–]	[124]
Wall-side			
Parameter	Value	Units	Reference
α_T	2.4×10^{-5}	$\left[\frac{\text{ml O}_2}{\text{ml tissue mmHg}}\right]$	[99]
D_T	0.9×10^{-9}	$\left[\frac{\text{m}^2}{\text{s}}\right]$	[99]
$PO_{2\text{-}M}$	2.5	[mmHg]	[125]
$\dot{q}_{max\text{-}art}$	2.1×10^{-5}	$\left[\frac{\text{ml O}_2}{\text{ml tissue s}}\right]$	[5]
$\dot{q}_{max\text{-}vein}$	4.4×10^{-5}	$\left[\frac{\text{ml O}_2}{\text{ml tissue s}}\right]$	[126]

Table 3.1: Parameters used in the fluid-wall coupled oxygen transport model.

As for wall-side oxygen transport, previous authors, including Moore and Ethier and Murphy *et al.*, assumed a constant oxygen tension of 45 mmHg at the *Vasa Vasorum* (VV) level, which usually corresponds with the media-adventitia interface [5, 11]. This condition is based on the assumption that the microvasculature in the adventitia is able to deliver oxygen to the rest of the wall, to meet the local metabolic demand, maintaining a constant oxygen tension throughout the

vascular portion of the wall. This is in line with the physiology, as nourishment of medium and large blood vessels is accomplished through at least two distinct mechanisms - diffusion and convection of nutrients from luminal blood through a steep mass boundary layer and diffusion from the medial and adventitial VV [127].

The VV is a complex network of microscopic vessels that supplies the wall of large arteries and veins with oxygen and nutrients and removes metabolic wastes. In large and medium arteries, in which the intraluminal pressure is higher, VV can only perfuse the outermost wall layers (normally the adventitial layer). For this reason, these blood vessels, having thick walls, rely on both diffusion from the adventitial VV and from luminal blood to ensure adequate oxygenation of the medial layer [19]. Conversely, in large veins, where the lumen oxygen tension is lower, the VV needs to be more dense to ensure proper wall oxygenation. Furthermore, as venous luminal pressures are generally lower than in the arterial system, these VV may never be compressed, thereby maintaining adequate flow also in the innermost layers of the vascular wall [19].

The formation of AVF exposes the local circulatory system, in particular the venous system, to highly unphysiological conditions that, in turn, could have unfavourable effects on wall oxygenation. Specifically, the high arterial pressure to which veins are exposed in newly formed AVF, could excessively distend the venous wall and prevent the adequate perfusion of the venous *vasa vasorum*, leading to wall hypoxia [3]. This effect, although hypothesized in previous clinical studies, has never been thoroughly investigated. However, there is consistent evidence in the literature that mechanical factors might contribute to the initiation and development of IH [3, 128]. For this reason, the use of a spatially constant oxygen tension at the adventitia could represent too strong a limitation, especially when vessels are exposed to unphysiological conditions. On the contrary, using an oxygen source that accounts for the oxygen supply from the VV, would allow one to

model how oxygenation levels change in the wall, in relation to tissue perfusion.

Including the vascular portion of the wall in the model means that a further boundary condition has to be defined at the interface between the adventitia and the surrounding tissue. Transmural oxygen tension profiles, measured by Buerk and Goldstick in rabbit aortas and dog femoral arteries using oxygen microelectrodes, exhibit a plateau in the adventitial layer [118], which suggests the existence of a negligible oxygen flux at the vessel outer surface. Hence, in line with this observation, a zero oxygen flux boundary condition was prescribed at this boundary.

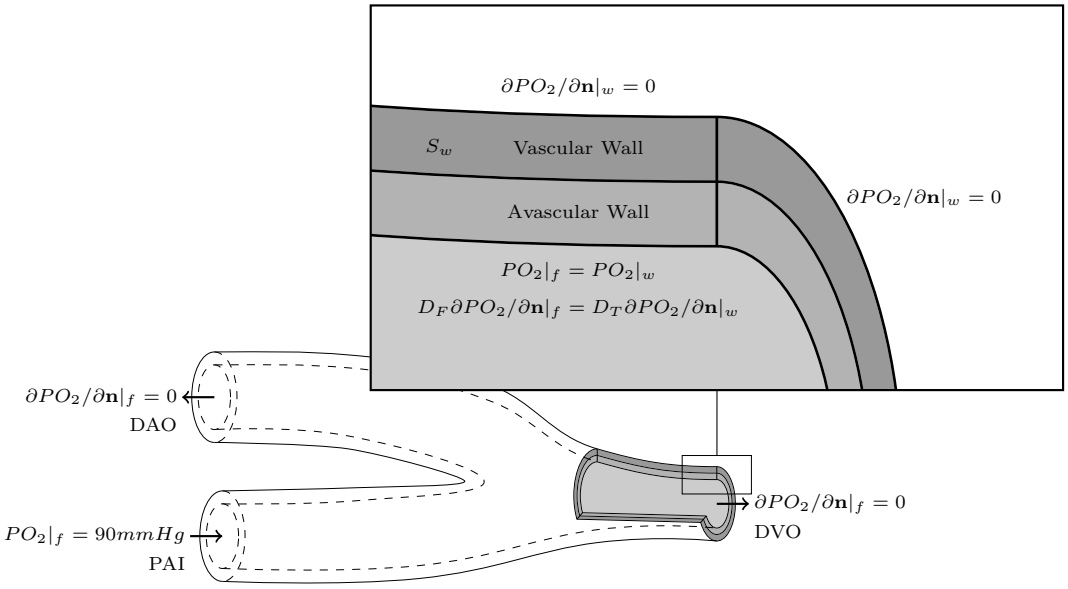

Figure 3.6: Boundary conditions for the oxygen transport model.

3.2.3 Tissue Oxygenation

Tissue oxygen transport has been studied since the early 20th century. The famous Krogh-Erlang tissue cylinder model [129] is one of early models to theoretically investigate microvascular oxygen transport into living tissues and has

served as the foundation for many subsequent studies. In this model, Krogh assumes a cylinder of tissue surrounding a single capillary, whose wall offers no resistance to oxygen diffusion. In addition, cylindrical symmetry and steady state transport are assumed, while axial diffusion is expected to be negligible [129].

Several studies derived from Krogh's model have investigated the oxygenation of healthy tissues, where the more regular and evenly spaced microvasculature can be adequately described by these simple assumptions [130, 117]. Other studies have focused on the oxygentation of unhealthy tissues, specifically tumor tissues, where, on the other hand, the distribution of microvessels is highly heterogenous, and causes the occurrence of microregions of hypoxia [131, 132, 125, 133, 134]. One of the main limitations of Krogh-Erlang's model, in fact, is that only oxygen transport around a single microvessel is taken into consideration, thus, making it inappropriate to study complex vascular networks. In recent years, the need to simulate such phenomena has driven the development of models with more realistic vascular geometries [125, 133, 135, 134, 136]. Most of these share a similar approach - *i.e.* each microvessel is represented as a discrete oxygen source - while a variety of numerical techniques and boundary conditions have been adopted to determine the oxygen field.

Secomb *et al.* calculated the oxygen field as the superposition of the fields resulting from single oxygen sources, using Green's functions to determine the effect of individual sources [133]. Conversely, in Dasu *et al.* [125] and Kelly *et al.* [135], a source term, representing the oxygen supply of single microvessels, was added to Equation 3.8. The oxygen field was then calculated from these distributed sources, assuming localised concentration spikes, corresponding to vessel positions [136]. However, the complexity of the VV network, along with the lack of a clear morphological characterisation, make this model impractical for the intents and purposes of this study. Hence, instead of modelling discrete microvessels, it is proposed to use a spatially-average source to model the supply of oxygen

from the VV. Using a spatially-average source has the obvious limitation that the model is not able to predict potential microregions of hypoxia. Nonetheless, this modelling approach is equally capable of describing wall oxygenation from a macroscopic perspective. In addition, such an approach offers a simple way to control the VV oxygen supply, by simply acting on the portion of perfused microvessels in the wall.

3.2.3.1 Vasa Vasorum Oxygen Source

To quantify the oxygen supplied from a single microvessel, let us consider a straight capillary, consisting of two concentric cylinders of radius $r_1 = R$ and $r_2 = R + t$, with R inner radius and t wall thickness. Oxygen transport across the wall is purely diffusive (convection can be neglected [5]), and the process can be considered steady, as the non-stationary evolution of the system is very short. According to Hill [137], in fact, any change in oxygenation patterns, due to perfusion-related events, have the time scale of minutes or hours, while the formation of new vessels through angiogenesis takes place over days or weeks. In addition, oxygen consumption within the wall of a single capillary can be neglected [136]. Under these assumptions, oxygen transport is described by the following differential equation [138],

$$\frac{1}{r}\frac{\partial}{\partial r}\left(r\frac{\partial PO_2}{\partial r}\right) = 0 \tag{3.10}$$

that has to be solved subject to the following boundary conditions $PO_2(r_1) = PO_{2\text{-}cap}$ and $PO_2(r_2) = PO_{2\text{-}tis}$ (see Fig. 3.7). In particular, the assumption that $PO_2(r_1) = PO_{2\text{-}cap}$ is based on the fact that mean velocities in the microcirculatory district are in the order of $10^{-2} m/s$, thus making the blood-side mass transfer resistance negligible [45]. Solution of Eq. 3.10 yields

$$PO_2(r) = a_1 \ln(r) + a_2 \tag{3.11}$$

with

$$a_1 = \frac{PO_{2\text{-}cap} - PO_{2\text{-}tis}}{\ln(r_1/r_2)}, \quad a_2 = \frac{PO_{2\text{-}tis}\ln(r_1) - PO_{2\text{-}cap}\ln(r_2)}{\ln(r_1/r_2)} \tag{3.12}$$

The diffusive flux F of a single capillary can be calculated as

$$F = -D_w \frac{\partial PO_2}{\partial r}\bigg|_R, \tag{3.13}$$

with D_w wall diffusivity. From Equation 3.10 it is easy to show that $\partial PO_2/\partial r = a_1/r$ and thus,

$$F = -D_w \frac{PO_{2\text{-}cap} - PO_{2\text{-}tis}}{R\ln(r_1/r_2)} = D_w \frac{PO_{2\text{-}cap} - PO_{2\text{-}tis}}{R\ln(1 + t/R)}. \tag{3.14}$$

Assuming that the wall thickness is much smaller than the radius, then $R\ln(1 + t/R) \sim 1/t$ and the flux becomes $F = P_m(PO_{2\text{-}cap} - PO_{2\text{-}tis})$, with the wall permeability $P_m = D_w/t$. Then the net rate of oxygen diffusing for a single capillary per unit volume is given by,

$$S_c = \frac{1}{\pi R^2 L}\int_0^{2\pi}\int_0^L FRd\theta dL = 2\frac{P_m}{R}(PO_{2\text{-}cap} - PO_{2\text{-}tis}). \tag{3.15}$$

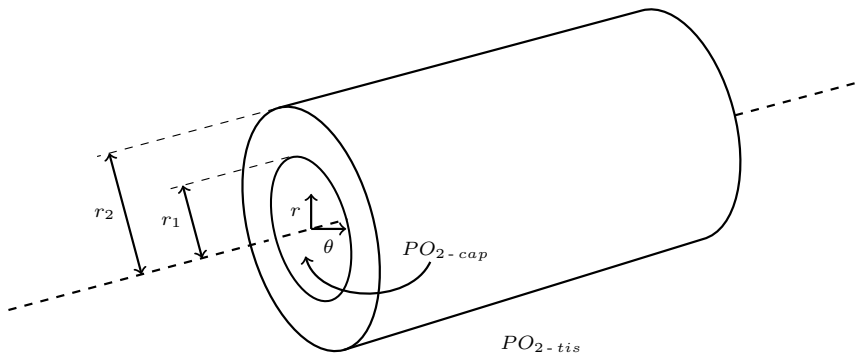

Figure 3.7: Simplified model of oxygen transport in a straight capillary, from [136].

This simple model was previously adopted in [135] by Kelly *et al.* and in [125] by Dasu *et al.* to study oxygenation in a tumor. The microvasculature was explicitly represented by individual vessels lying perpendicular to the 2D simulation domain. Two different sources were included in the reaction-diffusion equation (Eq. 3.8), to model oxygen gain from the arterioles, where the oxygen tension is between $80 - 100$ mmHg, and loss back to the capillaries and venules, where the oxygen tension is between $25 - 40$ mmHg [125]. As already anticipated in the previous section, it was decided to use a spatially-average oxygen source. Oxygenated and deoxygenated blood, contained respectively in the arterioles and in the capillaries/venules, can be considered as two different compartments, having spatially-average properties. These two compartments are assumed to exchange oxygen with the surrounding tissue, without altering their concentration, through the resistance $2P_m/R$. The average VV source per unit volume can be calculated from S_c considering an average microvessel volume fraction, for each compartment. This corresponds to adding to Equation 3.8 the following source term:

$$S_w = 2\frac{P_{m\text{-}oxy}}{R_{oxy}}(PO_{2\text{-}oxy} - PO_2)V_{f\text{-}oxy} + 2\frac{P_{m\text{-}deoxy}}{R_{deoxy}}(PO_{2\text{-}deoxy} - PO_2)V_{f\text{-}deoxy} \tag{3.16}$$

where $V_{f\text{-}oxy}$ and $V_{f\text{-}deoxy}$ are the volume fractions of microvessel per tissue volume in each compartment, R_{oxy} and R_{deoxy} the average microvascular radii, $P_{m\text{-}oxy}$ and $P_{m\text{-}deoxy}$ the average permeabilities of the two compartments.

Parameter	Units	Value	Reference
MVD	$\frac{\text{N vessels}}{\text{mm}^2}$	$0.2 - 3$	[139]
R_{oxy}	m	$18 - 30 \times 10^{-6}$	[140]
R_{deoxy}	m	$11 - 75 \times 10^{-6}$	[140]
ω_{art}	-	10%	[141]
ω_{cap}	-	15%	[141]
ω_{ven}	-	75%	[141]
PO_{2-oxy}	mmHg	95	[135]
$PO_{2-deoxy}$	mmHg	40	[135]
t	m	1×10^{-6}	[140]

Table 3.2: Parameters for the VV oxygen source in Eq. 3.16.

The mean microvascular volume fraction in tissue can be calculated from experimental Microvessel Densities (MVD), measured from histogical samples in number of vessels per unit area. Then, from the relative volume fraction of arterioles, capillaries and venules with respect to the microvasculature (ω_{art}, ω_{cap}, ω_{ven}) [141], the volume fraction of each compartment can be calculated as $V_{f\text{-}oxy} = V_f\omega_{art}$ and $V_{f\text{-}deoxy} = V_f(\omega_{cap} + \omega_{ven})$. In this simple model, tissutal oxygen supply can be modulated by acting on the volume fraction of perfused microvessels. The next section will describe how perfusion is regulated in response to wall stress.

3.3 Oxygen Transport In A Straight Vessel

To verify the implementation of the model in Star-CCM+, Equations 3.3 and 3.8 were solved under fully-developed steady flow in a straight vessel. Under these conditions, the following simplifying assumptions can be made:

- Steady-state solution: $\text{dPO}_2/\text{dt} = 0$;

- Fully-developed Poiseuille velocity profile: $\mathbf{v}(r) = 2\bar{v}\,(1-(r/R)^2)\,\hat{z}$, with $\bar{v}$ average inflow velocity and $\hat{z}$ unit vector is along z-axis (see Fig. 3.8);
- Axial symmetry: $\partial(\cdot)/\partial\theta = 0$, with θ azimuthal angle.

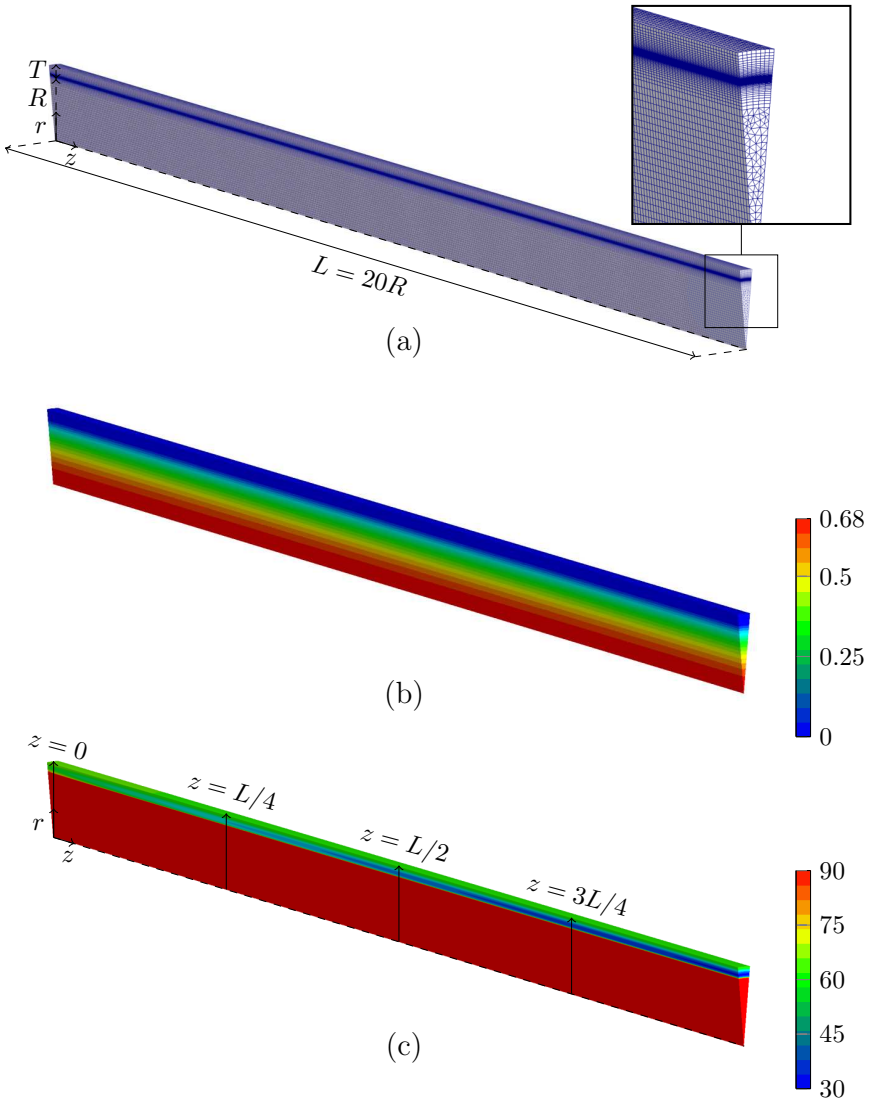

Figure 3.8: Oxygen transport in a straight vessel, solved in Star-CCM+: (a) the computational grid used; (b) velocity magnitude (m/s); (c) oxygen tension (mmHg).

In a cylindrical reference frame and under the previous assumptions, Equations

3.3 and 3.8 become respectively:

$$2\bar{v}\left(1-\frac{r}{R}^2\right)\frac{\partial PO_2}{\partial z}=\frac{1}{c_1}\left(\frac{\partial c_1}{\partial r}\frac{\partial PO_2}{\partial r}+\frac{\partial c_1}{\partial z}\frac{\partial PO_2}{\partial z}\right)+\frac{c_2}{c_1}\left(\frac{1}{r}\frac{\partial}{\partial r}\left(r\frac{\partial PO_2}{\partial r}\right)+\frac{\partial^2 PO_2}{\partial z^2}\right)$$

$$\frac{\partial}{\partial r}\left(r\frac{\partial PO_2}{\partial r}\right)+\frac{\partial^2 PO_2}{\partial z^2}=\frac{(-\dot{q}(PO_2)+S_w(PO_2))}{\alpha_t D_t} \tag{3.17}$$

These equations were integrated numerically using the Finite Difference method (FD) and solved using the Successive Over Relaxation method. The domain is discretised into a rectangular grid of size $N_r \times N_z$, and differential terms are written using a second-order central-difference scheme. Because luminal oxygen transport to the wall occurs only within a thin annulus next to the wall, *i.e.* mass transport boundary layer, only this region was considered in the model [142]. In contrast, the vessel geometry was modelled in Star-CCM+ using a five degree circumferential wedge, as shown in Figure 3.8-(a), and periodic boundary conditions were prescribed at the sides.

A vessel having radius $R = 0.003$ m, wall thickness $T = 0.0004$ m and length $L = 20R$ is considered. A physiological inflow Reynolds number of 600 is assumed, corresponding to a mean velocity $\bar{v} = 0.67$ m/s [45]. In healthy arteries, the ratio of adventitia thickness to total wall thickness is normally reported to be between $0.3 - 0.4$ [143]. According to the literature, VV are exclusively contained in this layer, thus the VV oxygen source S_w is prescribed only inside the outer third of the wall.

The following boundary conditions are prescribed:

- 'Well mixed' oxygen concentration at the entrance: $PO_{2f}|_{z=0} = 90mmHg$;
- Zero boundary-normal oxygen concentration gradients at the outlet: $dPO_2/dz|_{z=0,L} = 0$;
- Continuity of $PO_{2f}|_{r=R} = PO_{2w}|_{r=R}$ and oxygen flux $D_f \partial PO_{2f}/\partial \mathbf{n}|_{r=R} =$

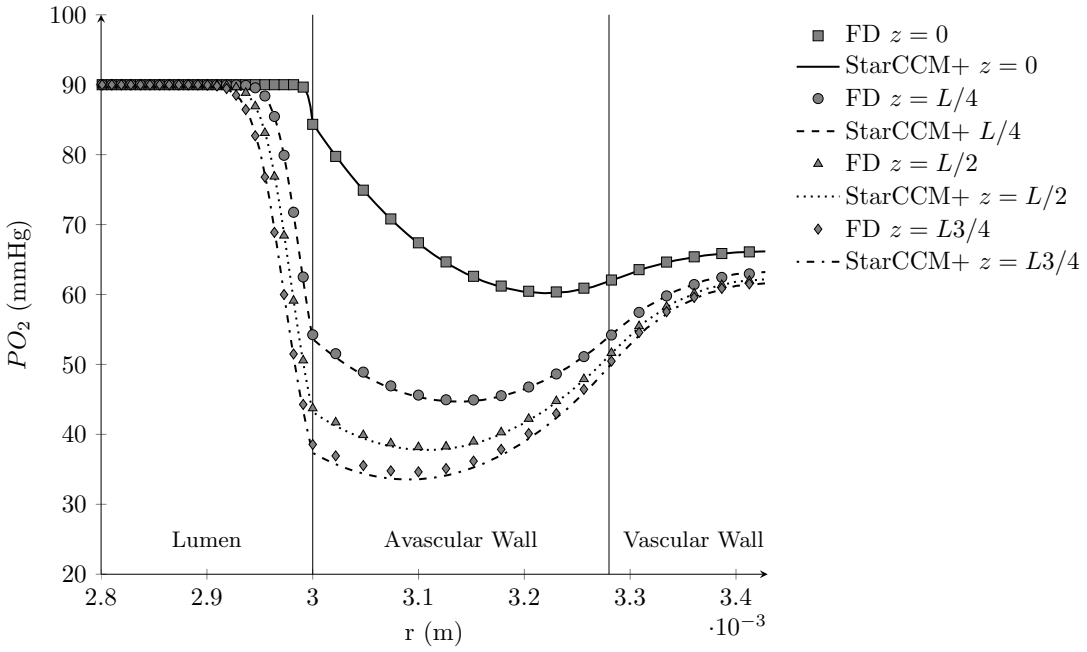

Figure 3.9: Oxygen tension profiles calculated in StarCCM+ and using the FD method. Sections with increasing values of z are shown (see Figure 3.8-(c)).

$D_w \partial PO_{2w}/\partial \mathbf{n}|_{r=R}$ at the wall-lumen interface;

- Zero oxygen flux at the external boundary: $dPO_{2w}/dt|_{r=R+T} = 0$;

Figure 3.9 shows oxygen tension in the boundary layer and the wall, obtained from Star-CCM+ and from the FD solver at increasing values of z. Good agreement is found between the two numerical techniques and the oxygen profiles obtained, appear to be similar to those measured in vivo by Buerk and Goldstick [118] and by Santilli *et al.* [17].

Previous studies used simplified models to reduce computational expense and complexity. Following the work of Moore and Ethier and Murphy *et al.* [5, 11], different modelling assumptions were tested, 'switching off' different parts of the model:

- *Model 1*: Full coupled fluid-wall model with normally perfused wall;
- *Model 2*: Both the free and bound oxygen are modelled and the wall is

considered normally perfused, but the non-linearity from Hill's Equation is removed ($dS/dPO_2 = \overline{dS/dPO_2}$);

- *Model 3*: Only free oxygen is modelled ($[HB] = 0$) and the wall is considered normally perfused;
- *Model 4*: Both the free and bound oxygen are modelled and the wall is considered normally perfused, but ($D_c = 0$), thus neglecting the shear-augmented dispersion of RBCs;
- *Model 5*: Both the free and bound oxygen are modelled but the wall is considered not perfused ($S_w = 0$).

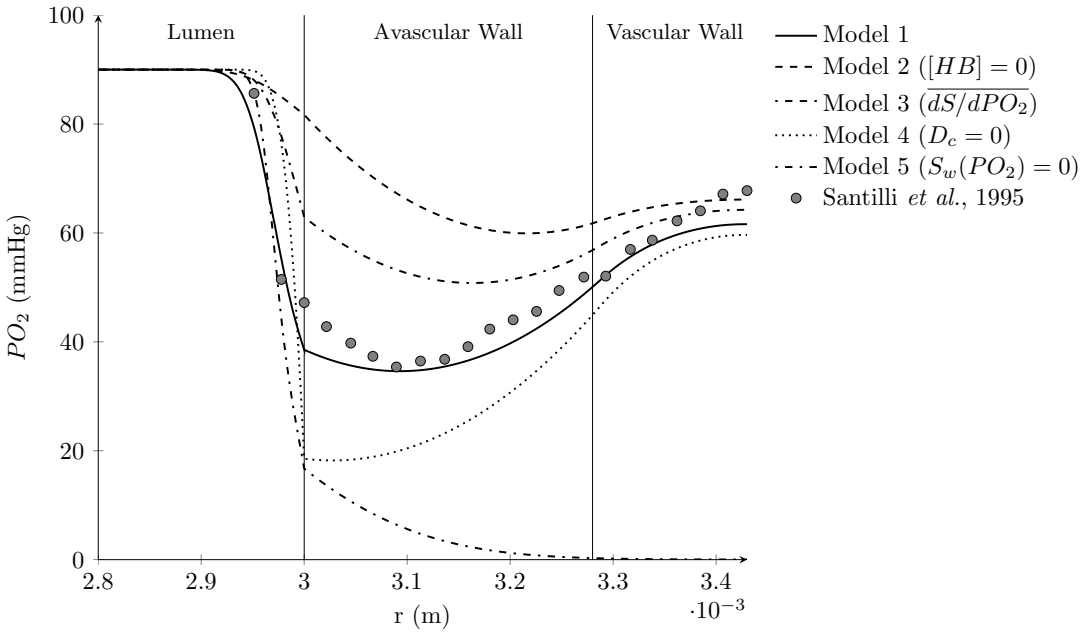

Figure 3.10: Comparison of the predicted oxygen concentration in the boundary layer and the wall. Results are shown for $z = L/2$. For comparison a typical oxygen concentration profile measured *in-vivo* by Santilli *et al.* is shown [17].

Results of these tests are shown in Figure 3.10 for $z = L/2$. Models 1 and 4 both retains the non-linearity of the haemoglobin saturation gradient $\mathrm{d}S/\mathrm{d}PO_2$. Free oxygen accounts for only 1.5% of the total transported oxygen, while the

most part is bound to oxyhaemoglobin. Neglecting the exchange of bound oxygen between the RBCs and the plasma can have a significant effect on the oxygen transport [5].

Models 2 and 3, where this effect is completely or partially lost, tend to overpredict the value of PO_2. In particular, Model 2 leads to large errors, as it completely fails to predict the steep oxygen gradient, observed by *in-vitro* studies [118, 144]. In Model 3, on the other hand, the non-linearity due to Hill's equation was removed by considering a linearised form of the derivative $\overline{\mathrm{d}S/\mathrm{d}PO_2} = n\bar{S}(1-\bar{S})P\bar{O}_2$, with $P\bar{O}_2 = 75mmHg$ and $\bar{S} = S(P\bar{O}_2)$. Moore and Ethier observed that the linearised model gives excellent results for physiologically realistic boundary conditions [5]. While this assumption makes the model computationally more efficient, its accuracy strongly relies on both the working oxygen tensions and the chosen mean oxygen $P\bar{O}_2$, about which S is linearised. What that means is that in those locations where the PO_2 within the boundary layer is lower than $P\bar{O}_2$, linearising dS/dPO_2 produces a higher diffusivity, leading to an overprediction of the local oxygen tension at the endothelium [11]. Conversely, Model 4, where no dispersion of RBCs is accounted for ($D_c = 0$), consistently underpredicts the value of PO_2, due to a lower effective diffusivity, which causes a diminished oxygen flux at the wall [11].

Finally, in Model 5, the effect of shutting off completely the VV oxygen source ($S_w = 0$) is tested. Physiologically, this corresponds to a completely non-perfused VV, that can occur for instance, when the VV are stripped from the wall [145], and implies that the wall entirely relies on luminal transport, to meet its metabolic demands. When the oxygen supplied by luminal blood is not sufficient, this leads to pathologically low values of oxygen tension.

3.3.1 Sensitivity to Modelling Parameters

The model described here presents a large number of parameters, some of which exhibit a degree of variability in reality. To assess the impact of individual parameters on the oxygen transport, a parametric analysis was carried out on the straight vessel model described in the previous section. Each of them was tested separately, according to the values listed in Table 3.3, and the deviation from a reference case of the minimum oxygen tension was used as a measure of sensitivity to that parameter (see Figure 3.11).

Parameter	Reference Case	Minimum	Maximum	Units
n	2.7	1.7	3.2	-
$PO_{2\text{-}50}$	26.6	23.1	30.6	[mmHg]
α_T	2.5×10^{-5}	2.5×10^{-5}	3.8×10^{-5}	$\left[\frac{\text{ml O}_2}{\text{ml blood mmHg}}\right]$
D_T	9.0×10^{-10}	7.2×10^{-10}	9.0×10^{-10}	$\left[\frac{\text{m}^2}{\text{s}}\right]$
$PO_{2\text{-}M}$	2.5	0.5	2.5	$[mmHg]$
$\dot{q}_{max}$	2.1×10^{-5}	1.05×10^{-5}	3.15×10^{-5}	$\left[\frac{\text{ml O}_2}{\text{ml tissue s}}\right]$
V_f	1.0×10^{-3}	0.5×10^{-3}	1.5×10^{-3}	$\left[\frac{\text{ml VV}}{\text{ml tissue}}\right]$
V_f depth	1/3	0	2/3	[mmHg]
Inflow Re	600	300	900	-

Table 3.3: Minimum and maximum parameters used in the sensitivity analysis

Among the parameters listed in Table 3.1, $[HB]$, α and D_b can be considered constant in human blood, under normal physiological conditions [123]. By contrast, the oxygen saturation curve follows the so-called Bohr effect, according to which haemoglobin's oxygen binding affinity is affected by blood temperature,

acidity and concentration of carbon dioxide. Bohr effect is particularly important in tissues with a high metabolic demand, as the local increase in temperature, CO_2 and pH result in a lower binding affinity and thus an augmented oxygen release from the haemoglobin proteins. This induces a horizontal shift and a change of slope in the saturation curve, which is due to changes in $PO_{2\text{-}50}$ and n, respectively [124]. Of the two parameters, n has the most significant effect, especially at its lower value, while changes due to $PO_{2\text{-}50}$ are almost negligible. Particularly, for n=1.7, the oxygen saturation S drops down at the values that are normally found in the boundary layer, inducing an increased oxygen release.

The oxygen solubility in the wall, α_T, remains relatively constant in normal vessels, as the cellular composition of the wall does not vary extensively. However, its value has been observed to be slightly increased in the intima of vessels having high fat and calcium content, *i.e.* a typical condition that occurs in the presence of a plaque lesion [99]. While this situation is not likely to happen in healthy vessels, increased oxygen solubility in the wall has a dramatic effect on the transport, lowering the wall-side oxygen transport resistance. However, as Murphy *et al.* observed, the presence of a plaque also causes lower values of wall oxygen diffusivity and thicker walls, which have been shown to have adverse effects on oxygen transport [11].

The oxygen diffusivity in arterial tissue, D_T, does not show large variability [99]. This parameter has a modest but not negligible effect on wall transport, as a lower D_T increases the wall-side oxygen transport resistance. However, according to Richardson, D_T is fairly constant in the arteries of healthy adults, as the lower value of D_T that has been used here, have been only reported in the intima of newborn babies [99]

As for the half-maximum oxygen consumption tension, several values have been reported in previous studies [146, 125]. A lower value of $PO_{2\text{-}M}$ has the effect of shifting the Michaelis-Menten reaction rate curve to the left, slightly

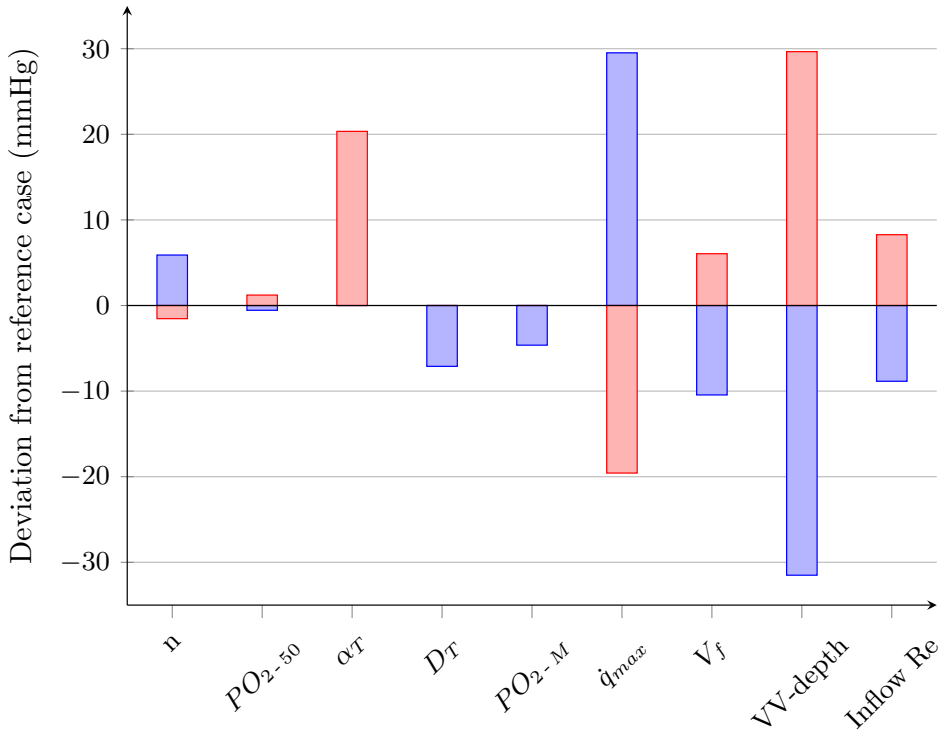

Figure 3.11: Deviation of the minimum oxygen tension from reference case, expressed in mmHg. Minimum and maximum parameter values in blue and red, respectively (see Table 3.3).

increasing the oxygen consumption in the wall. This, however, has only a modest effect on wall oxygen transport.

By contrast, oxygen tension in the wall appears to be very sensitive to changes in the maximum oxygen consumption rate - a ±50% variation was considered for $\dot{q}_{max}$. This is particularly significant, as this parameter exhibts a large physiological range. Schneiderman and Goldstick estimated values of 2.1 and 3.5 $ml\,O_2/(ml\,tissue\,s)$ respectively for the media and the intima of the human thoracic aorta [142], while Richardson measured values of 1.2 and 2.4 $ml\,O_2/(ml\,tissue\,s)$, respectively for the intima and media of healthy coronary arteries [99]. In peripheral veins this parameter assumes larger values, as measured by Piola *et al.* in human saphenous veins ($\dot{q}_{max} = 4.4\,\mathrm{ml\,O_2/(ml\,tissue\,s)}$) [126]. This large variability can be attributed to the difference in metabolic demand that exists between

tissues presenting different cellular composition. In particular, the higher oxygen consumption of peripheral veins can be explained by the larger presence of SMCs, that are known to have a higher metabolic demand than ECs and fibroblasts. Further, Hill observed significant differences between the consumption rate of muscle cells that are active or at rest [137].

To analyse the effect of the VV oxygen source, S_w, on the oxygen transport, two additional parameters were tested, namely the volume fraction of microvessels, V_f, and the depth to which the VV penetrates in the wall, VV-depth. A $\pm 50\%$ variation was considered for V_f, while a vascular region corresponding to two thirds of the wall and no VV perfusion were considered for VV-depth. Both parameters appear to have a significant effect on wall oxygen tension, particularly, VV-depth. This can be explained by the fact that changes in VV-depth not only affect the total amount of oxygen supplied to the wall, but also modify the thickness of the avascular wall. In fact, the oxygen tension in the vascular portion of the wall is the result of the balance between VV oxygen supply and consumption rate.

Finally, two additional values of inflow Re were tested to assess the sensitivity of oxygen transport to haemodynamics. As expected, changes in inflow Re have a significant effect on oxygen transfer. Results in Table 3.3 seem to partially contradict the findings of Moore and Ethier [5], who argue that oxygen transport is almost only dominated by the wall-side mass transfer resistance. This can be attributed to the balance between wall oxygen consumption and oxygen supply by the blood-side through the oxygen boundary layer resistance and by the VV. For instance, thick-walled vessels, like those used in Moore and Ethier's work, have an overall greater oxygen consumption and a thicker avascular wall, which offers a greater resistance to oxygen transport. This means that haemodynamic effects have only secondary importance in determining the wall oxygen tension. By contrast, in thinner vessels, oxygen transport is dominated by the oxygen

boundary layer resistance [147].

3.3.2 Grid Convergence

Grid convergence of the prism boundary layer mesh was assessed by running simulations of the straight vessel model on four successively finer discretisations, using Star-CCM+ v11.02.11. For each mesh, the number of prismatic layers, the overall number of elements in the prismatic layer N_{elem} and the first element thickness Δx are given in Table 3.4. A fixed total boundary layer thickness of $4.0 \times 10^{-4} m$, a geometric progression expansion and a fixed expansion rate of 1.15 were used throughout the convergence study. Also, a fixed number of prismatic layers (35) was used for the wall-side mesh, with the first element thickness (on the endothelium side) equal to its respective Δx on the blood-side mesh. A geometric progression expansion and a fixed expansion rate of 1.15 were also used for the wall-side mesh.

Mesh	Prismatic Layers	N_{elem}	Δx	$f = min(PO_2)$
0	15	6.0E4	$7.2 \times 10^{-6} m$	35.67 mmHg
1	25	1.0E5	$1.8 \times 10^{-6} m$	33.37 mmHg
2	35	1.4E5	$4.4 \times 10^{-7} m$	32.45 mmHg
3	45	1.8E5	$1.1 \times 10^{-7} m$	32.09 mmHg
	$\epsilon_{10} = 0.043$	$E_{10} = 0.064$	$GCI_{10} = 5.41\%$	$GCI_{21} r_{21}^{p} / GCI_{10} = 1.03$
	$\epsilon_{21} = 0.017$	$E_{21} = 0.027$	$GCI_{21} = 2.13\%$	$GCI_{32} r_{32}^{p} / GCI_{21} = 1.05$
	$\epsilon_{32} = 0.006$	$E_{32} = 0.011$	$GCI_{32} = 0.86\%$	-

Table 3.4: Grid convegence study.

Grid convergence was tested for the minimum PO_2, using the grid convergence index (GCI) method, which is based on Richardson extrapolation [148]. For each grid refinement, the following fractional error was estimated:

$$E_{i,j} = \frac{\epsilon_{i,j}}{r_{i,j}^{p} - 1} \tag{3.18}$$

where p is the convergence order, $r_{i,j} = \Delta x_i / \Delta x_j$ is the refinement ratio and $\epsilon_{i,j}$ is the relative error, which is defined as

$$\epsilon_{i,j} = \frac{f_i - f_j}{f_i} \tag{3.19}$$

with $f = min(PO_2)$. Then, the grid convergence index can be defined as:

$$GCI_{i,j} = F_a \left| E_{i,j} \right| \tag{3.20}$$

for a factor of safety $F_a = 1.25$ [148]. For a fixed refinement ratio $r \sim 4$, p can be estimated as follow,

$$p = \ln \left(\frac{f_2 - f_1}{f_3 - f_2} \right) / \ln(r). \tag{3.21}$$

The asymptotic value of f for a grid spacing equal to zero can be estimated as

$$f_{exact} \approx f_3 - \frac{f_3 - f_2}{r^p - 1} \tag{3.22}$$

and percentage errors from f asymptotic, calculated as $E_{exact} = (f_i - f_{exact})/f_{exact}$, are shown in Figure 3.12. A p of about 0.65 was calculated; this slow order of convergence reflects the stiff nature of the mass-transport equation. Based on the results presented in Table 3.4 and Figure 3.12, it was decided to use the prismatic layer from Mesh 2, for the simulations in this Chapter and in Chapter 5.

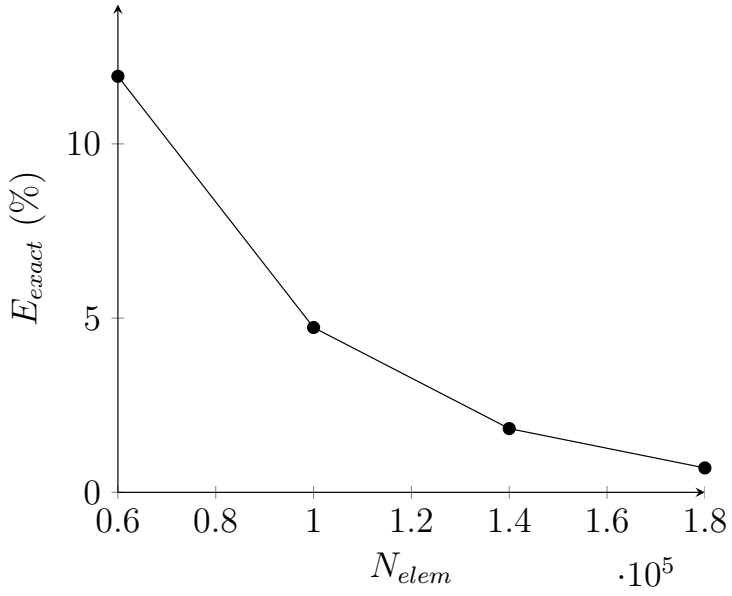

Figure 3.12: Percentage errors from E_{exact} plotted against N_{elem}.

Chapter 4

Developing a Model of Arterio-Venous Fistulae Surgery

As discussed in Chapter 3, the wall of medium and large blood vessels receives oxygen both from luminal blood and the VV network. While oxygen supplied by the luminal side depends on local features of the blood flow, adventitial oxygenation can be affected by inadequate VV perfusion [127].

Several studies speculate that VV perfusion can vary in response to external mechanical forces [128, 3, 19]. The formation of AVF exposes the local circulatory system, particularly the vein, to highly non-physiological conditions, such as increased flow rates, pressures and mechanical deformation [2]. To the author's knowledge, of all the studies that investigated vascular access from a mechanical standpoint, none has attempted to characterise VV perfusion, in relation to solid stress and deformation.

For this reason, an idealised FE model of AVF surgery was developed to determine wall stress and deformation and estimate wall perfusion. These wall perfusion fields will be then used in conjunction with the oxygen transport model described in Chapter 3, to define an oxygen source in the vascular portion of

the vascular wall and to calculate wall oxygenation. In the next section, a brief overview on microvascular perfusion and flow regulation is provided, and the major challenges associated with developing models of microvascular perfusion are highlighted.

4.1 Microvascular Perfusion

Blood flow in the microcirculation is controlled to meet the tissue metabolic demand and is achieved through the integration of multiple interacting mechanisms, including sensitivity to pressure, flow rate, metabolic levels and other chemical mediators [149].

Flow in a particular region of the body is regulated by modulating the number of recruited capillaries. The microvasculature plays an important role in regulating flows as 70% of flow resistance resides at the arteriolar level [45]. The number and location of recruited capillaries is controlled by terminal arterioles, which can modulate their muscle tone and in turn their vascular resistance, to control the flow to the capillary district they feed [150]. EC and SMC are thought to be the site of autoregulation, as they can sense and modulate their function when exposed to changes in the local biomechanical and chemical environment.

The myogenic response is a regulatory response of these arterioles, which can contract to counteract an increased luminal pressure that would overly distend the vessel lumen [151, 152]. Flow-mediated vasodilation is another potent autoregulatory mechanism, mediated by a local release of nitric oxide (NO), which occurs when the endothelium senses an increased WSS. Among all microvessels, large arterioles are most sensitive to this control mechanism [153, 152]. The third mechanism is a homeostatic response which modulates microvascular blood flow to meet the local metabolic demand. Although, it was initially thought to be mediated by adenosine, now it is widely accepted that a broad spectrum of metabolic mediators participate in the response [152].

4.1.1 Microvascular Perfusion in Response to Mechanical Forces

The physiology of microvascular perfusion has been the object of study for almost a century, and to this date, no model capable of predicting microvascular perfusion in response to mechanical forces can be found in the literature. However, there is substantial evidence suggesting that particular solid stress and deformation patterns can result in collapsed or poorly perfused microvessels.

4.1.1.1 Coronary Circulation

Coronary perfusion is, perhaps, one of the most well-studied physiological mechanisms. Myocardial contraction was first proposed as an impeding factor to coronary flow by Scaramucci in 1695 and Sabiston and Gregg were the first to observe coronary flow reduction in response to intramural stress, in 1957 [154].

Following these findings, a number of models sought to explain the link between myocardial contraction and reduced coronary flow [155, 156, 157, 158]. In the "vascular waterfall model", proposed by Downey and Kirk, the compression effects of intramyocardial pressure were assumed to be equal to ventricular pressure at the endocardium and to decrease linearly to zero at the epicardium. When tissue pressure exceeds the coronary luminal pressure, blood flow would cease. At lower pressures, only veins, which have a lower luminal pressure, are expected to be collapsed [155].

While the waterfall model is able to explain an overall increased vascular resistance and reduced coronary inflow, it fails to explain why venous outflow is increased during systole. Subsequent models, such as the "Intramyocardial Pump model" proposed by Spaan *et al.* in 1981, showed that vessel compliance is important to model this behavior, as compliant vessels appear to be filled in diastole and discharged in systole through the low-pressure venous side [156].

4.1.1.2 Compartment Syndrome

Compartment Syndrome (CS) is a condition that affects tissue blood supply of a body compartment. CS occurs in compartments enclosed by a non-elastic structure, *i.e.* osseus and connective tissue, where optimal perfusion can be compromised by the increase of tissue pressure.

Although tissue solid stress and pressure in CS have a different origin - a passive stress rather than an active contraction - *in-vivo* experiments show a reduction in blood flow correlated with increasingly high external pressures. This is also followed by an increase in venous pressure [159], which is thought to be a consequence of an increased interstitial fluid pressure (IFP). Elevated IFP is normally caused by high capillary filtration, as well as the inability of the lymphatics to drain interstitial fluid effectively.

The exact aetiology is still not clear, however evidence obtained in animal models indicates that whereas compressive solid stress can collapse fragile blood and lymphatic vessels, elevated IFP cannot [160]. Reneman *et al.* speculated that arterioles and venules are not the site where the cessation of blood flow occurs. In fact, blood flow is still present in most arterioles and venules [159]. Vollmar *et al.* observed that capillaries collapse at much lower pressures than venules and arterioles, and thus are thought to be the limiting factor for perfusion. Furthermore, upon capillary and venular collapse, flow in large arterioles did not cease, but was largely diverted along arteriole-venule shunts [160].

4.1.1.3 Tumor Perfusion

Changes in perfusion were also linked by several authors to mechanical conditions in human tumors [161, 162, 163]. Stylianopoulos *et al.* observed growth-induced solid stress in *in-vivo* murine tumors, which appears to compress microvessels, hinder tissue perfusion, and in turn, oxygen supply and therapy [161]. In particular, collapsed microvessels were found only in the periphery of tumors, where

radial stress is compressive and circumferential stress is tensile. In the interior, both stresses were compressive, leading to isotropic stress patterns, that do not appear to deform microvessels [161].

4.1.2 Vasa Vasorum Structure and Function

The vasa vasorum are the microvascular network that feeds the wall of medium and large blood vessels. Their function is strongly determined by their anatomy and structure. Arterial vasa vasorum (AVV) and venous vasa vasorum (VVV) show distinctive morphological features. AVV originate from the abluminal surface (*VV* externa) of a proximal artery or from the luminal surface (*VV* interna) of the main artery and then arborize in the adventitia and outer media [164, 19], where they feed a network of capillaries. These capillaries are drained by VVV laid down around the outer media, into veins that runs in close proximity to the host vessel [19]. These veins known as "companion veins" (*venae comitantes*) run parallel to the AVV feeder or to the largest branches of a main vein, where they penetrate every 5 to 15 mm [165, 166].

AVV are fewer in number, with smaller diameters (11.6 to 36.6 μm), compared to VVV (11.1 to 200.3 μm) [166]. Two anatomically distinct patterns of VV can be observed: first order VV run longitudinally to the host vessel centreline, while second order VV are arranged circumferentially [167]. AVV consist of layers of SMC laid around a single layer of EC, and as other resistance arterioles, that can regulate their tone, are neuronally innervated by sympathetic fibres [167].

Most large muscular arteries exhibit a dense network of vasa in the adventitia and outer media, which is likely to be related to the wall nutritional needs. When host vessel thickness exceeds the ability of nutrients to simply diffuse from the lumen, VV become more dense and penetrate more deeply in the wall [168]. This observation is in line with the findings that large veins, which have thin walls, but transport deoxygenated blood, are surrounded by an extensive VV.

In the past, VV have been described by several authors as a *plexus* or a network [169, 170]. However, more recent studies of Gossl *et al.* and Herbst *et al.* have shown using various techniques including micro-CT, micro-embolization and Scanning Electron Microscopy, that VV show a tree-like structure, and their function is similar to end arteries [164, 140]. This morphological feature is critical, as plexi can maintain perfusion of a district, even in the presence of an obstruction, through shunting and retrograde flow. Conversely, in a tree-like structure, the occlusion or compression of a proximal segment leads to a stopping of perfusion in more distal segments [164].

4.1.3 Perfusion Models

The microvascular circulation represents one of the most complex physiological system in terms of autoregulation and biomechanical interaction. Faithful modelling of tissue perfusion and mass transport is a challenging problem, due to its inherently integrative nature. Waters *et al.*, in their review on mathematical methods for coronary vascular biomechanics, highlight the different challenges faced in developing such models to investigate blood flow and mass transport in myocardial tissue [171]. Many of these hold true for other organ systems, including the VV circulation.

First of all, it has to be noted that a wide range of interacting spatial scales are involved in the modelling, *e.g.* from micro-scale transport processes to macro-scale mechanical interactions. When doing so, a further challenge is to embed the necessary micro-scale information into the larger scale model, without making the problems computationally intractable [171]. Lumped parameter models are a computationally convenient approach, as small-scale structures are represented by single compartments having average properties. However, they have the limitation of not representing any significant spatial variation. In homogenised models, fine-scale properties are spatially-averaged to obtain tissue-scale proper-

ties; this still represent a computationally efficient method, while retaining most of the local spatial variations [171].

Chapman and Shipley [172] and Shipley *et al.* [173] used homogenisation to study tumor circulation. Stokes flow is prescribed in the capillaries, which are assumed to form a periodic microstructure, whereas Darcy flow is assumed in the interstitium and microvasculature, which are treated as a double porous medium. The Darcy permeability tensors are estimated through canonical homogenisation from the micro-scale transport. As pointed out by Waters *et al.*, significant challenges arise, when the microvasculature needs to be represented in a physiologically realistic way [171]. The coronary circulation and similarly the VV are strongly hierarchical structures, arranged in a complex 3D topology, and exhibit a large spatial heterogeneity of structural and functional parameters. This makes simple homogenised models practically unusable to model VV circulation. A possible way to overcome this limitation is by dividing the microvasculature into compartments having similar properties. However, gathering information about VV network is challenging and a complete description of the complex topology and geometry of these vascular district is still outstanding.

4.1.4 Vasa Vasorum Perfusion

An aim of this study was to assess the relative importance of luminal and wall oxygen transport on the onset of hypoxia, rather than to model oxygen transport at a microscopic level as realistically as possible. For this and the reasons outlined above, particularly the lack of readily available VV morphological data, it was decided to use a simplified model of perfusion.

As introduced in Section 3.2.3.1 of Chapter 3, oxygen is assumed to be exchanged at a tissue level, between recruited microvessels and the interstitium, according to Eq. 3.16. The total volume fraction of recruited microvessels is modulated in response to the local stress/strain conditions.

Gossl *et al.* observed that VV present a tree-like structure and therefore, upon collapse of a proximal microvessel, distal segments are not perfused and blood flow is diverted towards low-resistance side branches [164]. While there is general agreement among researchers that VV perfusion can be affected by changes in wall mechanical conditions, *e.g.* hypertension, it is still not clear whether VV compression is driven by intramural stress or deformation/strain, and the problem deserves further *in-vivo* and *in-vitro* studies to clarify this [3, 164, 168, 19].

According to Ritman and Lerman, the branching architecture and anatomical location of VV determine how VV are perfused. In pressurized vessels, radial stress is compressive and equal to luminal blood pressure at the endothelium, while it falls off to zero towards the outer adventitia. As a result, they speculate that at the radial location where radial stress exceeds the VV perfusion pressure, no perfusion can be possible [19].

Conversely, Atta *et al.*, who studied vascular remodelling in lower extremity veins under elevated venous pressure, hypothesize that VV collapse could be attributed to increased circumferential stretch in the wall. This, in turn, can have a twofold effect: it activates, via mechanotransduction, pathways responsible for the the remodelling of the wall and it distorts the wall vasa vasorum, causing an increase in hydraulic resistance, which reduces the flow. This last effect, along with an increased metabolic demand could be responsible for wall hypoxia [174].

Furthmore, to support this hypothesis, several studies have shown that the use of an external support device in coronary artery bypass grafting surgery (CABG) can potentially increase patency [175]. This is clearly in contrast with the hypothesis that radial compression alone causes hypoxia, as such a device would expose the wall to even higher compression. However, an external support would limit the circumferential stretch experienced by VV, maintaining the hydraulic resistance in a normal range.

To account for both possible collapse mechanisms two distinct models are

proposed. The stress-based model rests on Ritman and Lerman's observation that VV collapse is caused by local radial stress exceeding the microvascular luminal pressure [19]. Figure 4.1 show typical microvascular pressures collected in different tissues. While the arteriolar side presents a large spread, the pressure in capillaries and venules appears to be always below 30 mmHg.

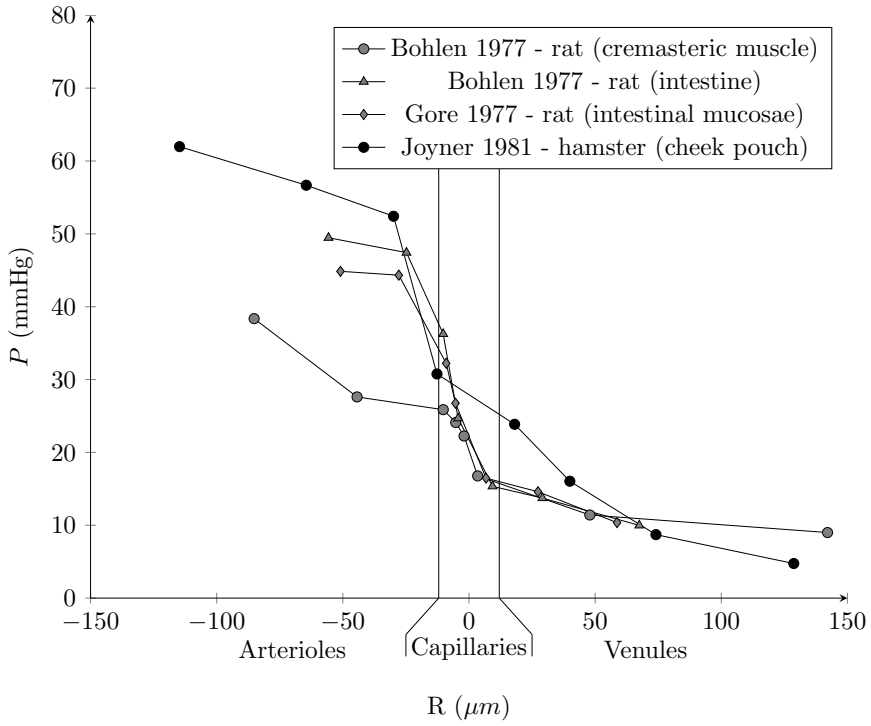

Figure 4.1: Microvascular luminal pressures from Bohlen *et al.* [176], Bohlen *et al.* [177], Gore *et al.* [178] and Joyner *et al.* [179].

Therefore, assuming that no flow is possible in capillaries and arteries, drained by a specific venule, when that venule is collapsed, a threshold pressure is chosen, above which the local tissue is not perfused. Specifically, this yields

$$\begin{aligned} \text{if} \quad -\sigma_{rr} > P_{thres} \quad \text{then:} \quad \overline{V}_f = 0, \\ \text{else:} \quad \overline{V}_f = 1, \end{aligned} \tag{4.1}$$

where σ_{rr} is the Cauchy stress in the radial direction, P_{thres} is the threshold

pressure and $\overline{V}_f$ is the normalized VV volume fraction.

The stretch-based model, on other hand, relies on the Atta *et al.* and Ben-Gal *et al.* hypothesis that wall deformation is responsible of VV distortion and their increase in hydraulic resistance [174, 175]. In particular, these observations are in line with those of Stylianopoulos *et al.* that collapsed microvessels are only found in regions where the circumferential stress is tensile and radial stress is compressive, and consequently deformation is strongly anisotropic. To quantify the degree of anisotropy in a deformed body, the following continuum mechanics definitions are introduced. These will be treated in greater detail in Section 4.4.

The deformation gradient $\mathbf{F}$ describes the continuum deformation of a body in the material description $\mathbf{X}$ into the deformed configuration $\mathbf{x} = \boldsymbol{\chi}(\mathbf{X})$, and can be decomposed through a polar decomposition into the right stretch tensor $\mathbf{U}$ and the orthogonal rotation tensor $\mathbf{R}$:

$$\mathbf{F} = \frac{\partial \mathbf{x}}{\partial \mathbf{X}} = \mathbf{R}\mathbf{U}. \tag{4.2}$$

Information on the stretch tensor can be obtained through eigen-decomposition of the right Cauchy-Green tensor $\mathbf{C}$ (note that both $\mathbf{C}$ and $\mathbf{U}$ are symmetric and positive definite) which is defined as follow

$$\mathbf{C} = \mathbf{F}^T\mathbf{F} = \mathbf{U}^T\mathbf{R}^T\mathbf{R}\mathbf{U} = \mathbf{U}^T\mathbf{U} = \mathbf{U}^2. \tag{4.3}$$

$\mathbf{C}$ can be decomposed in its eigenvectors $\mathbf{N}_1$, $\mathbf{N}_2$ and $\mathbf{N}_3$ and their corresponding eigenvalues λ_1^2, λ_2^2 and λ_3^2.

$$\mathbf{C} = \mathbf{N}\boldsymbol{\Lambda}^2\mathbf{N}^T = \mathbf{N}\begin{bmatrix}\lambda_1^2 & 0 & 0\\ 0 & \lambda_2^2 & 0\\ 0 & 0 & \lambda_3^2\end{bmatrix}\mathbf{N}^T, \quad \mathbf{U} = \mathbf{N}\boldsymbol{\Lambda}\mathbf{N}^T = \mathbf{N}\begin{bmatrix}\lambda_1 & 0 & 0\\ 0 & \lambda_2 & 0\\ 0 & 0 & \lambda_3\end{bmatrix}\mathbf{N}^T. \tag{4.4}$$

Then, the principal stretches of $\mathbf{U}$, λ_1, λ_2 and λ_3 (ordered as $\lambda_1 > \lambda_2 > \lambda_3$) can be simply calculated.

An intuitive way to measure the degree of anisotropic distortion was suggested by Cao, who defined the Distortion Index (DI) to quantify anisotropic expansion in lungs [180]. DI is defined as twice the ratio of maximum principal stretch λ_1 over the sum of the medium λ_2 and minimum principal stretch λ_3,

$$DI = 2\frac{\lambda_1}{\lambda_2 + \lambda_3}. \tag{4.5}$$

DI is always larger than or equal to 1, which in incompressible materials such as arteries (where $\lambda_1\lambda_2\lambda_3 = 1$) corresponds to no defomation, while large values of DI indicate an anisotropic deformation. Assuming that the hydraulic resistance

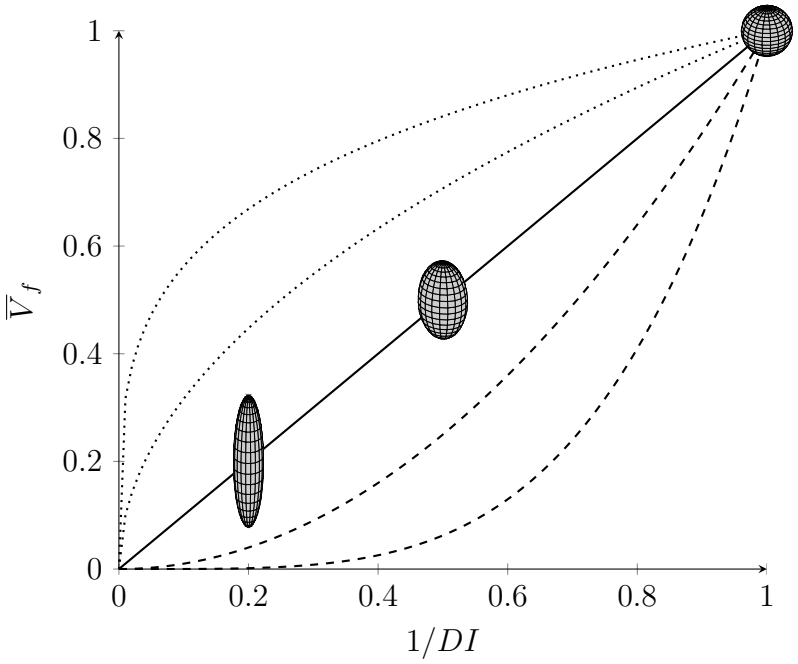

Figure 4.2: The normalized volume fraction $\overline{V}_f$ is assumed to be inversely proportional to the distortion index, according to Eq. 4.6. Higher values of DI corresponds to higher degrees of anisotropic deformation. Eq. 4.6 is shown for increasing values of κ.

in the VV is directly proportional to wall distortion, and that the volume fraction

of perfused microvessels inversely proportional to local hydraulic resistance, the following perfusion model is proposed:

$$\overline{V}_f = \left(\frac{1}{DI}\right)^{\kappa}, \tag{4.6}$$

where the exponent κ is arbitrarily chosen to modulate the response of $\overline{V}_f$ to DI.

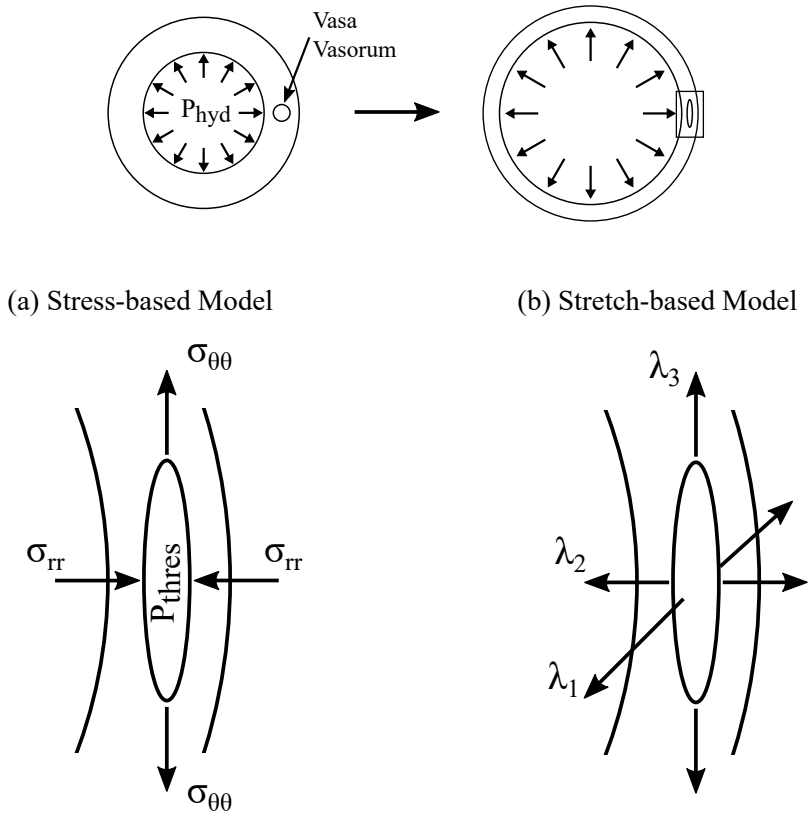

Figure 4.3: Schematic illustration of the two proposed perfusion models: (a) Stress-based and (b) Stretch-based. According to the Stress-based model, VV collapse due to the imbalance between compressive wall radial stress and VV luminal pressure. On the other hand, according to the Stretch-based model, VV collapse as an effect of the anisotropic distortion of the wall.

4.2 AVF Surgical Procedure

The intramural stress and strain, to which the wall of an AVF is exposed upon its formation, are calculated through an idealised numerical framework, using FE

analysis. The work presented in this chapter was mostly built on that of Gu *et al.* and of Cacho *et al.*, who employed FE to study the slit arteriotomy procedure, the surgical technique used to form AVF [103, 105]. However, considerable differences can be found between the two studies.

First of all, in the work by Gu *et al.*, shell elements were used to approximate the wall, under a thin-wall assumption. While this approach can represent a valid modelling strategy to assess as to whether the slit opens to a width sufficient for blood supply, to calculate through-the-wall stress and deformation, the vascular wall has to be modelled as a thick structure, using 3D elements, as in [105].

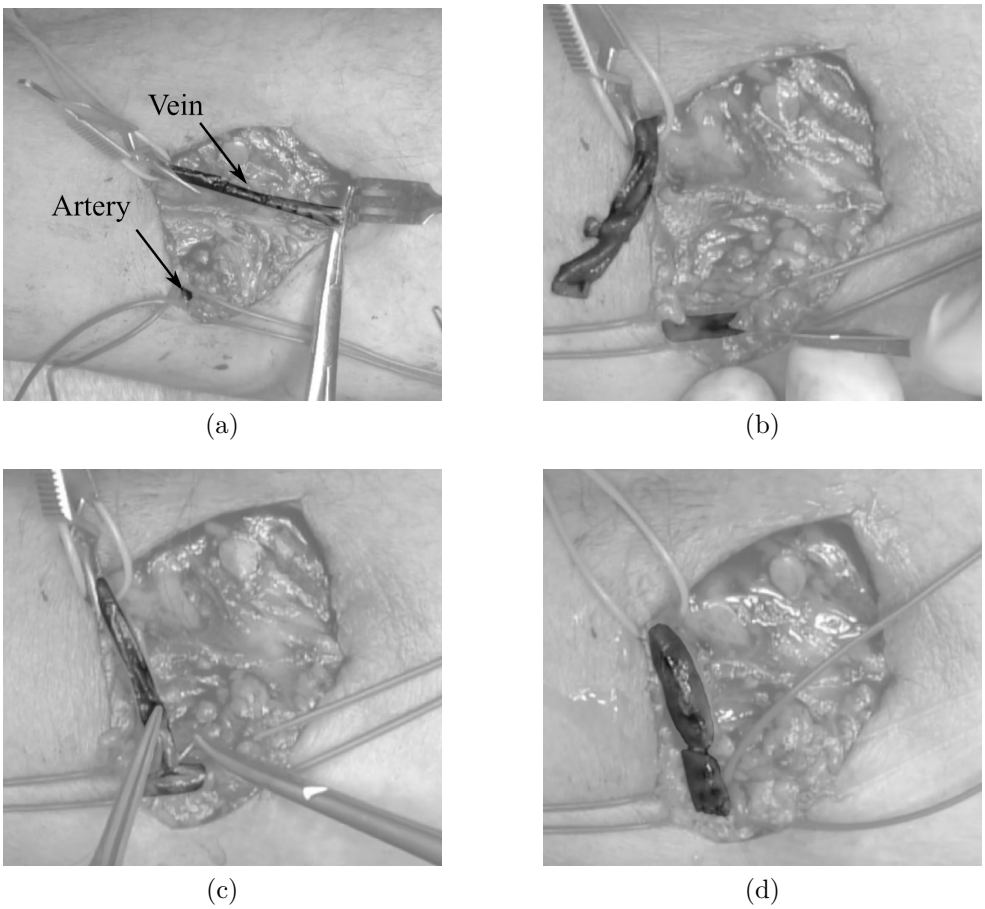

Figure 4.4: Slit arteriotomy procedure: (a) Step 1-2, (b) Step 3, (c) Step 4, (d) Step 5. Courtesy of Mr. Jeremy Crane.

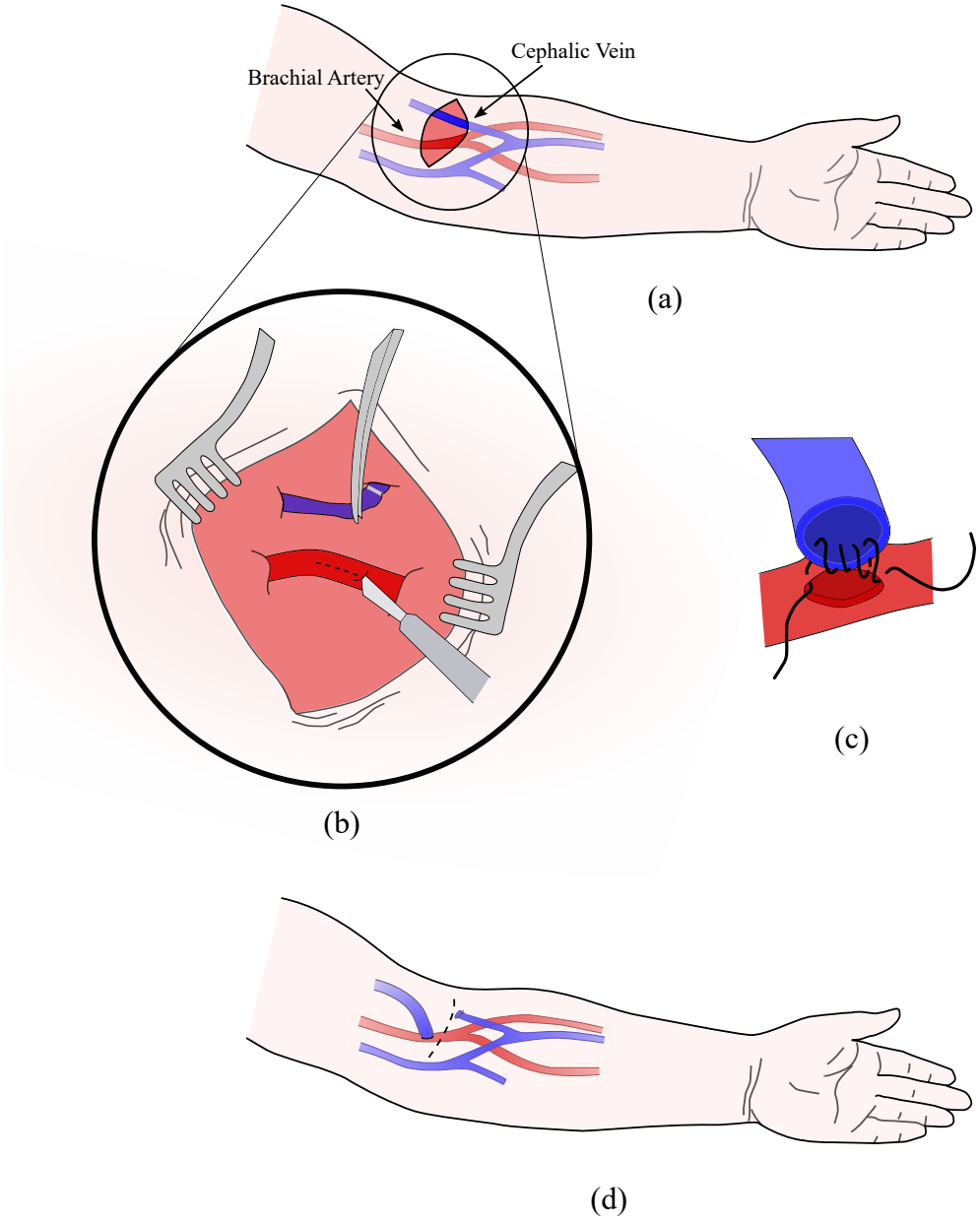

Figure 4.5: Slit arteriotomy procedure: (a) An incision is performed at the antecubital fossa to expose the brachial artery and cephalic vein. (b) The vein and artery are mobilised and clamped to interrupt blood flow. An arteriotomy is created in the artery. (c) The vein margins are stitched to the recipient artery, along the margins of the arteriotomy. (d) The clamps are released and blood flow is restored.

Furthermore, an isotropic hyperelastic constitutive law was used to model arterial tissue. However, this material fails to represent the typical stress stiffening observed in healthy blood vessels [104]. To overcome this limitation, Cacho *et al.* employed the hyperelastic anisotropic material proposed by Gasser *et al.* [106], which represents the state-of-the-art in vascular biomechanics, allowing to capture the typical stress stiffening due to the embedded collagen fibres.

Finally, the work of Cacho *et al.* presents a further improvement over that of Gu *et al.*, as residual stresses were included in the simulation. In Gu's model, residual stresses are considered to be negligible, however, several authors have shown that including them is essential, for realistic modelling of the wall mechanics [181, 182].

From a mechanical standpoint, the surgical procedure can be divided in the following steps:

1. The brachial artery and cephalic vein are compressed by vascular clamps, to temporarily interrupt blood flow;

2. A section of the vein is mobilised and cut transversely;

3. An arteriotomy is created on the recipient artery over a length that slightly exceeds the diameter of the cephalic vein;

4. The vein is stretched and stitched onto the recipient artery along the margins of the arteriotomy;

5. Clamps are released and blood flow is restored.

4.3 Governing Equations

For a given deformable body Ω, having surface Γ, conservation of momentum states that the time rate of change of the total linear momentum equates to the

vector sum of all the external forces acting on the body, which in Lagrangian form can be expressed as:

$$\int_{\Gamma} \mathbf{T}^{(\mathbf{n})} d\Gamma + \int_{\Omega} \rho \mathbf{b} d\Omega = \frac{D}{Dt} \int_{\Omega} \rho \mathbf{v} d\Omega, \tag{4.7}$$

where ρ is the material density, $\mathbf{T}^{(\mathbf{n})}$ is the traction vector, which represents the external surface forces per unit area, $\mathbf{b}$ represents the body forces per unit volume, D/Dt is the material derivative and $\mathbf{v}$ the velocity vector.

The traction vector $\mathbf{T}^{(\mathbf{n})}$, which acts in the direction $\mathbf{n}$, can be expressed in terms of the Cauchy stress tensor $\boldsymbol{\sigma}$, according to Cauchy's theorem $\mathbf{T}^{(\mathbf{n})} = \boldsymbol{\sigma} \cdot \mathbf{n}$. This formula can be substituted back in Eq. 4.7, and under the assumption of constant density, it yields

$$\int_{\Gamma} \boldsymbol{\sigma} \cdot \mathbf{n} d\Gamma + \int_{\Omega} \rho \left(\mathbf{b} - \frac{D\mathbf{v}}{Dt} \right) d\Omega = \mathbf{0}. \tag{4.8}$$

Applying the divergence theorem to Eq. 4.8 it yields:

$$\int_{\Omega} \left[\nabla \cdot \boldsymbol{\sigma} + \rho \mathbf{b} - \rho \frac{D\mathbf{v}}{Dt} \right] d\Omega = \mathbf{0}. \tag{4.9}$$

Finally, localizing the integral yields Cauchy's first equation of motion for a generic body in material description:

$$\nabla \cdot \boldsymbol{\sigma} + \rho \mathbf{b} - \rho \frac{D\mathbf{v}}{Dt} = \mathbf{0}, \tag{4.10}$$

which assuming no body forces and static equilibrium (*i.e.* no accelerations), reduces to

$$\nabla \cdot \boldsymbol{\sigma} = \mathbf{0}. \tag{4.11}$$

Equation 4.11 is solved in Abaqus/Standard, in a weak form, using the virtual work principle, under compatible boundary conditions. As the virtual work equa-

tion is a non linear function of the displacement field, it is solved by iteration, using a Newton-Raphson method.

4.4 Constitutive Law

Healthy vessels are highly deformable structures, having a non-linear stress-strain response with a typical stiffening at physiological strain levels, due to the engagement of anisotropically distributed wavy collagen fibrils, embedded inside an unstructured mesh of elastin fibres [102, 104, 183]. Their walls are composed of three distinct concentric layers, the intima, the media and the adventitia [106].

As observed by Gasser *et al.*, each layer presents a complex organization of fibroblasts, smooth muscle cells, water, different families of collagen fibrils and a network of elastin fibres [106]. Based on the histology, blood vessels are mechanically classified as 'mixture composites', having solid components immersed in a fluid matrix, but for many problems of interest, the wall is commonly regarded as a homogenised solid [184].

Collagen fibres are undulated, or crimped, in their natural state and, in blood vessels, anisotropically distributed about two principal directions forming a double helix [184, 182]. Elastin fibres are straight in their unstressed state and less stiff than collagen fibres, being able to withstand large stretches and reversibly recoil in their original shape. Conversely, collagen is not engaged at small stretches, but becomes the predominant stress-bearing component of tissues at high stretches [184]. In addition, given the high water content, at physiological loads, blood vessels are normally modelled as nearly-incompressible solids [185].

Testing of vascular tissue exhibits a pronounced visco-elastic response under high strain-rate, and a stress-softening hysteresis within the first few cycles of loading. The visco-elastic effect was first included by Fung, in his model of arterial tissue [186], but can be normally neglected when modelling materials in the low strain-rate regime. In addition, once the tissue is 'pre-conditioned'

through a few initial cycles of loading, it may be treated as pseudo-elastic and all inelastic phenomena can be neglected [106].

A large number of constitutive models exist in the literature. These can be classified into models based on a purely phenomenological approach and structural models, based on the underlying histology. In [106], Gasser *et al.* offer an exhaustive overview of the principal models. While purely phenomenological models [182, 106, 187, 188] often provide good fit to experimental data, a major limitation is that their constitutive parameters do not bear any physical meaning and thus have limited predictive capabilities [184].

Structural models [189, 190, 191, 192, 193], on the contrary, are based on parameters that can potentially all be measured experimentally. However, the unavailability of these micro-structural properties, *e.g.* fibre undulation and orientation, makes these models not readily available for use. Furthermore, no agreement can be found in the literature on the mechanism underlying the crimped fibre recruitment [184]. Finally, these models often present formulations that are not suitable for an convenient FE implementation, to investigate clinically relevant problems.

Simpler phenomenological models include exponential, Truesdell-like models for neo-Hookean and Mooney-Rivlin materials [194]. In these models, the strain energy function is a linear combination of the invariants of the left Cauchy-Green deformation tensor, which allows for a simple implementation and parameter estimation. This class of models, originally developed to study plastic and rubber-like materials, is still used extensively to predict the behaviour of biological tissues. However, experimental work shows that they might not be suitable for modelling anisotropic tissues such as arteries [195].

Early work on biological tissues carried out by Fung [196] showed that the stress in rabbit mesentery under uniaxial tension appears to increase exponentially as a function of increasing stretch. Based on these results, Fung *et al.*

suggested several forms of an exponential strain energy function, as a function of the Green-Lagrange strain [197]. This stress-strain relationship appears to approximate the behaviour of many biological soft tissues well, but only in a phenomenological sense, as there is no microstructural basis for the choice of the exponential function. In addition, while this is a widely adopted constitutive law, the convexity of these Fung-type potential depends on the choice of its parameters and a simple fitting of the model can result in non-convexity of the potential [182].

In 2001, Holzapfel *et al.* introduced a more general fibre-reinforced constitutive material, often referred to as the Holzapfel-Gasser-Ogden (HGO) model, which was developed to model concentric arterial layers [182]. Two families of collagen fibres are embedded in an isotropic non-collagenous matrix and subjected to uniaxial strain, resulting from the macroscopic strain tensor, and perfect matrix-fibre bonding is assumed. Collagen fibres have no response to compressive loading as they would buckle under compression and the stress-stretch law is described in a phenomenological sense. Arguably, this strain energy function represents one of the most significant developments in soft tissue biomechanics in the last 20 years. This model, in fact, has the clear advantage of retaining mathematical simplicity, whilst providing the required anisotropic and 'exponential-shaped' stress-strain behaviour, common to many biological materials. More recently, the HGO model have been further developed to account for dispersion of the collagen fibres about their principal direction [106]. For the above mentioned reasons, it was decided to adopt a strain energy function of the HGO family, for the simulations presented in this chapter. The main features of the model will be discussed in the next section.

4.4.1 Hyperelastic Strain Energy Function

Let $\Omega_0 \subset \mathbb{R}^3$ be the reference configuration of a continuous body and $\boldsymbol{\chi} : \Omega_0 \rightarrow \Omega$ the deformation field that transforms the material point $\mathbf{X} \in \Omega_0$ into the deformed configuration $\mathbf{x} = \boldsymbol{\chi}(\mathbf{X}) \in \Omega$ with $\Omega \subset \mathbb{R}^3$. Let $\mathbf{F}(\mathbf{X}) = \partial\mathbf{x}/\partial\mathbf{X}$ be the the deformation gradient and $J(\mathbf{X}) = det(\mathbf{F}(\mathbf{X}))$ the local volume ratio. The deformation gradient, using the multiplicative decomposition, can be divided $\mathbf{F} = (J^{1/3}\mathbf{I})\bar{\mathbf{F}}$ into a spherical $J^{1/3}\mathbf{I}$ and a distortional part $\bar{\mathbf{F}}$. Right and left Cauchy-Green tensors (respectively $\mathbf{C}$ and $\mathbf{B}$), and the modified counterparts (respectively $\bar{\mathbf{C}}$ and $\bar{\mathbf{B}}$) are defined as

$$\begin{aligned} \mathbf{C} &= \mathbf{F}^T\mathbf{F} = J^{2/3}\bar{\mathbf{C}}, \;\; \bar{\mathbf{C}} = \bar{\mathbf{F}}^T\bar{\mathbf{F}}, \\ \mathbf{B} &= \mathbf{F}\mathbf{F}^T = J^{2/3}\bar{\mathbf{B}}, \;\; \bar{\mathbf{B}} = \bar{\mathbf{F}}\bar{\mathbf{F}}^T. \end{aligned} \tag{4.12}$$

Two families of fibres are embedded in the continuum, and their directions are described by the referential vectors $\mathbf{a_1}, \mathbf{a_2}$ and the relative second order tensors $\mathbf{A_1} = \mathbf{a_1} \otimes \mathbf{a_1}, \mathbf{A_2} = \mathbf{a_2} \otimes \mathbf{a_2}$ which characterize the tissue structure. Also, the unimodular push-forward of each fibre direction can be calculated as $\bar{\mathbf{a}}_\mathbf{i} = \bar{\mathbf{F}}\mathbf{a_i}$.

For a material with two reinforcing fibres, the following invariants exist:

$$\begin{aligned} &\bar{I}_1 = tr(\bar{\mathbf{C}}),\; \bar{I}_2 = \tfrac{1}{2}\left[\bar{I}_1{}^2 - tr(\bar{\mathbf{C}}^2)\right],\; \bar{I}_3 = det(\bar{\mathbf{C}}), \\ &\bar{I}_4 = \mathbf{a_1}\cdot\bar{\mathbf{C}}\cdot\mathbf{a_1} = \bar{\mathbf{C}} : \mathbf{A_1},\; \bar{I}_5 = \mathbf{a_1}\cdot\bar{\mathbf{C}}^2\cdot\mathbf{a_1} = \bar{\mathbf{C}}^2 : \mathbf{A_1}, \\ &\bar{I}_6 = \mathbf{a_2}\cdot\bar{\mathbf{C}}\cdot\mathbf{a_2} = \bar{\mathbf{C}} : \mathbf{A_2},\; \bar{I}_7 = \mathbf{a_2}\cdot\bar{\mathbf{C}}^2\cdot\mathbf{a_2} = \bar{\mathbf{C}}^2 : \mathbf{A_2}, \\ &\bar{I}_8 = [\mathbf{a_1}\cdot\mathbf{a_2}]\,\mathbf{a_1}\cdot\bar{\mathbf{C}}\cdot\mathbf{a_2},\; \bar{I}_9 = [\mathbf{a_1}\cdot\mathbf{a_2}]^2. \end{aligned} \tag{4.13}$$

Then, let $\Psi(\mathbf{C}, \mathbf{A_1}, \mathbf{A_2})$ be a Helmholtz free-energy function, defined per unit reference volume. Its decoupled form is adopted, and Ψ is divided into $U(J)$ and $\bar{\Psi}(\bar{\mathbf{C}}, \mathbf{A_1}, \mathbf{A_2})$, respectively the purely volumetric and purely isochoric contributions.

An energy conjugate pair of objective tensors, such as $\mathbf{P}$ and $\mathbf{F}$, is chosen,

where $\mathbf{P}$ is the first Piola-Kirchhoff stress tensor. In pure deformation processes, which do not involve thermodynamic changes, internal energy dissipation is equal to zero, which describes a reversible process. Under this condition, the well-known Clausius-Planck inequality, becomes:

$$D_{int} = \mathbf{P} : \dot{\mathbf{F}} - \frac{\partial \Psi}{\partial t} = \boldsymbol{\sigma} : \mathbf{D} - \frac{\partial \Psi}{\partial t} = \frac{1}{2}\mathbf{S} : \dot{\mathbf{C}} - \frac{\partial \Psi}{\partial t} = 0, \tag{4.14}$$

where D_{int} denotes the internal dissipation, $\dot{\mathbf{F}}$ the material time derivative of the deformation gradient, $\dot{\mathbf{F}}$ the material time derivative of the deformation gradient, $\mathbf{D}$ the rate of deformation tensor, $\boldsymbol{\sigma}$ the Cauchy stress, $\mathbf{S}$ the second Piola-Kirchhoff stress tensor and $\mathbf{P} : \dot{\mathbf{F}}$, $\boldsymbol{\sigma} : \mathbf{D}$, $1/2\ \mathbf{S} : \dot{\mathbf{C}}$ the stress powers. This means that the rate of change of the strain energy density can be expressed as the stress power

$$\frac{\partial \Psi(\mathbf{F})}{\partial t} = \mathbf{P} : \dot{\mathbf{F}} = \boldsymbol{\sigma} : \mathbf{D} = 1/2\ \mathbf{S} : \dot{\mathbf{C}}. \tag{4.15}$$

The rate of change of $\Psi(\mathbf{F})$ can be evaluated also as:

$$\frac{\partial \Psi(\mathbf{F})}{\partial t} = \frac{\partial \Psi(\mathbf{F})}{\partial \mathbf{F}} : \frac{\partial \mathbf{F}}{\partial t} = \frac{\partial \Psi(\mathbf{F})}{\partial \mathbf{F}} : \dot{\mathbf{F}}, \tag{4.16}$$

and subsituting 4.16 in 4.15 yields

$$\mathbf{P} : \dot{\mathbf{F}} = \frac{\partial \Psi(\mathbf{F})}{\partial \mathbf{F}} : \dot{\mathbf{F}}. \tag{4.17}$$

As 4.17 must be true for a generic $\dot{\mathbf{F}}$, then

$$\mathbf{P} = \frac{\partial \Psi}{\partial \mathbf{F}}, \tag{4.18}$$

and choosing the pair of objective tensors $\mathbf{S}$ and $\mathbf{E}$, respectively the second Piola-

Kirchhoff stress tensor and the Lagrangian finite strain tensor,

$$\mathbf{S} = \frac{\partial \Psi}{\partial \mathbf{E}}, \tag{4.19}$$

and as $\mathbf{C} = 2\mathbf{E} + 1$,

$$\mathbf{S} = 2\frac{\partial \Psi}{\partial \mathbf{C}}. \tag{4.20}$$

The second Piola-Kirchhoff stress $\mathbf{S} = 2\partial\Psi(\mathbf{C}, \mathbf{A_1}, \mathbf{A_2})/\partial\mathbf{C}$ can now be decoupled into $\mathbf{S} = \mathbf{S}_{vol} + \bar{\mathbf{S}}$ with $\mathbf{S}_{vol} = 2\partial U(J)/\partial\mathbf{C}$ and $\bar{\mathbf{S}} = 2\partial\bar{\Psi}(\bar{\mathbf{C}}, \mathbf{A_1}, \mathbf{A_2})/\partial\mathbf{C}$. The following standard results can also be required:

$$\frac{\partial J}{\partial \mathbf{C}} = \frac{1}{2} J\mathbf{C^{-1}}, \quad \frac{\partial \bar{\mathbf{C}}}{\partial \mathbf{C}} = J^{-2/3}\left(\mathbb{I} - \frac{1}{3}\bar{\mathbf{C}} \otimes \bar{\mathbf{C}}^{-1}\right), \tag{4.21}$$

with $\mathbb{I}$, the fourth-order identity tensor, defined as

$$\mathbb{I}_{i,j,k,l} = \frac{\delta_{i,k}\delta_{j,l} + \delta_{i,l}\delta_{j,k}}{2}, \tag{4.22}$$

being $\delta_{i,j}$ the Kronecker delta. After some manipulations, Equation 4.22 becomes

$$\mathbf{S}_{vol} = pJ\mathbf{C}^{-1}, \quad \bar{\mathbf{S}} = J^{-2/3}\bar{\mathbb{P}} : \tilde{\mathbf{S}}, \tag{4.23}$$

with $p = \partial U/\partial J$ hydrostatic pressure, the isochoric contribution $\tilde{\mathbf{S}} = 2\partial\bar{\Psi}/\partial\bar{\mathbf{C}}$ and the fourth-order projection tensor $\bar{\mathbb{P}} = \mathbb{I} - \frac{1}{3}\bar{\mathbf{C}} \otimes \bar{\mathbf{C}}^{-1}$, which represents the deviatoric operator in Lagrangian description. When the material is incompressible, $p = \partial U/\partial J$ becomes a Langrange multiplier and is indeterminate from the deformation alone. The Kirchhoff stress tensor $\boldsymbol{\tau} = J\boldsymbol{\sigma}$ can be defined through a push forward of $\mathbf{S}$,

$$\boldsymbol{\tau}_{vol} = pJ\mathbf{I}, \quad \bar{\boldsymbol{\tau}} = \mathbb{P} : \tilde{\boldsymbol{\tau}} \tag{4.24}$$

with $\tilde{\boldsymbol{\tau}} = 2\bar{\mathbf{F}}(\partial\bar{\Psi}/\partial\bar{\mathbf{C}})\bar{\mathbf{F}}^T$ and $\mathbb{P} = \mathbb{I} - \frac{1}{3}\bar{\mathbf{I}} \otimes \bar{\mathbf{I}}$ the deviatoric operator in Eulerian description. The following strain energy function proposed by Gasser *et al.* [106]

is used. It is assumed that the isochoric part $\bar{\Psi}$ of the strain energy function can be obtained by superposition of an isotropic and anisotropic contribution,

$$\bar{\Psi}(\bar{\mathbf{C}}, \mathbf{A_1}, \mathbf{A_2}) = \bar{\Psi}_{iso}(\bar{\mathbf{C}}) + \bar{\Psi}_{aniso}(\bar{\mathbf{C}}, \mathbf{A_1}, \mathbf{A_2}). \tag{4.25}$$

The well-known incompressible isotropic Neo-Hookean model is used to model the non-collagenous groundmatrix,

$$\bar{\Psi}_{iso}(\bar{\mathbf{C}}) = \frac{C_{10}}{2}\left(\bar{I}_1 - 3\right), \tag{4.26}$$

where C_{10} denotes the Neo-Hooken parameter. For a given fibre direction, Gasser *et al.* define a generalized structure tensor $\mathbf{H_i} = k\mathbf{I} + (1-3k)\mathbf{a_i} \otimes \mathbf{a_i}$ and its push-forward $\bar{\mathbf{h}}_\mathbf{i} = k\bar{\mathbf{B}} + (1-3k)\bar{\mathbf{a}}_\mathbf{i} \otimes \bar{\mathbf{a}}_\mathbf{i}$ which represent the fibre dispersion in an 'integral sense' and describe the degree of anisotropy.

In order to model the transversely isotropic contribution of the *i-th* family of embedded collagen fibres, Gasser *et al.* assumes the following exponential law,

$$\bar{\Psi}_{aniso}(\bar{\mathbf{C}}, \mathbf{A_1}, \mathbf{A_2}) = \sum_{i=1,2} \bar{\Psi}_{fi}(\bar{\mathbf{C}}, \mathbf{H_i}), \tag{4.27}$$

where

$$\bar{\Psi}_{fi}(\bar{\mathbf{C}}, \mathbf{H_i}) = \frac{k_1}{2k_2}\{exp\left[k_2(E_i)^2\right] - 1\}, \tag{4.28}$$

and $E_i = tr(\bar{\mathbf{h}}_\mathbf{i}) - 1$. Parameters $k_1 > 0$ and $C_{10} > 0$ are stress-like, while $k_2 > 0$ and $k \in [0, 1/3]$ are dimensionless. Particularly, k represents the fibre dispersion; when $k = 1/3$ the material can be considered isotropic (as the fibres are completely dispersed) while for $k = 0$ no fibre dispersion is present, meaning that the fibres are perfectly aligned.

As already introduced in 4.24, the Kirchhoff stress tensor $\boldsymbol{\tau}$ can be obtained as the deviatoric part of $\tilde{\boldsymbol{\tau}}$. The isochoric Neo-Hookean part of $\tilde{\boldsymbol{\tau}}$ can be determined as $\tilde{\boldsymbol{\tau}}_{iso} = C_{10}\bar{\mathbf{B}}$, a well-known result from the literature. The transversely isotropic

contribution can be determined for each *i-th* fibre as $\tilde{\mathbf{S}}_{f\,i} = 2\partial\,\bar{\Psi}_{f\,i}/\partial\bar{\mathbf{C}} = 2\bar{\Psi'}_{f\,i}\mathbf{H_i}$. The Kirchhoff stress, calculated as the push-forward of second Piola Kirchhoff tensor, is $\tilde{\boldsymbol{\tau}_{f\,i}} = 2\bar{\Psi'}_{f\,i}\mathbf{h_i}$, where $\bar{\Psi'} = k_1 E_i exp(k_2 {E_i}^2)$ [106]. A convenient approach to enforce the incompressibility constraint is based on a 'penalty method'. In this approach, a penalty term, $\Psi_{vol}(J)$, associated to the volumetric strain is added to the strain energy function

$$\Psi_{vol}(J) = B\frac{(J^2-1)}{2}, \tag{4.29}$$

where B is the material bulk modulus. Full incompressibility is enforced asymptotically for $B \to \infty$ which corresponds to a Poisson's ratio $\nu \to 0.5$.

4.4.2 Tangent Modulus Calculation

The anisotropic hyperelastic law, presented in the previous section, was implemented into the commercial implicit FE code Abaqus/Standard 6.13-2, via a customised Fortran User-Material (UMAT) subroutine. Abaqus 6.13-2 provides an implementation of the HGO material. However, in this implementation the structure cannot be pre-loaded with residual strains, thus it cannot be used to model residual stresses.

Non-linear initial boundary-value problems are usually solved using a Newton-iterative method. The tangent modulus tensor, which is used as an iterative operator in the Newton scheme, needs to be calculated for each integration point, to ensure fast convergence of the solver. Analytical determination of this fourth-order tensor is non-trivial.

Sun *et al.* determined an efficient numerical approximation that can be easily implemented in FE codes, regardless of the chosen material model [198]. Abaqus/Standard, as many other implicit FE softwares, requires to define the tangent modulus tensor in a corotational, or Jaumann, reference frame. This

tensor representation can be derived from the Jaumann rate of Kirchhoff stress, written as:

$$\overset{\triangledown}{\boldsymbol{\tau}} = \dot{\boldsymbol{\tau}} - \mathbf{W}\boldsymbol{\tau} - \boldsymbol{\tau}\mathbf{W}^T = \mathbb{C}^{\tau\, J} : \boldsymbol{D}, \tag{4.30}$$

where $\boldsymbol{W}$ and $\boldsymbol{D}$ are respectively the symmetric and antisymmetric part of $\boldsymbol{L}$ the spatial velocity gradient and $\mathbb{C}^{\tau\, J}$ is the Jaumann tangent modulus tensor. Following Miehe [199], a linearised incremental form of 4.30 can be written as:

$$\Delta\boldsymbol{\tau} - \Delta\mathbf{W}\boldsymbol{\tau} - \boldsymbol{\tau}\Delta\mathbf{W}^T = \mathbb{C}^{\tau\, J} : \Delta\boldsymbol{D}, \tag{4.31}$$

where

$$\begin{aligned} \Delta\boldsymbol{D} &= \frac{\Delta\boldsymbol{F}\boldsymbol{F}^{-1} + (\Delta\boldsymbol{F}\boldsymbol{F}^{-1})^T}{2}, \\ \Delta\boldsymbol{W} &= \frac{\Delta\boldsymbol{F}\boldsymbol{F}^{-1} - (\Delta\boldsymbol{F}\boldsymbol{F}^{-1})^T}{2}. \end{aligned} \tag{4.32}$$

The (i,j) component of $\Delta\boldsymbol{D}$ corresponds to

$$\Delta\boldsymbol{D}^{(i,j)} = \frac{\Delta\boldsymbol{F}^{(i,j)}\boldsymbol{F}^{-1} + (\Delta\boldsymbol{F}^{(i,j)}\boldsymbol{F}^{-1})^T}{2}. \tag{4.33}$$

$\Delta\boldsymbol{F}^{(i,j)}$ is the perturbation of $\boldsymbol{F}$ on its (i,j) component:

$$\Delta\boldsymbol{F}^{(i,j)} = \varepsilon\frac{e_i \otimes e_j\boldsymbol{F} + e_j \otimes e_i\boldsymbol{F}}{2} \tag{4.34}$$

and from 4.34 and 4.32:

$$\begin{aligned} \Delta\boldsymbol{D}^{(i,j)} &= \varepsilon\frac{e_i \otimes e_j + e_j \otimes e_i}{2}, \\ \Delta\boldsymbol{W}^{(i,j)} &= 0. \end{aligned} \tag{4.35}$$

Then the perturbed gradient is $\hat{\boldsymbol{F}}^{(i,j)} = \boldsymbol{F} + \Delta\boldsymbol{F}^{(i,j)}$ and the perturbed Kirchhoff stress is $\Delta\boldsymbol{\tau} \approx \boldsymbol{\tau}(\hat{\boldsymbol{F}}^{(i,j)}) - \boldsymbol{\tau}(\boldsymbol{F})$ and from 4.31 we obtain $\boldsymbol{\tau}(\hat{\boldsymbol{F}}^{(i,j)}) - \boldsymbol{\tau}(\boldsymbol{F}) \approx \mathbb{C}^{\tau\, J} : \varepsilon\frac{e_i \otimes e_j + e_j \otimes e_i}{2}$. The components of $\mathbb{C}^{\tau\, J}$ obtained from a perturbation $\Delta\boldsymbol{F}^{(i,j)}$ are

calculated as

$$\mathbb{C}^{\tau\, J(i,j)} \approx \frac{\boldsymbol{\tau}(\hat{\boldsymbol{F}}^{(i,j)}) - \boldsymbol{\tau}(\boldsymbol{F})}{\varepsilon}. \tag{4.36}$$

Therefore, to calculate the 21 components of the 6×6 symmetric tangent modulus tensor, the deformation gradient has be to perturbed 6 times. Sun *et al.* determined an optimal value for $\varepsilon = 10^{-8}$, resulting in the minimum number of increments [198]. This numerical approximation was adopted to calculate the tangent modulus tensor, in the Fortran UMAT implementation.

4.5 Residual Stress

At the unloaded state - when all external loads acting on vascular tissues are removed - blood vessels are not stress-free. In fact, experimental evidence suggests the existence of residual stresses within the wall [200]. Transversally cutting a blood vessel causes it to spring back along its axial direction,revealing the presence of an internal axial stress field, while longitudinal cuts release circumferential stress, making the ring of tissue open up. Furthermore, it has been shown that residual stresses may play an important role on the stress distribution within the arterial wall [201], thus, including them in the analysis is essential for realistic modelling of the wall mechanics

A widely used method to obtain information about the stress-free configuration is the so-called "opening angle method". The experiment consists in two parallel cuts, to obtain a thin ring of vascular tissue, and a longitudinal cut, made through the ring. Typically, the ring opens up releasing almost all the residual stress in the artery. In previous numerical analyses, residual stresses have been included in FE analysis, by applying suitable boundary conditions, starting from the opened up configuration, and displacing all the nodes along the cut edges, to obtain the closed configuration [105]. However, this method is impractical and presents various limitations, especially on patient-specific 3-D geometries. To

overcome this problems in the present study, it was decided to use the approach described by Alastrué *et al* [181].

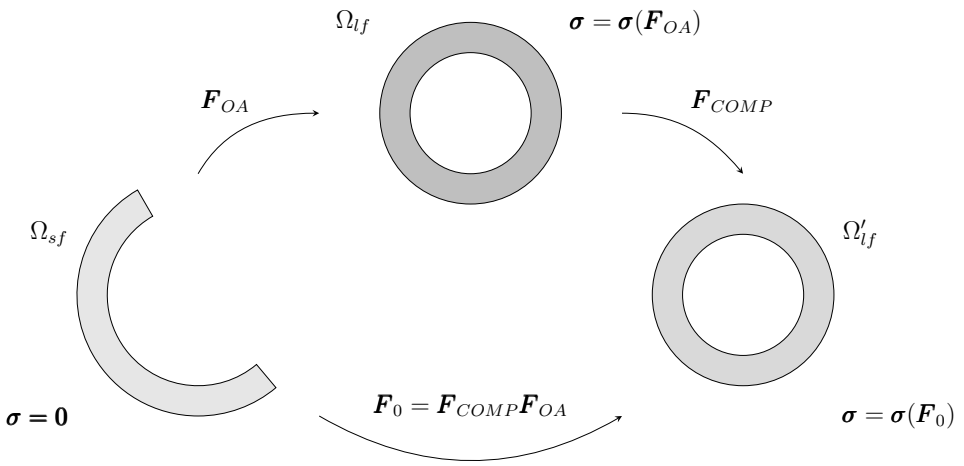

Figure 4.6: Pre-strain is included in the reference closed configuration Ω_{lf}, to account for the residual stresses due to the opening angle experiment. Enforcing equilibrium, a compatible deformation tensor $\mathbf{F}_{COMP}$, that maps Ω_{lf} in $\Omega\prime_{lf}$, can be found.

This method is based on the work of Chuong and Fung [202], who assumed that the deformation from the open to the closed configuration was a plane strain deformation, particularly pure bending. Let Ω_{sf} be the initial stress-free state, and Ω_{lf} a successive state, that can be reached through a non-compatible deformation tensor $\mathbf{F}_{OA}$ that enforces residual stresses. Since $\mathbf{F}_{OA}$ may lead to an unbalanced situation, a third state $\Omega\prime_{lf}$ enforcing equilibrium is required, with $\mathbf{F}_{COMP}$ a compatible deformation tensor that maps Ω_{lf} in $\Omega\prime_{lf}$. These two configurations should be similar, and thus $\mathbf{F}_{COMP} \sim \mathbf{I}$ (see Fig. 4.6).

An analytical approximation of $\mathbf{F}_{OA}$ can be calculated pointwise, using the work of Chuong and Fung. A bending moment is applied to the open configuration Ω_{sf} to get the closed configuration Ω_{lf} (see Fig. 4.7). The cylindrical coordinate system identified by $\{\mathbf{E}_R, \mathbf{E}_\Theta, \mathbf{E}_Z\}$ is defined for Ω_{sf} and $\{\mathbf{e}_r, \mathbf{e}_\theta, \mathbf{e}_z\}$ for Ω_{lf}. Assuming material incompressibility, the transformation that takes $\{R, \Theta, Z\}$ into

$\{r, \theta, z\}$ is:

$$r = \sqrt{\frac{R^2 - R_i^2}{\beta\lambda_z} + r_i^2},\ \theta = \beta\Theta,\ z = \lambda_z Z, \tag{4.37}$$

where $\beta = 2\pi/(2\pi - \alpha)$ is a measure of the opening angle, α is the opening angle, and λ_z, assumed constant, is the axial stretch. Also, the other two principal stretches can be determined,

$$\lambda_r = \frac{\partial r}{\partial R} = \frac{R}{r\beta\lambda_z},\ \lambda_\theta = \frac{r}{R}\frac{\partial\theta}{\partial\Theta} = \frac{\beta r}{R}. \tag{4.38}$$

The incompressibility restriction prescribes that $\lambda_r\lambda_\theta\lambda_z = 1$ and thus $\mathbf{F}_{OA}$ can be written as:

$$\mathbf{F}_{OA} = (\lambda_\theta\lambda_z)^{-1}\mathbf{e}_r \otimes \mathbf{E}_R + \lambda_\theta\mathbf{e}_\theta \otimes \mathbf{E}_\Theta + \lambda_z\mathbf{e}_z \otimes \mathbf{E}_Z, \tag{4.39}$$

$\mathbf{F}_{OA}$ is implemented in Abaqus, through a Python macro. The stretches are calculated analytically and written to a file, for each Gauss point of the grid. At the beginning of the analysis, the residual stress deformation gradient is loaded in the Fortran UMAT and the deformation gradient is pre-multiplied by $\mathbf{F}_{OA}$. Then, a static equilibrium step is solved, and a compatible pre-stressed configuration is found.

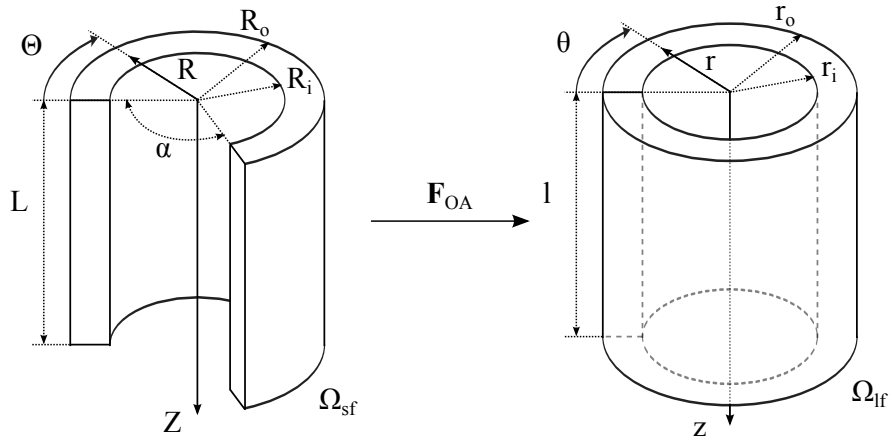

Figure 4.7: Open Ω_{sf} and closed Ω_{lf} configurations. $\mathbf{F}_{OA}$ can be analytically estimated assuming pure bending and plane strain, from [202].

4.6 Benchmarks

4.6.1 UMAT Benchmark

To verify the UMAT subroutine implemented in Fortran, it was decided to replicate the uniaxial tensile tests on adventitial strips, carried out by Gasser *et al.* in [106]. Abaqus 6.13-2 provides an implementation of the model of Gasser *et al.*, which was used as a benchmark. For the tests, circumferential and axial specimens were considered. It was assumed that the mean orientations of the families of collagen fibres $\mathbf{a}_1$ and $\mathbf{a}_2$ have no radial component, and the following material parameters $C_{10} = 7.64$ kPa, $k_1 = 996.6$ kPa, $k_2 = 524.6$ and structure parameters $\gamma = 49.98°$, $k = 0$ and $k = 0.226$ were chosen. The angle γ represents the angle between the circumferential direction and the fibres mean orientation. Adventitial strips of length $L = 10.0$ mm, width $W = 3.0$ mm and thickness $T = 0.5$ mm are considered throughout this test. Results for the 4 different cases are shown in Figure 4.8. Figure 4.9 illustrates the predicted tensile load/displacement (T/u) response. Here u and T denote the displacement between the two strips ends, and the force acting there. As noted by Gasser, in case of perfect alignment ($k = 0$, Figure 4.8(a)-(c)), the collagen fibres need to rotate nearly into the loading direction before they can carry load [106], which causes a large extension in the radial direction. In turn, the incompressibility constraint causes a decrease in width of the specimens. By contrast, for the material presenting fibre dispersion ($k = 0.226$, Figure 4.8(b)-(d)), less rotation of the collagen fibres is required before they carry load, which results in a stiffer response of the specimens. Good agreement between the Abaqus HGO material and the implemented User Material is shown in Figures 4.8 and 4.9.

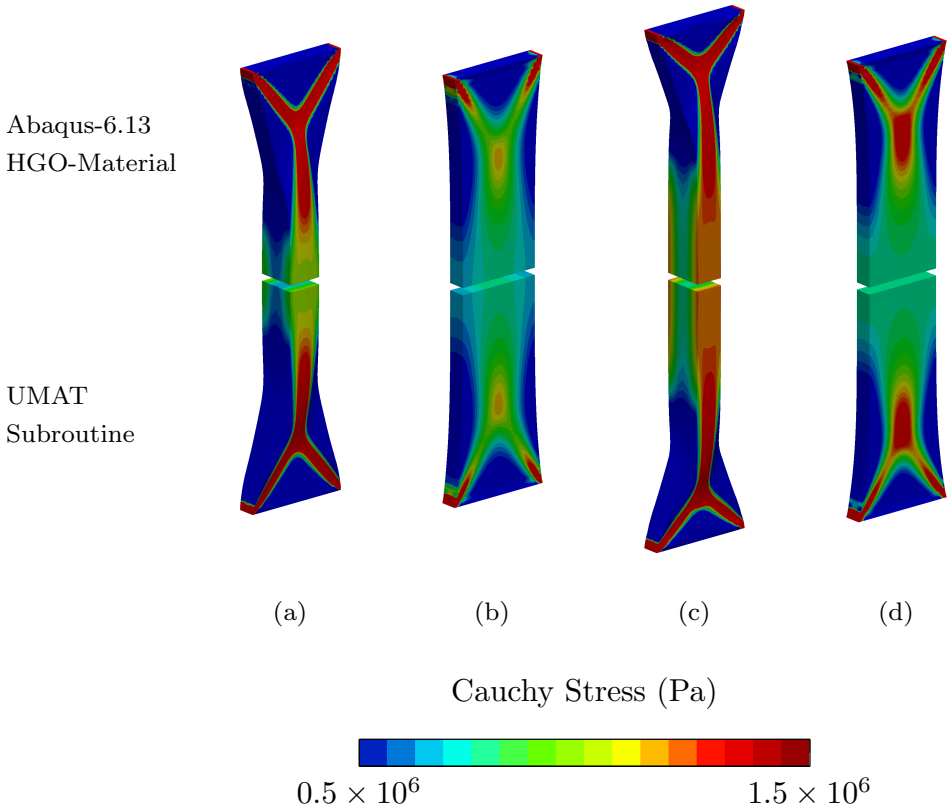

Figure 4.8: Cauchy stress in the direction of the applied load in an iliac adventitial strip in the axial (a-b) and circumferential (c-d) directions. Results are shown for 1.0 N tensile load and for different values of dispersion ($k = 0.0$ in (a) and (c), $k = 0.226$ in (b) and (d)). Results on the top half are obtained using the Abaqus HGO material, on the bottom half using the UMAT subroutine.

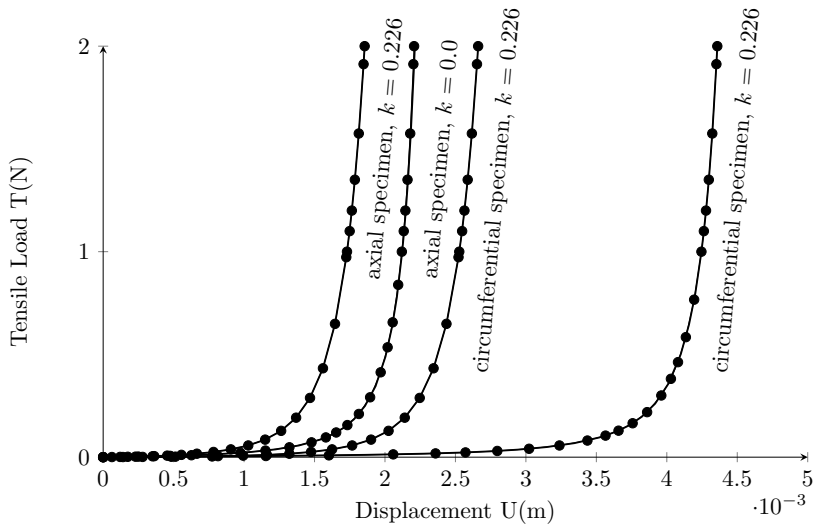

Figure 4.9: Computed tensile load/displacement (T/u) response of the circumferential and axial specimens. Dashed and dotted curves are with ($k = 0.266$) and without ($k = 0$) dispersion of the collagen fibres. Results obtained using the implemented UMAT subroutine are in solid lines, using Abaqus HGO material are in dots.

4.6.2 Residual Stress Benchmark

A simple two-dimensional benchmark was conducted to assess, on a ring of vascular tissue, the effectiveness of the method proposed by Alastruè *et al.* [181] . A ring of adventitial tissue, with material parameters chosen to test the UMAT subroutine, is initially pre-stressed. An initial closed configuration having outer radius $r_o = 0.00243$ m and wall thickness $T = 0.00043$ m is used. The residual stress field is then defined by means of an opening angle $\alpha = 110°$, an outer radius $R_o = 0.0036$ m and longitudinal stretch $\lambda_z = 1.0$. Residual stress is initially applied to a thin ring of adventitial tissue. Subsequently, after the ring is cut longitudinally, it opens up, releasing almost entirely the residual stresses (see Fig.4.10). Further, it can be noted that the measured opening angle in Fig.4.10-(c) (112°) is very close to the initial α used to compute the residual deformation gradient.

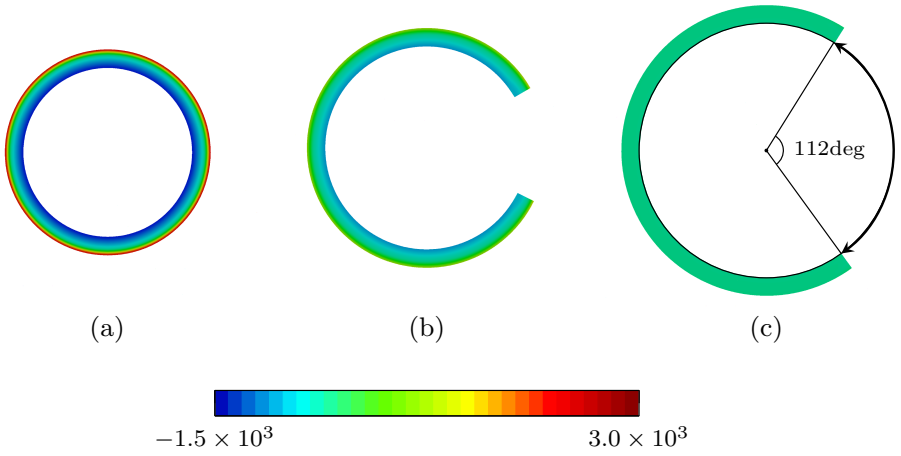

Figure 4.10: Circumferential stress in a ring of venous tissue, after the application of residual strain (a), at 50% of the equilibrium step (b) and for the open configuration (c). When the ring is opened, residual stresses are almost entirely released.

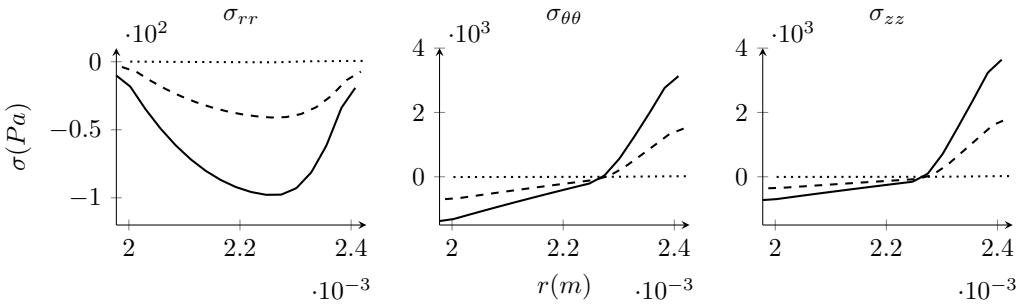

Figure 4.11: Radial σ_{rr}, circumferential $\sigma_{\theta\theta}$ and axial σ_{zz} stress in a ring of adventitial tissue, after the application of residual stress. Solid line: applied residual stress; dashed line: 50% of the equilibrium step; dotted line: end of the equilibrium step.

4.7 Reference Configuration for the FE Model

For the sake of simplicity, it was assumed that both the host artery and vein run parallel and are located in the same plane. Their geometry was created by sweeping a circular cross-section of constant radius, along the straight vessel centreline. This assumption clearly does not allow one to fully represent the totality

of brachio-cephalic AVF configurations, some of which exhibit non-planarity and a large spectrum of geometric features, such as curvature and taper. However, such an assumption was assumed to be as a good first approximation of the initial geometry, to characterise the state of stress and strain, in newly formed AVF.

	Artery		Vein		
Parameter	Value	Reference	Value	Reference	Units
R	2	[203]	2	[204]	mm
T	0.43	[203]	0.2	[204]	mm
T_v	$0.3T_A$	[164]	$0.5T_V$	[140]	-
L	60 $(15 \times 2R_A)$	-	52 $(13 \times 2R_V)$	-	mm
	AVF Dimensions				
Parameter	Value				Units
a	3.2				mm
b	0.8				mm
$d_{a\text{-}v}$	25				mm
L_m	20				mm

Table 4.1: Geometric parameters used to construct the FE model, shown in Figure 4.12.

A value of 2.0 mm was used for the radii of both vessels, at the unloaded state. Constant wall thicknesses of 0.43 mm and 0.2 mm were chosen respectively for the artery and the vein, in line with *in-vivo* measurements [203, 204]. The wall was divided into two layers of constant thickness, corresponding to the intima-media and adventitia layers, which represent respectively the avascular and vascular portion of the wall. The vascular layer was assumed to occupy the external third

of the host artery wall ($T_{v\text{-}A} = 0.3\ T_A$) [164, 205], and the external half of the vein wall ($T_{v\text{-}V} = 0.5\ T_V$) [140].

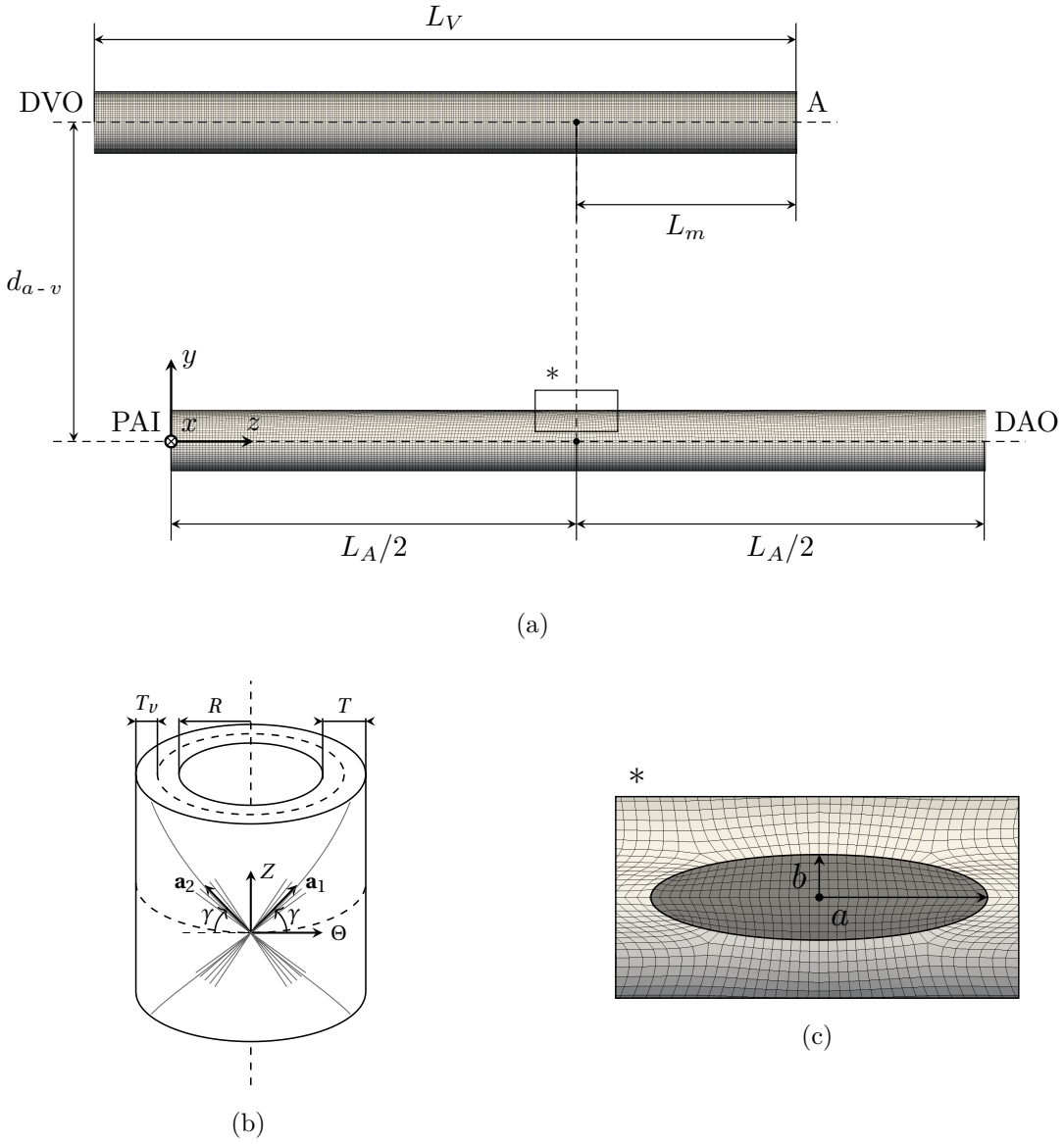

Figure 4.12: (a) Schematic illustration of the idealised model of native brachial artery and cephalic vein, used to form the AVF; (b) diagram showing the mean orientation of two families of collagen fibres $\mathbf{a}_1$ and $\mathbf{a}_2$ and the vascular and avascular layers; (c) close-up view of the anastomosis site on the artery: in dark gray, the elements removed to form the elliptical arteriotomy.

This represents a common practice in several numerical studies [105, 5, 11], as healthy blood vessels normally show constant wall thickness. In addition the current imaging resolution of MRI and CT scans, does not allow to distinguish the wall and more importantly the layers from the vessel lumen. More invasive techniques, such as intravascular ultrasound, would be required to obtain an exact wall characterization.

The distance $d_{a\text{-}v}$, between the brachial artery and cephalic vein centrelines, was chosen to be 25 mm, in line with geometries reconstructed from patient specific MRI scans [44]. To ensure the reduction of any boundary effect, artery and vein length, L_A and L_V, were chosen, respectively, to be equal to 15 and 13 diameters, and the centre of anastomosis is located in the middle of the host artery. The goodness of this assumption was checked *a-posteriori*, by verifying that no stress concentration appears near the domain boundaries.

The autogenous brachio-cephalic access is normally formed in the upper arm across the antecubital fossa, along the cephalic/median antecubital vein. The vein is dissected free from the surrounding tissue for approximately 3-4 cm [206]. The vein must be mobilised sufficiently to deliver it medially, into the deeper plane where the artery resides. Depending on the local vascular anatomy, the length of available vein can vary, producing tighter and loopier geometries [51]. In the idealised model shown in Figure 4.12, the length of mobilised vein $L_m = 20$ mm identifies the excess of vein from the anastomosis centre, projected onto the vein centreline.

Two main types of arteriotomy, slit and elliptical/oval, are reported in the literature for end-to-side anastomosis. While no significant difference in patency rates were observed by Zoubos *et al.* between the two procedures, the elliptical arteriotomy appears to facilitate suture placement and overall leads to lower aneurysm formation [207]. Scheltes *et al.* speculate that this better outcome could be attributable to the reduction of stress concentration, in comparison

with the slit arteriotomy, which can reduce the risk of tearing and endothelial damage [208].

An ellipse, having semi-minor axis $b = 0.8$ mm and semi-major axis $a = 4b = 3.2$ mm, was projected onto the vein surface (see Figure 4.12) and used to model an elliptical arteriotomy. Parameters a and b were chosen so that the ellipse perimeter matched the vein perimeter, to ensure proper contact between the faces and avoid kinking.

4.7.1 Boundary Conditions

A local cylindrical reference frame is defined for each of the PAI, DAO and DVO faces (see Figure 4.12). The displacement of the nodes on these faces is fixed in the local longitudinal and angular direction, which corresponds to the following boundary conditions

$$d_\theta = 0 \ , \ d_z = 0, \tag{4.40}$$

with $d_\theta = 0$ and $d_z = 0$ displacements in the longitudinal and angular directions, respectively.

A uniform pressure load is applied to the elements on the luminal surface which corresponds to the following equation

$$\boldsymbol{\sigma} \cdot \mathbf{n} = p_{diast}, \tag{4.41}$$

where $\boldsymbol{\sigma}$ is the Cauchy stress tensor, $\mathbf{n}$ the local surface normal and p_{diast} the applied diastolic pressure.

4.8 Mechanical Parameters

Due to the lack of readily available mechanical properties in the literature for brachial arteries and cephalic veins, the values of the material parameters used

in the HGO constitutive model, shown in Table 4.2, were determined based on measurements available for blood vessels, that have similar size and properties. Furthermore, due to the lack of layer specific tensile tests measurements, each vessel was treated as a single layer of homogenous material, having average mechanical properties.

Specifically, parameters for the brachial artery (BA) were calculated based on uniaxial tensile tests of common carotid arteries (CCA) [209], by fitting the HGO constitutive model to axial and circumferential stress-stretch curves, according to the method described by Holzapfel *et al.* in [143]. In fact, BA and CCA have similar diameter and thickness, are exposed to similar pressures and located close in the circulatory system, and show similar stiffness.

Saphenous veins (SV) were used as a surrogate for the cephalic veins (CV). CV and SV are both superficial, peripheral veins that have similar dimensions and have been used interchangeably, depending on the availability, as bypass grafts [210, 211]. The main difference between the two vessels resides in the different hydrostatic pressure acting on them - due to the erect posture, lower limb veins are exposed to high transmural pressures than arm vessels. Eiken *et al.* observed that CV exhibit similar distensibility to SV and are only slightly more distensible at higher pressures, probably due to the thinner wall [212]. Parameters for the CV were taken from the work of Vesely *et al.*, who studied the mechanical properties of SV used for CABG [213]. The mean collagen fibre orientations $\mathbf{a}_1$ and $\mathbf{a}_2$ were defined in a local element basis (see Figure 4.12-(b)), as forming an angle of γ and $\pi - \gamma$, with the local circumferential direction $\boldsymbol{\Theta}$.

In order to reliably predict the stress state in the wall, residual stresses were included in the simulation, according to the method proposed by Alastruè *et al.* and described in Section 4.5 [181]. An opening angle of 110° and axial pre-stretch od $\lambda_z = 1.05$ were used for the brachial artery, based on the measurements of Delfino *et al.* [214], and an opening angle of 120° and axial pre-stretch od $\lambda_z = 1.0$

were used for the cephalic vein, based on the measurements of Vesely *et al.* [213].

	Artery		Vein		
Parameter	Value	Reference	Value	Reference	Units
C_{10}	88.5	[209]	5.3	[213]	kPa
k_1	490	[209]	2.5	[213]	kPa
k_2	33.2	[209]	31	[213]	-
k	0.1	[209]	0.01	[213]	-
γ	42.5	[209]	41	[213]	deg

Table 4.2: Material parameters for the HGO strain energy function.

4.9 Computational Grid

The geometry of the reference configuration, shown in Figure 4.12, was discretised using $\sim 420K$ elements, $\sim 164K$ in the artery and $\sim 256K$ in the vein. Three-dimensional, first-order, reduced-integration, hexahedral elements (Abaqus - Standard C3D8R brick elements) were used to mesh the structure [215]. The use of such elements is motivated by the fact that first-order fully-integrated elements, under bending-dominated problems, experience overly stiff behaviour. This effect is called "shear locking" and is caused by energy going into shearing the element rather than bending it.

Reduced-integration elements, having less integration points, exhibit lower stiffness than fully-integrated elements, but are more prone to "hourglassing", a spurious deformation mode, resulting from the excitation of zero-energy degrees of freedom. Typically, it manifests as a patchwork of zig-zag or hourglass like element shapes, where individual elements are severely deformed, while the overall

mesh section is undeformed. Hourglassing can be evaluated in terms of energy and generally be reduced by having a minimum number of elements, through the section experiencing bending. To reduce hourglassing, in all simultions, eight elements were used through the wall thickness.

Reduced-integration elements also helps to reduce volumetric-locking. The incompressibility restriction would be numerically ill-posed, if discretised using a classical formulation. Spurious pressure stresses develop at the integration points, causing an element to behave too stiffly for almost isochoric deformations [215].

4.10 Simulation Procedure

A series of non-linear static and quasi-static equilibrium steps were used to model the surgical procedure. Prior to anastomosis, the cephalic vein was mobilised and cut transversally at 90°, with respect to the vessel axis. The artery and the vein, initially unloaded at the beginning of the analysis, were pre-stressed, by applying the opening angle deformation gradient $\mathbf{F}_{OA}$, calculated from opening angle parameters and local Gauss point coordinates. Then, a displacement field is applied to the nodes located on the newly cut distal vein end, so that they match the margins of the anastomosis opening (see Figure 4.13(b)). The displacement field was determined by mapping the nodes on the vein end over the arterial wall, using the Laplacian mesh deformation proposed by Sorkine [216].

Once this is achieved the host artery and the vein were mechanically attached and the anastomosis was created, by removing elements contained in the ellipse shown in Figure 4.12-(c) and 4.13. This mechanical tie was modelled as a hard contact with a surface-to-surface formulation and solved using Lagrange multipliers. After contact between the parts was established, normal and tangential relative motion between the faces was prohibited.

This mechanical attachment mimics the effect of the suture, with the exception that the vein and host artery material are not pressed together by the stitches.

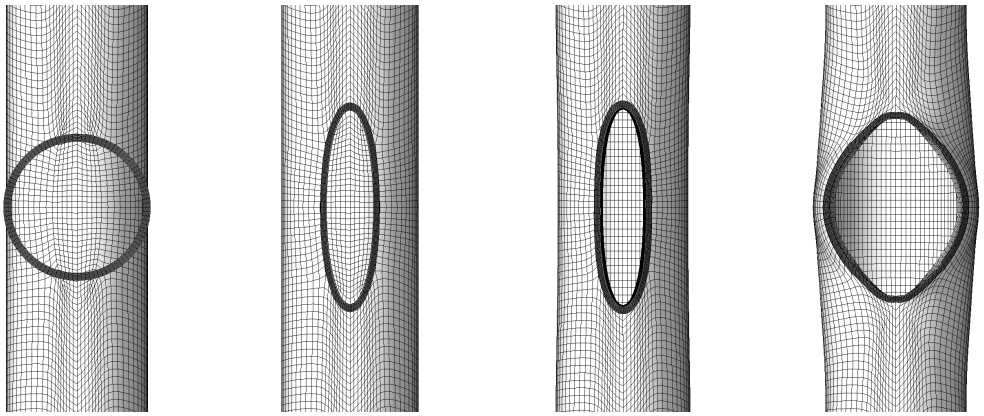

(a) (b) (c) (d)

Figure 4.13: In dark gray, elements on the newly cut distal vein end, in light gray, brachial artery. (a) Reference configuration; (b) nodes on the vein end are mapped and tied to the arterial wall; (c) elements on the artery wall are removed to form an elliptical arteriotomy; (d) loaded configuration.

In addition, during the actual surgical operation, depending on the geometries and material properties of the vessels, this step may lead to vessel injury, and consequently to anastomotic remodelling or healing, which contributes to peri-anastomotic IH formation [2].

After the vessels are connected, a static step was used to allow the structure to reach equilibrium (Figure 4.13-(c)). Then all the wet internal surfaces were pressurised to the arterial systolic pressure, which was assumed to be 16 kPa (120 mmHg). Finally the distal vein end (DVO) was brought to its final position, shown in Figure 4.14-(e), and the internal pressure lowered to 13.33 kPa (100 mmHg). This sequence of steps was chosen, rather than the actual surgery, to speed-up convergence. In fact, bending the thin unloaded vein can lead to buckling, which is known to sensibly slow down convergence. In all the steps, nodes on the PAI, DAO and DVO faces were simply supported and only radial displacement, with respect to the vessel centreline, was allowed.

The numerical framework here described was developed through a set of Python macros, to automate the geometry/mesh creation and solution, and allow

to easily vary geometric and mechanical parameters. Each simulation was carried out on 8 cores of a Dell AMD Opteron 64-core server with 512 GB RAM, and required approximately 6 hours to complete.

4.11 Results

Figure 4.14 shows side-on views of the simulation steps outlined in the previous section, coloured by $\sigma_{\theta\theta}$. The distribution of the residual stresses at the unloaded state is shown in Figure 4.14-(b) . In the circumferential direction, the artery has a compressive residual stress of 18 kPa at the inner wall and a tensile stress of 29 kPa at the outer wall. In the vein, the compressive and tensile circumferential stresses are 0.5 kPa and 0.4 kPa, respectively.

These values of stress, especially in the vein, are small compared with stresses at loaded states, shown in Figures 4.14-(e) and (f). However, their presence appears to have a large effect on the stress conditions of the wall and is thought to help maintaining blood vessels in a state of homogeneous strain at the loaded state. Figure 4.16 shows circumferential Cauchy stress at the loaded state, with and without residual strains applied. It is apparent that including residual deformation in the analysis reduces stress concentration and normalize transmural stress, lowering the maximum $\sigma_{\theta\theta}$ in the vein, from ≈ 370 kPa to ≈ 220 kPa.

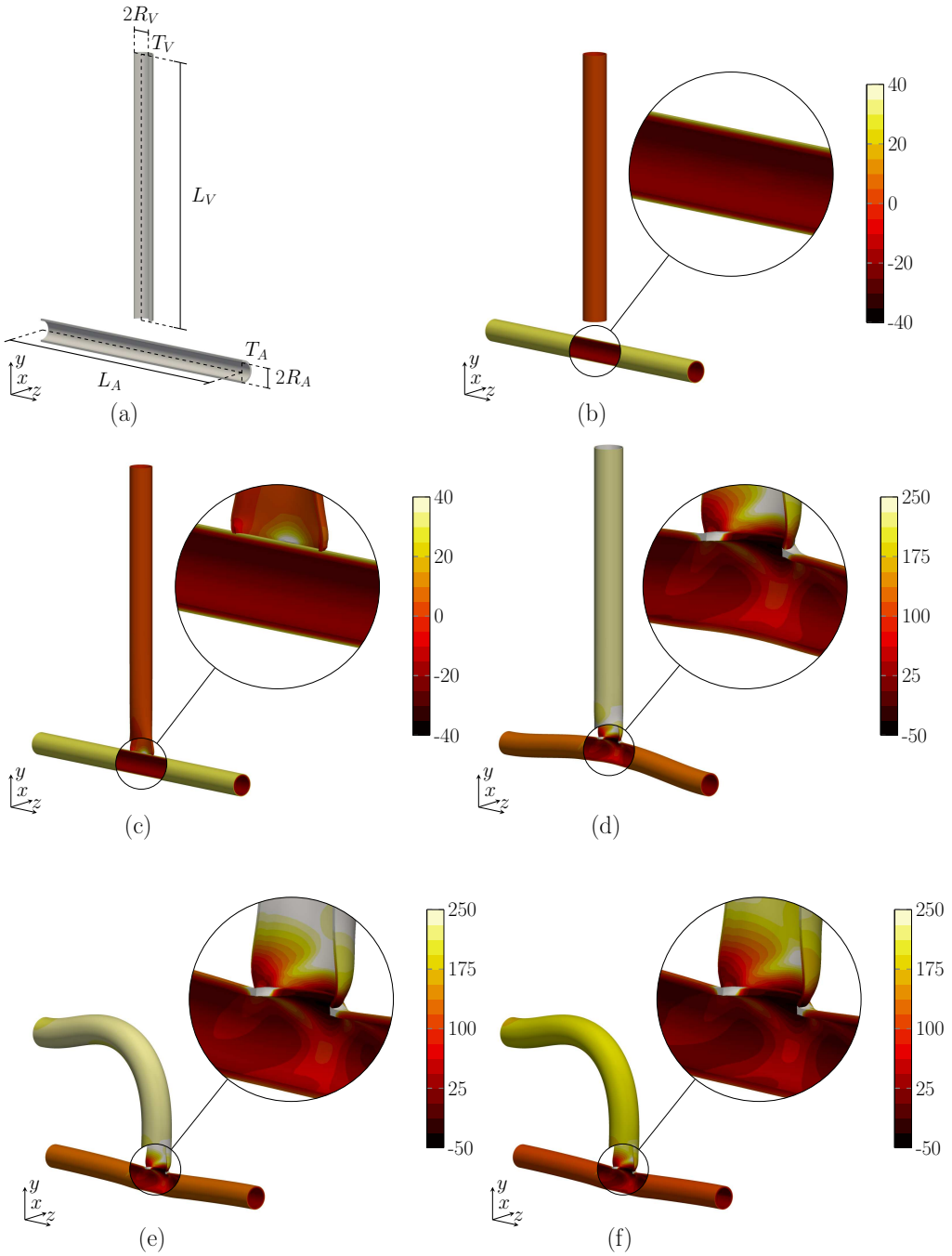

Figure 4.14: FE model of the AVF surgery, coloured by $\sigma_{\theta\theta}$, in kPa: (a) initial geometry; (b) residual stress is loaded; (c) the nodes on the cut vein end are connected to the arterial outer wall; (d) the elliptical arteriotomy is formed and an internal pressure of 120 mmHg is applied; (e) DVO is moved to its final position (according to Figure 4.12); (f) the internal pressure is lowered to 100 mmHg.

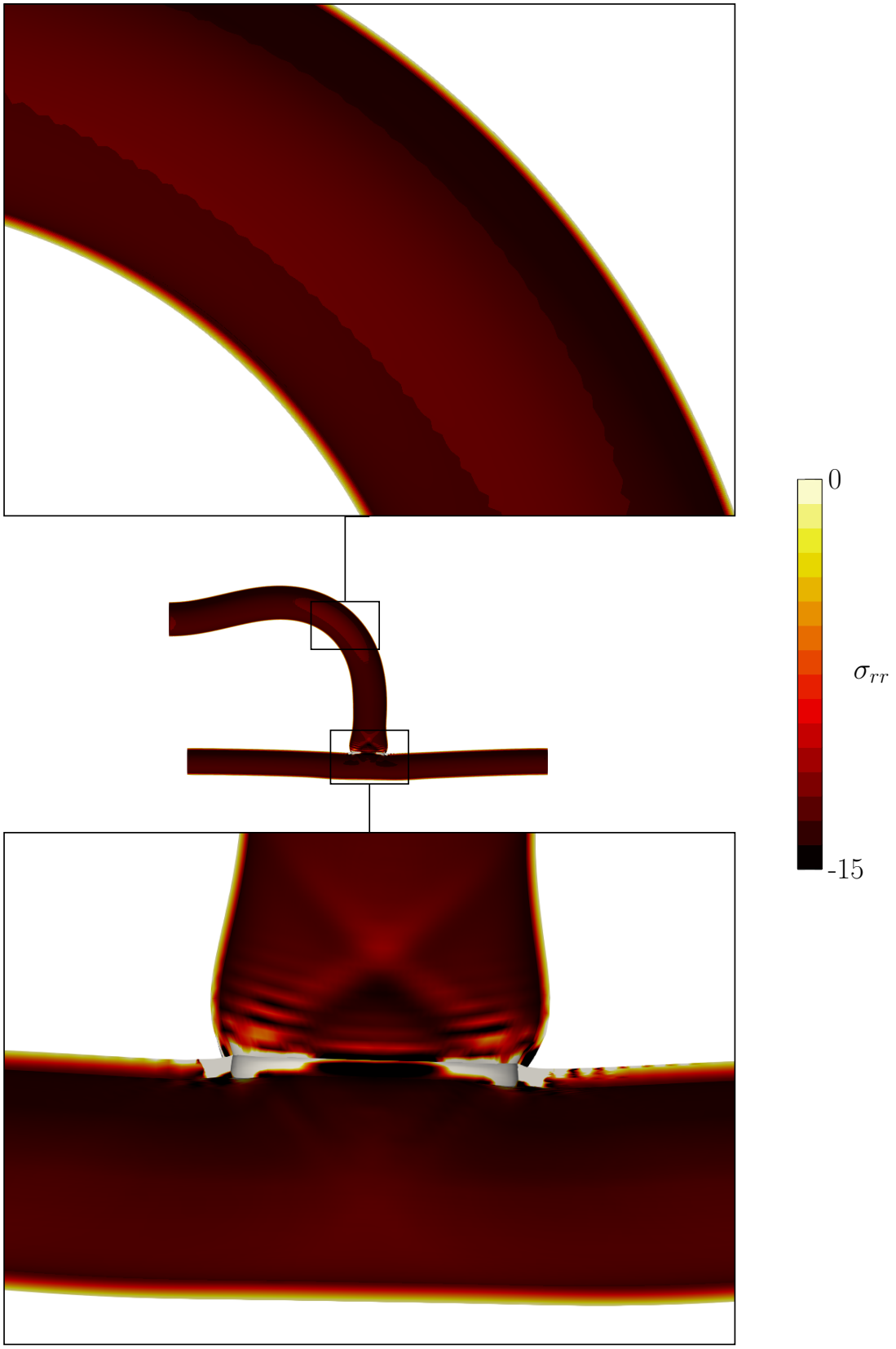

Figure 4.15: Close-up distributions of radial stress (σ_{rr}) in kPa, shown at two locations, at the end of the loading cycle (Fig. 4.14-f)

Furthermore, it causes inversion of the stress distribution in the artery. This has been hypothesized to have a protective effect on the endothelium, shifting the maximum stress from the inner to the outer wall surface [217].

The high stress in the cephalic vein under arterial pressure is to be expected, given its smaller thickness and lower stiffness. The average venous pressure measured in healthy CVs is reported to be 7 mmHg [218], about fourteen times smaller than the diastolic pressure, applied in the simulations. As a result, the vein diameter undergoes a significant expansion, ($\approx 30\%$), much larger than that experienced by the artery ($\approx 5\%$).

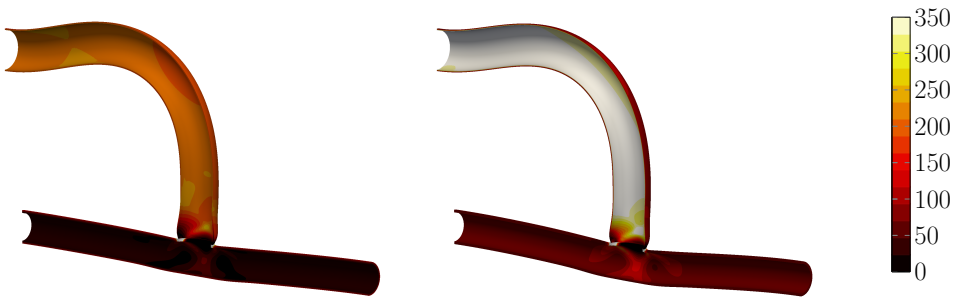

(a) Residual Stress (b) No Residual Stress

Figure 4.16: Distributions of $\sigma_{\theta\theta}$ (in kPa), at the loaded state, with (a) and without (b) residual stress. Including residual stress reduces stress concentration at the endothelium and normalize transmural stress.

Severe changes in the mechanical environment appear along the transitions between arterial and venous tissue, and in particular stress concentration can be observed at the incision ends. These sharp mechanical discontinuities have been hypothesized to contribute to IH, as observed by Trubel *et al.* and Perktold *et al.* in regions of compliance mismatch and elevated mechanical stress [101, 219]. However, whether their importance in inducing vascular disease is comparable to haemodynamic factors, hypoxia or other inflammatory responses, is still an open question, that deserves further research.

Previous studies have shown that geometric parameters, such as blood vessel

sizes, incision length and insertion angle can play a significant role in the mechanics of an anastomosis [103, 105]. Figures 4.17-(a),(b) and (c) show three different AVF geometries, obtained from varying L_m to 1, 2 and 3 cm. For comparison, Figure 4.17-(d) shows brachio-cephalic AVF geometries, reconstructed from MRI scan images of haemodialysis patients'at St.Mary's Hospital. Good visual agreement can be observed between the geometries produced with the idealised FE model and the reconstructed AVF. Also, it appears that shorter mobilised veins are more common among the patients with brachio-cephalic AVFs.

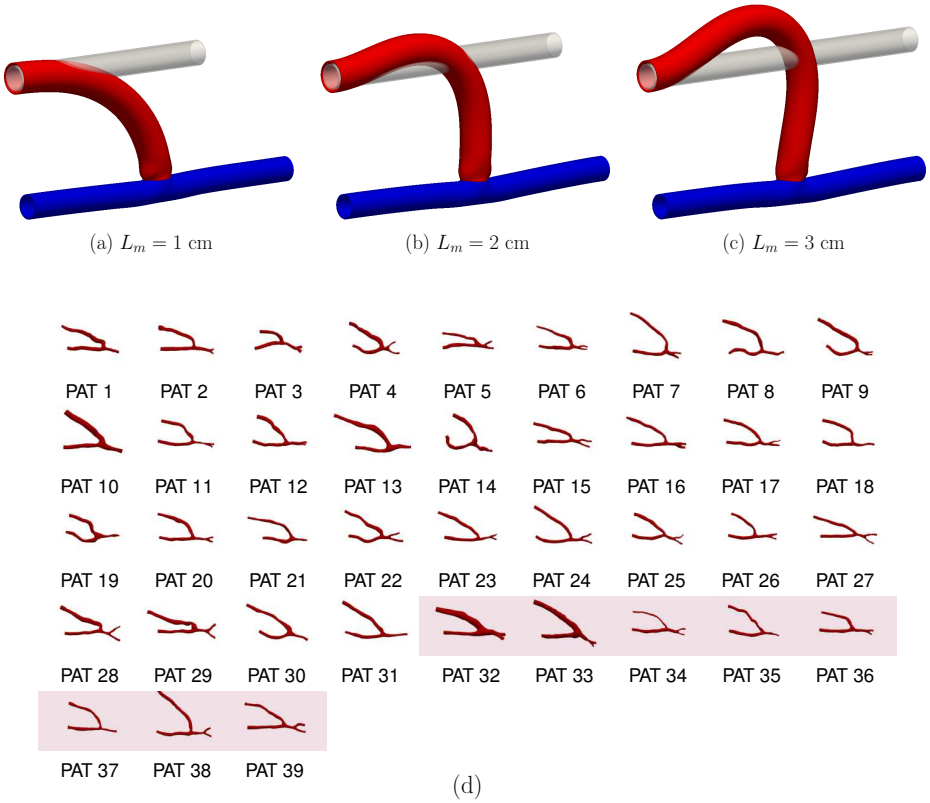

(a) $L_m = 1$ cm (b) $L_m = 2$ cm (c) $L_m = 3$ cm

(d)

Figure 4.17: AVF configurations obtained from varying L_m to 1, 2 and 3 cm, respectively (a), (b) and (c). (d) shows brachio-cephalic AVF geometries, reconstructed from MRI scan images of haemodialysis patients at St.Mary's Hospital (courtesy of Lorenza Grechy and Richard Corbett); in red, primary failures.

The length of mobilised vein is a parameter arbitrarily chosen by the vascular surgeon, during the intervention, determined by the patient's anatomy. In gen-

eral, it is preferred to cut the vein short to avoid kinking; long cephalic veins are also not usually available.

Figure 4.18 shows the maximal principal stress, σ_1, in three AVF configurations, with increasing values of L_m.

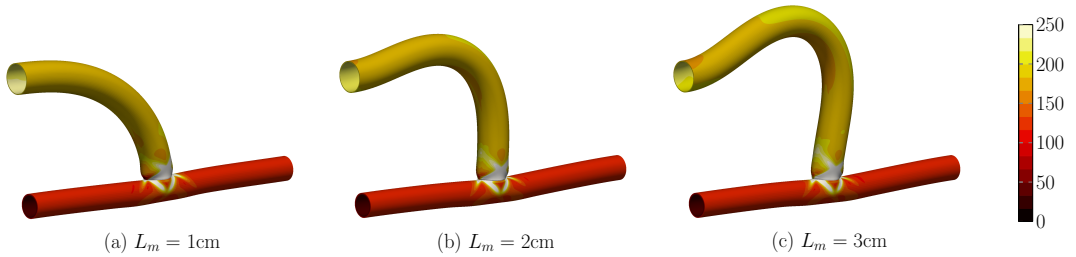

(a) $L_m = 1$cm (b) $L_m = 2$cm (c) $L_m = 3$cm

Figure 4.18: Distribution of maximal principal stress σ_1 (in kPa), with increasing values of L_m to 1, 2 and 3 cm, respectively (a), (b) and (c).

It is apparent that bending of the vein has the effect of concentrating stresses around the site of bend and in particular, longer veins lead to more severe stress concentration (Fig. 4.18-(c)). In addition, in the straight lengths of the artery and vein, the maximal principal stress is equal to the circumferential stress (Fig. 4.14-(f) and Fig. 4.18-(b)). This is to be expected, as for both vessels, the collagen fibres, are mainly oriented in the circumferential direction, to maximise the vessel load-bearing capacity.

4.11.1 Perfusion Field

From the FE model, distributions of VV perfusion in the vascular wall were calculated, through Equation 4.1 and 4.6, respectively for the stress- and stretch-based model. Figure 4.19-(a) shows radial stress in the loaded state. Radial stress is compressive and equal to the applied internal pressure, 13.33 kPa (100 mmHg) at the inner wall, and curvilinearly goes to zero, at the outer wall.

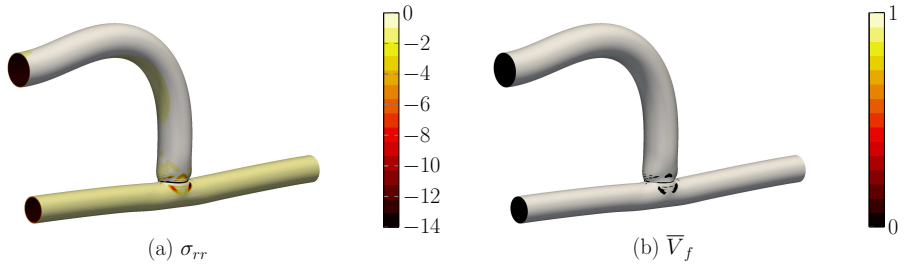

(a) σ_{rr} (b) $\overline{V}_f$

Figure 4.19: Distributions of (a) radial Cauchy stress, σ_{rr} (in kPa) and (b) normalized volume fraction of perfused VV, $\overline{V}_f$, calculated assuming $P_{thres} = 30$ mmHg.

In the stress-based model, the normalized volume fraction of perfused VV, $\overline{V}_f$, is calculated from σ_{rr}, through Equation 4.1, (Figure 4.19-(b) shows $\overline{V}_f$, assuming a pressure threshold, $P_{thres} = 30$ mmHg). This results in perfused VV that are only located in a thin external layer of the adventitia. To facilitate the visualization of such a field, $\overline{V}_f$ was averaged over the wall thickness, for each point of the endothelial surface. Results of this operation are shown in Figure 4.20. Specifically, Figure 4.20-(i) shows the AVF configuration having $L_m = 2$ cm, for different values of P_{thres} (15, 30 and 45 mmHg), while Figure 4.20-(ii) shows configurations with increasing values of L_m and constant $P_{thres} = 30$ mmHg.

From Figure 4.20-(i), it is clear that $\overline{V}_f$ is very sensitive to changes in P_{thres}. When $P_{thres} = 45$ mmHg, the depth-average $\overline{V}_f$ is equal to 0.3 and 0.5 in the artery and in the vein, respectively. This result corresponds to perfectly perfused adventitial layers - the vascular adventitia occupies the external third of the artery wall and the external half of the vein wall.

Lower values of P_{thres} result in a reduction in wall perfusion, especially in the vein. Conversely, the artery, having a thicker wall and more superficial VV, appears to be less sensitive to changes in P_{thres}. Stress concentration in the vein also causes a reduction in wall perfusion on the inside of the bend (see Figure 4.20-(i)-V2).

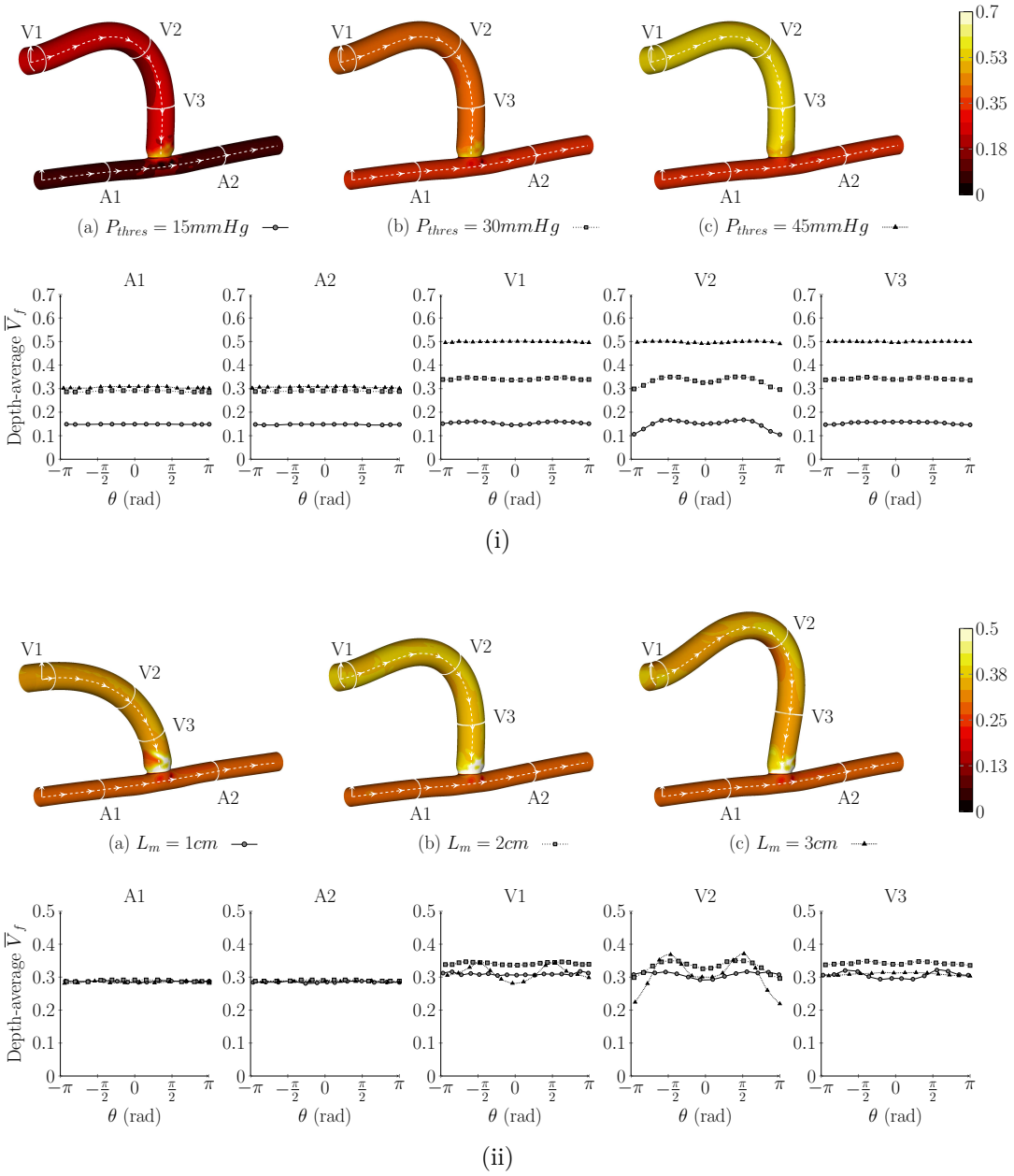

Figure 4.20: Distribution of normalized volume fraction of perfused VV, $\overline{V}_f$, averaged over the wall thickness and plotted at the endothelium. (i) AVF configuration having $L_m = 2$ and P_{thres} = (a) 15, (b) 30 and (c) 45 mmHg; (ii) $P_{thres} = 30$ mmHg and L_m = (a) 1, (b) 2 and (c) 3 cm.

Changes in L_m do not appear to affect the arterial perfusion. However, an even shorter vein could distort the artery, inducing kinking in the structure. On

the other hand, a longer vein accentuates stress concentration, further reducing perfusion at the site of bend (see Figure 4.20-(i)-V2).

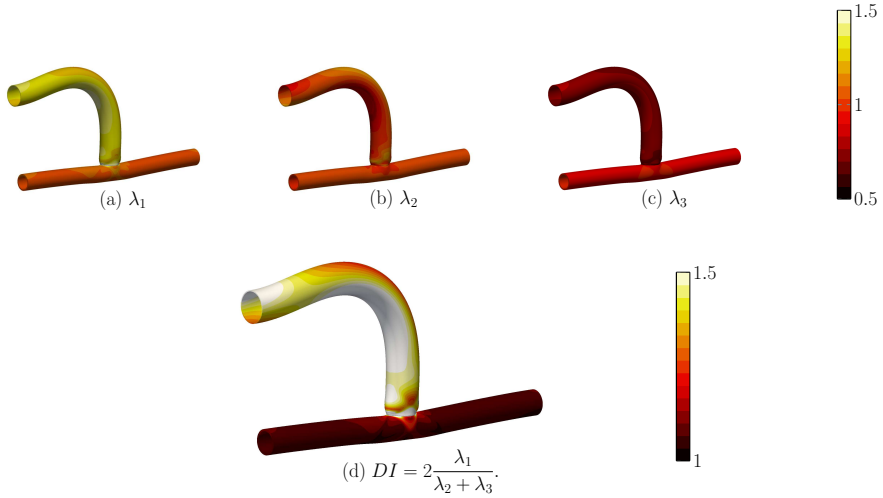

Figure 4.21: Distributions of principal stresses (a) λ_1, (b) λ_2, (c) λ_3 and (d) Distortion Index, DI.

Figures 4.21-(a), (b) and (c) illustrate principal stretches λ_1, λ_2 and λ_3, respectively, which were used to calculate DI, shown in Figure 4.21-(d). In the loaded state, the vein wall is exposed, especially on the inside of the bend, to large values of distortion, whereas, in the artery, modest wall deformation translates into values of DI close to 1.

In the stretch-based model, the normalized volume fraction of perfused VV, $\overline{V}_f$, was calculated from the Distortion Index, DI, through Equation 4.6. Transmural distributions of DI are uniform across the wall - again, only the external third of the artery wall and the external half of the vein wall are assumed to contain VV. Hence, distributions of $\overline{V}_f$ are presented in Figure 4.22, for the entire wall.

The parameter κ was included in the stretch-based model to allow to modulate the response of $\overline{V}_f$ to DI. From Figure 4.22-(i), it is clear that changing varying κ has a major effect on $\overline{V}_f$. When $\kappa = 0.5$, $\overline{V}_f$ is between to 0.8 and 0.9 in

the vein and about 0.95 in the artery, which corresponds to well perfused VV. Higher values of κ, however, induce a reduction in wall perfusion, particularly in the vein. Again, regions of the venous wall, exposed to stress concentration, experience a reduced wall perfusion (see Figure 4.20-(i)). Arterial perfusion also appears not to be altered by changes in L_m.

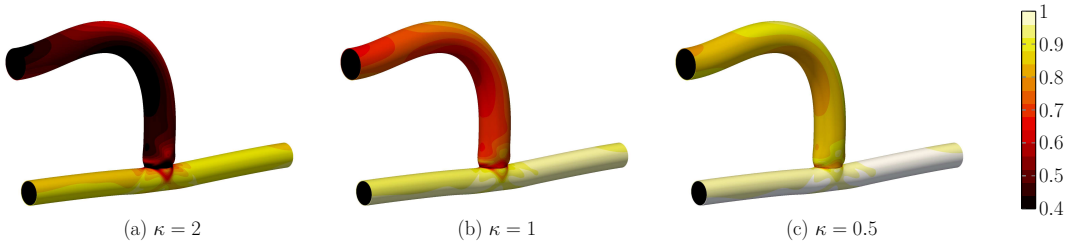

(a) $\kappa = 2$ (b) $\kappa = 1$ (c) $\kappa = 0.5$

(i)

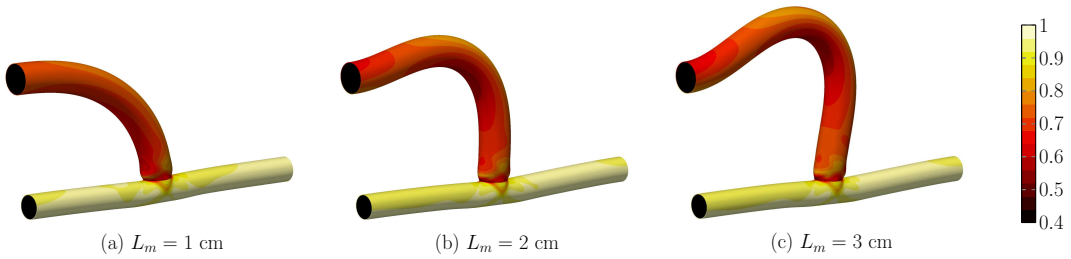

(a) $L_m = 1$ cm (b) $L_m = 2$ cm (c) $L_m = 3$ cm

(ii)

Figure 4.22: Distribution of normalized volume fraction of perfused VV, $\overline{V}_f$. (i) AVF configuration having $L_m = 2$ and $\kappa =$ (a) 2, (b) 1 and (c) 0.5; (ii) $\kappa = 1$ and $L_m =$ (a) 1, (b) 2 and (c) 3 cm.

4.11.2 Grid Independence

Grid independence of the FE mesh was assessed by running simulations of the configuration with $L_m = 2$ cm, on five successively finer discretisations. Convergence was verified for transmural distributions of radial stress (σ_{rr}) and Distortion Index (DI), which are the two quantities used to calculate $\overline{V}_f$, in the two perfusion models. Plots showing transmural σ_{rr} and DI in three locations, are presented in

Figure 4.23. Based on these results, meshes with resolutions similar to Mesh 4 were employed for all FE simulations.

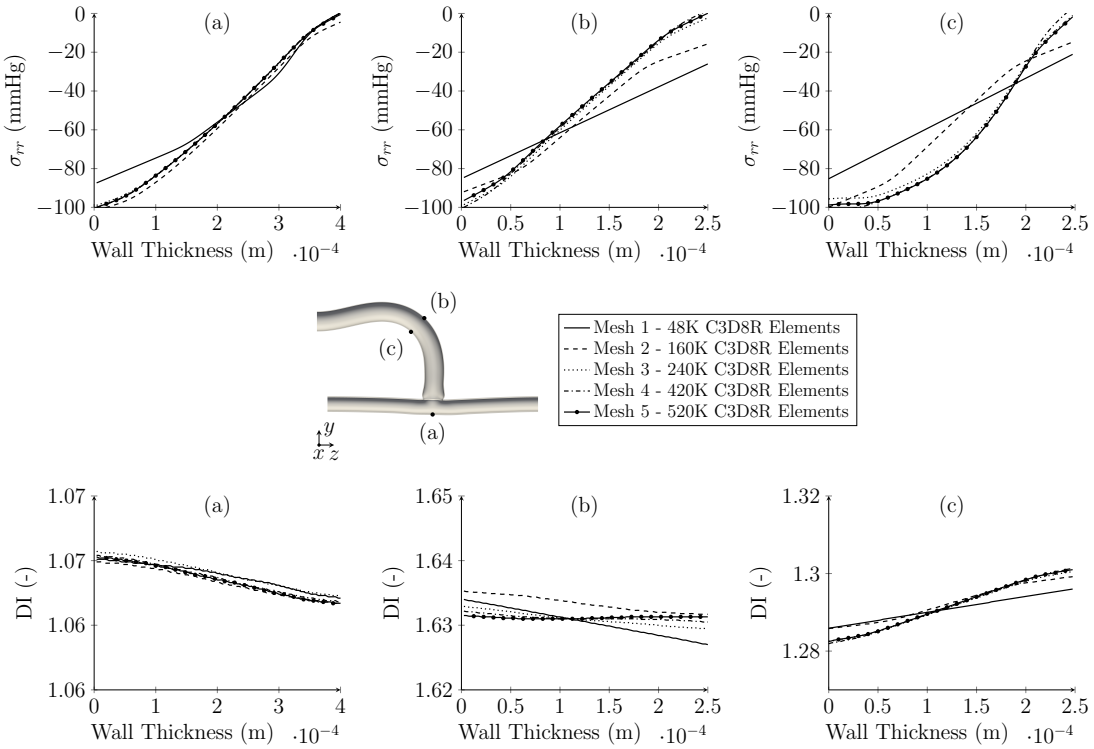

Figure 4.23: Grid independence study: transmural distributions of radial stress (σ_{rr}) and Distortion Index (DI), are shown at three different locations, for increasingly finer meshes.

4.12 Discussion

In this chapter, a structural FE model of the AVF surgery was developed. Solid stress and deformation fields from the FE simulations were used to calculate VV perfusion, according the two models (stress-based and stretch-based) introduced in section 4.1.4. The AVF geometries obtained from the FE simulations bear a good resemblance with those extracted from patients MRI scan images [44]. The vein, due to its thinner, less stiff wall undergoes a larger deformation and circumferential stress, compared to the artery, when pressurised to a reference arterial pressure of 100 mmHg. Stress concentration, due to bending the vein from its

normally straight configurations, appears in the vein at the site of bend. In addition, stress concentration can also be observed in the artery, at the incision ends. Changes in the normal wall mechanical environment, which occur in various locations of the vein, distal artery, and floor of the anastomosis, have been suggested in several studies to contribute to IH [68, 67]. However, other studies argue that increased wall stretch is associated with the upregulation of hypoxia inducible factors [69, 39, 70], which are transcriptor factors released during tissue hypoxia. Therefore, it is unclear whether mechanical risk factors act as a primary cause of IH, or the correlation between them and IH is indirectly due to suboptimal VV perfusion and wall hypoxia.

One limitation of this study is related to the choice of material properties. The main puropose of this chapter was to develop a numerical framework to study the AVF surgical procedure and quantify stress and deformation. However, material properties and vessel dimensions have an intrinsic variability from patient to patient. Hence, it is important that further work is done to assess the sensitivity of these results to changes in geometric parameters and mechanical properties.

Sutures are unavoidable sources of trauma to the tissue, and promote scar tissue growth, along the suture line [105]. Determining stresses induced by individual sutures was considered beyond the scope of this study. Therefore, a detailed stress analysis of the individual stitches was deliberately omitted, and sutures were modelled in a "global sense".

Another limitation is represented by the lack of interaction with surrounding tissue, and the cardiac-induced blood vessel motion. The relatively large distension of the vein observed in the simulation and in the surgery, is mostly due to the vein filling up with blood at arterial pressure, a situation that occurs immediately after the clamps are released by the surgeon, while wall displacement induced by pulsating pressure is normally much smaller [107, 108]. In addition, the cephalic vein, is located near the surface of the arm and normally connected

to the brachial artery, in the *antecubital fossa*, a region where the artery is more superficial and there is little or no muscular tissue. However, the surrounding tissue could represent anatomical constraints when forming an AVF, and their role in determining the AVF shape. Finally, it is possible that the morphology of an AVF changes when a patient moves or bends their arm.

Future work should be done to address shortcomings of the current modelling approach. Both bench-top, *in-vivo* and *ex-vivo* experiments, are needed to validate the computational results. In spite of the mentioned limitations, the proposed methodology represents a novel computational approach to analyse a clinically relevant problem, in order to quantify the role of mechanical factors in the development of IH, particularly in relation to VV perfusion and hypoxia.

Chapter 5

Simulating Oxygen Transport in Arterio-Venous Fistulae

In the previous Chapter, FE simulations were used to calculate wall stress and deformation and estimate wall perfusion, in an idealised AVF. The resulting wall geometry and perfusion fields are used in the present Chapter, to solve for blood flow (Eq. 3.1) and oxygen transport (Eq. 3.3).

As discussed in Section 2.4.1.3, when dealing with biological systems, idealised and patient-specific modelling approches are possible, both of which exhibit advantages and drawbacks. In the present study, given the model complexity and lack of readily available patient-specific blood and wall properties, it was chosen to initially undertake an idealised study, to assess the model performance in a controlled setting.

The oxygen transport model described in Chapter 3 requires a number of parameters, which have been extracted from the existing literature, and exhibit a strong inter- and intra-patient variability and can vary in response to external stimuli. Oxygen transport and wall oxygenation have been shown to be sensitive to changes in blood and wall properties [5, 11]. Therefore, instead of using popu-

lation mean values, it was decided to analyse these model uncertainties, through a parametric study. The aim of this study was to assess, under different haemodynamic and perfusion conditions, whether oxygen transport is affected by local changes in vasa vasorum perfusion or dominated by haemodynamic forces.

5.1 Parameter Space

As shown in Section 3.3.1, oxygen transport appears to be sensitive to changes in wall parameters. Specifically, among all the properties considered, oxygen solubility in the wall, α_T, maximum oxygen consumption rate, $\dot{q}_{max}$, and VV perfusion have the largest impact on oxygen transport (see Figure 3.11).

Oxygen solubility in the wall remains relatively constant in healthy vessels, as the cellular composition of the wall does not vary extensively, thus, is assumed not to change in the parametric study. By contrast, maximum oxygen consumption rate exhibts a large physiological range, which is to be attributed to the different metabolic demands, existing in tissues with different cellular composition [142, 99, 126]. Significant differences are also observed between the consumption rate of active or resting SMC [137]. Hence, three values of oxygen consumption, $\dot{q}_{max}$, (the average population value, as well as $\pm 50\%$ variation) were considered.

VV perfusion, and lack thereof, has also been proposed as a cause of wall hypoxia and IH development [19]. However the mechanism underlying microvascular collapse is not yet fully understood. To account for this, in the previous chapter, two distinct perfusion models were proposed: a stress-based and a stretch-based model (Section 4.1.4). In addition, given the highly speculative nature of the perfusion models, three different values of P_{thres} and κ were considered in the analysis.

Haemodynamic forces are expected to have a significant effect on blood-side oxygen transport mainly for two reasons. Firstly, oxygen transport is highly convective (the Peclet number for oxygen transport has values of $\approx 10^6$); secondly,

haemoglobin diffusivity in blood D_c, is assumed to be a function of the shear rate $\dot{\gamma}$, in line with Murphy's model [11]. To elicit different haemodynamic responses, three flow splits were included in the analysis, a 20:80, 50:50, and 80:20 flow-split between the DAI and DVO, while the inflow Reynolds number at the PAI was fixed at 800.

A total number of 54 cases were considered for the parametric study (see Table 5.1). Three supplementary cases - one for each flow split - with medium $\dot{q}_{max}$ and zero perfusion were also included in the analysis.

$\dot{q}_{max}$	Perfusion Model	Perfusion Coefficient	Flow Split
Art - 1.05 Vein - 2.2 $\times 10^{-5}\left[\frac{ml\,O_2}{ml\,tissue\,s}\right]$	Stress-based model	$P_{thres} = 15mmHg$ / $\kappa = 0.5$	20:80
Art - 2.10 Vein - 4.4 $\times 10^{-5}\left[\frac{ml\,O_2}{ml\,tissue\,s}\right]$	Stretch-based model	$P_{thres} = 30mmHg$ / $\kappa = 1.0$	50:50
Art - 3.15 Vein - 6.6 $\times 10^{-5}\left[\frac{ml\,O_2}{ml\,tissue\,s}\right]$		$P_{thres} = 45mmHg$ / $\kappa = 2.0$	80:20
3X	2X	3X	3X
			Total Cases = 54

Table 5.1: Parameter space used in the study.

5.2 Methods

The blood flow and oxygen transport equations, described in Chapter 3, were used throughout this study to investigate wall oxygenation. The geometry, resulting from the idealised AVF surgical procedure, developed in Chapter 4, was employed in all simulations. Specifically, the configuration with vein length $L_v = 2$ cm, was taken as the reference case and used throughout this chapter.

5.2.1 Discretisation Of Computational Domain

A polyhedral unstructured volume mesh, with a prismatic boundary layer mesh adjacent to the wall, was constructed for the fluid-domain. The mesh was refined near the anastomosis.

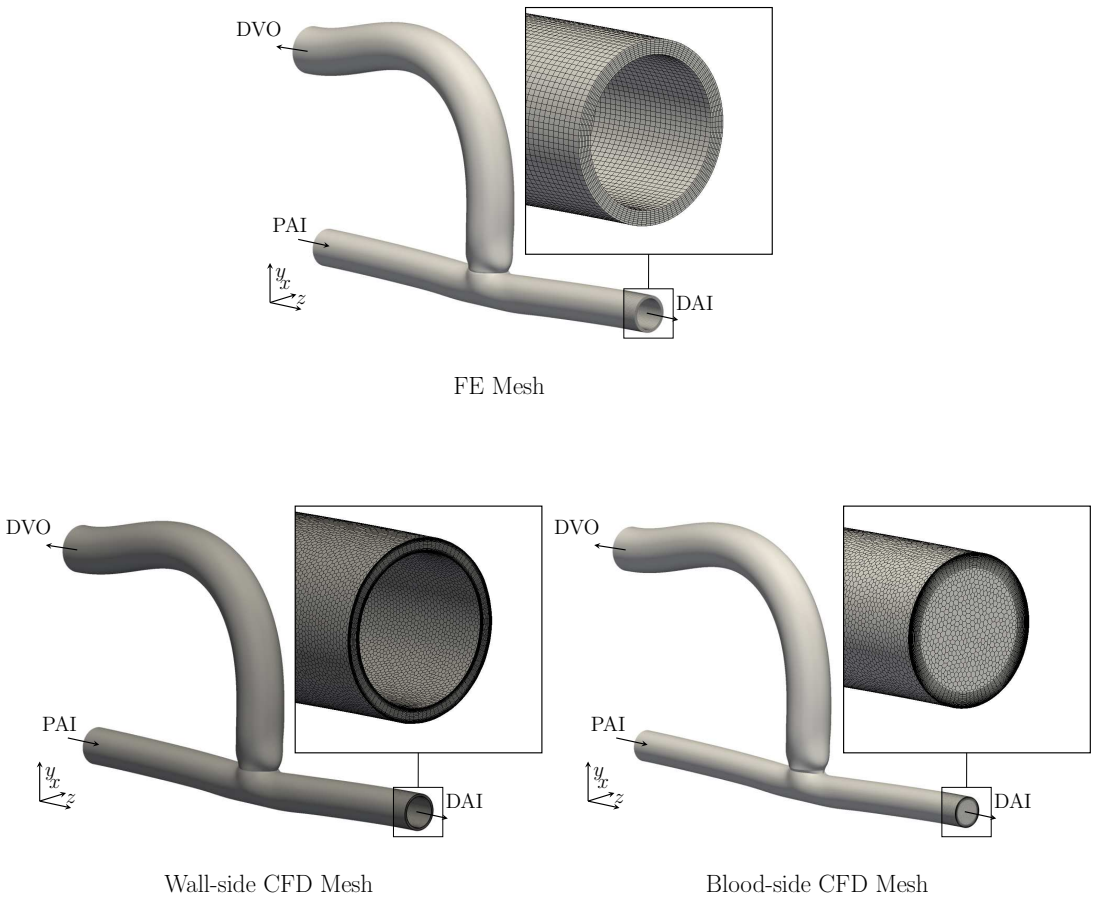

Figure 5.1: Mesh and Computational Domain: the geometry is obtained from the FE model in Chapter 4. The blood-side part of the CFD domain was meshed using polyhedral cells, and a prismatic boundary layer mesh adjacent to the wall. The wall was meshed with prismatic polygonal cells. The final mesh had $\approx 12.5 \times 10^6$ cells in total, $\approx 3.7 \times 10^6$ in the wall and $\approx 8.8 \times 10^6$ in the fluid.

Specifically, cells near the anastomosis had an average size of $\approx 8 \times 10^{-5}$ m,

expanding progressively to $\approx 1.5 \times 10^{-4}$ m beyond a distance of ≈ 0.05 m from the anastomosis. The prismatic boundary layer mesh were 28 elements thick, with the first element having a thickness of less than $\approx 3 \times 10^{-6}$ m in line with the mesh convergence study in Chapter 3 - Section 3.3.2 and with meshes employed in previous numerical studies [8, 15, 110]. *A posteriori* verification of the resolution criteria set out by Valen-Sendstad, was required to ensure appropriate spatial and temporal resolutions. [85].

A prismatic polygonal unstructured mesh, with a prismatic boundary layer mesh adjacent to the endothelial and adventitial surface, and having a number of cells of $\approx 1.5 \times 10^{-4}$ m, was constructed for the wall-domain. The prismatic boundary layer mesh was 15 elements thick, with the first element having a thickness of less than $\approx 3 \times 10^{-6}$ m. The final mesh had $\approx 12.5 \times 10^{6}$ cells in total - $\approx 3.7 \times 10^{6}$ in the wall and $\approx 8.8 \times 10^{6}$ in the fluid.

5.2.2 Governing Equations

For all configurations blood was treated as an incompressible Newtonian fluid. Specifically, blood flow was modelled using the time-dependent incompressible 3D Navier-Stokes equations for a fluid with constant viscosity (Eq. 3.1). For all cases, values of $\mu = 3.5 \times 10^{-3}\text{Pa} \cdot \text{s}$ and $\rho = 1060\text{kg} \cdot \text{m}^{-3}$ were employed.

Blood-side oxygen transport was modelled using the time-dependent modified advection diffusion equation developed by Moore and Ethier [5] (Eq. 3.3), which accounts for oxygen binding to haemoglobin. The model introduced by Murphy *et al.* was adopted (Eq. 3.7), to take into account changes in the haemoglobin dispersion coefficient, due to shear-augmented dispersion of RBCs in the flow. Blood-side oxygen transport was coupled to wall-side oxygen transport and consumption.

Wall transport of oxygen was modelled through a time dependent reaction-diffusion equation (Eq. 3.8), as convection can be neglected in the wall [5]. In

line with previous studies, a first order Michaelis-Menten kinetics was adopted to model the wall reaction rate (Eq. 3.9). Parameters listed in Table 3.1 were used for the fluid-wall coupled oxygen transport model.

5.2.3 Boundary Conditions

A steady-state parabolic velocity profile was applied at the PAI with an average velocity of 0.62 m/s into the configuration (equivalent to 502 ml/min), which resulted in a Reynolds number of 800. At the DAO, steady state parabolic velocity profiles with average velocities of 0.54 - 0.34 - 0.13 m/s out of the domain (equivalent to 402 - 251 - 100 ml/min, respectively), corresponding to flow splits between the DVO and the DAO of 20:80 - 50:50 and 80:20, respectively. Finally, a constant (and arbitrary) pressure was applied at the DVO, and a zero-velocity no-slip condition was applied at the arterial and venous walls, which were assumed to be rigid.

A steady-state spatially-constant oxygen concentration of 90 mmHg, was applied at the PAI, in line with the assumption that oxygen is "well-mixed" upstream of the domain. A zero boundary-normal oxygen concentration gradient was prescribed at the two outlets (DAO and DVO): $\partial PO_2/\partial n|_{\Gamma=DAO,DVO} = 0$. At the wall-lumen interface, continuity of oxygen concentration $PO_{2f}|_f = PO_{2w}|_w$ and oxygen flux $D_F \partial PO_2/\partial \mathbf{n}|_f = D_w \partial PO_2/\partial \mathbf{n}|_w$ were required. Coupling between fluid and wall oxygen transport was satisfied using an explicit scheme: at each inner iteration, the oxygen concentration field was mapped from the fluid to the wall domain, and the oxygen concentration gradient was mapped from the wall to the fluid domain. Zero boundary-normal oxygen concentration gradients were applied at all the remaining surfaces of the wall-domain.

According to the literature, in healthy vessels, VV are exclusively contained in the adventitial layer, thus the VV oxygen source S_w (Eq. 3.16) is only prescribed within this region [164, 168]. The ratio of adventitia thickness to total wall

thickness is normally reported as 0.33 for medium size arteries and as 0.5 for medium size veins [143]. For an in-depth discussion on the modelling assumptions and the choice of boundary conditions, see Chapter 3.

5.2.4 Computational Method

Solutions for the blood velocity field and the oxygen concentration were obtained using Star-CCM+ v12.02.011-R8 via the following procedure:

- Three preliminary simulations were used to determine average velocity and pressure fields. These simulations were initialised with zero velocity and pressure and run with a segregated steady solver, until momentum and continuity residuals fell below 10^{-9}. Each simulation was then used as the initial condition for a segregated implicit unsteady solver, which advanced solutions 0.1 s in time. A time step of 0.0005 s was used. After the end of the initial transient, the simulations were then advanced further 0.4 s, during which velocity and pressure were time-averaged.

- For each of the 57 cases, time-averaged velocity and pressure, calculated in the previous step, were used to solve for oxygen transport. A segregated steady solver was run until the oxygen transport residuals fell below 10^{-9}. Then each simulation was advanced for a total of 0.3 s in time, using a segregated unsteady solver, with a time step of 0.0005 s. The inital 0.1 s was discarded, and data were exported for analysis, only during the last 0.2 s.

Each simulation was carried out on Cx1, one of Imperial College HPC, on two nodes, each having 20 cores 22GB of RAM, and required approximately 3 days to complete.

5.3 Results

5.3.1 Blood Flow and Wall Shear Stress

Figure 5.2 shows time snapshots of velocity magnitude and plane-normal vorticity on the AVF symmetry. Unsteady flow can be observed for the 50:50 and 80:20 flow split, despite the steady inflow conditions, while flow in the 20:80 case appears to be completely steady.

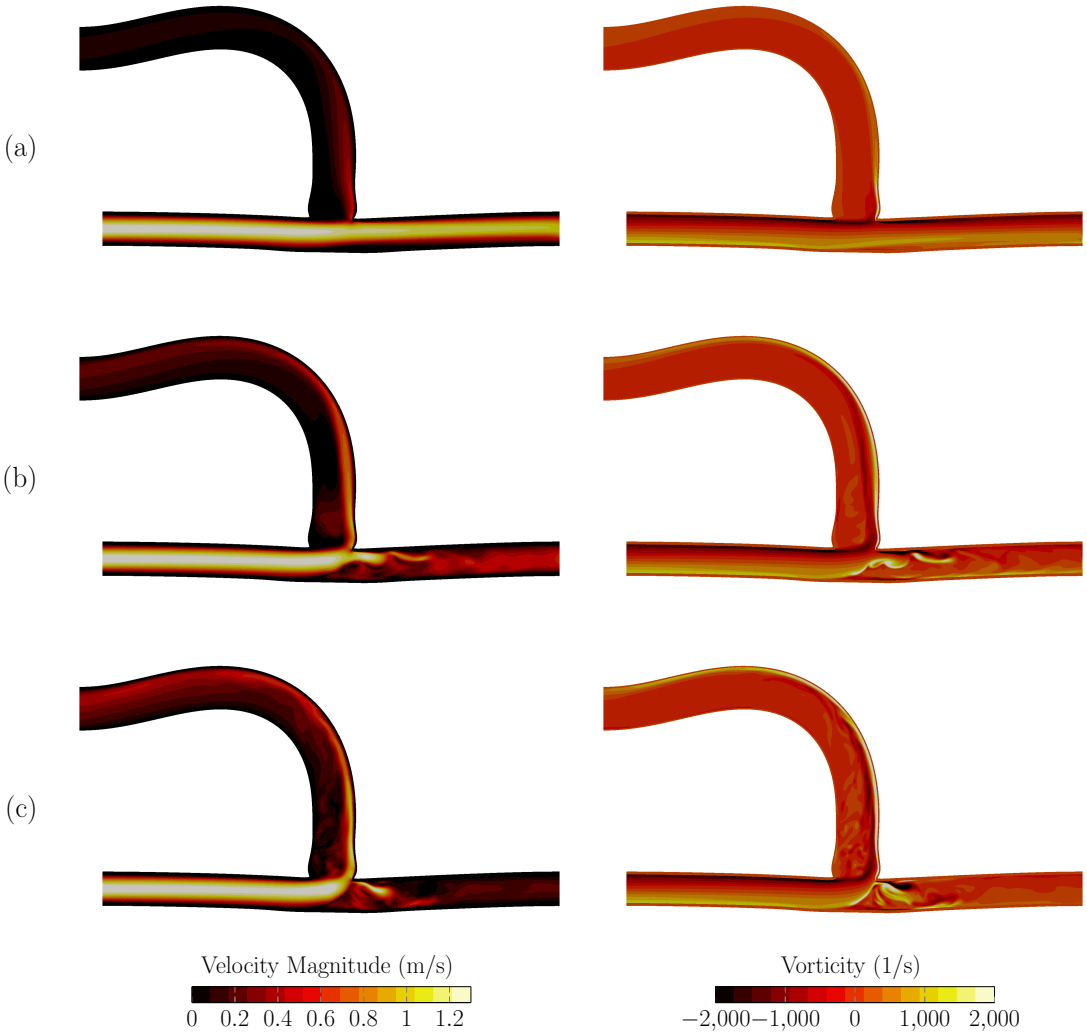

Figure 5.2: Snapshots of velocity magnitude and plane-normal vorticity on the AVF symmetry plane, for different flow splits: (a) 20:80, (b) 50:50, (c) 80:20.

Specifically, for a 50:50 flow split, unsteady vortex shedding can be observed only in the arterial section, while for a 80:20 flow split, the velocity and vorticity fields appear to be disrupted also in the venous section. This result is in line with previous simulations of Iori *et al.*, in which unsteady venous flow was predicted for arteries and veins of equal diameter for an 80:20 flow split [15].

Whilst the causes leading to venous flow instabilities are not clear, arterial vortex shedding can be explained by the mechanism outlined in [15]. For a straight vessel, the bulk of the axial arterial blood flow (the high speed region of the flow) is within the center of the artery. Consequently, it must traverse the artery laterally in order to enter the vein. This process causes the shear layer on the wall opposite the anastomosis to detach, leading to a free-shear layer in the artery that induces unsteadiness [15].

As discussed in Chapter 2, there is substantial evidence in the literature suggesting that unsteady blood flow patterns can disturb the normal vascular physiology, leading to vascular diseases [220, 61]. In the next section, quantitative assessment of the degree of unsteadiness was undertaken using snapshot Proper Orthogonal Decomposition (POD) [221, 222, 223, 15, 110] and Fourier analysis of the wall shear stress (WSS) and oxygen field at the endothelial surface.

5.3.2 Frequency Analysis

Snapshot POD and Fourier Transform were employed to analyse oxygen concentration and WSS vector at the endothelium. POD is a statistical procedure, similar to Principal Component Analysis, that uses an orthogonal projection to convert a space-time field into a summation of orthonormal spatial POD modes, each modulated by an associated temporal POD mode. POD was originally used in the context of fluid dynamics by Lumley *et al.* for identification of coherent structures in turbulent flow [221].

Classical POD is computationally expensive, hence it was seldom applied to

large CFD datasets, until Sirovich, in 1987 [222], proposed the snapshot POD method, This technique was used by Iori *et al.* [15] to analyse WSS vectors in quasi-steady simulations of blood flow in idealised models of AVF, and by Grinberg *et al.* [223] and Grechy *et al.* [110] to assess unsteadiness in pulsatile transient flows, respectively in a stenosed carotid artery and a brachio-cephalic AVF. See Appendix A.1 for a detailed description of snapshot POD.

In terms of Fourier analysis, the Spectral Power Index, introduced by Khan *et al.* [79], was used to analyse oxygen and flow temporal fluctuations. Given a Fourier-transformed signal $Y(n\omega_0)$, the SPI is defined as,

$$SPI = \frac{\sum_{n=n_c}^{+\inf} |Y(n\omega_0)|^2}{\sum_{n=0}^{+\inf} |Y(n\omega_0)|^2} \tag{5.1}$$

where ω_0 is the fundamental angular frequency, and n_c is harmonic corresponding to the cut-off frequency considered. Effectively, this index calculates the energy content in the power spectra for harmonics above n_c, normalized by the total energy content. As inflow and outflow boundary conditions are stationary, the cut-off frequency harmonic n_c was set to 1, to determine the relative importance of any flow instability, with respect to the time averaged flow.

The WSS vector, $\boldsymbol{w}$, is the tangential component of the viscous stress vector $\mathbf{t}$, and is defined as

$$\boldsymbol{w} = \mathbf{t} - (\mathbf{t} \cdot \mathbf{n})\mathbf{n} \tag{5.2}$$

where

$$\begin{aligned} \mathbf{t} &= \boldsymbol{\mathcal{T}} \cdot \mathbf{n} \\ \boldsymbol{\mathcal{T}} &= \mu(\nabla \mathbf{u} + (\nabla \mathbf{u})^T) \end{aligned} \tag{5.3}$$

and $\mathbf{n}$ is the outward facing wall normal.

Figures 5.3-(a), 5.4-(a) and 5.5-(a) show the five most energetic POD temporal modes, $a_1(t), .., a_5(t)$, for WSS and oxygen concentration fields, and 20:80, 50:50 and 80:20 flow-splits, respectively. Results are shown for the three supplementary

cases, with shut-off perfusion. Figures 5.3-(c), 5.4-(c) and 5.5-(c) show the five most energetic POD spatial modes, $\Phi_1(t), .., \Phi_5(t)$, for WSS, and 20:80, 50:50 and 80:20 flow-splits, respectively POD modes are hierarchical, with the first mode representing the main features of the decomposed field, and the higher order modes containing finer spatial and temporal features [223].

Figures 5.3-(b), 5.4-(b) and 5.5-(b) contain the eigenspectra computed for the different flow splits. The spectrum slope provides an indication of the flow regime: fast decay is associated with a laminar regime, while slow decay features a transitional/turbulent regime.

In line with previous qualitative observations, WSS eigenspectra and temporal modes extracted from the 50:50 and 80:20 flow splits both exhibit a clear transitional regime (slow eigenspectra decay and fluctuations in higher temporal modes), while the 20:80 case appears to be completely laminar. Conversely, oxygen concentration in all cases does not seem to be affected by flow fluctuations. This is in line with previous observations by Tada and Tarbell [7], who undertook oxygen transport simulations in a compliant carotid bifurcation model. In their model, large temporal differences in Sherwood number (Sh) - the non-dimensional oxygen flux into the wall - were observed during the cardiac cycle, which however did not translate into significant differences in the time-averaged Sh, when compared with steady BC model, with rigid walls [7].

Finally, Figures 5.3-(d)-(e), 5.4-(d)-(e) and 5.5-(d)-(e) show the SPI for $|\boldsymbol{w}|$ and PO_2, in the three analysed cases. In particular, 5.4-(d) and 5.5-(d) highlight the regions of artery and vein that are exposed to oscillatory flow. Dominant frequencies up to $\approx$ 40 Hz for the 50:50 case and up to $\approx$ 60 Hz for the 80:20 case can be observed on the toe of the anastomosis. The frequency and vortex shedding structure found in the 80:20 case appear to be in line with previous work done in [15].

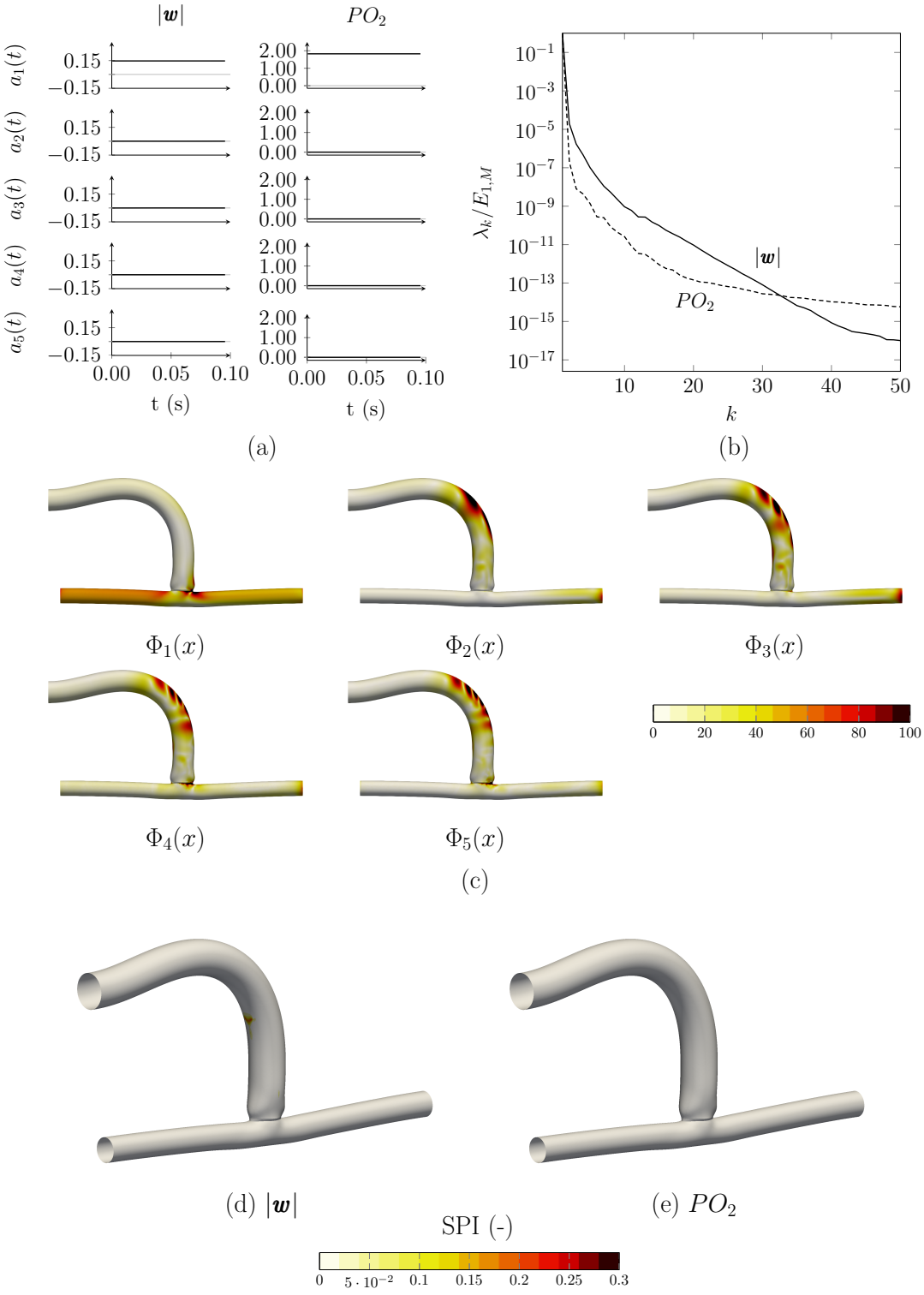

Figure 5.3: (a) the five most energetic POD temporal modes $(a_1(t), .., a_5(t))$, calculated on the endothelium for $|\boldsymbol{w}|$ and oxygen concentration, PO_2. (b) POD energy spectra distribution (λ_k is energy content of the k-th mode, normalized by the total energy content $E_{1,M} = \sum_{k=1}^{M} \lambda_k$). (c) Distributions of the five most energetic spatial POD modes Φ of $|\boldsymbol{w}|$. (d)-(e) distributions of the SPI. Results are shown for a 20-80 flow split.

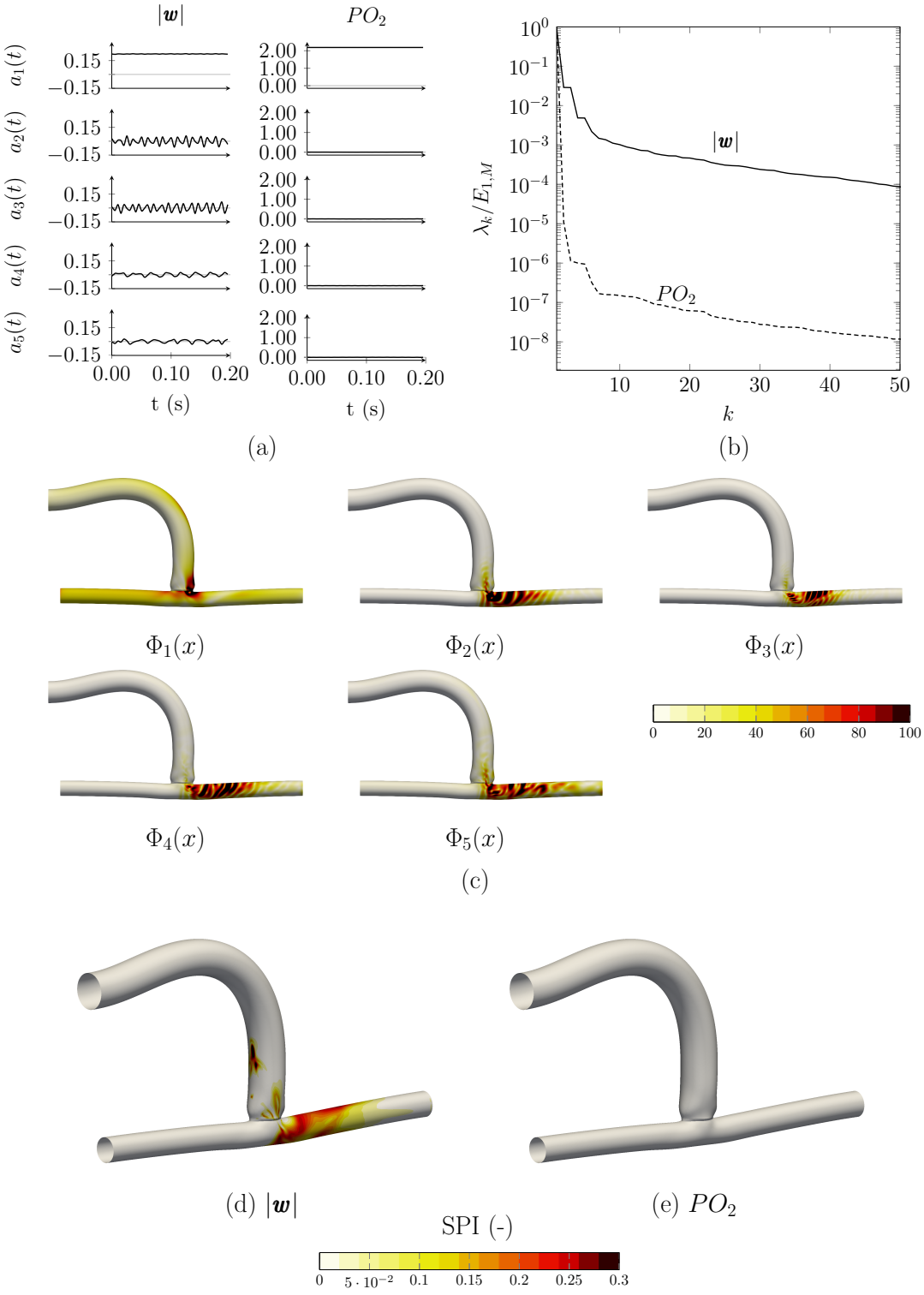

Figure 5.4: (a) the five most energetic POD temporal modes $(a_1(t), .., a_5(t))$, calculated on the endothelium for $|\boldsymbol{w}|$ and oxygen concentration, PO_2. (b) POD energy spectra distribution (λ_k is energy content of the k-th mode, normalized by the total energy content $E_{1,M} = \sum_{k=1}^{M} \lambda_k$). (c) Distributions of the five most energetic spatial POD modes Φ of $|\boldsymbol{w}|$. (d)-(e) distributions of the SPI. Results are shown for a 50-50 flow split.

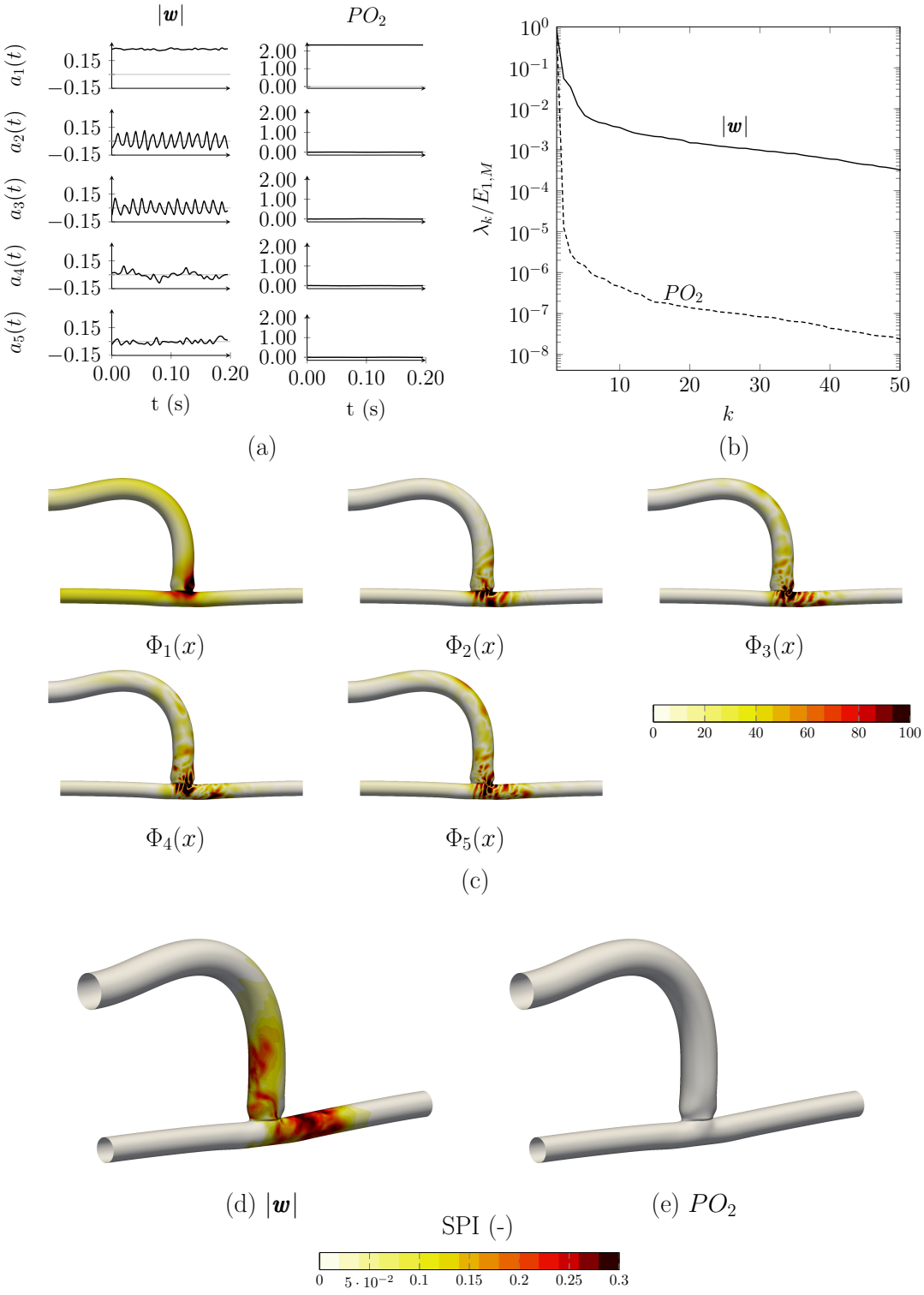

Figure 5.5: (a) the five most energetic POD temporal modes $(a_1(t), .., a_5(t))$, calculated on the endothelium for $|\boldsymbol{w}|$ and oxygen concentration, PO_2. (b) POD energy spectra distribution (λ_k is energy content of the k-th mode, normalized by the total energy content $E_{1,M} = \sum_{k=1}^{M} \lambda_k$). (c) Distributions of the five most energetic spatial POD modes Φ of $|\boldsymbol{w}|$. (d)-(e) distributions of the SPI. Results are shown for a 80-20 flow split.

5.3.3 Wall Shear Stress

Figure 5.6 shows temporal averages of the WSS magnitude, $|\overline{\boldsymbol{w}}|$, for the three different flow splits considered. In all three cases, a large recirculation zone is evident in the floor of the anastomosis - *i.e.* the area on the arterial wall opposite to where the vein is connected - a site where IH formation is often observed.

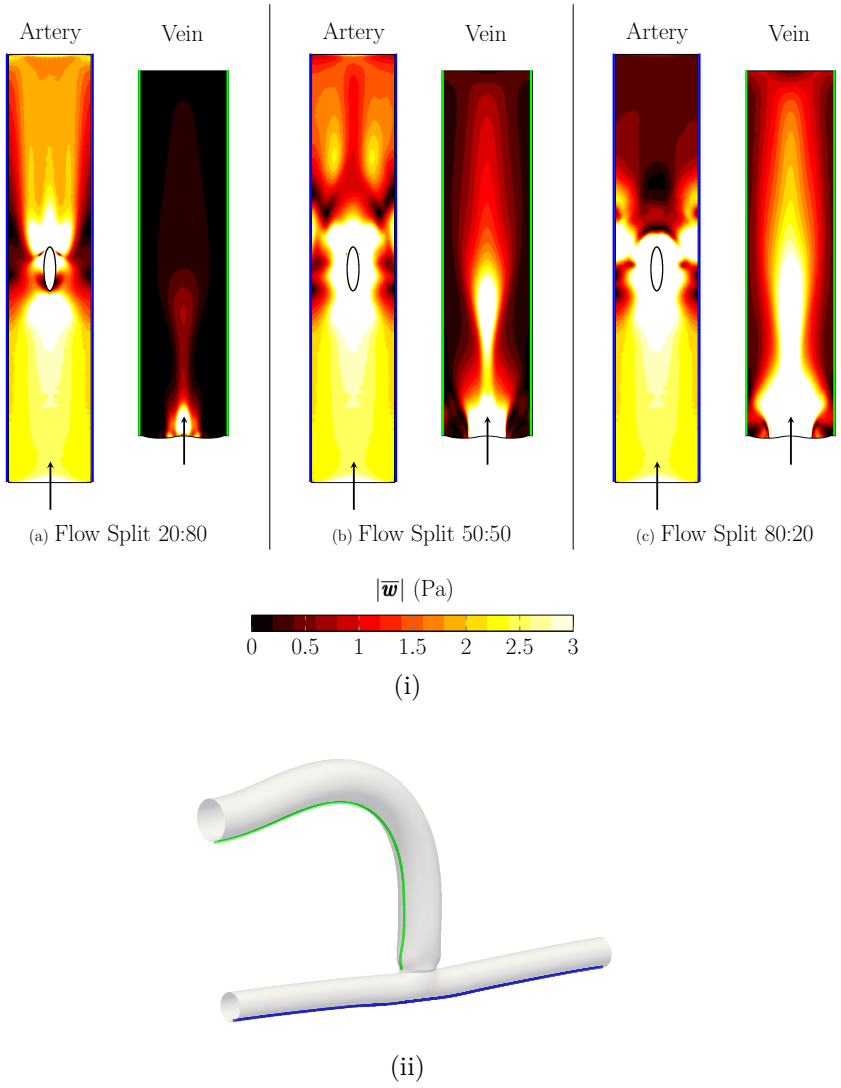

Figure 5.6: Time Averaged WSS magnitude, $|\overline{\boldsymbol{w}}|$, in excised and flattened views for different flow splits: (a) 20:80, (b) 50:50, (c) 80:20. The arrows indicate the bulk flow direction. Blue and green lines, show the excision sites.

The three flow splits elicit, especially in the artery, different WSS magnitude patterns. WSS patterns in the vein are more consistent: high WSS is found on the outside of the bend, while a large recirculation zone and low WSS can be observed for the entire vein length, on the inside of the bend. A 20:80 flow split is obviously an extreme, undesirable situation. Upon AVF formation, the baseline flow in the feeding brachial artery increases, to accomodate for the extra blood that is shunted to the venous system [1]. Clinical evidence shows a correlation between primary failure at 4-8 weeks, and the lack of increase in baseline blood flow in the feeding artery and in the venous segment, at day 0 [1].

According to several authors, the main failure mechanism is stenosis due to the development of IH, in response to disturbed flow and abnormal shear stress [1, 2]. Previous studies on atherosclerosis and arterial bypass grafts have found a positive correlation between the development of IH and the presence of low and oscillating WSS [220, 61, 224]. This could explain IH formation in the anastomotic "toe" and floor. However, the abnormal shear stress and oscillatory pattern rapidly disappear beyond 1 cm of the anastomosis and may not explain areas of venous stenosis found further downstream [1].

5.3.4 Depth-Averaged Oxygen Concentration

Variations of the oxygen concentration field are all concentrated in a thin mass transport boundary layer and the wall. Thus, to facilitate its visualization, for each point of the endothelial surface mesh, the time averaged oxygen field, $\overline{PO}_2$, was depth-averaged over the wall thickness. Figures 5.7, 5.8 and 5.9 shows excised and flattened views of the 57 cases of the parametric study set out in 5.1, coloured by, $\widehat{PO}_2$, the depth-averaged of $\overline{PO}_2$.

Direct qualitative comparison of depth-integrated O2 concentration and WSS field 5.6 reveals significant spatial correlation between oxygen transport and flow.

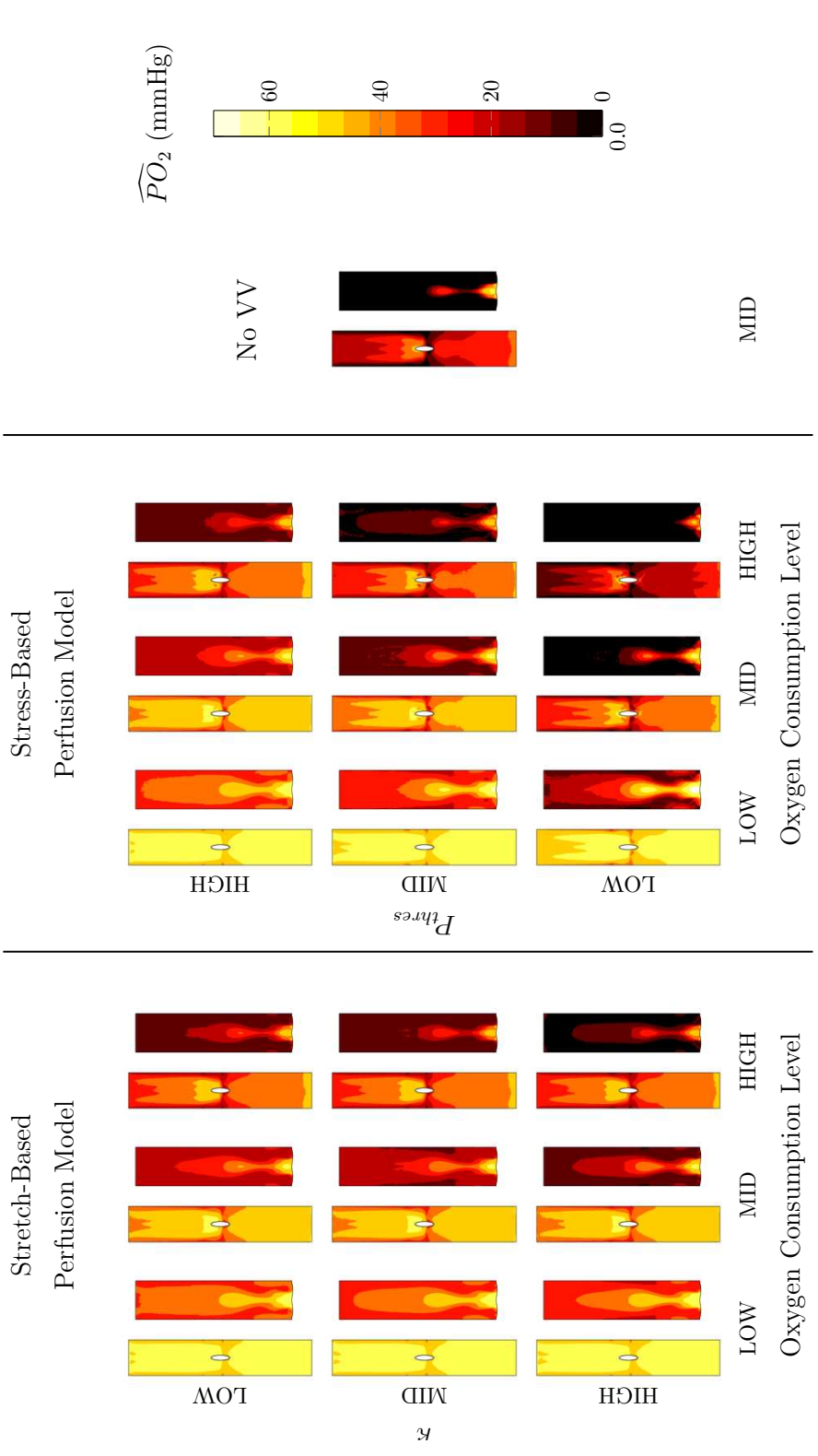

Figure 5.7: Excised and flattened views of the depth-averaged temporal mean oxygen field, $\widehat{PO}_2$, for two different perfusion models (Stretch, Stress), three perfusion levels and three oxygen consumption rates. The case with shut-off perfusion (NoVV) is also included in the analysis. The results are presented for a 20:80 flow split.

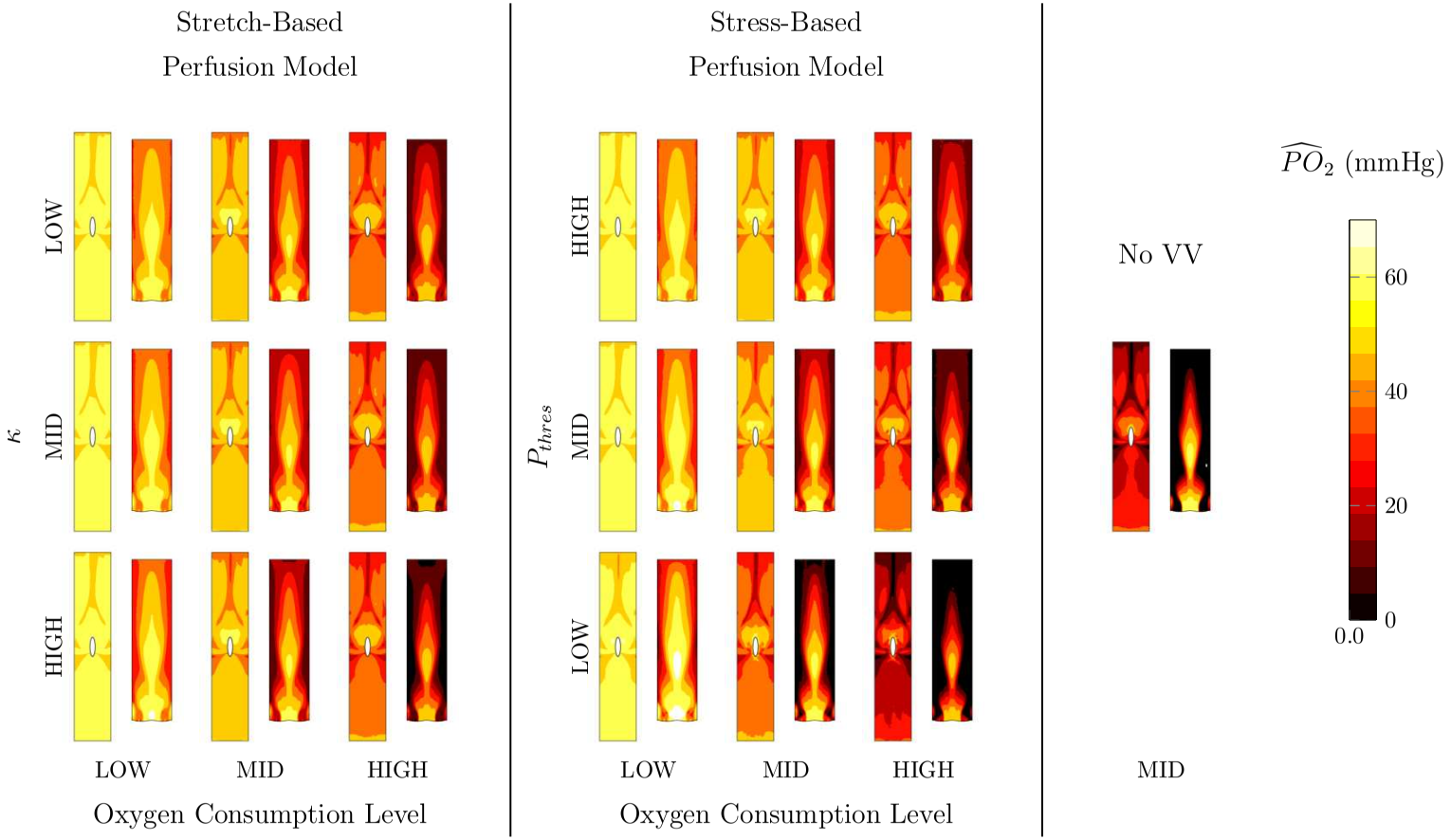

Figure 5.8: Excised and flattened views of the depth-averaged temporal mean oxygen field, $\widehat{PO_2}$, for two different perfusion models (Stretch, Stress), three perfusion levels and three oxygen consumption rates. The case with shut-off perfusion (NoVV) is also included in the analysis. The results are presented for a 50:50 flow split.

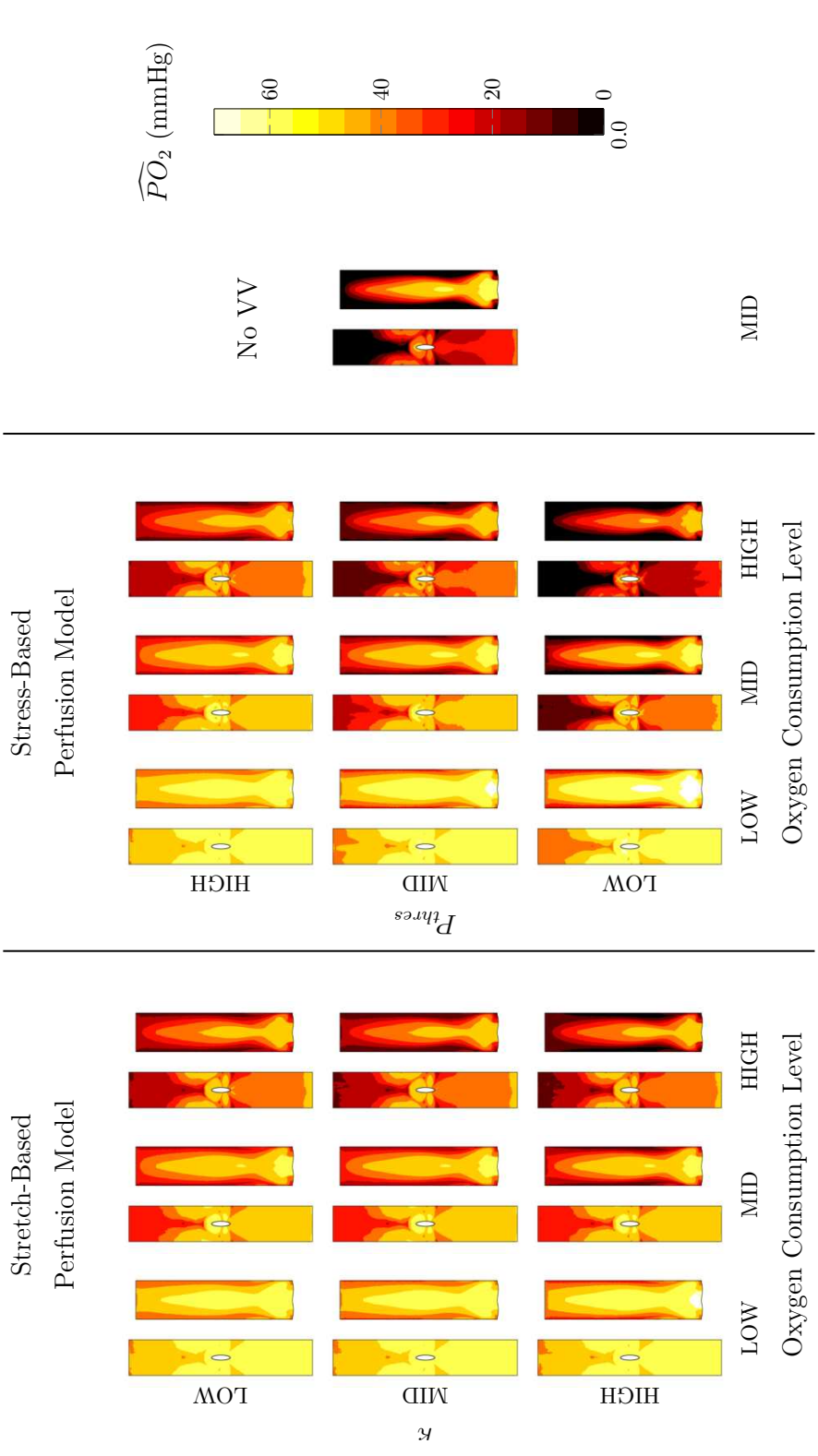

Figure 5.9: Excised and flattened views of the depth-averaged temporal mean oxygen field, $\widehat{PO}_2$, for two different perfusion models (Stretch, Stress), three perfusion levels and three oxygen consumption rates. The case with shut-off perfusion (NoVV) is also included in the analysis. The results are presented for a 80:20 flow split.

However, while spatial patterns are similar, the actual $\widehat{PO}_2$ values also depends on other oxygen transport wall parameters, *i.e.* the oxygen consumption rate and VV perfusion. Specifically, increasingly high levels of oxygen consumption rate have the effect of shifting the baseline oxygen field down.

Wall oxygenation also appears to be a function of VV perfusion. Particularly, completely switching off any VV perfusion has dramatic effects on wall oxygenation, as it leaves the wall to rely solely on fluid-phase oxygen transport. Conversely, normally perfused VV are able to meet the wall metabolic needs, even at locations where the fluid-phase transport is sub-optimal.

Bar charts showing the percentage area of endothelium surface exposed to low (orange - $10mmHg \leq \widehat{PO}_2 < 30mmHg$) and hypoxic (red - $\widehat{PO}_2 < 10mmHg$) oxygen levels are shown in Figure 5.10. Excised and flattened tri-color maps of normal (green - $\widehat{PO}_2 \geq 30mmHg$), low (orange - $10mmHg \leq \widehat{PO}_2 < 30mmHg$) and hypoxic (red - $\widehat{PO}_2 < 10mmHg$) oxygen levels are included for reference in the Appendix (see A.4).

As expected and in agreement with qualitative observation drawn from Fig.5.7-5.8-5.9, two trends can be observed: first, increasing the oxygen consumption rate, exposes both the artery and vein to higher levels of low and hypoxic oxygen concentration; secondly, decreasing VV perfusion also increases, albeit to a lesser extent, the percentage of wall exposed to low and hypoxic oxygen levels. However, the largest effect, especially on the vein oxygenation, can be attributed to changes in flow patterns. At flow splits of 20:80 and 50:50, the vein is exposed to hypoxic levels up to $\approx 90\%$ of the total surface. With an 80:20 flow split, this value is less than a half, and interestingly, lowering the flow in the distal arterial segment, does not seem to affect negatively arterial wall oxygenation to the same extent. This is likely due to the vein geometry: on the inside of the bend, shear layer separation in the vein, coupled with low, fully laminar flow, creates a barrier to oxygen diffusion.

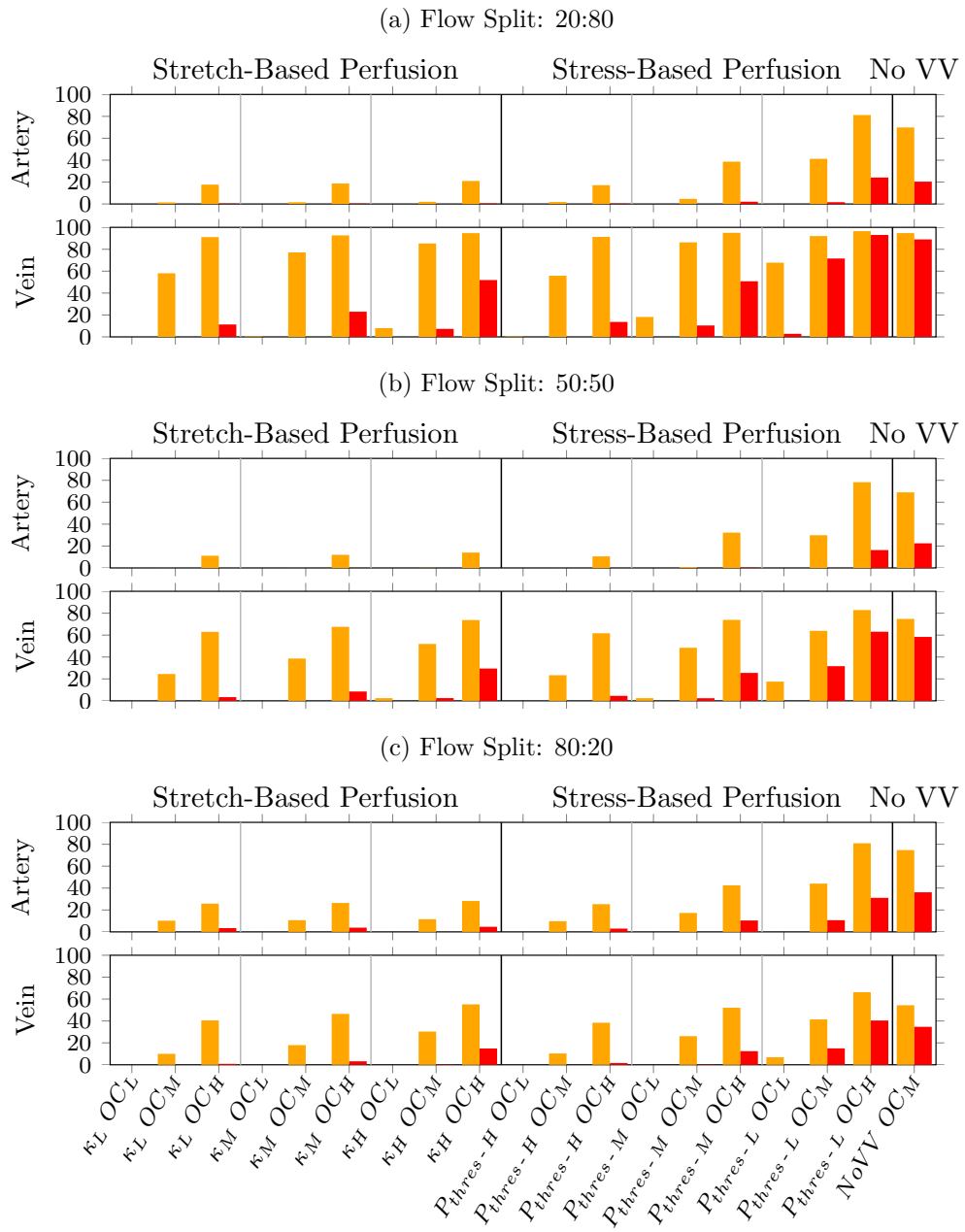

Figure 5.10: Bar charts showing the percentage of endothelium surface exposed to low (orange - $10mmHg \leq \widehat{PO_2} < 30mmHg$) and hypoxic (red - $\widehat{PO_2} < 10mmHg$) oxygen levels for two different perfusion models (Stretch, Stress), three perfusion levels and three oxygen consumption rates. The cases with shut-off perfusion (NoVV) is also included in the analysis. Please refer to Figures 5.7, 5.8 and 5.9, for the abbreviations.

On the other hand, transitional flow appears to improve oxygen transport, as it

increases mixing through stirring. Further quantitative assessment of the observations drawn in this section is undertaken using sensitivity analysis.

5.4 Sensitivity Analysis

Sensitivity analysis (SA) is a class of methods widely used in engineering design. Using SA, model outcomes can be recalculated under alternative assumptions, to determine the impact of each input variable. This technique has proven to be useful for a range of purposes. These include model simplification and uncertainty reduction, which allow one to identify and prioritize the most influential inputs, and identify non-influential inputs in order to fix them to nominal values.

These methods may take a local or global approach. Local SA techniques aim to determine how small variations of the model inputs around a nominal point affect the value of the output. Therefore, the calculated sensitivities depend on the choice of the nominal point, around which the model is perturbed. If the output has strong non-linear dependence on the inputs, local methods can produce misleading results [225]. Conversely, global SA takes into account the uncertainty space on model predictions and measures how the output variation can be apportioned to variation in the input parameters.

A widely used class of global SA methods is Variance-based SA, proposed by Sobol in 1993 [226]. This technique is based on the analysis of variance (ANOVA) and allows one to decompose the variance of the model output into fractions, called Sensitivity or Sobol indices, which can attributed to simple inputs or sets of them. See Appendix A.2 for a detailed description of Sobol's method.

Sobol's method allows accurate estimation of the sensitivity indices, but comes at a high computational cost. A number of approaches have been devised to reduce the computational cost of the estimator, including High-dimensional model representations (HDMR) and Fourier Amplitude Sensitivity Test (FAST) [225]. However, the main source of computational expense comes from the sampling.

Sobol's original method uses Monte Carlo sampling, requiring a large number of samples to converge, which prohibits its application to complex 3D numerical simulations.

A widely used technique to reduce computational cost is using meta-models, also known as surrogate models or emulators [71, 227]. The idea behind this approach is to use a drastically simplified surrogate model, which is able to represent the model within an acceptable margin of error. Once the metamodel is fitted, or trained, sensitivity measures can be directly calculated from it. In fact, given that the surrogate model is much less computationally expensive, Sobol samples can be efficiently generated.

5.4.1 Surrogate Model

A large spectrum of surrogate models have been used in the past, including classical polynomial and spline interpolation, traditional non-parametric regression, such as Locally Weighted Scatterplot Smoothing (LOWESS) and additive models (GAMs) and more recent ones, such as Gaussian Process Regression, Artificial Neural Network (ANN), Random Forest (RF) and Gradient Boosting Machine (GBM) [228, 227, 229]

Following the work of Wang *et al.* [228], a *Stochastic ordinary* Kriging-based surrogate model was used as predictor in the sensitivity analysis. Kriging modelling, also known as Gaussian Process Regression, is an non-parametric regression technique that has its origins in the field of geo-statistics and is now very popular in many engineering fields. This approach presents many desirable properties. Kriging models consist of a sum of a regression model and a realization of a zero-mean Gaussian process, and implicitly provide a predictor error, quantified as MSE, allowing the user to gain insight about the model's reliability. In addition, the hyperparameters for the predictor can be determined without user input by using Maximum Likelihood Estimation. A detailed description of

Kriging modelling, is given in Appendix A.3.

5.4.2 Model Inputs and Output

In order to quantify the relative importance of luminal and wall oxygen transport on the onset of hypoxia, time averaged WSS magnitude $|\overline{\boldsymbol{w}}|$ and depth-integrated VV perfusion $\widehat{V_f}$ were chosen as inputs, while depth-averaged oxygen concentration, $\widehat{PO_2}$, was chosen as ouput of the sensitivity analysis. WSS magnitude acts as a proxy for the flow-mediated oxygen supply to the endothelium, while depth-integrated VV perfusion measures the VV oxygen supply. Depth-averaged oxygen concentration is an average measure of wall oxygenation. This choice of inputs/output provides three scalar fields that are all available at the endothelium.

5.4.3 Sampling Procedure

The first step in the sensitivity analysis procedure described here, is to train a Kriging predictor, based on model inputs and outputs. Training samples for the predictor were extracted from 54 of parametric study cases. The three shut-off perfusion cases were left out as they contain no information on the VV perfusion field.

To ensure uniform representation of the extracted sample, the Vascular Modelling Tool Kit (VMTK) [230] was used to discretise each case's surface into a finite number of contiguous patches, inside which the fields are spatially averaged, as in [231]. Figures 5.11-(a) and (b) show the AVF endothelial surface mapping, while Figures 5.11-(c),(d) and (e) show the patched WSS field for the 80:20 flow split, with an increasing number of patches. A number of 2645 patches were produced for each case, with 23 patches distributed circumferentially and 115 patches distributed in the direction of the vessel axis (Fig. 5.11-(e)).

The datasets resulting from this process exhibit a clear tendency to clustering.

This property can make the corresponding correlation matrix ill-conditioned and affect accuracy of the Kriging predictor [232, 233, 234]. Using a subset of the training data can avoid this and speed up the fitting and prediction process [232].

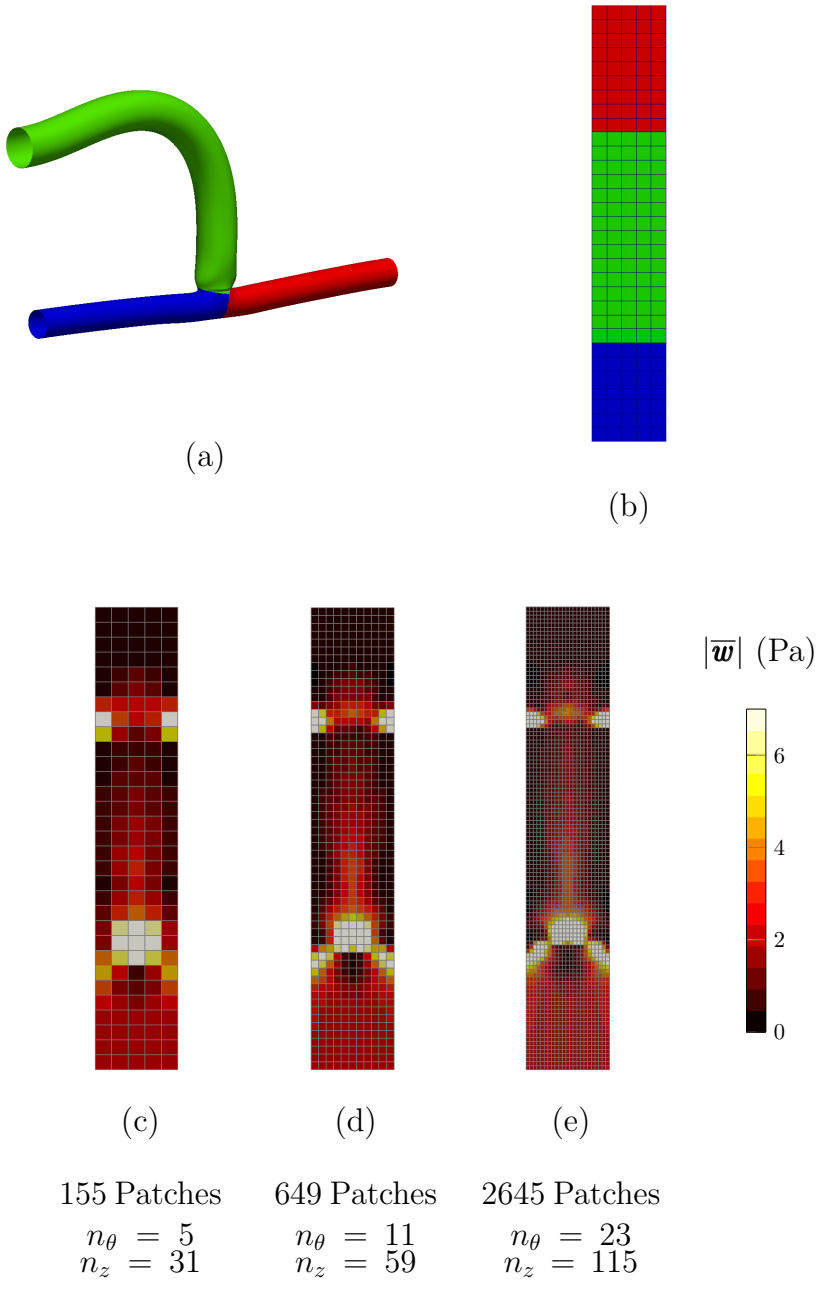

Figure 5.11: Figures (a) and (b) show the AVF endothelial surface mapping; Figures 5.11-(c),(d) and (e) show the patched $|\overline{\boldsymbol{w}}|$ field for the 80:20 flow split, with an increasing number of patches.

Figure 5.12 shows the declustering procedure, applied to one of the 54 cases: an increasingly finer, uniform grid is overimposed; for each bin in the grid the closest point to the bin centroid is extracted. A grid of 30×30 bins was estimated to produce convergent sensitivity indices and was used throughout the analysis.

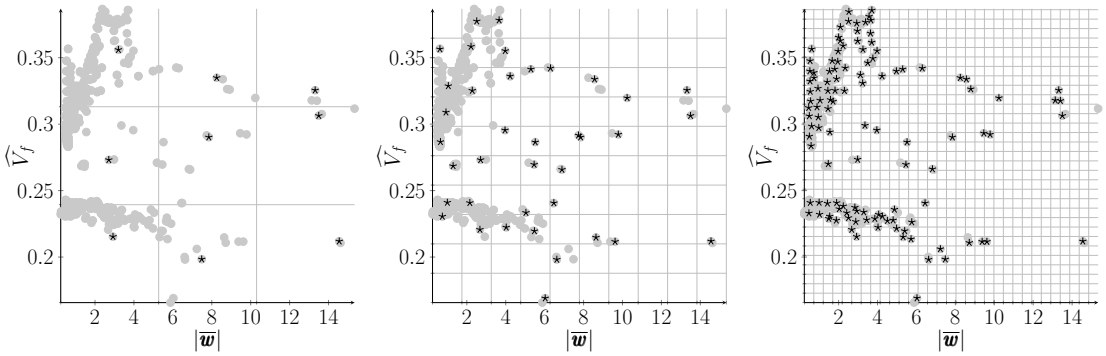

(a) 3×3 (b) 10×10 (c) 30×30

Figure 5.12: Declustering procedure for one case, with increasingly finer grids spacing: in gray, original dataset; in black, the extracted subset. The grey lines show the bins.

5.4.3.1 Sensitivity Indices

Samples, extracted according to the procedure outlined in the previous section, were used to train Stochastic Ordinary Kriging surrogate models, on which Sobol indices were calculated. The Kriging predictors were calculated using the Matlab ooDACE Toolbox [235], while Sobol indices were calculated using the Matlab GSAT Toolbox [236]. A total number of 4000 Sobol samples were used to calculate the sensitivity indices.

Initially, the 54 cases were analysed in an aggregated form. Figure 5.13 shows the training samples, in black, and Kriging predictors, light gray surface, for the full dataset and four different subsets, two of which consider only samples from the artery or from the vein, and other two which consider only Stretch-based perfusion or Stress-based perfusion models.

Main effects S_i, first-order interactions $S_{i,j}$ and total S_{Ti} sensitivity indices

and their associated Standard Error, for each of the 5 datasets considered, are shown in Table 5.2. Results show that most of the variance in $\widehat{PO_2}$ can be explained by spatial variations of WSS. Wall perfusion has only weak effects, when considering samples extracted from the artery, and with Stretch-based perfusion model. Overall, this means that flow-mediated effects, measured through $|\overline{\boldsymbol{w}}|$, are consistently more important than VV perfusion effects, in determining spatial oxygen distributions.

For comparison, Spearman rank correlation coefficients ρ were computed between the pairs $|\overline{\boldsymbol{w}}|$ and $\widehat{PO_2}$, and $\widehat{V_f}$ and $\widehat{PO_2}$. Spearman correlation was chosen because the variables considered are not normally distributed. Following Evans' indications, the strength of a correlation can be interpreted as very weak for $\rho \in [0, 0.2)$, weak for $\rho \in [0.2, 0.4)$, moderate for $\rho \in [0.4, 0.6)$, strong for $\rho \in [0.6, 0.8)$, and very strong for $\rho \in [0.8, 1]$ [237].

Spearman correlation coefficients were calculated in Matlab for the 5 aggregated datasets and are shown in Table 5.3. All of them are statistically significant, with associated p-values below the 5% level. Overall, results appear to be in agreement with Sobol indices, as the WSS exhibits moderate to strong correlation, while $\widehat{V_f}$ appear only to be weakly correlated with $\widehat{PO_2}$.

For the sake of completeness, the sensitivity analysis was also undertaken separately, on each of the 54 cases: a Kriging predictor was constructed and sensitivities were calculated using Sobol's method. Figure 5.14 shows the sensitivity indices $S_{|\overline{\boldsymbol{w}}|}$, $S_{\widehat{V_f}}$ and $S_{|\overline{\boldsymbol{w}}|,\widehat{V_f}}$ calculated over each of the 54 cases. Please refer to Figures 5.7, 5.8 and 5.9, for the abbreviations on the footer. No clear trend can be identified from the distribution of sensitivities and, overall, similar conclusions can be drawn from analysing the aggregated dataset. On average, local oxygen patterns exhibit high sensitivity to WSS patterns, while spatial distributions of VV perfusion seems to have only a minor effect on wall oxygen concentration.

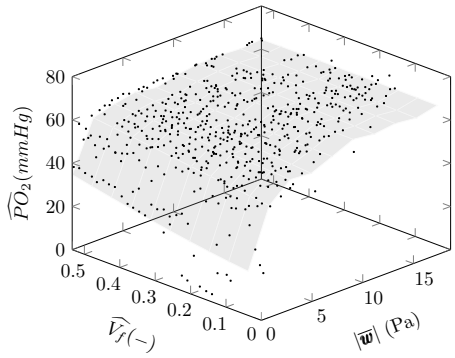

(a) Full dataset

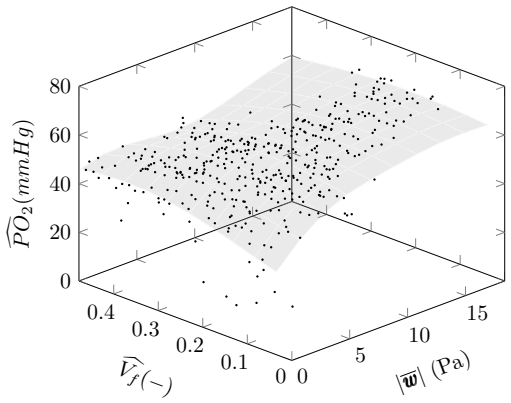

(b) Artery

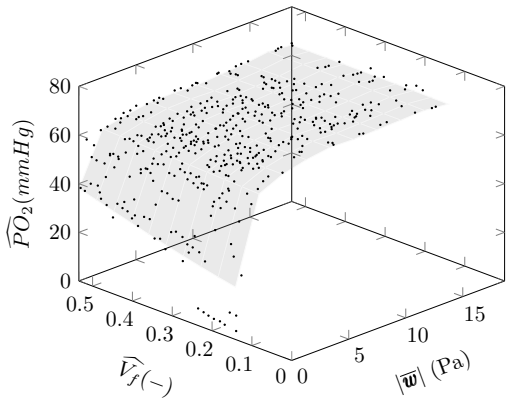

(c) Vein

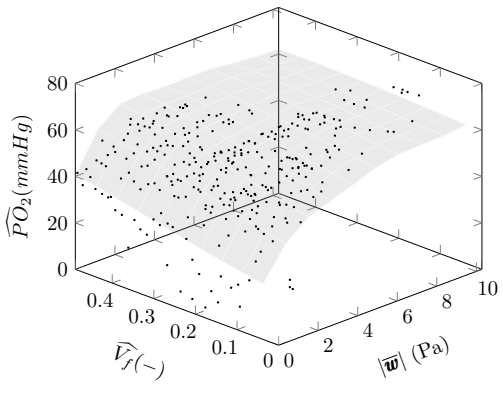

(d) Stretch-Based Perfusion

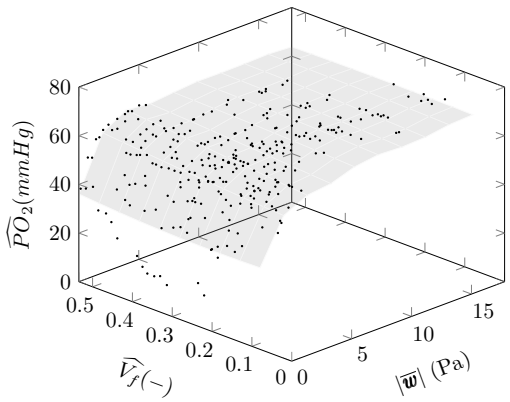

(e) Stress-Based Perfusion

Figure 5.13: Kriging predictors, light gray surface, and training samples, in black, shown for the full aggregated dataset (a) and for different subsets: (b) Artery, (c) Vein, (d) Stretch-Based Perfusion, (e) Stress-Based Perfusion.

Table 5.2: Main effects S_i, first-order interactions $S_{i,j}$ and total S_{Ti} Sobol sensitivity indices, and their associated Standard Error (SE), for $|\overline{\boldsymbol{w}}|$ and $\widehat{V_f}$. S_{sum} represents the sum of all effects.

Dataset	$S_{\lvert\overline{\boldsymbol{w}}\rvert} \pm SE$	$S_{\widehat{V_f}} \pm SE$	$S_{\lvert\overline{\boldsymbol{w}}\rvert,\widehat{V_f}} \pm SE$	$S_{sum} \pm SE$
Full	0.935 ± 0.045	0.031 ± 0.001	0.035 ± 0.002	1.001 ± 0.048
Artery	0.704 ± 0.015	0.164 ± 0.003	0.132 ± 0.005	1.000 ± 0.023
Vein	0.969 ± 0.052	0.002 ± 0.001	0.033 ± 0.003	1.000 ± 0.055
Stretch-Based Model	0.762 ± 0.023	0.186 ± 0.003	0.052 ± 0.002	0.999 ± 0.028
Stress-Based Model	0.961 ± 0.041	0.028 ± 0.001	0.010 ± 0.001	1.001 ± 0.042

	$S_{T\lvert\overline{\boldsymbol{w}}\rvert} \pm SE$	$S_{T\widehat{V_f}} \pm SE$
Full	0.969 ±0.001	0.065 ±0.045
Artery	0.835 ±0.003	0.296 ±0.015
Vein	1.002 ±0.001	0.031 ±0.052
Stretch-Based Model	0.814 ±0.003	0.238 ±0.023
Stress-Based Model	0.972 ±0.001	0.039 ±0.041

Table 5.3: Spearman rank correlation coefficients calculated for the 5 aggregated datasets, between $\widehat{PO}_2$ and $|\overline{\boldsymbol{w}}|$ / $\widehat{V_f}$. 95% confidence intervals are shown in brackets.

Set	$\rho_{\lvert\overline{\boldsymbol{w}}\rvert}$	$\rho_{\widehat{V_f}}$
Full	0.664 $[0.666, 0.661]$	-0.043 $[-0.039, -0.048]$
Artery	0.470 $[0.475, 0.465]$	0.205 $[0.21, 0.199]$
Vein	0.710 $[0.713, 0.707]$	0.144 $[0.15, 0.138]$
Stretch-Based Model	0.716 $[0.721, 0.712]$	-0.354 $[-0.346, -0.361]$
Stress-Based Model	0.704 $[0.709, 0.700]$	-0.039 $[-0.030, -0.048]$

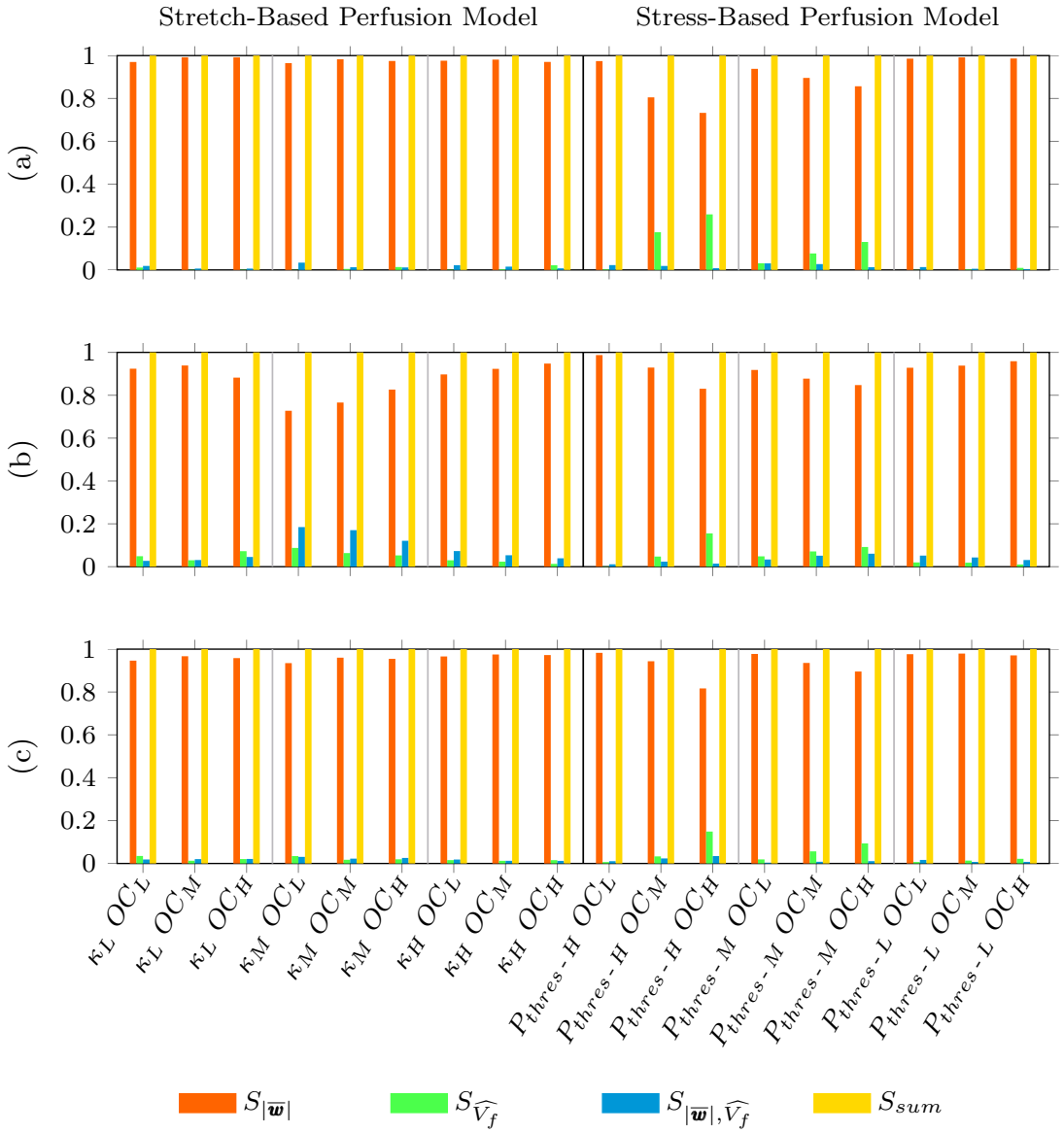

Figure 5.14: Sensitivity indices $S_{|\overline{w}|}$, $S_{\widehat{V_f}}$ and $S_{|\overline{w}|,\widehat{V_f}}$ calculated, separately, on each of the 54 cases. Please refer to Fig. 5.7, 5.8 and 5.9, for the abbreviations.

5.4.3.2 Sample Size

The analysis procedure described in the previous sections requires the user to adequately size the training sample, as well the Sobol sample. To ensure independence of the sensitivities from the sampling procedure, convergence of Sobol sensitivity indices with increasingly large sample sizes is needed.

Figure 5.15 shows sensitivity indices and their associated error bars, calculated on one of the 54 cases, for increasingly finer patches extracted with VMTK (see Fig: 5.11 for reference). Convergence is obtained with a number of 2645 patches, with 23 circumferential divisions and 115 axial divisions.

Figure 5.16 shows sensitivity indices and their associated error bars, calculated on the full aggregated dataset, for successively larger numbers of Kriging training points, (see Fig: 5.12 for reference). Convergence is obtained with a 30×30 declustering grid, corresponding to 620 training points. The same declustering grid was used throughout the study.

Finally, the convergence of the Sobol method is tested on an increasing number of Sobol sampling points. Converged sensitivity indices are achieved for sample sizes above 2000, as shown in Figure 5.17. A number of 4000 Sobol samples was used throughout the study, to further reduce the estimation error.

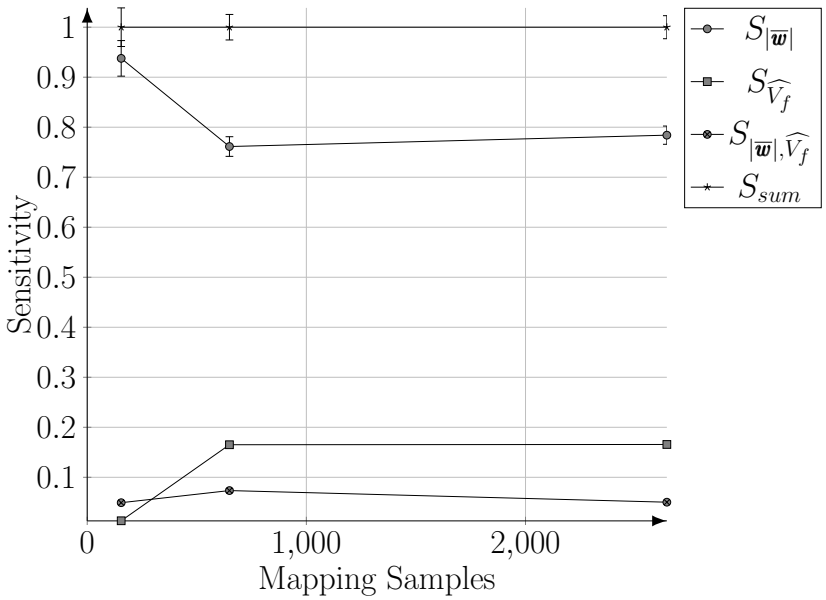

Figure 5.15: Sensitivity indices $S_{|\overline{\boldsymbol{w}}|}$, $S_{\widehat{V_f}}$ and $S_{|\overline{\boldsymbol{w}}|,\widehat{V_f}}$ and their associated error bars, calculated on one of the 54 cases, for increasingly finer VMTK patches.

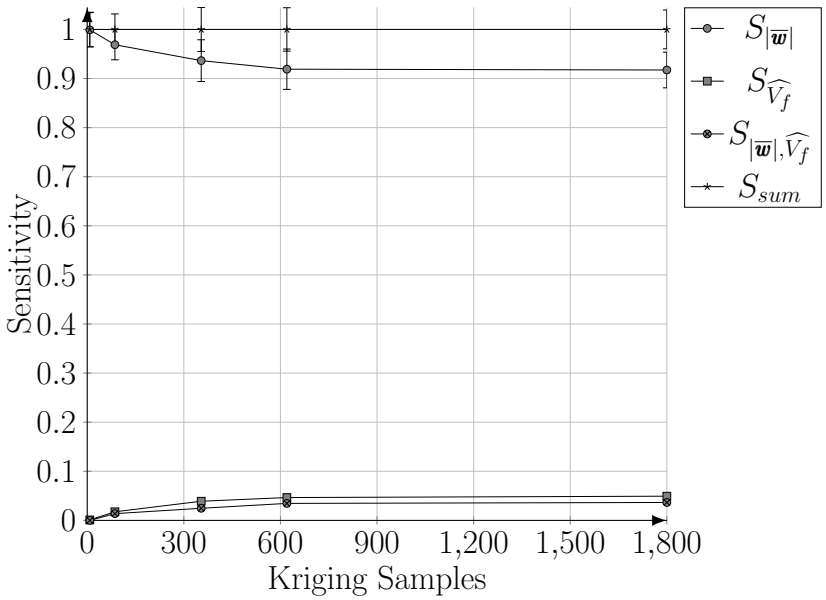

Figure 5.16: Sensitivity indices $S_{|\overline{\boldsymbol{w}}|}$, $S_{\widehat{V_f}}$ and $S_{|\overline{\boldsymbol{w}}|,\widehat{V_f}}$ and their associated error bars, calculated on the full aggregated dataset, for successively larger numbers of Kriging training points.

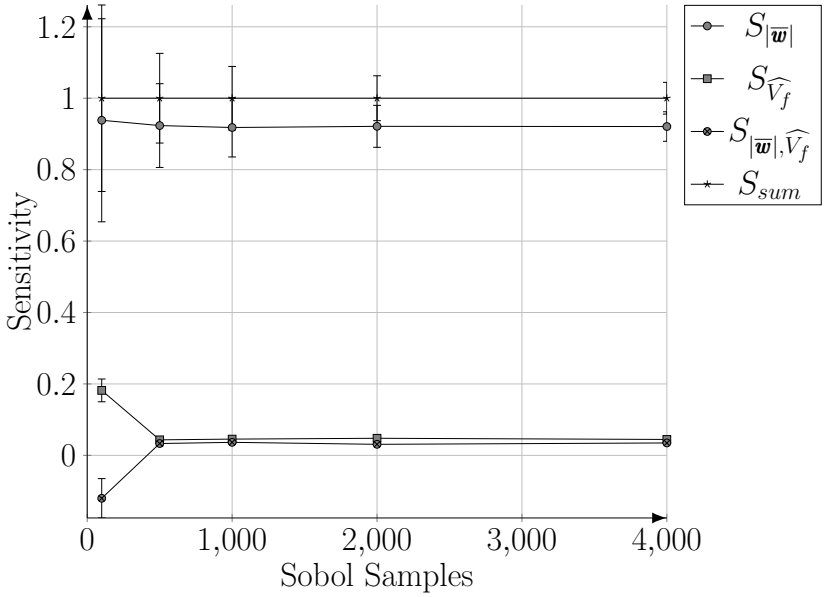

Figure 5.17: Sensitivity indices $S_{|\overline{\boldsymbol{w}}|}$, $S_{\widehat{V_f}}$ and $S_{|\overline{\boldsymbol{w}}|,\widehat{V_f}}$ and their associated error bars, calculated on the full aggregated dataset, for successively larger numbers Sobol sampling points.

5.5 Discussion

In this chapter, a model of oxygen transport, capable of accounting for VV perfusion, was developed. Vessel geometry and wall perfusion fields obtained from mechanical simulations shown in Chapter 4, were used to prescribe a VV oxygen source in the adventitial layer, according to Eq. 3.16. Two different VV perfusion mechanism, a stress-based and a stretch-based models, are included in the study, to account for the different microvascular collapse mechanisms, that are postulated in the literature. To test the effect of varying flow conditions and bulk wall parameters, a parametric study was undertaken.

The present study was the first to solve oxygen transport also in the adventitial layer. In previous studies, oxygen transport was either solved only in the lumen, neglecting wall diffusion/reaction (Tarbell's model [6]), or in the wall, assuming constant oxygen concentration in the adventitial layer (Moore's model [5]). Both approaches have been shown to produce physiologically relevant results, when studying healthy vessels, allowing to predict potential regions of wall hypoxia. However, evidence suggests that adverse wall mechanical conditions, which commonly occur in a number of vascular interventions (intra-vascular stents, arterio-venous fistulae and grafts and coronary artery bypass grafts) affected by IH [174, 17, 18, 19], can negatively affect VV perfusion and hinder optimal adventitial oxygen supply [127, 17, 18]. For these problems, omitting adventitial oxygen supply could represent an inadequate modelling assumption.

In newly formed AVF, oxygen transport can be influenced by changes in the native blood vessels 3-D geometry, which can negatively affect the haemodynamics and cause an altered wall-mechanics, that can prevent adequate VV perfusion [6, 10, 19, 3]. Despite the abundant literature documenting oxygen transport in blood vessels, it is still uncertain which between fluid-side or wall-side transport has the greatest relative importance, on the onset of hypoxia. In particular,

the aim of this work was to ascertain what is most important in determining wall-oxygen levels: (i) modified luminal flow field; (ii) mechanically-modified VV perfusion.

In the following paragraphs, the terms local and overall wall-oxygen levels are used to refer to spatial distributions and to average values of oxygen in the wall, respectively. Results suggest that for a given set of wall parameters, the local wall-oxygen levels are governed by the flow field, while spatial distributions of mechanically-modified VV perfusion are shown to have negligible effects on the local wall-oxygen levels. Qualitative visual comparison of $\widehat{PO}_2$ and WSS magnitude, which is used as a proxy of the flow, suggests strong spatial correlation between flow and O_2 transport. This finding is in agreement with Tarbell's observation that oxygen transport is fluid-phase limited. Global SA and Spearman rank correlation were used to quantify this link. Both separate and aggregated analysis show that spatial distributions of $\widehat{PO}_2$ are almost exclusively sensitive to local patterns of WSS.

However, overall wall-oxygen levels are highly sensitive to changes in bulk wall parameters. Specifically, at increased oxygen consumption rates, switching-off completely VV perfusion results in critically low overall wall oxygen levels, as the wall can only rely on luminal transport to supply O_2 to the entire wall.

This means that the local variability in the VV perfusion field does not translate significantly into changes of wall oxygenation, which are mostly explained by local WSS patterns. In contrast, overall wall oxygen levels depend on the balance between luminal and VV oxygen supplies, and wall oxygen consumption. This means that if one is interested in determining the actual oxygen concentration within the wall, a more physiological model of wall-side oxygen transport is needed. Therefore, further experimental work is necessary to determine better estimates of parameters, such as oxygen consumption rate and VV microvascular density and to clarify the role of the biomechanical forces in the mechanism of

microvascular perfusion.

Chapter 6

Reducing Hypoxia in Arterio-Venous Fistulae

6.1 Introduction

Results from the previous Chapter show that local wall oxygen levels are determined in the most part by flow patterns. For a given set of wall parameters, *e.g.* oxygen consumption rate, the mechanically-modified VV perfusion have negligible effects on local wall oxygen levels. This suggest that while forming an AVF exposes the artery and vein to an altered haemodynamics and oxygen transport, the altered biomechanics does not appear to translate into significant spatial variations in wall oxygen levels. In this chapter, these observations were used to develop a simplified oxygen transport model, that is combined with a Mesh Adaptive Direct Search (MADS) optimisation framework to identify an optimal AVF configuration with reduced hypoxia levels. In the simplified model, spatially constant VV perfusion in the adventitial layer was assumed. Additionally, it was shown in the previous chapter that the oxygen concentration field is not affected by temporal fluctuations in the flow field. For this reason, average steady-state

inflow and outflow conditions were used to reduce the cost of each cost function evaluation, and oxygen transport was solved using the procedure described in Section 6.2.3.2.

6.2 Optimisation

6.2.1 Overview

The optimisation approach presented in this chapter is rooted in the work of Grechy *et al.* [111], and uses the MADS method, proposed by Audet and Dennis [238, 239], and Kriging surrogate models to reduce the optimisation cost. The optimization procedure was fully automated, to include parametrisation and generation of three-dimensional solid geometries and meshes, CFD simulation and post-processing. Similar methods have been recently used by Marsden *et al.* and Yang *et al.* to optimise Y-grafts for Fontan procedures [240, 241, 242], and by by Gundert *et al.* and Bressloff *et al.* to design cardiovascular stents [243, 244].

6.2.2 Parametrisation

Both vessel geometries were constructed by sweeping circular sections of diameter $\mathrm{D_A} = 6mm$, along the vessel centreline. Brachial arteries exhibit an inherently curved geometry in the ante-cubital fossa, the site where BC-AVF are normally formed [1], which can potentially be leveraged during the surgery. The curved arterial section $\mathbf{x_A}$ is based on the recent work of Iori *et al.* [15] and Grechy *et al.* [111] and defined as

$$\mathbf{x_A} = [0, 20\mathrm{D_A}\cos(\beta), 20 - 20\mathrm{D_A}\sin(\beta)] \tag{6.1}$$

with $\beta \in [-\pi/6, +\pi/6]$. The vein centreline, $\mathbf{x_V}$, was constructed using a two-piece cubic hermitian spline of the form

$$\mathbf{h}_i(\mathbf{s}) = (2s^3-3s^2+1)\mathbf{p}_i+(s^3-2s^2+s)\mathbf{m}_i+(-2s^3+3s^2)\mathbf{p}_{i+1}+(s^3-s^2)\mathbf{m}_{i+1} \quad (6.2)$$

with $s \in [0, 1]$. The vein centreline is defined as

$$\mathbf{x_V} = h_0(s) \cup h_1(s). \quad (6.3)$$

with $\mathbf{p}_0 = \mathbf{O}$, the intersection between the venous and arterial centrelines, for construction, origin of the reference system, $\mathbf{p}_1 = [x_{p1}, y_{p1}, z_{p1}]$, the mid-point of the venous centreline, $\mathbf{p}_2 = [\mathrm{d_{av}}\sin(\xi), -10\mathrm{D_A}, \mathrm{d_{av}}\cos(\xi)]$, the DVO location. The parameters $\mathbf{m}_i$ identify the cubic spline tangents and are set as: $\mathbf{m}_0 = [10\mathrm{D_A}\sin(\theta)\sin(\phi), 10\mathrm{D_A}\cos(\theta), 10\mathrm{D_A}\sin(\theta)\cos(\phi)]$, the vein direction where the arterial and venous centrelines meet, $\mathbf{m}_1 = 3((\mathbf{p}_2 - \mathbf{p}_0) - (\mathbf{m}_2 + \mathbf{m}_0))/4$, the tangent at the venous mid-point, defined such that $\mathbf{x_V}$ is $C2$-continuous and finally $\mathbf{m}_2 = [0, -10\mathrm{D_A}, 0]$, the tangent at the DVO.

The resulting idealised AVF geometry is parametrised by a set of six parameters $[x_{p1}, y_{p1}, z_{p1}, \theta, \phi, \xi]$, which are constrained such that $x_{p1} \in [-5\mathrm{D_A}, 5\mathrm{D_A}]$, $y_{p1} \in [-5\mathrm{D_A}, 5\mathrm{D_A}]$, $z_{p1} \in [-5\mathrm{D_A}, 5\mathrm{D_A}]$, $\theta \in [0, \pi]$, $\phi \in [0, \pi]$ and $\xi \in [0, 2\pi]$ [111]. The parameters were chosen to ensure clinical and anatomical relevance to the geometry. In addition, during the geometry generation, the variables were constrained such that self-intersection was avoided, venous length did not exceed $20\mathrm{D_A}$, the maximum venous curvature did not exceed $1.5/\mathrm{D_A}$ and the whole geometry fitted within an infinitely long cylinder, aligned with the y-axis, having radius of $7.5\mathrm{D_A}$ [111]. A schematic illustration of the arterial and venous centrelines is shown in Figure 6.1.

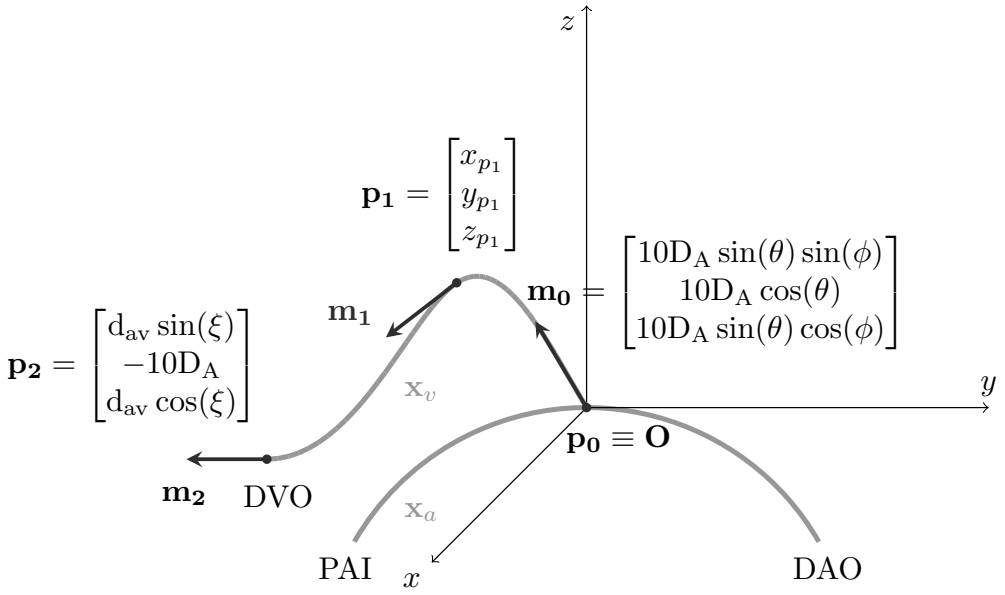

Figure 6.1: Schematic illustration of arterial and venous centrelines, x_a and x_v respectively, along with their associated parametrisation. Courtesy of Dr. Grechy [111].

6.2.3 Optimisation Framework

MADS optimisation framework was used to identify the optimal AVF configuration. MADS is a pattern search algorithm, a type of derivative-free optimisation methods, which have a well established convergence theory [245]. When performing optimisation, the number of samples required to survey the cost function space grows exponentially with the dimensionality of the parameter space. On top of that, each cost function call requires the solution of a computationally expensive CFD simulation, making direct evaluations of the cost function infeasible, for large parameter spaces. Using a surrogate model improves the efficiency of the optimisation process, as the cost function is not directly evaluated. The MADS algorithm is comprised of two parts: a first exploratory search step, which employs a surrogate model, in this case ordinary Kriging, to select points that are likely to minimise the cost function, and a poll step, in which points neighboring

the current optimum, are evaluated, in a set of directions, to check whether the current optimum is a local optimiser for the cost function [245, 239, 238].

6.2.3.1 Cost Function

As pointed out by Marsden, the choice of an appropriate cost function to minimise is highly problem specific and one of the most critical aspect of applying optimisation to mechanobiological systems [245]. In the context of reducing areas of low oxygen transport, a simple cost function that evaluates the percentage of vascular wall, exposed to critical values of PO_2, is proposed. Specifically, the cost function is defined as

$$\Psi = \left(1/V \int_{\Omega} \psi(\mathbf{x}) d\Omega\right) \times 100, \tag{6.4}$$

where Ω is the vascular wall and V is the wall volume and

$$\psi = \begin{cases} 1 \ : \ PO_2 < 15mmHg \\ 0 \ : \ elsewhere. \end{cases} \tag{6.5}$$

6.2.3.2 Computational Method

Star-CCM+ v12.02.011-R8 (Siemens PLM, Plano, TX USA) was used to solve Equations 3.1-3.3-3.8 to determine blood velocity field and the oxygen concentration, for a given AVF configuration.

In the previous chapter, it was shown that the oxygen field does not appear to be affected by flow temporal fluctuations. For this reason, to produce cheaper simulations, the following procedure was used to solve oxygen trasport. Initially, 1000 iterations of the segregated steady-state solver were used to solve Navier-Stokes equations, and then the segregated implicit unsteady solver was run with a time-step $dt = 0.0005$ s, for 300 time-steps, corresponding to a total time of 0.15 s. The first 50 time-steps (0.025 s) were discarded, and the remaining 250

(0.125 s) were used to calculate the time average velocity vector. Considering flow fluctuations have frequencies of about 60-100 Hz, 0.125 s was deemed sufficient to allow the flow to develop and produce a good estimate of the average flow field.

Subsequently, the average velocity field was used to solve oxygen transport. A segregated steady solver was run until the oxygen transport residuals fell below 10^{-9}. For each configuration, polyhedral unstructured volume meshes were generated, with prismatic boundary layer meshes adjacent to the wall, similar to that used in Chapter 5. Each mesh had $\approx 6 \times 10^6$ cells in total ($\approx 3 \times 10^6$ in the fluid and $\approx 3 \times 10^6$ in the wall). Wall and prismatic boundary layers having similar size to those used in the previous chapter were generated while, in the fluid, significant lower spatial resolution was used. Performance of the optimal configuration, with respect to the simplifying assumptions, will be assessed with a higher-resolution pulsatile simulation, in Section 6.4.

6.2.3.3 Initial Seeding

The Kriging surrogate model was initially trained on a set of samples generated using Latin Hypercube Sampling (LHS). Specifically, 600 LHS samples were generated, constrained such that $x_{p1} \in [-5\mathrm{D_A}, 5\mathrm{D_A}]$, $y_{p1} \in [-5\mathrm{D_A}, 5\mathrm{D_A}]$, $z_{p1} \in [-5\mathrm{D_A}, 5\mathrm{D_A}]$, $\theta \in [0, \pi]$, $\phi \in [0, \pi]$ and $\xi \in [0, 2\pi]$. Of these 600 configurations, 475 were rejected, because they did not satisfy the imposed constraints on maximum venous curvature and length, overall size, or because of self-intersections. The first 100 of the remaining 125 feasible AVF configurations, were run and for each of them the cost function Ψ was calculated. Figure 6.2 shows the 100 LHS samples and their relative cost function.

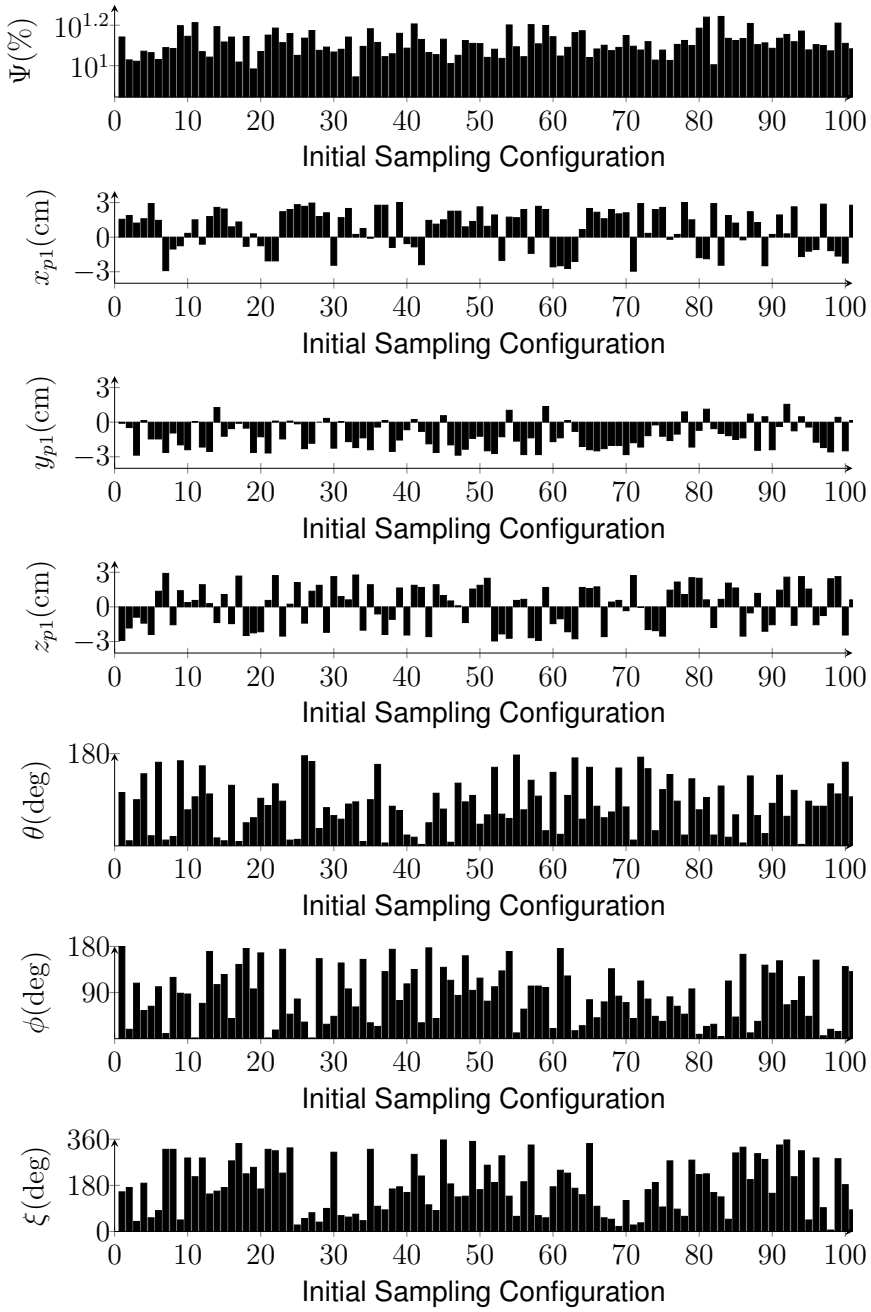

Figure 6.2: Values of x_{p_1}, y_{p_1}, z_{p_1}, θ, ϕ, ξ and Ψ, for the 100 initial training points used to seed the Kriging-based surrogate.

6.2.3.4 Mesh Adaptive Direct Search

The MADS method is a derivative-free, pattern search family, optimisation algorithm, introduced by Dennis and Audet [238, 239]. Given the cost function Ψ and its Kriging-based surrogate Ψ_e, MADS was used to search for the sample point $\mathbf{s}^*$ that minimises the cost function

$$\mathbf{s}^* = \underset{\mathbf{s}\in\mathbf{S}}{\text{minimise}}\ \Psi(\mathbf{s}) \tag{6.6}$$

with $\mathbf{S}$, set of all feasible configurations.

MADS is an iterative method divided into two main steps: SEARCH and POLL. Figure 6.3 shows the block diagram of the MADS method. During the SEARCH step, the surrogate model Ψ_e is calculated on a finite set of trial points. The set, $\tilde{\mathbf{S}}_k$, represents the set of parameters tried during the optimisation, which led to feasible geometries and is defined as

$$\tilde{\mathbf{S}}_k = \mathbf{S}_k - W(\mathbf{S}_k) \tag{6.7}$$

where $\mathbf{S}_k$ is the full set of tried parameters, and $W(\mathbf{S}_k)$ is a subset of $\mathbf{S}_k$, which contains simulation that could not be solved, *e.g.* because of violating one or more constraints. At $k = 0$, the set $\tilde{\mathbf{S}}_0$ is the initial dataset, generated during LHS.

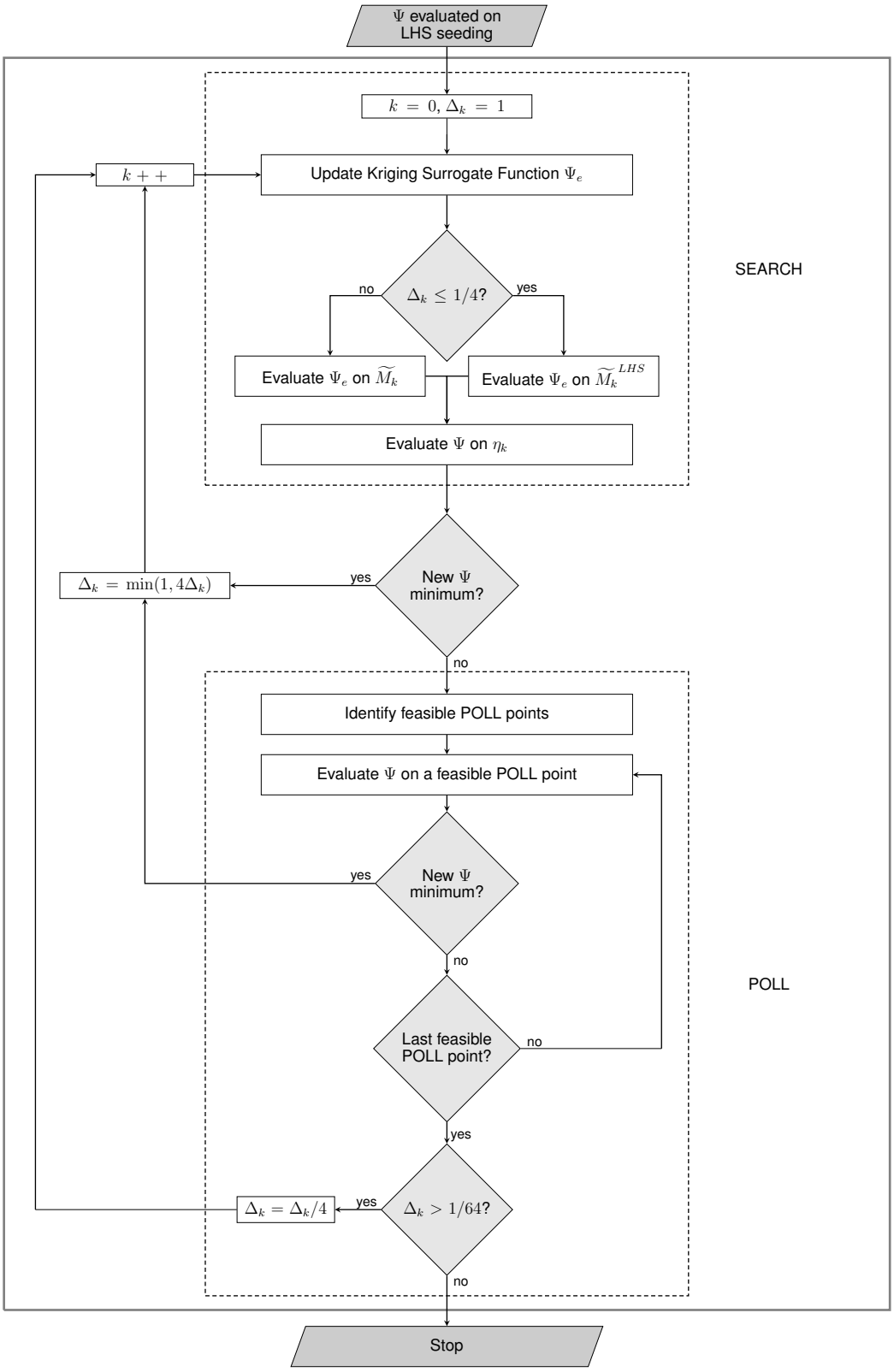

Figure 6.3: Block diagram of the MADS method; courtesy of Dr. Lorenza Grechy.

At each iteration k, the surrogate model, Ψ_e, was built over the already tested samples, $\tilde{\mathbf{S}}_k$, and evaluated on a grid $\tilde{M}_k$ defined as follows,

$$\tilde{M}_k = M_k - \Gamma(M_k) - \Pi(M_k), \tag{6.8}$$

where $\Gamma(M_k)$ is the set of M_k configurations, which violate the geometry constraint, and $\Pi(M_k)$ is the set of M_k configurations, which have venous centrelines within 1 mm of venous centrelines, associate with all previous tried $\mathbf{S}_k$ configurations. The grid M_k is defined as follows

$$M_k = \bigcup_{\mathbf{s}\in\mathbf{S}_k} \{\mathbf{s} + \Delta_k^m \mathbf{D}\mathbf{z} : \mathbf{z} \in \mathbb{N}^{n_D}\}, \tag{6.9}$$

where n is the parameter space dimension, n_D is $2n$, D is an $n \times n_D$ positive spanning matrix, $\mathbf{z}$ is a vector of integers of length $2n$ and Δ_k^m is the mesh spacing at iteration k. The grid is defined as the union of sets over $\mathbf{S}_k$. In this way, it is ensured that all previously visited points lie on the mesh, and the new trial points can be selected around any of them using the directions in $\mathbf{D}$. In line with [111], it was chosen to use $\mathbf{D} = [\mathbf{I}_n, -\mathbf{I}_n]$, with $\mathbf{I}_n$, the identity matrix of dimension n.

For a mesh spacing $\Delta_k^m \leq 1/4$, Ψ_e is evaluated over the entire $\tilde{M}_k$, otherwise, Ψ_e is evaluated on a subset of $\tilde{M}_k$, calculated from LHS of M_k, and containing 10^4 points, which will be called $\tilde{M}_k^{LHS}$.

The set of four configurations, η_k, that have the lowest Ψ_e, are extracted from $\tilde{M}_k$ or $\tilde{M}_k^{LHS}$. To ensure good parameter space exploration, only configurations which have venous centrelines, that depart from each other by at least 1 mm are chosen.

At iteration k, the point, $\mathbf{s}_k$, represents the current optimal configuration, that minimises Ψ. At this point, a CFD simulation is run for each predicted trial point in η_k. If Ψ assumes a smaller value at any of the newly tested points,

the current optimum, $\mathbf{s}_k$, is updated, the grid is coarsened $\Delta^m_{k+1} = min(4\Delta^m_k, 1)$, $k = k + 1$ and the SEARCH step is repeated, with updated Ψ_e and $\tilde{\mathbf{S}}_k$. On the other hand, if no trial point improves the cost function, the algorithm enters the POLL step.

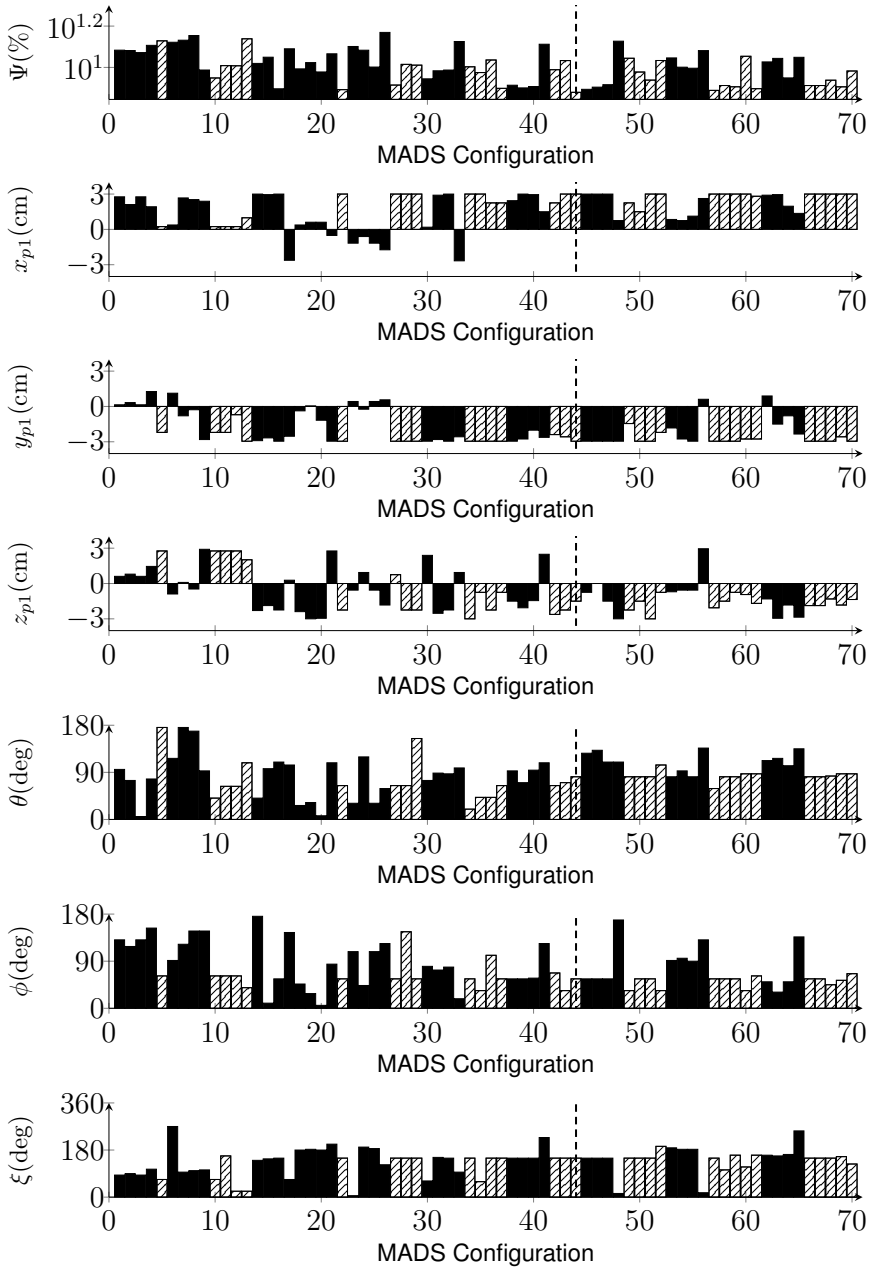

Figure 6.4: Values of objective function Ψ and parameters x_{p_1}, y_{p_1}, z_{p_1}, θ, ϕ, ξ against the number of the feasible simulations during the MADS optimisation. In black, bars corresponding to potential minima, predicted during the SEARCH step; hatched bars correspond to feasible simulation runs, tried during the POLL step. A dashed line indicates the optimum of Ψ. The optimal geometry was found during a POLL step.

During the POLL, the cost function is evaluated on a set of points P_k defined as

$$P_k = \{\mathbf{s}_k + \Delta_k^m \mathbf{d} : \mathbf{d} \in \mathbf{D}_k\} \subset M_k, \tag{6.10}$$

where $\mathbf{D}_k$ is a positive spanning set of $n+1$ dimension, with $\Delta_k^m \|\mathbf{d}\|_\infty \leq \Delta_k^p$ and Δ_k^p, the poll size parameter.

Following [111], the poll size parameter is defined as $\Delta_k^p = n\sqrt{\Delta_k^m}$. Generation of the basis of directions, $\mathbf{D}_k$, follows the rules described in [239]. Given that strong geometric constraint on the vein, it is required that the POLL step has to find at least one feasible configuration, otherwise a new poll set is recomputed. As Δ_k^m and Δ_k^p goes to zero, the number of POLL points increases.

If during the POLL step, an improved mesh point is found, $\mathbf{s}_k$ is updated, the grid is coarsened $\Delta_{k+1}^m = min(4\Delta_k^m, 1)$, $k = k+1$, otherwise, $\mathbf{s}_{k+1} = \mathbf{s}_k$, the grid is refined $\Delta_{k+1}^m = \Delta_k^m/4$, $k = k+1$. Then the optimisation framework returns to the SEARCH step, and newly evaluated trial points, P_k, added to $\mathbf{S}_k$. SEARCH and POLL are repeated until the convergence criteria, $\Delta_k^m < \Delta_{k\,min}^m$ is met ($\Delta_{k\,min}^m = 1/64$).

Figure 6.4 shows new samples $\mathbf{S}_k$ and their relative cost function, tried during the SEARCH and POLL steps. During the optimisation, Ψ was evaluated in 70 new samples, and the optimal geometry was found at the 44th simulation, leading to $\Psi = 7.58\%$. The optimal geometry was found during a POLL step.

The geometry of the 100 LHS and subsequent 70 MADS samples are omitted in the discussion, but shown in the Appendix A.5. The richness of the parameter space is apparent.

6.3 Results

The minimum value of Ψ obtained from the optimisation was 7.58%. The optimal AVF configuration is shown in Figure 6.5 and the associated geometric parameters

are reported in Table 6.5-(d). a The angle $\xi = 149.06°$, along with the position of $\mathbf{p}_1$ produces a venous geometry, resambling a section of helix. Secondary flows and swirling, induced by helical-shaped vessels, are well-known to enhance mixing, and thus mass transport, by reducing areas of potential flow stagnation [8, 9, 246].

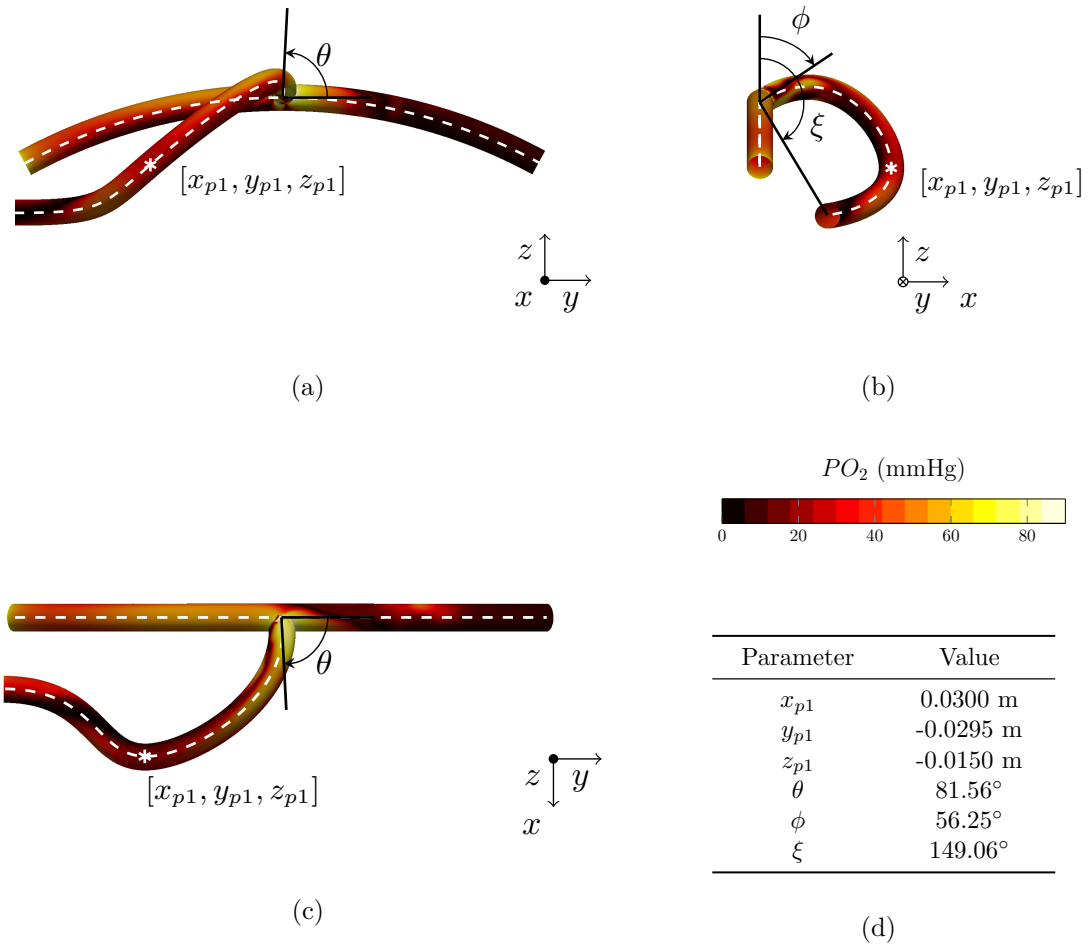

Parameter	Value
x_{p1}	0.0300 m
y_{p1}	-0.0295 m
z_{p1}	-0.0150 m
θ	81.56°
ϕ	56.25°
ξ	149.06°

Figure 6.5: Orthogonal side-on (a), end-on (b) and top-on (c) views of the optimal AVF configuration. Salient aspects include an out-of-plane anastomosis, on the side of the arterial bend and an inherently non-planar venous section. The endothelial surface is colored by PO_2. Table (d) contains the optimal design parameters.

In order to assess the effectiveness of the surrogate optimisation framework

to determine improved designs, cost functions evaluations of the first 100 latin hypercube samples are comparated with the successive 70 MADS samples. Figure 6.6 plots median, inter-quartile range, and range of Ψ, for the two groups.

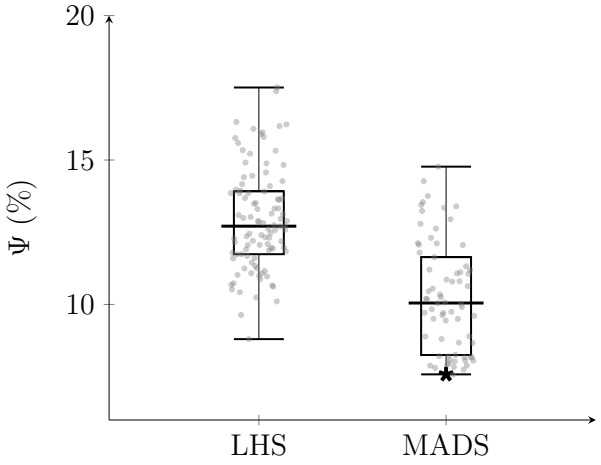

Figure 6.6: Box plots of the median (horizontal black line), inter-quartile range (white box), and range (whiskers) of Ψ, for the first 100 LHS and the successive 70 MADS samples. The black star indicate Ψ for the optimal configuration.

The MADS produces a reduction in Ψ, with respect to the LHS configurations, of 13.8% from the group minimum ($\Psi = 8.80\%$). In addition, a 40.3% reduction from the group median ($\Psi = 12.71\%$) and 56.7% reduction from the maximum ($\Psi = 17.51\%$) can be observed, with respect to randomly generated LHS designs, which shows the effectiveness of the MADS in finding improved designs.

6.3.1 Sensitivity

Having identified an optimal configuration, it is useful to assess the sensitivity of Ψ to each of the six geometric parameters. Figure 6.7 plots the median, inter-quartile range, and range, of parameters associated with good design configurations, that achieve $\Psi < median(\Psi)$. Three parameters, in particular, θ, ϕ and ξ vary little during the optimisation and remain close to the optimal values.

The other three parameters show a larger variability, meaning that the position of $\mathbf{P}_1$ is not as critical in producing optimal AVF configurations.

This can be explained by two observations. First of all, the anastomosis angles, in particular ϕ, produce an out of plane connection that breaks the symmetry of the Dean flow, inducing rotation and swirling flow in the distal section of the artery.

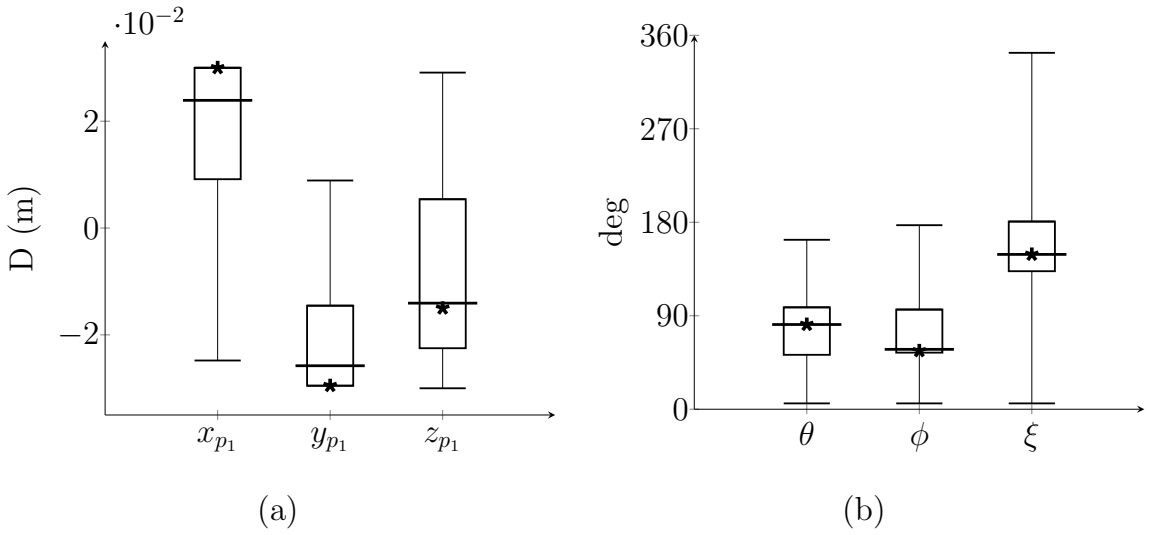

Figure 6.7: Box plots of the median (horizontal black line), inter-quartile range (white box), and range (whiskers), of parameters associated with configurations that achieve $\Psi < median(\Psi)$. Black stars indicate the parameter values of the optimal set.

Secondly, oxygen transport appears to be improved by the inherent non-planarity of the vein, which, as already mentioned, may induce secondary flows and swirling. In particular, with the given optimal θ and ϕ, the position of the final end of the anastomosis, $\mathbf{P}_2$, which is a function of ξ, appears more important in determining an helical venous shape, than the location of the middle point $\mathbf{P}_1$, determined by x_{p_1}, y_{p_1}, z_{p_1}. In both cases, swirling helps reducing flow stagnation and enhancing mixing, both of which have a positive effect on oxygen transport.

6.3.2 Local Normalized Helicity and Oxygen Transport

Molecular diffusion of low-molecular-weight species between the blood and the arterial wall is a slow process, especially considering the distance over which mass transport must occur [247, 6]. Several authors found a correlation between WSS and mass transport of such species. In particular, it has been observed that hypoxia often occurs in regions of low WSS [48, 247, 6].

Secondary flow and cross mixing can induce relatively uniform distributions of WSS, by suppressing flow stagnation/separation, that normally occur in vascular bends and bifurcations. Therefore, mixing can be expected to enhance the transport of oxygen between the blood and the vessel wall [8, 247, 9].

In previous studies, swirling flows have been quantified using helicity density, a flow property introduced by Shtilman [248]. Helicity density measures the potential of a moving fluid to evolve into a helical flow, and is defined as follows

$$h = \mathbf{u} \cdot (\nabla \times \mathbf{u}), \tag{6.11}$$

where the curl of the velocity field, $\nabla \times \mathbf{u}$, is the vorticity vector.

Based on Shtilman's h, Grigioni *et al.* [249] defined the Local Normalized Helicity (LNH) as

$$LNH = \frac{\mathbf{u} \cdot (\nabla \times \mathbf{u})}{|\mathbf{u}||\nabla \times \mathbf{u})|}. \tag{6.12}$$

LNH is a non-dimensional quantity that measures the alignment between the velocity and the vorticity vector, and can be used as an indicator of flow rotation [250].

Figure 6.8 shows iso-surfaces of LNH, in blue LNH=-0.7 and in red LNH=0.7, within the four best (i)-(ii)-(iii)-(iv) and the four worst (1)-(2)-(3)-(4) AVF configurations.

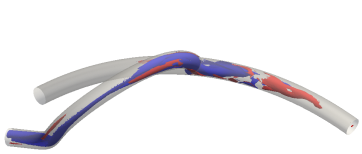

(i) MADS 44, Ψ=0.0758, $|\widetilde{LNH}|$=0.3008

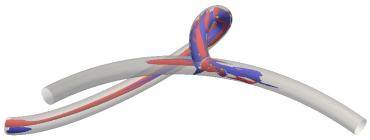

(1) LHS 83, Ψ=0.1751, $|\widetilde{LNH}|$=0.2399

(ii) MADS 57, Ψ=0.0774, $|\widetilde{LNH}|$=0.3106

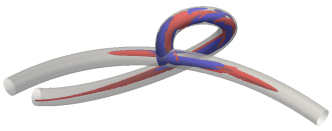

(2) LHS 81, Ψ=0.1738, $|\widetilde{LNH}|$=0.2510

(iii) MADS 22, Ψ=0.0780, $|\widetilde{LNH}|$=0.3056

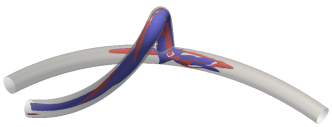

(3) LHS 11, Ψ=0.1634, $|\widetilde{LNH}|$=0.2586

(iv) MADS 45, Ψ=0.0784, $|\widetilde{LNH}|$=0.3094

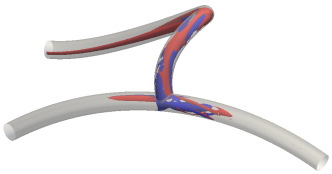

(4) LHS 99, Ψ=0.1623, $|\widetilde{LNH}|$=0.2549

Figure 6.8: Iso-surfaces of LNH (blue LNH=-0.7 and red LNH=0.7) within the four best (i)-(ii)-(iii)-(iv) and the four worst (1)-(2)-(3)-(4) AVF configurations.

The four worst AVF configurations (which have the highest Ψ) were randomly generated during LHS. For all of them, the vein is connected on the outside of the arterial bend. Conversely, the four best AVF configurations were all generated during MADS, and for all of them, the vein is connected laterally to the arterial bend. This generates rotating flow in the distal arterial section, which is high-

lighted by the presence of helical structures, which are not present in the worst configurations.

Lower values of, $|\widetilde{LNH}|$, the spatially-averaged absolute value of LNH, can be observed in worst AVF configurations. In particular, a significant, negative correlation, with Pearson's correlation index of R=-0.58, exists between the cost function Ψ and $|\widetilde{LNH}|$ (see Figure 6.9).

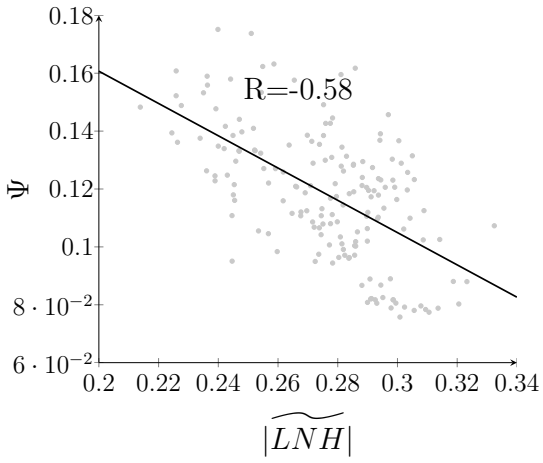

Figure 6.9: Scatter plot of Ψ against $|\widetilde{LNH}|$, for the 170 AVF configurations, generated during the LHS and MADS. A significant, negative correlation, with Pearson's correlation index of R=-0.58, is observed. In black the fitted linear regression.

6.4 Pulsatile Simulation

A high resolution pulsatile simulation was undertaken to verify that the optimal configuration behaves broadly as the simplified model, used to reduce the optimisation cost.

Patient-specific proximal inflow and and distal outflows Ultrasound measurments were performed by Dr. Richard Corbett, at the time of the AVF surgery, on a sample of 49 patients [44]. From these, population average waveforms were extracted and used to prescribe realistic boundary conditions.

6.4.1 Boundary Conditions

Modelling the pulsatile behaviour of blood requires a proper description of the time-dependent effects of the up and downstream vasculature. At the PAI, a time-varying, spatially-constant velocity boundary condition was imposed, having an average velocity of 0.31 m/s (equivalent to 8.82 ml/min), which resulted in an average Reynolds number of 567. The PAI inflow rate Q_{PAI} is shown in Figure 6.12-(b). The velocity was prescribed normal to the PAI inflow plane.

The distal vascular bed was modelled by means of a 3-elements Windkessel model (Fig. 6.10), which was deemed to be appropriate to capture the effect of the proximal and peripheral vascular resistance and compliance [251].

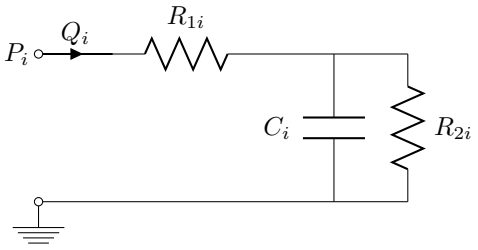

Figure 6.10: Three elements RCR Windkessel model. The series resistor (R_{1i}) represent proximal vascular resistances, while the parallel resistor-capacitor (R_{2i} - C_i) describes peripheral vessels resistance and compliance.

At each outlet, a Resistor-Capacitor-Resistor (RCR) Windkessel model was applied, resulting in the following ordinary differential equations:

$$P_{DAO} = Q_{DAO}R_{1DAO} - R_{2DAO}C_{DAO}\frac{\mathrm{d}}{\mathrm{dt}}(P_{DAO} - R_{1DAO}Q_{DAO}), \tag{6.13}$$

and

$$P_{DVO} = Q_{DVO}R_{1DVO} - R_{2DVO}C_{DVO}\frac{\mathrm{d}}{\mathrm{dt}}(P_{DVO} - R_{1DVO}Q_{DVO}), \tag{6.14}$$

where P_{DAO} and P_{DVO} are spatially averaged pressures at the DAO and DVO,

Q_{DAO} and Q_{DVO} are the outflow rates at the DAO and DVO, and R_{1DAO}, R_{2DAO}, C_{DAO} R_{1DVO}, R_{2DVO}, C_{DVO} are the relevant Windkessel parameters, that needs to be determined.

Specifically, at each time-step, the pressure outlet boundary conditions, P_{DAO} and P_{DVO} were updated and mass-flow rates Q_{DAO} and Q_{DVO} calculated from the CFD solver. Equations 6.13 and 6.14 were explicitly coupled with the CFD solver and solved using an implicit Euler method.

The RCR parameters were estimated using the approach outlined by Grechy *et al.* in [110, 111], such that the pressure at the PAI had a physiological range of 80-125 mmHg, and the outflows matched the AVF population average flow rates (shown in Fig. 6.11), measured by Dr. Corbett [44].

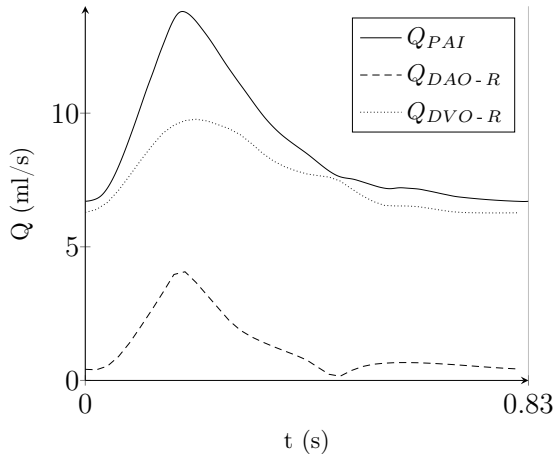

Figure 6.11: AVF population average inflow and outflow rates, measured by Dr. Corbett [44].

Values for the RCR parameters were obtained using an iterative approach that aimed to minimise

$$\Phi = \left(\frac{|max(P_{PAI}) - P_{RS}|}{P_{RS}}\right)^2 + \left(\frac{|min(P_{PAI}) - P_{RD}|}{P_{RD}}\right)^2 + \left(\frac{\int |Q_{DVO} - Q_{DVO\text{-}R}|\mathrm{dt}}{\int |Q_{DVO\text{-}R}|\mathrm{dt}}\right)^2 \tag{6.15}$$

where P_{PAI} is the pressure waveform calculated at the PAI, $P_{RS} = 125mmHg$ and

$P_{RD} = 80mmHg$ are the reference systolic and dyastolic pressures, and $Q_{DVO\text{-}R}$ is the reference outflow rate waveform, measured at the DVO [44]. The integrals are calculated over a single pulse period, when the solution has become period independent.

The iterative process combined a 0D lumped parameter model, with a low-resolution 3D CFD model. The 0D model, shown in Figure 6.12, is a reduced order representation of the 3D model: each of the three vascular segments is represented in terms of an inductor and a quadratically non-linear resistor.

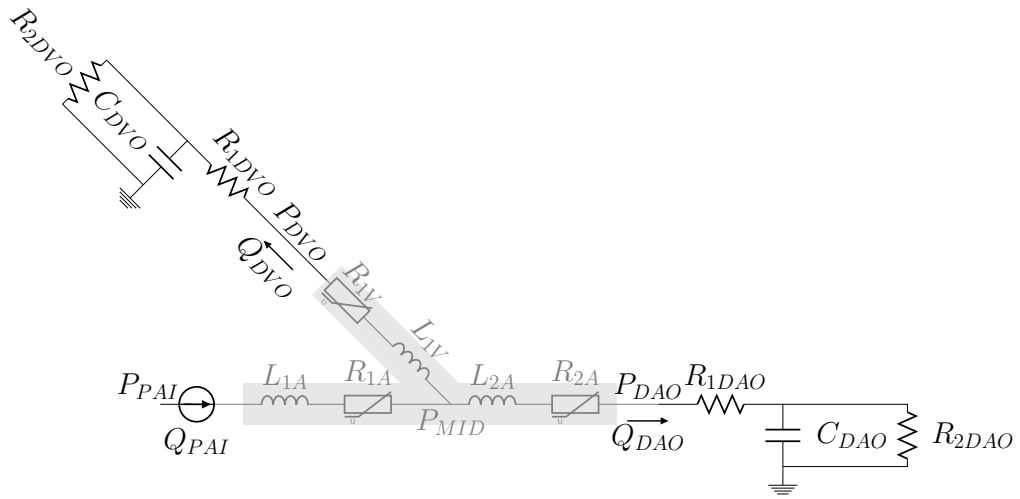

Figure 6.12: Schematic illustration of the 0D model used in the Windkessel parameter estimation process. Gray components represents an approximation of the low-resolution 3D model.

At the beginning of the iteration, the 0D lumped parameters were initially estimated and the 0D reduced-order model was used to identify Windkessel parameters that minimise Φ, using the Nelder-Mead simplex algorithm, implemented in the *fminsearch* Matlab function. Then, the Windkessel parameters were used to prescribe outflow boundary conditions to the 3D model, which was solved with until the solution reached period independence. From the 3D solution, pressure losses, $(P_{PAI} - P_{MID})$, $(P_{MID} - P_{DAO})$ and $(P_{MID} - P_{DVO})$ and the relative

flow-rates were extracted, and improved estimates for the 0D parameters were calculated. The process repeated until the Windkessel parameters were seen to converge.

Parameter	Value
R_{1DAO}	8.63 $(mmHg\ ml^{-1}\ s)$
R_{2DAO}	45.51$(mmHg\ ml^{-1}\ s)$
C_{DAO}	0.02 $(mmHg^{-1}\ ml)$
R_{1DVO}	8.13 $(mmHg\ ml^{-1}\ s)$
R_{2DVO}	0.67 $(mmHg\ ml^{-1}\ s)$
C_{DVO}	0.51 $(mmHg^{-1}\ ml)$

Table 6.1: Estimated Windkessel parameters, used in the pulsatile simulation.

6.4.2 Computational Method

Initially, zero flow, constant $PO_2 = 90mmHg$ and a reference pressure of 80 mmHg were set as initial conditions for the coupled steady-state solver, implemented in Star-CCM+ v12.02.011-R8, which was used to solve Navier-Stokes and oxygen transport equations (Eq. 3.1 - 3.3 and 3.8), until momentum, oxygen and mass continuity residuals fell below 10^{-9}.

The resulting initial steady-state solution was then set as the initial condition for the coupled implicit unsteady solver, implemented in Star-CCM+ v12.02.011-R8. The first pulse period, from 0 to 0.83 s, was run to allow transient "start-up" phenomena to dissipate.

The subsequent two pulse periods, from 0.83 to 2.49 s, were run and data were exported for analysis and to verify period convergence. A time-step of 4.15×10^{-4} s was used and each time-step was run until all residuals fell below 10^{-9}. Coupling between fluid and wall oxygen transport was satisfied using an explicit scheme, following the strategy outlined in 5.2.3.

A polyhedral unstructured volume mesh was generated, with prismatic bound-

ary layer mesh adjacent to the wall, similar to that used in the optimisation. A total of $\approx 11.3 \times 10^6$ ($\approx 5.2 \times 10^6$ in the fluid and $\approx 6.1 \times 10^6$ in the wall) cells were used to discretise the domain.

Prismatic boundary layers, with same number of elements and first element thickness as that used in the optimisation were constructed, while significantly higher spatial resolution was used to generate the polyhedral meshes of the wall and fluid. Cells having an average size of 1×10^{-4} m were used to mesh the anastomosis, where the flow is expected to be more complex, and expanding progressively to 2×10^{-4} m, were used beyond a distance of 3×10^{-2} m, away from the anastomosis.

6.4.3 Results

6.4.3.1 Flow

Figure 6.13 shows inlet and outlet pressure and flow-rate waveforms from the high-resolution pulsatile simulation. The estimated Windkessel parameters produce boundary conditions that are in line with the pressure and flow conditions, that were required in the Windkessel parameter estimation. Specifically, the maximum and minimum inlet pressure, P_{PAI}, match the physiological range of 80-125 mmHg, and the outflow rates, Q_{DAO} and Q_{DVO}, also follows the measured outflow rates, $Q_{DAO\text{-}R}$ and $Q_{DVO\text{-}R}$.

The simulation was initialised from a steady state solution, as per Section 6.4.2, and advanced 2.49 s in time (3 pulse periods, T=0.83 s). The first period, $t \in [0, 0.83]$ s, was discarded, to allow to the transient phenomena to disappear, and period convergence was assessed on the second and third pulse periods. Figure 6.14 shows the magnitude of the velocity vector extracted at different points, along the arterial and venous centrelines. Visually, it appears that good period independence is attained during the second and third period.

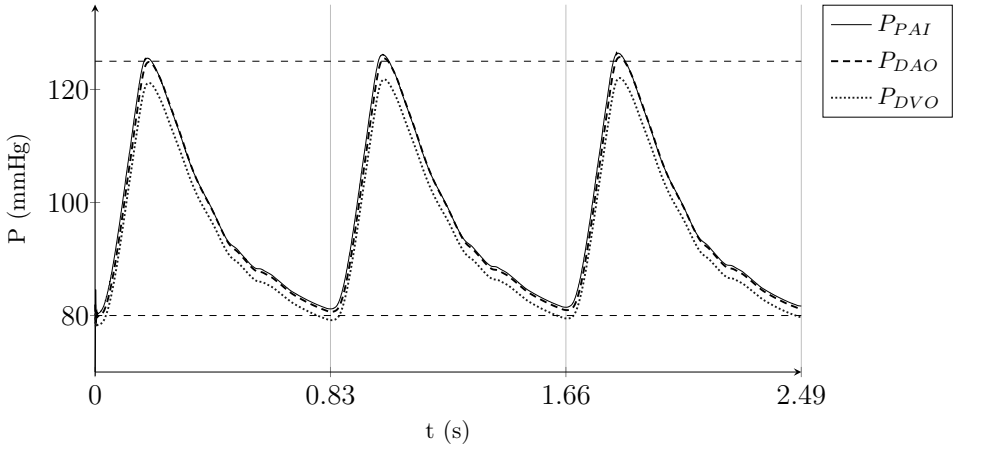

(a)

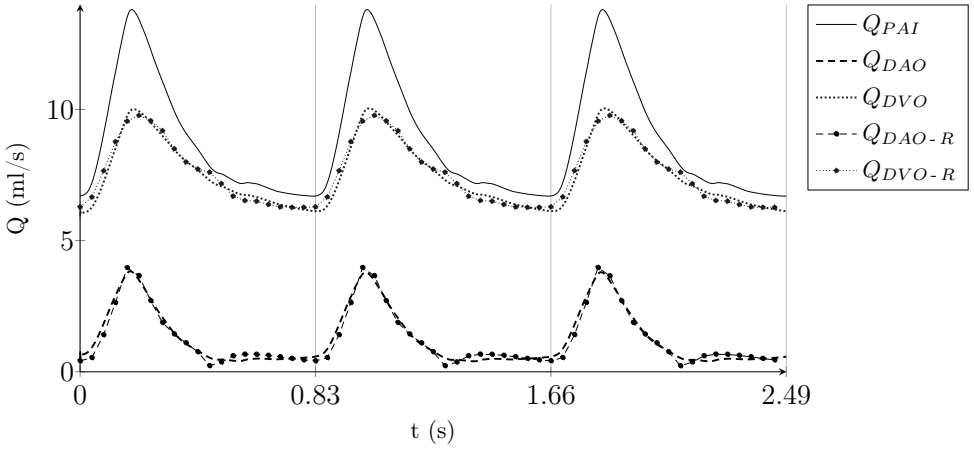

(b)

Figure 6.13: Pressure (a) and flow-rate (b) waveforms from the high-resolution pulsatile simulation. The horizontal dashed lines show the physiological range of 80-125 mmHg, used to estimate Windkessel parameters for the outflow conditions. Q_{PAI} was imposed at PAI, Q_{DAO} and Q_{DVO} are the outflow rates obtained at the DAO and DVO, respectively. $Q_{DAO\text{-}R}$ and $Q_{DVO\text{-}R}$ are the measured outflows from [44].

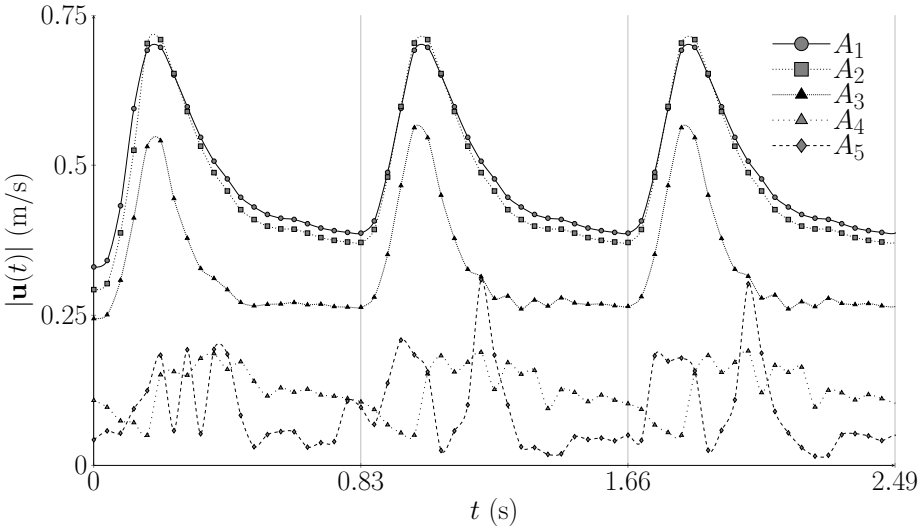

(a)

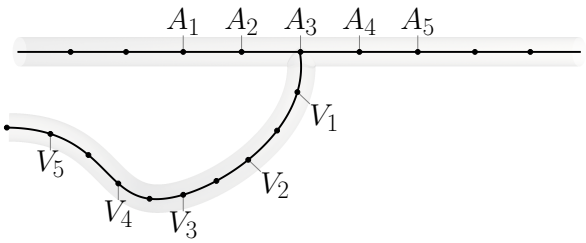

(b)

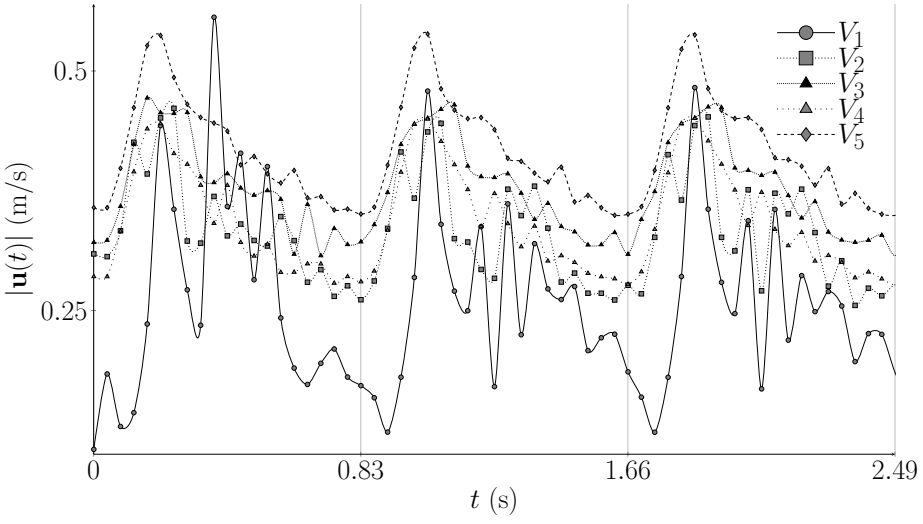

(c)

Figure 6.14: Temporal traces of the velocity vector magnitude extracted at different points, along the arterial (a) and venous (c) centrelines. The location of the extracted velocities are shown in (b). Good period independence is attained during the second and third period.

Despite the lower average Reynolds number at the inlet, compared with previous simulations of Iori and Grechy [15, 110, 111], transitional flow can be observed in the distal artery and the vein, from the temporal traces of the velocity magnitude, shown in Fig. 6.14. In particular, the largest fluctuations appear in the deceleration phase of the diastole, right after the end of the systole.

To measure how these flow instabilities translate into oxygen transport, Snapshot POD and SPI of oxygen concentration and WSS vector were compared at the endothelium. The five most energetic POD temporal modes, $a_1(t), .., a_5(t)$, for WSS and oxygen concentration fields, are shown in Figure 6.15-(a), while Figure 6.15-(b) contains the POD eigenspectra.

Figures 5.3-(c)-(d) shows the SPI for $|\boldsymbol{w}|$ and PO_2, calculated with a harmonic threshold of $n_c\omega_0/(2\pi)$ >10 Hz. This value was chosen based on the prescribed inflow Q_{PAI}, such that the signal reconstructed with harmonics up to n_c, contained 99% of the energy in the driving flow rate.

In line with previous observations made in Section 5.3.2 and by Tada and Tarbell [7], oxygen concentration does not appear to be affected by the flow fluctuations. A large change in the order of magnitude can be observed between the first temporal mode, $a_1(t)$, which essentially contains average spatial and temporal features of the field, and the subsequent ones. This can be also observed as a fast decay of the energy distribution, $E_{1,M} = \sum_{k=1}^{M} \lambda_k$.

Finally, the SPI, calculated on $|\boldsymbol{w}|$ with a cut-off frequency of 10 Hz, confirms the presence of diastolic instabilities - with frequencies of about 20 Hz - in the distal artery and proximal vein section. These finer temporal features are completely filtered in the oxygen concentration field (Figure 6.15-(d)), as only temporal features, having frequencies lower than 10 Hz are retained.

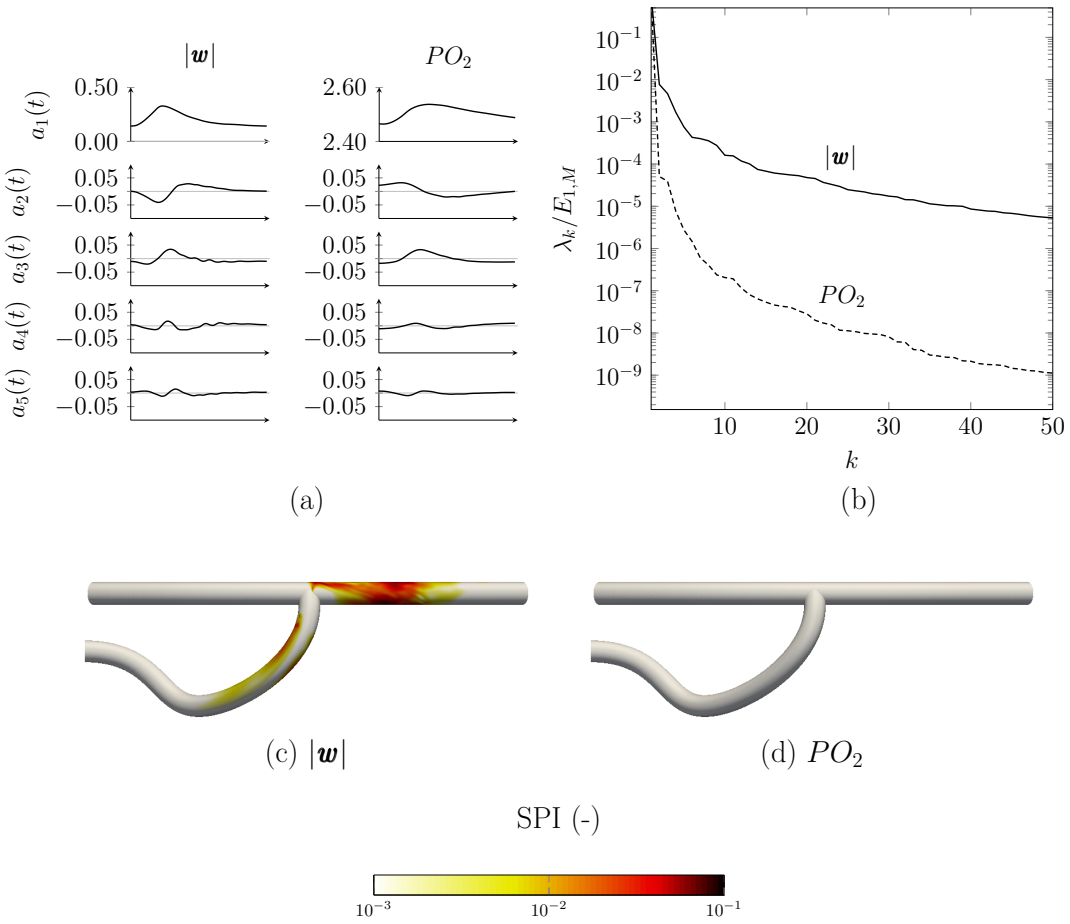

Figure 6.15: (a) the five most energetic POD temporal modes $(a_1(t), .., a_5(t))$, calculated on the endothelium for $|\boldsymbol{w}|$ and oxygen concentration, PO_2. (b) POD energy spectra distribution (λ_k is energy content of the k-th mode, normalized by the total energy content $E_{1,M} = \sum_{k=1}^{M} \lambda_k$). (c)-(d) spatial distributions of the SPI.

6.4.3.2 Pulsatile vs Steady Boundary Conditions

The high-resolution, pulsatile simulation presented in the previous sections, was compared to a lower resolution, steady-state simulation, similar to those used to reduce the optimisation cost, to assess the adequacy of the chosen simplified assumptions. Specifically, average inflow and outflow rates, calculated from the measured proximal and distal flow rates in Figure 6.12, were used to prescribe matching boundary conditions to the Low-Res simulation.

In Figure 6.16, the time-averaged PO_2 field obtained from the pulsatile simulation were compared to the PO_2 field resulting from the simplified, steady model. Figure 6.16 presents orthogonal top-on (a) and end-on (b) views of the two models, colored by the time-averaged PO_2 and iso-surfaces of low oxygen concentration (PO_2 = 20 mmHg). Overall, good visual agreement of between the two models can be observed, for both the distributions of PO_2 and the critical PO_2 iso-surfaces.

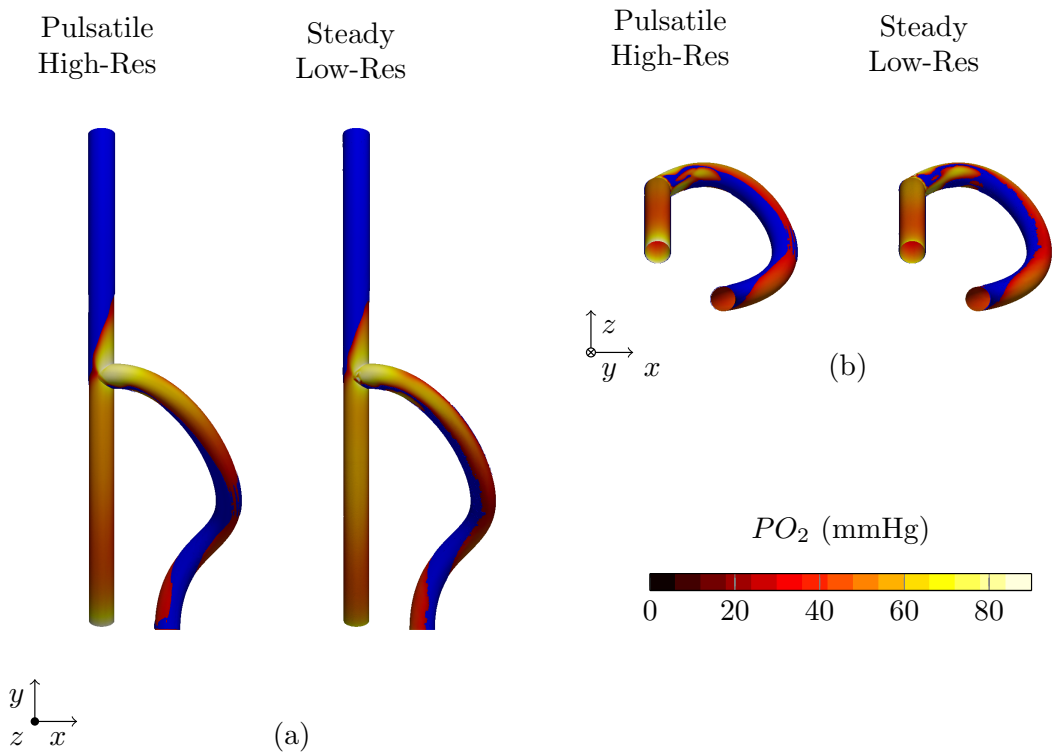

Figure 6.16: Orthogonal top-on (a) and end-on (b) views of the optimal AVF configuration, colored by the time-averaged PO_2 (Pulsatile High-Res), and PO_2 (Steady Low-Res). In blue, iso-surfaces of critical oxygen concentration (PO_2 = 20 mmHg).

In addition, the percentage wall volume of critical oxygen concentration ($PO_2 <$ 10, 20 and 30 mmHg, respectively), is presented in Figure 6.17, for both models. This quantity is essentially the cost function used during the optimisation. Once

again, good agreement is found between the two models, with a deviations from the high-res pulsatile model of less than 5%.

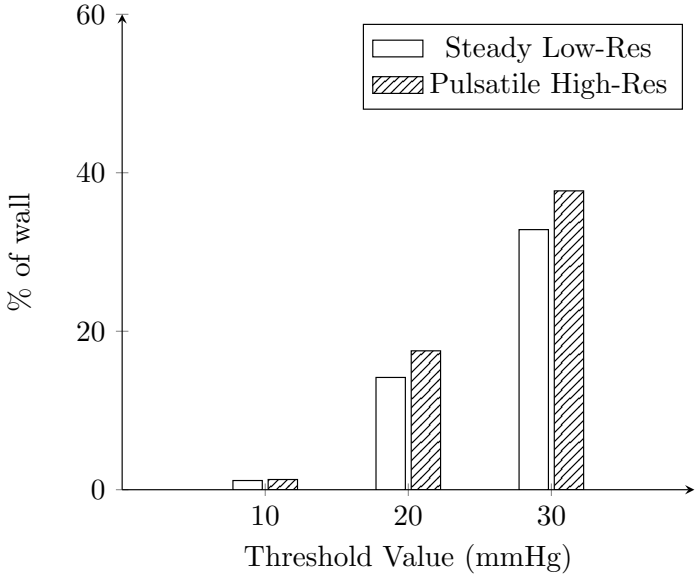

Figure 6.17: Bar chart showing the percentage wall volume of $PO_2 < 10$, 20 and 30 mmHg, for the Steady Low-Res and Pulsatile High-Res models.

6.5 Conclusion

In previous studies, low oxygen transport has been associated with development of IH [12, 3, 17, 18]. In this Chapter, a MADS optimisation framework along with CFD simulations were used to design an idealised AVF configuration that minimises hypoxia [111].

Following findings of Chapter 5, a simplified CFD model of AVF, with steady boundary conditions, was used during the optimisation process. In addition, the effect of mechanical stress and deformation on wall perfusion was ignored. A surrogate model of the cost function was used to further reduce computational cost, by performing less CFD simulations. The optimisation framework was able to determine an optimal geometry, which is able to significantly reduce the wall

volume percentage of critical oxygen concentration, with respect to randomly generated AVF configurations.

The optimal geometry features an out-of-plane anastomosis, connected laterally to one side of the arterial bend, and a non-planar looped vein, resambling a section of helix. In line with previous studies, it is postulated that mixing, and thus oxygen transport, is enhanced by the presence of secondary and swirling flow, induced by the out-of-plane anastomotic angle and the helical-shaped vein [8, 9, 246]. This is also supported by a significant correlation between the cost function Ψ and the spatially averaged LNH.

Previous work by Iori *et al.* and Grechy *et al.* showed that, if one wants to suppress unsteady flows, non-planar anastomosis, formed on the outside of an arterial bend, are preferred [15, 111]. While both the current optimal configuration and the geometry determined by Grechy *et al.* exhibit high non-planarity, substantial difference can be observed in the position of the vein with respect of the artery [111]. In particular, the following observations can be drawn. If one subscribes to the hypothesis that IH is caused by unsteady disturbed flow, AVF should be formed via a vein graft onto the outer curvature of a curved artery. However, if one is interested in maximising oxygen transport, the anastomosis should be formed laterally, on one side of a curved artery. While IH is likely a multifactorial process [2], the recommendations in this work and previous studies by Grechy and Iori [15, 111] are apparently incompatible, which highlights the importance of ascertaining the exact mechanisms underlying development of IH in AVF.

Chapter 7

Conclusions

The research presented in this work investigated oxygen transport in idealised models of AVF, with a focus on the effect of stress and deformation on vasa vasorum perfusion. In Chapter 4, a structural FE model of the AVF surgery was developed. The AVF geometries obtained from FE simulations bears a good resemblance with geometries extracted from patients MRI scan images [44]. Results show that AVF formed from shorter mobilised veins, are prevalent in the AVF sample observed in [44]. This is likely attributable to the fact that the length of vein is arbitrarily chosen by the vascular surgeon, during the intervention, based on the patient's anatomy. In general, long vein sections are not available and it is preferable to mobilise shorter veins, to avoid kinking [1]. The vein, due to its thinner, less stiff wall compared to the artery, undergoes a larger deformation and circumferential stress, when pressurised to a reference arterial pressure of 100 mmHg. Bending the vein, from its normally straight configuration, to connect its end to the hole created in the arterial wall, induces stress concentration at the bend. In addition, stress concentration can also be observed in the artery, at the incision ends. In line with previous study, the inclusion of residual stress in the model have the effect of normalizing the stress in the wall

[201]. Dobrin *et al.* and Bassiouny *et al.* speculate that changes in the normal wall mechanical environment, occurring in various locations of the vein, distal artery, and floor of the anastomosis, may contribute to IH [68, 67]. Other studies argue that increased wall stretch is associated with the upregulation of hypoxia inducible factors [69, 39, 70], which are transcriptor factors released during tissue hypoxia. It is unclear whether the importance of mechanical risk factors, with respect to IH development, is comparable to haemodynamic factors and hypoxia or the correlation with IH is indirectly due to VV suboptimal perfusion and thus hypoxia.

To account for the different microvascular collapse mechanisms, that are postulated in the literature, two different perfusion mechanism were proposed, a stress-based and a stretch-based model. In Chapter 5, the perfusion fields obtained from the mechanical simulations in Chapter 4, were used to prescribe a VV oxygen source in the adventitial layer. This is the first numerical study to include a VV oxygen source into the model. Previous studies either solved oxygen transport only in the vessel lumen or included the wall but assumed constant oxygen concentration in the adventitial layer. In Tarbell's model, oxygen trasport was solved as a passive scalar specie dissolved in blood, with constant diffusivity and a spatially constant oxygen concentration applied at the endothelium. This choice was based on the assumption that oxygen transport is fluid-phase limited, and hypoxia is assumed to occur in areas of the wall, where the total wall oxygen consumption exceeds the wall normal oxygen flux into the endothelium [6]. Conversely, in studies based on Ethier and Moore's work, oxygen transport is solved in the wall but neglected in the adventitia. Instead, a constant oxygen concentration is prescribed at the interface between the media and adventitia, under the assumption of optimal VV perfusion [5]. Both modelling approaches have been shown to produce physiologically relevant results, allowing to predict potential regions of hypoxia when studying healthy vessels. However, several *in-vivo* and

in-vitro studies argue that the perfusion of VV can be negatively affected by adverse wall mechanical conditions [128, 3, 19], which can compromise the optimal advential oxygen supply [127, 17, 18]. This situation has been hypothesised to occur in a number vascular conditions affected by IH [174, 17, 18, 19]. These include intra-vascular stents, arterio-venous fistulae and grafts and coronary artery bypass grafts, all of which have in common an altered biomechanical environment [17, 18]. For these problems, neglecting adventitial oxygen supply could represent an inadequate modelling assumption.

In summary, luminal oxygen supply is affected by a disrupted haemodynamics, while, altered wall-mechanics can prevent adequate VV perfusion [6, 10, 19, 3]. The principal aim of the work was to ascertain what is most important in determining wall-oxygen levels: (i) modified luminal flow field; (ii) mechanically-modified VV perfusion. To assess the effect of varying flow conditions and bulk wall parameters, a parametric study was undertaken. Results suggest that for a given set of wall parameters, the local wall-oxygen levels are governed by the flow field, while mechanically-modified VV perfusion is shown to have negligible effects. Spatial patterns of PO_2 exhibit a significant correlation with WSS, which is used as a proxy of the flow in the boundary layer, in line with Tarbell's observation that oxygen transport is fluid-phase limited. However, overall wall-oxygen levels appear to be sensitive to changes in bulk wall parameters. Specifically, at increased oxygen consumption rates, shutting-off completely VV perfusion results in critically low overall wall oxygen levels. This means that the local variability in the VV perfusion field does not translate significantly into changes of wall oxygenation, which are mostly explained by local WSS patterns. In contrast, overall wall oxygen levels depend on the balance between luminal and VV oxygen supplies, and wall oxygen consumption. Therefore, further experimental work is necessary to determine better estimates of parameters, such as oxygen consumption rate and VV microvascular density and to clarify the role

of the biomechanical forces in the mechanism of microvascular perfusion.

In Chapter 6, results from Chapter 5 were used to develop a simplified oxygen transport model, that is combined with a MADS optimisation framework and Kriging surrogate models to identify an optimal AVF configuration with reduced hypoxia levels. Specifically, in the simplified model spatially constant VV perfusion in the adventitial layer and steady inflow and outflow conditions are assumed. The optimal configuration identified by the optimisation framework features an out-of-plane anastomosis and a helical shaped vein, laterally connected to an arterial bend. Such a geometry is believed to enhance oxygen transport by inducing swirling/secondary flows, in agreement with observations by Caro and Coppola [252, 8, 9]. A high resolution pulsatile simulation within the optimal configuration was undertaken to verify that the optimal configuration behaves broadly as the simplified model, used to reduce the optimisation cost. Good visual and quantitative agreement was found between the high resolution pulsatile and lower resolution steady-state simulations.

7.1 Future Work

In summary, the present study provides new evidence suggesting that although local wall oxygen patterns are primarily governed by the flow field, disrupted VV perfusion and increased wall oxygen consumption can severely affect the overall wall oxygen levels. However, future work is needed to address some of the limitations of this study. In particular, it is necessary to design *in-vivo* and *in-vitro* experiments to quantify the effect of mechanical stretch and/or stress on the microvasculature of medium and large blood vessels. A deeper insight into the mechanics of perfusion will allow to develop an improved model of VV oxygen supply. Subsequently, such an improved model of oxygen transport could be used to undertake patient specific simulations and correlate wall hypoxia with the observed clinical outcome. This would allow to validate/disprove the relationship

between the development IH and hypoxia and quantify its relative importance in relation to other well-established haemodynamic risk factors, such as low and unsteady WSS.

The optimal geometry identified through the optimisation framework presented in Chapter 6, could be used to develop a prototype device to hold an AVF in the optimal configuration, as proposed by the proof-of-concept study by Grechy *et al.* [111]. A device of this type is envisaged to be fabricated from a bio-compatible material such as a bio-compatible silicone or bio-resorbable hydrogel and be slotted/implanted onto the AVF to facilitate the anastomosis formation and hold the newly formed AVF in the proposed optimal configuration [111]. Whether or not such a device can enhance oxygen transport within AVF, reducing the prevalence of IH, still remains unknown. In addition, it is still uncertain whether prescribing such an AVF configuration can produce adverse (low/oscillatory) WSS patterns, which could lead to unfavourable remodelling and unintentionally cause IH. Future work, including benchtop and animal models (porcine/rabbit), is needed to address these questions and clarify whether a device of this type has the potential to be used in clinical practice to improve AVF patency rates.

Bibliography

[1] B. S. Dixon. Why don't fistulas mature? *Kidney international*, 70(8):1413–1422, 2006.

[2] P. Roy-Chaudhury, L. Arend, J. Zhang, M. Krishnamoorthy, Y. Wang, R. Banerjee, A. Samaha, and R. Munda. Neointimal hyperplasia in early arteriovenous fistula failure. *American journal of kidney diseases : the official journal of the National Kidney Foundation*, 50(5):782–790, 2007.

[3] S. G. Barker, a. Talbert, S. Cottam, P. a. Baskerville, and J. F. Martin. Arterial intimal hyperplasia after occlusion of the adventitial vasa vasorum in the pig. *Arteriosclerosis, Thrombosis, and Vascular Biology*, 13(1):70–77, 1993.

[4] E. S. Lee, G. E. Bauer, M. P. Caldwell, S. M. Santilli, and D. Ph. Association of artery wall hypoxia and cellular proliferation at a vascular anastomosis. *J Surg Res*, 91(1):32–37, 2000.

[5] J. A. Moore and C. R. Ethier. Oxygen mass transfer calculations in large arteries. *Journal of biomechanical engineering*, 119(4):469–75, 1997.

[6] J. M. M. Tarbell and Y. Qiu. Arterial wall mass transport: the possible role of blood phase resistance in the localization of arterial disease. *The Biomedical Engineering Handbook, 2nd edn. CRC ...*, 2000.

[7] S. Tada and J. M. Tarbell. Oxygen mass transport in a compliant carotid bifurcation model. *Annals of biomedical engineering*, 34(9):1389–1399, 2006.

[8] G. Coppola and C. Caro. Oxygen mass transfer in a model three-dimensional artery. *Journal of the Royal Society, Interface / the Royal Society*, 5:1067–1075, 2008.

[9] G. Coppola and C. Caro. Arterial geometry, flow pattern, wall shear and mass transport: potential physiological significance. *Journal of the Royal Society, Interface / the Royal Society*, 6(35):519–528, 2009.

[10] S. Tada. Numerical study of oxygen transport in a carotid bifurcation. *Physics in medicine and biology*, 55:3993–4010, 2010.

[11] E. A. Murphy, A. S. Dunne, D. M. Martin, and F. J. Boyle. Oxygen Mass Transport in Stented Coronary Arteries. *Annals of Biomedical Engineering*, 44(2):508–522, 2015.

[12] W. C. Heuper. Arteriosclerosis: the anoxemia theory. *Arch Pathol*, 126(10):642, 1944.

[13] C. Lata, D. Green, J. Wan, S. Roy, and S. M. Santilli. The role of short-term oxygen administration in the prevention of intimal hyperplasia. *Journal of vascular surgery*, 58(2):452–459, 2013.

[14] F. Kuwahara, H. Kai, K. Tokuda, R. Shibata, K. Kusaba, N. Tahara, H. Niiyama, T. Nagata, and T. Imaizumi. Hypoxia-inducible factor-1alpha/vascular endothelial growth factor pathway for adventitial vasa vasorum formation in hypertensive rat aorta. *Hypertension*, 39(1524-4563):46–50, 2002.

[15] F. Iori, L. Grechy, R. W. Corbett, W. Gedroyc, N. Duncan, C. G. Caro, and P. E. Vincent. The effect of in-plane arterial curvature on blood flow and oxygen transport in arterio-venous fistulae. *Physics of Fluids*, 27(3):031903, 2015.

[16] B. Ene-Iordache and A. Remuzzi. Blood Flow in Idealized Vascular Access for Hemodialysis: A Review of Computational Studies. *Cardiovascular Engineering and Technology*, pages 1–18, 2017.

[17] S. M. Santilli, R. B. Stevens, J. G. Anderson, W. D. Payne, and M. D. Caldwell. Transarterial wall oxygen gradients at the dog carotid bifurcation. *American Journal of Physiology - Heart and Circulatory Physiology*, 268(1):H155–H161, 1995.

[18] A. N. Cheema, T. Hong, N. Nili, A. Segev, J. G. Moffat, K. E. Lipson, A. R. Howlett, D. W. Holdsworth, M. J. Cole, B. Qiang, F. Kolodgie, R. Virmani, D. J. Stewart, and B. H. Strauss. Adventitial microvessel formation after coronary stenting and the effects of SU11218, a tyrosine kinase inhibitor. *Journal of the American College of Cardiology*, 47(5):1067–1075, 2006.

[19] E. L. Ritman and A. Lerman. The dynamic vasa vasorum. *Cardiovascular research*, 75(4):649–58, 2007.

[20] A. Grassmann, S. Gioberge, S. Moeller, and G. Brown. ESRD patients in 2004: global overview of patient numbers, treatment modalities and associated trends. *Nephrology, dialysis, transplantation : official publication of the European Dialysis and Transplant Association - European Renal Association*, 20(12):2587–93, 2005.

[21] G. M. Fleming. Renal replacement therapy review: Past, present and future. *Organogenesis*, 7(1):2–12, 2011.

[22] W. J. Kolff, H. T. Berk, M. ter Welle, a. J. van der LEY, E. C. van Dijk, and J. van Noordwijk. The artificial kidney: a dialyser with a great area. 1944. *Journal of the American Society of Nephrology : JASN*, 8(12):1959–1965, 1997.

[23] H. I. Feldman, S. Kobrin, and A. Wasserstein. Hemodialysis vascular access morbidity. *Journal of the American Society of Nephrology : JASN*, 7(4):523–35, 1996.

[24] M. J. Brescia, J. E. Cimino, K. Appell, B. J. Hurwich, and B. H. Scribner. Chronic hemodialysis using venipuncture and a surgically created arteriovenous fistula. *Journal of the American society of nephrology*, 10(1):193–199, 1966.

[25] N. K. Foundation. KDOQI Clinical Practice Guidelines and Clinical Practice Recommendations for 2006 Updates: Hemodialysis Adequacy, Peritoneal Dialysis Adequacy and Vascular Access. *Am J Kidney Dis*, suppl 1(48):S1—-S322, 2006.

[26] T. Lee, M. Mokrzycki, L. Moist, I. Maya, M. Vazquez, and C. E. Lok. Standardized definitions for hemodialysis vascular access. *Seminars in dialysis*, 24(5):515–524, 2011.

[27] K. Konner. The Arteriovenous Fistula. *Journal of the American Society of Nephrology*, 14(6):1669–1680, 2003.

[28] K. Konner. History of vascular access for haemodialysis. *Nephrology, dialysis, transplantation : official publication of the European Dialysis and Transplant Association - European Renal Association*, 20(12):2629–2635, 2005.

[29] A. Besarab. Resolved: fistulas are preferred to grafts as initial vascular access for dialysis. *Journal of the American society of nephrology*, 19(9):1629–1631, 2008.

[30] P. Roy-Chaudhury, V. P. Sukhatme, and A. K. Cheung. Hemodialysis vascular access dysfunction: a cellular and molecular viewpoint. *Journal of the American society of nephrology*, 17(4):1112–1127, 2006.

[31] B. S. Dixon, L. Novak, and J. Fangman. Hemodialysis vascular access survival: upper-arm native arteriovenous fistula. *American journal of kidney diseases*, 39(1):92–101, 2002.

[32] M. Allon and R. M. L. Increasing arteriovenous fistulas in haemodialysis patients: Problems and solutions. *Kidney Int*, 62:1109–1124, 2002.

[33] M. C. Riella and P. Roy-Chaudhury. Vascular access in haemodialysis: strengthening the Achilles' heel. *Nature reviews. Nephrology*, 9(6):348–357, 2013.

[34] S. Pastan, J. M. Soucie, and W. M. McClellan. Vascular access and increased risk of death among hemodialysis patients. *Kidney international*, 62(2):620–626, 2002.

[35] T. C. Rothuizen and C. Y. Wong. Arteriovenous access failure: more than just intimal hyperplasia? *Nephrology Dialysis Transplantation*, 2013.

[36] O. J. Badero, M. O. Salifu, H. Wasse, and J. Work. Frequency of Swing-Segment Stenosis in Referred Dialysis Patients With Angiographically Documented Lesions. *American Journal of Kidney Diseases*, 51(1):93–98, 2008.

[37] K. B. Quencer and M. Arici. Arteriovenous fistulas and their characteristic sites of stenosis. *American Journal of Roentgenology*, 205(4):726–734, 2015.

[38] G. Iaccarino, L. A. Smithwick, R. J. Lefkowitz, and W. J. Koch. Targeting G signaling in arterial vascular smooth muscle proliferation: A novel strategy to limit restenosis. *Proceedings of the National Academy of Sciences*, 96(7):3945–3950, 1999.

[39] H. Song, A. L. Mowbray, M. C. Sykes, and H. Jo. Emerging Role of IGF-1R in Stretch-Induced Neointimal Hyperplasia in Venous Grafts. *Arteriosclerosis, Thrombosis, and Vascular Biology*, 27(8):1679–1681, 2007.

[40] T. H. Spaet, M. L. Tiell, J. Cintron, and J. Won. Selective arterial medial injury fails to produce intimal hyperplasia in experimental animals. *Thrombosis research*, 27:205–210, 1982.

[41] Y. Shi, J. E. O'Brien, A. Fard, J. D. Mannion, D. Wang, and A. Zalewski. Adventitial Myofibroblasts Contribute to Neointimal Formation in Injured Porcine Coronary Arteries. *Circulation*, 94(7):1655–1664, 1996.

[42] Y. Shi, J. E. O'Brien, J. D. Mannion, R. C. Morrison, W. Chung, A. Fard, and A. Zalewski. Remodeling of Autologous Saphenous Vein Grafts : The Role of Perivascular Myofibroblasts. *Circulation*, 95(12):2684–2693, 1997.

[43] A. Brahmbhatt, A. Remuzzi, M. Franzoni, and S. Misra. The molecular mechanisms of hemodialysis vascular access failure. *Kidney International*, 89(2):303–316, 2016.

[44] G. Lorenza. *Computational Studies of Unsteady Flow in Arterio-Venous Fistulae*. PhD thesis, Imperial College London, 2017.

[45] C. G. Caro, T. J. Pedley, and R. C. Schroter. *The Mechanics of the Circulation*. Cambridge University Press, 2011.

[46] D. L. Fry. Acute vascular endothelial changes associated with increased blood velocity gradients. *Circulation research*, 22(2):165–197, 1968.

[47] C. G. Caro, J. M. Fitz-Gerald, and R. C. Schroter. Arterial wall shear and distribution of early atheroma in man. *Nature*, 223:1159–1161, 1969.

[48] C. G. G. Caro, J. M. Fitz-Gerald, and R. C. Schroter. Atheroma and arterial wall shear observation, correlation and proposal of a shear dependent mass transfer mechanism for atherogenesis. *Proceeding of the Royal Society of London*, 177(1046):109–133, 1971.

[49] A. Gnasso, C. Carallo, C. Irace, V. Spagnuolo, G. De Novara, P. L. Mattioli, and A. Pujia. Association between intima-media thickness and wall shear stress in common carotid arteries in healthy male subjects. *Circulation*, 94(12):3257–62, 1996.

[50] M. K. Krishnamoorthy, R. K. Banerjee, Y. Wang, J. Zhang, A. S. Roy, S. F. Khoury, L. J. Arend, S. Rudich, and P. Roy-Chaudhury. Hemodynamic wall shear stress profiles influence the magnitude and pattern of stenosis in a pig AV fistula. *Kidney international*, 74(11):1410–1419, 2008.

[51] E. Rajabi-Jagahrgh, M. K. Krishnamoorthy, Y. Wang, A. Choe, P. Roy-Chaudhury, and R. K. Banerjee. Influence of Temporal Variation in Wall Shear Stress on Intima-Media Thickening in Arteriovenous Fistulae. *Seminars in dialysis*, 26(4):511–519, 2013.

[52] L. Jia, L. Wang, F. Wei, H. Yu, H. Dong, B. Wang, Z. Lu, G. Sun, H. Chen, J. Meng, B. Li, R. Zhang, X. Bi, Z. Wang, H. Pang, and A. Jiang. Effects of wall shear stress in venous neointimal hyperplasia of arteriovenous fistulae. *Nephrology*, 20(5):335–342, 2015.

[53] Y. Yamamoto, O. Kawarada, S. Sakamoto, K. Harada, T. Noguchi, H. Ogawa, and S. Yasuda. Progression of Intimal Hyperplasia and Multiple-Channel Formation After Fogarty Thrombectomy. *JACC: Cardiovascular Interventions*, 8(15), 2015.

[54] S. L. Meyerson, J. Moawad, F. Loth, C. L. Skelly, H. S. Bassiouny, J. F. McKinsey, B. L. Gewertz, and L. B. Schwartz. Effective hemodynamic diameter: an intrinsic property of vein grafts with predictive value for patency. *Journal of vascular surgery*, 31(5):910–7, 2000.

[55] E. J. Mattsson, T. R. Kohler, S. M. Vergel, and A. W. Clowes. Increased blood flow induces regression of intimal hyperplasia. *Arteriosclerosis, thrombosis, and vascular biology*, 17(10):2245–9, 1997.

[56] D. N. Ku, D. P. Giddens, C. K. Zarins, and S. Glagov. Pulsatile flow and atherosclerosis in the human carotid bifurcation. Positive correlation between plaque location and low

oscillating shear stress. *Arteriosclerosis, Thrombosis, and Vascular Biology*, 5(3):293–302, 1985.

[57] Y. Mohamied, S. J. Sherwin, and P. D. Weinberg. Understanding the fluid mechanics behind transverse wall shear stress. *Journal of biomechanics*, 50:102–109, 2017.

[58] N. DePaola, M. a. Gimbrone, P. F. Davies, and C. F. Dewey. Vascular endothelium responds to fluid shear stress gradients [published erratum appears in Arterioscler Thromb 1993 Mar;13(3):465]. *Arteriosclerosis, Thrombosis, and Vascular Biology*, 12(11):1254–1257, 1992.

[59] J. M. Dolan, J. Kolega, and H. Meng. High wall shear stress and spatial gradients in vascular pathology: a review. *Annals of biomedical engineering*, 41(7):1411–1427, 2013.

[60] M. Lei, J. P. Archie, and C. Kleinstreuer. Computational design of a bypass graft that minimizes wall shear stress gradients in the region of the distal anastomosis. *Journal of vascular surgery*, 25(4):637–646, 1997.

[61] M. F. Fillinger, E. R. Reinitz, R. a. Schwartz, D. E. Resetarits, a. M. Paskanik, D. Bruch, and C. E. Bredenberg. Graft geometry and venous intimal-medial hyperplasia in arteriovenous loop grafts. *Journal of vascular surgery*, 11(4):556–566, 1990.

[62] T. N. Huynh, B. K. Chacko, X. Teng, B. C. Brott, M. Allon, S. S. Kelpke, J. A. Thompson, R. P. Patel, and A. S. Anayiotos. Effects of venous needle turbulence during ex vivo hemodialysis on endothelial morphology and nitric oxide formation. *Journal of Biomechanics*, 40(10):2158–2166, 2007.

[63] F. Loth, S. a. Jones, C. K. Zarins, D. P. Giddens, R. F. Nassar, S. Glagov, and H. S. Bassiouny. Relative Contribution of Wall Shear Stress and Injury in Experimental Intimal Thickening at PTFE End-to-Side Arterial Anastomoses. *Journal of Biomechanical Engineering*, 124(1):44, 2002.

[64] M. Bozzetto, B. Ene-Iordache, and A. Remuzzi. Transitional Flow in the Venous Side of Patient-Specific Arteriovenous Fistulae for Hemodialysis. *Annals of Biomedical Engineering*, 44(8):2388–2401, 2016.

[65] V. Peiffer, S. J. Sherwin, and P. D. Weinberg. Does low and oscillatory wall shear stress correlate spatially with early atherosclerosis? A systematic review. *Cardiovascular research*, 99(2):242–250, 2013.

[66] E. S. Lee, M. P. Caldwell, A. S. Tretinyak, and S. M. Santilli. Supplemental oxygen controls cellular proliferation and anastomotic intimal hyperplasia at a vascular graft-to-artery anastomosis in the rabbit. *Journal of vascular surgery*, 33(3):608–13, 2001.

[67] H. S. Bassiouny, S. White, S. Glagov, E. Choi, D. P. Giddens, and C. K. Zarins. Anastomotic intimal hyperplasia: mechanical injury or flow induced. *Journal of vascular surgery*, 15(4):708–16; discussion 716–7, 1992.

[68] P. B. Dobrin. Mechanical Factors Associated With the Development of Intimal and Medial Thickening in Vein Grafts Subjected to Arterial Pressure : A Model of Arteries Exposed to Hypertension. *Hypertension*, 26(1):38–43, 1995.

[69] H. Chang, K. G. Shyu, B. W. Wang, and P. Kuan. Regulation of hypoxia-inducible factor-1alpha by cyclical mechanical stretch in rat vascular smooth muscle cells. *Clin Sci (Lond)*, 105(4):447–456, 2003.

[70] C. S. Lim, X. Qiao, O. M. Reslan, Y. Xia, J. D. Raffetto, E. Paleolog, A. H. Davies, and R. A. Khalil. Prolonged mechanical stretch is associated with upregulation of hypoxia-inducible factors and reduced contraction in rat inferior vena cava. *Journal of Vascular Surgery*, 53(3):764–773, 2011.

[71] C. Wang, B. M. Baker, C. S. Chen, and M. A. Schwartz. Endothelial cell sensing of flow direction. *Arteriosclerosis, Thrombosis, and Vascular Biology*, 33(9):2130–2136, 2013.

[72] H. A. Himburg, D. M. Grzybowski, A. L. Hazel, J. A. LaMack, X. M. Li, and M. H. Friedman. Spatial comparison between wall shear stress measures and porcine arterial endothelial permeability. *Am J Physiol Heart Circ Physiol*, 286(5):H1916–22, 2004.

[73] C. M. Potter, M. H. Lundberg, L. S. Harrington, C. M. Warboys, T. D. Warner, R. E. Berson, A. V. Moshkov, J. Gorelik, P. D. Weinberg, and J. A. Mitchell. Role of shear stress in endothelial cell morphology and expression of cyclooxygenase isoforms. *Arteriosclerosis, Thrombosis, and Vascular Biology*, 31(2):384–391, 2011.

[74] V. Peiffer, S. J. Sherwin, and P. D. Weinberg. Computation in the rabbit aorta of a new metric - the transverse wall shear stress - to quantify the multidirectional character of disturbed blood flow. *Journal of Biomechanics*, 46(15):2651–2658, 2013.

[75] P. W. Longest and C. Kleinstreuer. Computational haemodynamics analysis and comparison study of arterio-venous grafts. *Journal of medical engineering & technology*, 24(3):102–10, 2000.

[76] M. Ojha. Wall shear stress temporal gradient and anastomotic intimal hyperplasia. *Circulation research*, 74(6):1227–31, 1994.

[77] P. F. Davies, A. Remuzzi, E. J. Gordon, C. F. Dewey, and M. A. Gimbrone. Turbulent fluid shear stress induces vascular endothelial cell turnover in vitro. *Proceedings of the National Academy of Sciences of the United States of America*, 83(7):2114–7, 1986.

[78] H. A. Himburg and M. H. Friedman. Correspondence of low mean shear and high harmonic content in the porcine iliac arteries. *Journal of biomechanical engineering*, 128(6):852–856, 2006.

[79] M. O. Khan, C. Chnafa, D. Gallo, F. Molinari, U. Morbiducci, D. A. Steinman, and K. Valen-Sendstad. On the quantification and visualization of transient periodic instabilities in pulsatile flows. *Journal of Biomechanics*, 52:179–182, 2017.

[80] B. D. Gelfand, F. H. Epstein, and B. R. Blackman. Spatial and spectral heterogeneity of time-varying shear stress profiles in the carotid bifurcation by phase-contrast MRI. *Journal of Magnetic Resonance Imaging*, 24(6):1386–1392, 2006.

[81] K. Valen-Sendstad and D. A. Steinman. Mind the gap: impact of computational fluid dynamics solution strategy on prediction of intracranial aneurysm hemodynamics and rupture status indicators. *AJNR. American journal of neuroradiology*, 35(3):536–43, 2014.

[82] Y. Ventikos. Resolving the Issue of Resolution. *American Journal of Neuroradiology*, 35(3), 2014.

[83] D. N. Ku and G. W. Woodruff. Blood flow in arteries. *Annu. Rev. Fluid Mech*, 29(1):399–434, 1997.

[84] K. Avila, D. Moxey, A. de Lozar, M. Avila, D. Barkley, and B. Hof. The Onset of Turbulence in Pipe Flow. *Science*, 333(6039), 2011.

[85] K. Valen-Sendstad, K.-A. Mardal, and D. A. Steinman. High-resolution CFD detects high-frequency velocity fluctuations in bifurcation, but not sidewall, aneurysms. *Journal of biomechanics*, 46(2):402–407, 2013.

[86] B. Ene-Iordache and A. Remuzzi. Disturbed flow in radial-cephalic arteriovenous fistulae for haemodialysis: low and oscillating shear stress locates the sites of stenosis. *Nephrology, dialysis, transplantation : official publication of the European Dialysis and Transplant Association - European Renal Association*, 27(1):358–368, 2012.

[87] B. Ene-Iordache, L. Cattaneo, G. Dubini, and A. Remuzzi. Effect of anastomosis angle on the localization of disturbed flow in 'side-to-end' fistulae for haemodialysis access. *Nephrology, dialysis, transplantation : official publication of the European Dialysis and Transplant Association - European Renal Association*, 28(4):997–1005, 2013.

[88] S. J. Sherwin and O. Shah. The influence of out-of-plane geometry on the flow within a distal end-to-side anastomosis. *Journal of . . .*, 122(February 2000), 2000.

[89] Y. Papaharilaou, D. J. Doorly, S. J. Sherwin, J. Peiro, C. Griffith, N. Cheshire, V. Zervas, J. Anderson, B. Sanghera, N. Watkins, and C. G. Caro. Combined MR imaging and numerical simulation of flow in realistic arterial bypass graft models. *Biorheology*, 39(3-4):525–531, 2002.

[90] L. D. Browne, P. Griffin, K. Bashar, S. R. Walsh, E. G. Kavanagh, and M. T. Walsh. In Vivo Validation of the In Silico Predicted Pressure Drop Across an Arteriovenous Fistula. *Annals of Biomedical Engineering*, 43(6):1275–1286, 2015.

[91] S. J. Sherwin and D. J. Doorly. Flow dynamics within model distal arterial bypass grafts. *Advances in Fluid Mechanics*, pages 1–44, 2003.

[92] M. Sigovan, V. Rayz, W. Gasper, H. F. Alley, C. D. Owens, and D. Saloner. Vascular Remodeling in Autogenous Arterio-Venous Fistulas by MRI and CFD. *Annals of Biomedical Engineering*, 41(4):657–668, 2012.

[93] Z. Kharboutly, J. M. Treutenaere, I. Claude, and C. Legallais. Arterio-venous fistula: two cases realistic numerical blood flow simulations. *Conference proceedings : ... Annual International Conference of the IEEE Engineering in Medicine and Biology Society. IEEE Engineering in Medicine and Biology Society. Conference*, 2007:2980–2983, 2007.

[94] Z. Kharboutly, V. Deplano, E. Bertrand, and C. Legallais. Numerical and experimental study of blood flow through a patient-specific arteriovenous fistula used for hemodialysis. *Medical engineering & physics*, 32(2):111–118, 2010.

[95] P. M. McGah, D. F. Leotta, K. W. Beach, R. Eugene Zierler, and A. Aliseda. Incomplete restoration of homeostatic shear stress within arteriovenous fistulae. *Journal of biomechanical engineering*, 135(1):11005, 2013.

[96] P. M. McGah, D. F. Leotta, K. W. Beach, and A. Aliseda. Effects of wall distensibility in hemodynamic simulations of an arteriovenous fistula. *Biomechanics and modeling in mechanobiology*, 13(3):679–695, 2014.

[97] P. E. Vincent, A. M. Plata, A. A. E. Hunt, P. D. Weinberg, and S. J. Sherwin. Blood flow in the rabbit aortic arch and descending thoracic aorta. *Journal of the Royal Society, Interface / the Royal Society*, 8(65):1708–19, 2011.

[98] D. A. Vorp, D. H. Wang, M. W. Webster, and W. J. Federspiel. Effect of intraluminal thrombus thickness and bulge diameter on the oxygen diffusion in abdominal aortic aneurysm. *Journal of biomechanical engineering*, 120:579–583, 1998.

[99] R. B. Richardson. Age-dependent changes in oxygen tension, radiation dose and sensitivity within normal and diseased coronary arteries-Part C: oxygen effect and its implications on high- and low-LET dose. *International journal of radiation biology*, 84(10):858–865, 2008.

[100] T. Zheng, J. Wen, W. Jiang, X. Deng, and Y. Fan. Numerical investigation of oxygen mass transfer in a helical-type artery bypass graft. *Computer methods in biomechanics and biomedical engineering*, pages 37–41, 2012.

[101] K. Perktold, A. Leuprecht, M. Prosi, T. Berk, M. Czerny, W. Trubel, and H. Schima. Fluid dynamics, wall mechanics, and oxygen transfer in peripheral bypass anastomoses. *Annals of Biomedical Engineering*, 30(4):447–460, 2002.

[102] C. S. Roy. The Elastic Properties of the Arterial Wall. *The Journal of physiology*, 3(2):125–59, 1881.

[103] H. Gu, A. Chua, B. K. Tan, and K. Chew Hung. Nonlinear finite element simulation to elucidate the efficacy of slit arteriotomy for end-to-side arterial anastomosis in microsurgery. *Journal of Biomechanics*, 39(3):435–443, 2006.

[104] M. R. Roach and A. C. Burton. The reason for the shape of the distensibility curves of arteries. *Canadian journal of biochemistry and physiology*, 35(8):681–90, 1957.

[105] F. Cacho, M. Doblaré, and G. a. Holzapfel. A procedure to simulate coronary artery bypass graft surgery. *Medical & biological engineering & computing*, 45(9):819–827, 2007.

[106] T. C. Gasser, R. W. Ogden, and G. a. Holzapfel. Hyperelastic modelling of arterial layers with distributed collagen fibre orientations. *Journal of the Royal Society, Interface / the Royal Society*, 3(6):15–35, 2006.

[107] M. N. Ngoepe, B. D. Reddy, D. Kahn, C. Meyer, P. Zilla, and T. Franz. A Numerical Tool for the Coupled Mechanical Assessment of Anastomoses of PTFE Arterio-venous Access Grafts. *Cardiovascular Engineering and Technology*, 2(3):160–172, 2011.

[108] I. Decorato, Z. Kharboutly, T. Vassallo, J. Penrose, C. Legallais, and A. V. Salsac. Numerical simulation of the fluid structure interactions in a compliant patient-specific arteriovenous fistula. *International Journal for Numerical Methods in Biomedical Engineering*, 30(2):143–159, 2014.

[109] D. E. Brooks, J. W. Goodwin, and G. V. Seaman. Interactions among erythrocytes under shear. *Journal of applied physiology (Bethesda, Md. : 1985)*, 28(2):172–177, 1970.

[110] L. Grechy, F. Iori, R. W. Corbett, W. Gedroyc, N. Duncan, C. G. Caro, and P. E. Vincent. The Effect of Arterial Curvature on Blood Flow in Arterio-Venous Fistulae: Realistic Geometries and Pulsatile Flow. *Cardiovascular Engineering and Technology*, pages 1–17, 2017.

[111] L. Grechy, F. Iori, R. W. Corbett, S. Shurey, W. Gedroyc, N. Duncan, C. G. Caro, and P. E. Vincent. Suppressing unsteady flow in arterio-venous fistulae. *Physics of Fluids*, 29(10):101901, oct 2017.

[112] H. Schmid-Schönbein and E. Volger. Red cell aggregation and deformability in diabetes. *Diabetes*, 25(2 SUPPL):897–902, 1976.

[113] G. Schneiderman, L. F. Mockros, and T. K. Goldstick. Effect of pulsatility on oxygen transport to the human arterial wall. *Journal of biomechanics*, 15(11):849–58, 1982.

[114] M. K. Kolandavel, E. T. Fruend, S. Ringgaard, and P. G. Walker. The effects of time varying curvature on species transport in coronary arteries. *Annals of Biomedical Engineering*, 34(12):1820–1832, 2006.

[115] A. V. Hill. The Combinations of Haemoglobin with Oxygen and with Carbon Monoxide. I. *Biochemical Journal*, 7(5):471–480, 1913.

[116] S. Kenjereš and A. de Loor. Modelling and simulation of low-density lipoprotein transport through multi-layered wall of an anatomically realistic carotid artery bifurcation. *Journal of the Royal Society, Interface*, 11(91):20130941, 2014.

[117] D. Goldman. Theoretical models of microvascular oxygen transport to tissue. *Microcirculation (New York, N.Y. : 1994)*, 15(8):795–811, 2008.

[118] D. G. Buerk and T. K. Goldstick. Arterial wall oxygen consumption rate varies spatially. *The American journal of physiology*, 243(6):H948–58, 1982.

[119] B. A. Shapiro. Temperature correction of blood gas values. *Respiratory care clinics of North America*, 1(1):69–76, 1995.

[120] Y.-C. Chu, C.-Z. Chen, C.-H. Lee, C.-W. Chen, H.-Y. Chang, and T.-R. Hsiue. Prediction of arterial blood gas values from venous blood gas values in patients with acute respiratory failure receiving mechanical ventilation. *Journal of the Formosan Medical Association = Taiwan yi zhi*, 102(8):539–43, 2003.

[121] Y. Qiu and J. M. Tarbell. Numerical simulation of oxygen mass transfer in a compliant curved tube model of a coronary artery. *Annals of biomedical engineering*, 28(1):26–38, 2000.

[122] D. K. Stangeby and C. R. Ethier. Computational Analysis of Coupled Blood-Wall Arterial LDL Transport. *Journal of Biomechanical Engineering*, 124(1):1, 2002.

[123] R. N. Pittman. Regulation of Tissue Oxygenation. *Colloquium Series on Integrated Systems Physiology: From Molecule to Function*, 3(3):1–100, 2011.

[124] C. Hamilton, B. Steinlechner, E. Gruber, P. Simon, and G. Wollenek. The oxygen dissociation curve: quantifying the shift. *Perfusion*, 19(3):141–144, 2004.

[125] A. Dasu, I. Toma-Dasu, and M. Karlsson. Theoretical simulation of tumour oxygenation and results from acute and chronic hypoxia. *Phys. Med. Biol*, 48:2829–2842, 2003.

[126] M. Piola, F. Prandi, G. B. Fiore, M. Agrifoglio, G. Polvani, M. Pesce, and M. Soncini. Human Saphenous Vein Response to Trans-wall Oxygen Gradients in a Novel Ex Vivo Conditioning Platform. *Annals of Biomedical Engineering*, 44(5):1449–1461, 2016.

[127] M. Järvilehto and P. Tuohimaa. Vasa vasorum hypoxia: initiation of atherosclerosis. *Medical hypotheses*, 73(1):40–1, 2009.

[128] J. K. McGeachie, S. Meagher, and F. J. Prendergast. Vein-to-artery grafts: the long-term development of neo-intimal hyperplasia and its relationship to vasa vasorum and sympathetic innervation. *The Australian and New Zealand journal of surgery*, 59:59–65, 1989.

[129] A. Krogh. The number and distribution of capillaries in muscles with calculations of the oxygen pressure head necessary for supplying the tissue. *The Journal of physiology*, 52(6):409–15, 1919.

[130] A. S. Popel. Theory of oxygen transport to tissue. *Critical reviews in biomedical engineering*, 17(3):257–321, 1989.

[131] R. H. Thomlinson and L. H. Gray. The Histological Structure of Some Human Lung Cancers and the Possible Implications for Radiotherapy. *British journal of cancer*, 9(4):539–549, 1955.

[132] I. F. Tannock. Oxygen diffusion and the distribution of cellular radiosensitivity in tumours. *The British Journal of Radiology*, 45(535):515–524, 1972.

[133] T. W. Secomb, R. Hsu, E. Y. H. Park, and M. W. Dewhirst. Green ' s Function Methods for Analysis of Oxygen Delivery to Tissue by Microvascular Networks. *Annals of biomedical engineering*, 32(11):1519–1529, 2004.

[134] A. C. Skeldon, G. Chaffey, D. J. B. Lloyd, V. Mohan, D. A. Bradley, and A. Nisbet. Modelling and detecting tumour oxygenation levels. *PLoS ONE*, 7(6):1–17, 2012.

[135] C. J. Kelly and M. Brady. A model to simulate tumour oxygenation and dynamic [18F]-Fmiso PET data. *Physics in medicine and biology*, 51(22):5859–73, 2006.

[136] I. Toma-Dasu and A. Dasu. Modelling tumour oxygenation, reoxygenation and implications on treatment outcome. *Computational and Mathematical Methods in Medicine*, 2013, 2013.

[137] L. Hill and M. Flack. The influence of oxygen inhalations on muscular work. *The Journal of Physiology*, 40(5):347–372, 1910.

[138] L. T. Baxter and R. K. Jain. Transport of fluid and macromolecules in tumors. III. Role of binding and metabolism. *Microvascular research*, 41(1):5–23, 1991.

[139] O. Galili, J. Herrmann, J. Woodrum, K. J. Sattler, L. O. Lerman, and A. Lerman. Adventitial vasa vasorum heterogeneity among different vascular beds. *Journal of Vascular Surgery*, 40(3):529–535, 2004.

[140] M. Herbst, T. J. Hölzenbein, and B. Minnich. Characterization of the Vasa Vasorum in the Human Great Saphenous Vein: A Scanning Electron Microscopy and 3D-Morphometry Study Using Vascular Corrosion Casts. *Microscopy and Microanalysis*, 20:1120–1133, 2014.

[141] N. Lai, H. Zhou, G. M. Saidel, M. Wolf, K. McCully, L. B. Gladden, and M. E. Cabrera. Modeling oxygenation in venous blood and skeletal muscle in response to exercise using near-infrared spectroscopy. *Journal of applied physiology (Bethesda, Md. : 1985)*, 106(6):1858–74, 2009.

[142] G. Schneiderman and T. K. Goldstick. Significance of luminal plasma layer resistance in arterial wall oxygen supply. *Atherosclerosis*, 31:11–20, 1978.

[143] G. A. Holzapfel, G. Sommer, C. T. Gasser, and P. Regitnig. Determination of layer-specific mechanical properties of human coronary arteries with nonatherosclerotic intimal

thickening and related constitutive modeling. *American journal of physiology. Heart and circulatory physiology*, 289(5):H2048–58, 2005.

[144] A. G. Tsai, P. C. Johnson, and M. Intaglietta. Oxygen Gradients in the Microcirculation. *Physiological Reviews*, 83(3):933–963, 2003.

[145] M. Dreifaldt, D. S. R. Souza, A. Loesch, J. R. Muddle, M. G. Karlsson, D. Filbey, L. Bodin, L. Norgren, and M. R. Dashwood. The "no-touch" harvesting technique for vein grafts in coronary artery bypass surgery preserves an intact vasa vasorum. *Journal of Thoracic and Cardiovascular Surgery*, 141(1):145–150, 2011.

[146] D. A. Beard. Computational framework for generating transport models from databases of microvascular anatomy. *Annals of Biomedical Engineering*, 29(10):837–843, 2001.

[147] L. H. Back, J. R. Radbill, and D. W. Crawford. Analysis of oxygen transport from pulsatile viscous blood flow to diseased coronary arteries of man. *Journal of biomechanics*, 10(11/12):763–74, 1977.

[148] P. J. Roache. Quantification of Uncertainty in Computational Fluid Dynamics. *Annual Review of Fluid Mechanics*, 29(1):123–160, 1997.

[149] J. C. Arciero, B. E. Carlson, and T. W. Secomb. Theoretical model of metabolic blood flow regulation: roles of ATP release by red blood cells and conducted responses. *AJP: Heart and Circulatory Physiology*, 295(4):H1562–H1571, jul 2008.

[150] B. C. Fry, T. K. Roy, and T. W. Secomb. Capillary recruitment in a theoretical model for blood flow regulation in heterogeneous microvessel networks. *Physiological reports*, 1(3):e00050, aug 2013.

[151] W. M. Bayliss. On the local reactions of the arterial wall to changes of internal pressure. *The Journal of physiology*, 28(3):220–31, may 1902.

[152] M. J. Davis, M. A. Hill, and L. Kuo. Local Regulation of Microvascular Perfusion. In *Comprehensive Physiology*. John Wiley & Sons, Inc., Hoboken, NJ, USA, jan 2011.

[153] L. Kuo, M. J. Davis, and W. M. Chilian. Longitudinal gradients for endothelium-dependent and -independent vascular responses in the coronary microcirculation. *Circulation*, 92(3):518–525, aug 1995.

[154] D. E. Gregg and D. C. Sabiston. Effect of cardiac contraction on coronary blood flow. *Circulation*, 15(1):14–20, jan 1957.

[155] J. M. Downey and E. S. Kirk. Inhibition of coronary blood flow by a vascular waterfall mechanism. *Circulation research*, 36(6):753–60, jun 1975.

[156] J. A. Spaan, N. P. Breuls, and J. D. Laird. Diastolic-systolic coronary flow differences are caused by intramyocardial pump action in the anesthetized dog. *Circulation research*, 49(3):584–93, sep 1981.

[157] P. Bruinsma, T. Arts, J. Dankelman, and J. a. Spaan. Model of the coronary circulation based on pressure dependence of coronary resistance and compliance. *Basic research in cardiology*, 83(5):510–524, 1988.

[158] R. Krams, P. Sipkema, and N. Westerhof. Varying elastance concept may explain coronary systolic flow impediment. *The American journal of physiology*, 257(5 Pt 2):H1471–9, nov 1989.

[159] R. S. Reneman, D. W. Slaaf, L. Lindbom, G. J. Tangelder, and K. E. Arfors. Muscle blood flow disturbances produced by simultaneously elevated venous and total muscle tissue pressure. *Microvascular research*, 20(3):307–18, nov 1980.

[160] B. Vollmar, S. Westermann, and M. D. Menger. Microvascular response to compartment syndrome-like external pressure elevation: an in vivo fluorescence microscopic study in the hamster striated muscle. *The Journal of trauma*, 46(1):91–6, jan 1999.

[161] T. Stylianopoulos, J. D. Martin, M. Snuderl, F. Mpekris, S. R. Jain, and R. K. Jain. Coevolution of solid stress and interstitial fluid pressure in tumors during progression: Implications for vascular collapse. *Cancer Research*, 73(13):3833–3841, 2013.

[162] T. Roose, P. A. Netti, L. L. Munn, Y. Boucher, and R. K. Jain. Solid stress generated by spheroid growth estimated using a linear poroelasticity model. *Microvascular research*, 66(3):204–12, nov 2003.

[163] T. P. Padera, B. R. Stoll, J. B. Tooredman, D. Capen, E. di Tomaso, and R. K. Jain. Pathology: Cancer cells compress intratumour vessels. *Nature*, 427(6976):695–695, feb 2004.

[164] M. Gössl, M. Rosol, N. M. Malyar, L. a. Fitzpatrick, P. E. Beighley, M. Zamir, and E. L. Ritman. Functional anatomy and hemodynamic characteristics of vasa vasorum in the walls of porcine coronary arteries. *The anatomical record. Part A, Discoveries in molecular, cellular, and evolutionary biology*, 272(January):526–537, 2003.

[165] H. Nakajima, N. Imanishi, S. Aiso, and T. Fujino. Venous drainage of the radial forearm and anterior tibia1 reverse flow flaps: anatomical and radiographic perfusion studies.

British Journal of Plastic Surgery The British Association of Plastic Surgeons, 50:389–401, 1997.

[166] M. J. Mulligan-Kehoe. The vasa vasorum in diseased and nondiseased arteries. *AJP: Heart and Circulatory Physiology*, 298(2):H295–H305, feb 2010.

[167] R. S. Scotland, P. J. T. Vallance, and A. Ahluwalia. Endogenous factors involved in regulation of tone of arterial vasa vasorum: implications for conduit vessel physiology. *Cardiovascular Research*, 46:403–411, 2000.

[168] A. Lametschwandtner, B. Minnich, D. Kachlik, M. Setina, and J. Stingl. Three-dimensional arrangement of the vasa vasorum in explanted segments of the aged human great saphenous vein: scanning electron microscopy and three-dimensional morphometry of vascular corrosion casts. *The anatomical record. Part A, Discoveries in molecular, cellular, and evolutionary biology*, 281(2):1372–82, dec 2004.

[169] J. Williams and D. D. Heistad. Structure and function of vasa vasorum. *Trends in Cardiovascular Medicine*, 6(2):53–57, 1996.

[170] D. P. Tsikaras, K. Natsis, P. Hytiroglou, L. Lazos, and P. Gigis. Microanatomy of the vasa vasorum of the human thoracic aorta: a study utilizing a polyester resin casting technique. *Morphologie : bulletin de l'Association des anatomistes*, 81(252):21–2, mar 1997.

[171] S. L. Waters, J. Alastruey, D. A. Beard, P. H. Bovendeerd, P. F. Davies, G. Jayaraman, O. E. Jensen, J. Lee, K. H. Parker, A. S. Popel, T. W. Secomb, M. Siebes, S. J. Sherwin, R. J. Shipley, N. P. Smith, and F. N. van de Vosse. Theoretical models for coronary vascular biomechanics: Progress & challenges, 2011.

[172] S. J. Chapman, R. J. Shipley, and R. Jawad. Multiscale modeling of fluid transport in tumors. *Bulletin of Mathematical Biology*, 70(8):2334–2357, nov 2008.

[173] R. J. Shipley and S. J. Chapman. Multiscale Modelling of Fluid and Drug Transport inÂăVascular Tumours. *Bulletin of Mathematical Biology*, 72(6):1464–1491, aug 2010.

[174] H. M. Atta. Varicose veins: role of mechanotransduction of venous hypertension. *International journal of vascular medicine*, 2012:538627, jan 2012.

[175] Y. Ben-Gal, D. P. Taggart, M. R. Williams, E. Orion, G. Uretzky, R. Shofti, S. Banai, L. Yosef, and G. Bolotin. Expandable external support device to improve Saphenous Vein Graft Patency after CABG. *Journal of cardiothoracic surgery*, 8(1):122, jan 2013.

[176] R. W. Gore and H. G. Bohlen. Microvascular pressures in rat intestinal muscle and mucosal villi. *The American journal of physiology*, 233(6):H685–93, dec 1977.

[177] H. G. Bohlen, R. W. Gore, and P. M. Hutchins. Comparison of microvascular pressures in normal and spontaneously hypertensive rats. *Microvascular Research*, 13(1):125–130, jan 1977.

[178] R. W. Gore and H. G. Bohlen. Microvascular pressures in rat intestinal muscle and mucosal villi. *The American journal of physiology*, 233(6):H685–93, dec 1977.

[179] M. J. Davis, W. L. Joyner, and J. P. Gilmore. Microvascular pressure distribution and responses of pulmonary allografts and cheek pouch arterioles in the hamster to oxygen. *Circulation research*, 49(1):125–32, jul 1981.

[180] K. Cao. *Mechanical analysis of lung CT images using nonrigid registration.* PhD thesis, University of Iowa, 2012.

[181] V. Alastrué, E. Peña, M. Á. Martínez, and M. Doblaré. Assessing the use of the "opening angle method" to enforce residual stresses in patient-specific arteries. *Annals of Biomedical Engineering*, 35(10):1821–1837, 2007.

[182] G. A. Holzapfel and T. C. Gasser. A viscoelastic model for fiber-reinforced composites at finite stains: Continuum basis, computational aspects and applications. *Computer Methods in Applied Mechanics and Engineering*, 190(34):4379–4403, may 2001.

[183] Z. J. Samila and S. A. Carter. The effect of age on the unfolding of elastin lamellae and collagen fibers with stretch in human carotid arteries. *Canadian journal of physiology and pharmacology*, 59(10):1050–7, oct 1981.

[184] W. Zhang, Y. Liu, and G. S. Kassab. Flow-induced shear strain in intima of porcine coronary arteries. *Journal of applied physiology (Bethesda, Md. : 1985)*, 103(2):587–93, may 2007.

[185] T. E. Carew, R. N. Vaishnav, and D. J. Patel. Compressibility of the arterial wall. *Circulation research*, 23(1):61–8, jul 1968.

[186] Y. Fung. *Biomechanics: mechanical properties of living tissues.* Biomechanics / Y. C. Fung. Springer-Verlag, 1981.

[187] R. Rezakhaniha and N. Stergiopulos. A structural model of the venous wall considering elastin anisotropy. *Journal of biomechanical engineering*, 130(3):031017, jun 2008.

[188] G. Martufi and T. C. Gasser. A constitutive model for vascular tissue that integrates fibril, fiber and continuum levels with application to the isotropic and passive properties of the infrarenal aorta. *Journal of biomechanics*, 44(14):2544–50, sep 2011.

[189] Y. Lanir. Constitutive equations for fibrous connective tissues. *Journal of biomechanics*, 16(1):1–12, 1983.

[190] M. a. Zulliger, P. Fridez, K. Hayashi, and N. Stergiopulos. A strain energy function for arteries accounting for wall composition and structure. *Journal of biomechanics*, 37(7):989–1000, jul 2004.

[191] R. Grytz and G. Meschke. Constitutive modeling of crimped collagen fibrils in soft tissues. *Journal of the Mechanical Behavior of Biomedical Materials*, 2(5):522–533, 2009.

[192] M. Marino and G. Vairo. Stress and strain localization in stretched collagenous tissues via a multiscale modeling approach. *Computer Methods in Biomechanics and Biomedical Engineering*, 17(1):11–30, 2014.

[193] A. Gizzi, M. Vasta, and A. Pandolfi. Modeling collagen recruitment in hyperelastic bio-material models with statistical distribution of the fiber orientation. *International Journal of Engineering Science*, 78:48–60, may 2014.

[194] C. Truesdell and W. Noll. The Non-Linear Field Theories of Mechanics. In *The Non-Linear Field Theories of Mechanics*, pages 1–579. Springer Berlin Heidelberg, Berlin, Heidelberg, 2004.

[195] T. Shearer. A new strain energy function for the hyperelastic modelling of ligaments and tendons based on fascicle microstructure. 2014.

[196] Y. C. Fung. Elasticity of soft tissues in simple elongation. *The American journal of physiology*, 213(6):1532–44, dec 1967.

[197] Y. C. Fung. Biorheology of soft tissues. *Biorheology*, 10(2):139–155, jun 1973.

[198] W. Sun, E. L. Chaikof, and M. E. Levenston. Numerical approximation of tangent moduli for finite element implementations of nonlinear hyperelastic material models. *Journal of biomechanical engineering*, 130(6):061003, 2008.

[199] C. Miehe. Numerical computation of algorithmic (consistent) tangent moduli in large-strain computational inelasticity. *Computer Methods in Applied Mechanics and Engineering*, 134(96):223–240, aug 1996.

[200] Y. C. Fung. What are the residual stresses doing in our blood vessels? *Annals of Biomedical Engineering*, 19(3):237–249, 1991.

[201] S. J. Peterson and R. J. Okamoto. Effect of residual stress and heterogeneity on circumferential stress in the arterial wall. *Journal of biomechanical engineering*, 122(4):454–6, aug 2000.

[202] C. J. Chuong and Y. C. Fung. On residual stresses in arteries. *Journal of biomechanical engineering*, 108:189–192, 1986.

[203] H. A. Chami, M. J. Keyes, J. A. Vita, G. F. Mitchell, M. G. Larson, S. Fan, R. S. Vasan, G. T. O'Connor, E. J. Benjamin, and D. J. Gottlieb. Brachial artery diameter, blood flow and flow-mediated dilation in sleep-disordered breathing. *Vascular medicine (London, England)*, 14(4):351–60, nov 2009.

[204] A. Kiray, I. Ergür, H. Tayefi, H. A. BaÄ§riyanik, and A. K. BacakoÄ§lu. Anatomical evaluation of the superficial veins of the upper extremity as graft donor source in microvascular reconstructions: a cadaveric study. *Acta orthopaedica et traumatologica turcica*, 47(6):405–10, jan 2013.

[205] M. Gössl, M. Zamir, and E. L. Ritman. Vasa vasorum growth in the coronary arteries of newborn pigs. *Anatomy and Embryology*, 208:351–357, 2004.

[206] J. E. Fischer. *Fischer's mastery of surgery*. Wolters Kluwer Health/Lippincott Williams & Wilkins, 2012.

[207] A. B. Zoubos, A. V. Seaber, and J. R. Urbaniak. Hemodynamic and histological differences in end-to-side anastomoses. *Microsurgery*, 13(4):200–3, 1992.

[208] J. S. Scheltes, C. J. van Andel, P. V. Pistecky, and C. Borst. Coronary anastomotic devices: blood-exposed non-intimal surface and coronary wall stress. *The Journal of thoracic and cardiovascular surgery*, 126(1):191–9, jul 2003.

[209] A. V. Kamenskiy, I. I. Pipinos, J. N. MacTaggart, S. A. J. Kazmi, and Y. A. Dzenis. Comparative analysis of the biaxial mechanical behavior of carotid wall tissue and biological and synthetic materials used for carotid patch angioplasty. *Journal of biomechanical engineering*, 133(11):111008, nov 2011.

[210] I. D. A. Vellar and J. C. Doyle. The Use of the Cephalic and Basilic Veins as Peripheral Vascular Grafts. *Australian and New Zealand Journal of Surgery*, 40(1):52–57, aug 1970.

[211] F. Brochado-Neto, M. Albers, C. Pereira, J. Gonzalez, and M. Cinelli Jr. Prospective Comparison of Arm Veins and Greater Saphenous Veins as Infrageniculate Bypass Grafts. *European Journal of Vascular and Endovascular Surgery*, 22(2):146–151, aug 2001.

[212] O. Eiken and R. Kolegard. Comparison of vascular distensibility in the upper and lower extremity. *Acta Physiologica Scandinavica*, 181(3):281–287, jul 2004.

[213] J. Veselý, L. Horný, H. Chlup, T. Adámek, M. Krajíček, and R. Žitný. Constitutive modeling of human saphenous veins at overloading pressures. *Journal of the Mechanical Behavior of Biomedical Materials*, 45:101–108, 2015.

[214] A. Delfino, N. Stergiopulos, J. E. Moore, and J. J. Meister. Residual strain effects on the stress field in a thick wall finite element model of the human carotid bifurcation. *Journal of biomechanics*, 30(8):777–786, 1997.

[215] Abaqus (SIMULIA). *ABAQUS/Standard Analysis User's Manual*. USA, 2014.

[216] O. Sorkine. Differential Representations for Mesh Processing. *Computer Graphics Forum*, 25(4):789–807, dec 2006.

[217] C. Wang, X. Guo, and G. S. Kassab. A new observation on the stress distribution in the coronary artery wall. *Journal of biomechanical engineering*, 131(11):111011, nov 2009.

[218] A. Ochsner, R. Colp, and G. E. Burch. Normal blood pressure in the superficial venous system of man at rest in the supine position. *Circulation*, 3(5):674–680, may 1951.

[219] W. Trubel, H. Schima, M. Czerny, K. Perktold, M. G. Schimek, and P. Polterauer. Experimental comparison of four methods of end-to-side anastomosis with expanded polytetrafluoroethylene. *British Journal of Surgery*, 91(2):159–167, feb 2004.

[220] M. Fillinger, E. Reinitz, R. Schwartz, D. Resetarits, A. Paskanik, and C. Bredenberg. Beneficial effects of banding on venous intimal-medial hyperplasia in arteriovenous loop grafts. *American Journal of Surgery*, 158(2):87–94, aug 1989.

[221] J. L. Lumley. The Structure of Inhomogeneous Turbulent Flows. In A. M. Yaglom and V. I. Tatarski, editors, *Atmospheric turbulence and radio propagation*, pages 166–178. Nauka, Moscow, 1967.

[222] L. Sirovich and J. D. Rodriguez. Coherent structures and chaos: A model problem. *Physics Letters A*, 120(5):211–214, feb 1987.

[223] L. Grinberg, A. Yakhot, and G. E. Karniadakis. Analyzing transient turbulence in a stenosed carotid artery by proper orthogonal decomposition. *Annals of Biomedical Engineering*, 37(11):2200–2217, nov 2009.

[224] F. Loth, P. F. Fischer, and H. S. Bassiouny. Blood Flow in End-to-Side Anastomoses*. *Annual Review of Fluid Mechanics*, 40(1):367–393, 2008.

[225] A. Saltelli, M. Ratto, T. Andres, F. Campolongo, J. Cariboni, D. Gatelli, M. Saisana, and S. Tarantola. *Global Sensitivity Analysis. The Primer*. John Wiley & Sons, Ltd, Chichester, UK, dec 2008.

[226] I. M. Sobol. Sensitivity analysis for nonlinear mathematical models. *Math. Model. Computer.Exp*, 1(4):407–414, 1993.

[227] S. Li, B. Yang, and F. Qi. Accelerate global sensitivity analysis using artificial neural network algorithm: Case studies for combustion kinetic model. *Combustion and Flame*, 168:53–64, 2016.

[228] P. Wang, Z. Lu, and Z. Tang. An application of the Kriging method in global sensitivity analysis with parameter uncertainty. *Applied Mathematical Modelling*, 37(9):6543–6555, may 2013.

[229] C. B. Storlie, L. P. Swiler, J. C. Helton, and C. J. Sallaberry. Implementation and evaluation of nonparametric regression procedures for sensitivity analysis of computationally demanding models. *Reliability Engineering and System Safety*, 94(11):1735–1763, nov 2009.

[230] L. Antiga, M. Piccinelli, L. Botti, B. Ene-Iordache, A. Remuzzi, and D. Steinman. An image-based modeling framework for patient-specific computational hemodynamics. *Medical and Biological Engineering and Computing*, 46(11):1097–1112, 2008.

[231] S.-W. Lee, L. Antiga, and D. A. Steinman. Correlations among indicators of disturbed flow at the normal carotid bifurcation. *Journal of biomechanical engineering*, 131(6):061013, 2009.

[232] G. Rennen and G. Rennen. Subset selection from large datasets for Kriging modeling. *Struct Multidisc Optim*, 38:545–569, 2009.

[233] G. Davis and M. Morris. Six factors which affect the condition number of matrices associated with kriging. *Mathematical Geology*, 29(5):669–683, 1997.

[234] A. J. Booker, J. E. Dennis, P. D. Frank, D. B. Serafini, V. Torczon, and M. W. Trosset. A rigorous framework for optimization of expensive functions by surrogates. *Structural Optimization*, 17(1):1–13, feb 1999.

[235] I. Couckuyt, T. Dhaene, and P. Demeester. ooDACE Toolbox: A Flexible Object-Oriented Kriging Implementation. *Journal of Machine Learning Research*, 15:3183–3186, 2014.

[236] F. Cannavó. Sensitivity analysis for volcanic source modeling quality assessment and model selection. *Computers and Geosciences*, 44:52–59, jul 2012.

[237] J. D. Evans. *Straightforward statistics for the behavioral sciences*. Brooks/Cole Pub. Co, 1996.

[238] A. J. Booker, J. E. Dennis, P. D. Frank, D. B. Serafini, V. Torczon, and M. W. Trosset. A rigorous framework for optimization of expensive functions by surrogates. *Structural Optimization*, 17(1):1–13, 1999.

[239] C. Audet and J. E. Dennis. Mesh Adaptive Direct Search Algorithms for Constrained Optimization. *SIAM Journal on Optimization*, 17(1):188–217, jan 2006.

[240] A. L. Marsden, J. A. Feinstein, and C. A. Taylor. A computational framework for derivative-free optimization of cardiovascular geometries. *Computer Methods in Applied Mechanics and Engineering*, 197(21-24):1890–1905, apr 2008.

[241] W. Yang, J. A. Feinstein, and A. L. Marsden. Constrained optimization of an idealized Y-shaped baffle for the Fontan surgery at rest and exercise. *Computer Methods in Applied Mechanics and Engineering*, 199(33-36):2135–2149, jul 2010.

[242] W. Yang, J. A. Feinstein, S. C. Shadden, I. E. Vignon-Clementel, and A. L. Marsden. Optimization of a Y-Graft Design for Improved Hepatic Flow Distribution in the Fontan Circulation. *Journal of Biomechanical Engineering*, 135(1):011002, dec 2013.

[243] T. J. Gundert, A. L. Marsden, W. Yang, and J. F. LaDisa. Optimization of Cardiovascular Stent Design Using Computational Fluid Dynamics. *Journal of Biomechanical Engineering*, 134(1):011002, jan 2012.

[244] N. W. Bressloff, G. Ragkousis, and N. Curzen. Design Optimisation of Coronary Artery Stent Systems. *Annals of Biomedical Engineering*, 44(2):357–367, feb 2016.

[245] A. L. Marsden. Optimization in Cardiovascular Modeling. *Annual Review of Fluid Mechanics*, 46(1):519–546, jan 2014.

[246] A. N. Cookson, D. J. Doorly, and S. J. S. Sherwin. Mixing through stirring of steady flow in small amplitude helical tubes. *Annals of biomedical engineering*, 37(4):710–721, apr 2009.

[247] H. J. T. A. M. Huijbregts, P. J. Blankestijn, C. G. Caro, N. J. W. Cheshire, M. T. C. Hoedt, R. P. Tutein Nolthenius, and F. L. Moll. A Helical PTFE Arteriovenous Access Graft to Swirl Flow Across the Distal Anastomosis: Results of a Preliminary Clinical Study. *European Journal of Vascular and Endovascular Surgery*, 33(4):472–475, apr 2007.

[248] L. Shtilman, E. Levich, S. A. Orszag, R. B. Pelz, and A. Tsinober. On the role of helicity in complex fluid flows. *Physics Letters A*, 113(1):32–37, nov 1985.

[249] M. Grigioni, C. Daniele, U. Morbiducci, C. Del Gaudio, G. D'Avenio, A. Balducci, and V. Barbaro. A mathematical description of blood spiral flow in vessels: Application to a numerical study of flow in arterial bending. *Journal of Biomechanics*, 38(7):1375–1386, jul 2005.

[250] U. Morbiducci, R. Ponzini, M. Grigioni, and A. Redaelli. Helical flow as fluid dynamic signature for atherogenesis risk in aortocoronary bypass. A numeric study. *Journal of Biomechanics*, 40(3):519–534, jan 2007.

[251] N. Westerhof, J.-W. Lankhaar, and B. E. Westerhof. The arterial Windkessel. *Medical & biological engineering & computing*, 47(2):131–141, feb 2009.

[252] C. G. Caro, N. J. Cheshire, and N. Watkins. Preliminary comparative study of small amplitude helical and conventional ePTFE arteriovenous shunts in pigs. *Journal of the Royal Society, Interface / the Royal Society*, 2(3):261–266, 2005.

Appendix A

A.1 Proper Orthogonal Decomposition

The Proper Orthogonal Decomposition (POD) is a numerical technique that allows to process large amounts of high-dimensional data with the aim of obtaining low-dimensional descriptions that capture much of the phenomena of interest. POD was already known as Principal Component Analysis and Karhumen-Loéve expansion, but was first introduced in the fluid-mechanics community by Lumley in 1967 [221].

Let us consider a random generalized process $u(\mathbf{x}, t_i)$, with $i = 1, ..., M$, which is a sequence of numerical or experimental observations. The time-average of the sequence is defined by

$$\overline{u}(\mathbf{x}) = \langle u(\mathbf{x}, t_i) \rangle = \frac{1}{M} \sum_{i=1}^{M} u(\mathbf{x}, t_i) \tag{A.1}$$

and assumed to be zero without loss of generality. The POD decomposes the signal $u(\mathbf{x}, t_i)$ in a set of time-independent orthonormal basis functions, $\Phi_k(\mathbf{x})$,

and time-dependent orthonormal amplitude coefficients, $a_k(t_i)$, such that

$$u(\mathbf{x}, t_i) = \sum_{k=1}^{M} a_k(t_i)\Phi_k(\mathbf{x}), \quad i = 1, ..., M. \tag{A.2}$$

The POD is optimal in the sense that the average least-squares truncation error

$$\epsilon_m = \langle \| u(\mathbf{x}, t_i) - \sum_{k=1}^{m} a_k(t_i)\Phi_k(\mathbf{x}) \|^2 \rangle \tag{A.3}$$

is minimum for any given number m of basis functions, where $\| \cdot \| = (\cdot, \cdot)$ is the L^2-norm and $(\cdot, \cdot)$ is the standard inner product. Equation A.3 is equivalent to finding the set of POD modes $\Phi_k(\mathbf{x})$ that maximise the projection of u onto Φ

$$\max_{\Phi} \frac{\langle |(\Phi(\mathbf{x}), u(\mathbf{x}, t_i)|^2 \rangle}{\|\Phi(\mathbf{x})\|^2}. \tag{A.4}$$

This corresponds to maximising the following functional:

$$\frac{(R(t, t'), \Phi(t)\Phi^*(t'))}{\|\Phi(\mathbf{x})\|^2} = \lambda > 0 \tag{A.5}$$

where $R(t, t') = \langle u(t)u(t') \rangle$ is the autocorrelation function of $u(t)$ and $u(t')$ and $\cdot^*$ is the complex conjugate. It can be shown that Eq.A.5 corresponds to solving the following integral eigenvalue problem

$$\int R(t, t')\Phi^*(t')dt' = \lambda\Phi(t). \tag{A.6}$$

The solution of this equation produces a set of orthonormal functions $\Phi_k(\mathbf{x})$, and associated eigenvalues λ_k. The temporal modes, $a_k(t_i)$, are calculated by projecting the data set on the spatial POD modes as

$$a_k(t) = (u(\mathbf{x}, t_i), \Phi_k(\mathbf{x})). \tag{A.7}$$

In addition, it can be shown that temporal and spatial modeds are uncorrelated and the following orthogonality properties hold,

$$\begin{aligned} \langle a_j(t_i)a_k(t_i)\rangle &= \delta_{jk}\lambda_j \\ \Phi_j^*(\mathbf{x})\Phi_k(\mathbf{x}) &= \delta_{jk} \end{aligned} \tag{A.8}$$

where δ_{jk} is the Kronecker delta.

A popular technique for solving the eigenvalue problem in Eq. A.6 is the Method of Snapshot, developed by Sirovich [222]. This method allows a more efficient solution of the eigenvalue problem when the resolution of the spatial domain is higher than the number of temporal observations. This method is based on the fact that POD modes Φ_k and data vectors $\mathbf{u}_i = [u(x_1,t_i), u(x_2,t_i), ...u(x_N,t_i)]$ span the same linear space [222]. Therefore, the POD modes can be written as a linear combination of the data vectors

$$\Phi_k = \sum_{i=1}^{M} v_i^k \mathbf{u}_i,\ k = 1, ..., M. \tag{A.9}$$

The coefficients v_i^k are obtained from the solution of the following eigenvalue problem

$$\mathbf{C}\mathbf{v} = \lambda\mathbf{v}. \tag{A.10}$$

where $\mathbf{C}$ is a symmetric M×M matrix defined by $C_{ij} = \frac{1}{N}(u_i(\mathbf{x}), u_j(\mathbf{x}))$.

A.2 Variance-based Global Sensitivity Analysis

From a black-box perspective any model can be interpreted as a function $Y = f(\mathbf{X})$, where $\mathbf{X}$ is the vector of model inputs $\{X_1, X_2, ..., X_n\}$ and Y is a chosen model output. The inputs, without loss of generality can be considered indepen-

dently and uniformly distributed in the unit n-dimensional cube

$$K^n = \{\mathbf{X}|X_i \in [0,1]; i = 1,2,...,n\} \tag{A.11}$$

Consider a group of indices, $i_1,...,i_s$ where $1 < i_1 < ... < i_s < n$ and $s = 1,...,n$; it is possible to introduce a notation for a sum over all the different groups of indices:

$$\widehat{\sum} T_{i_1,...,i_s} = \sum_{i=1}^{n} T_i + \sum_{1\leq i<j\leq n}^{n} T_{i,j} + ... + T_{1,...,n}. \tag{A.12}$$

The model function can be decomposed as an expansion into summands of different dimensions:

$$\begin{aligned} Y = f_0 + \widehat{\sum} f_{i_1,...,i_s}(X_{i_1},...,X_{i_s}) = \sum_{i=1}^{n} f_i(X_i) + \sum_{1\leq i<j\leq n}^{n} f_{i,j}(X_i,X_j) + ... \\ + f_{1,...,n}(X_1,...,X_d) \end{aligned} \tag{A.13}$$

where f_0 is a constant, $f_i(X_i)$ are referred to as main effects and functions of X_i, while $f_{i,j}(X_i,X_j)$ are referred to as first-order interactions and are functions of X_i and X_j and so on. A condition for this decomposition to be valid is that the integrals of the summands $f_{i_1...i_s}$, with respect to any of their own variables are zero:

$$\int_0^1 f_{i_1,...,i_s}(X_{i_1},...,X_{i_s}) dX_{i_k} = 0 \tag{A.14}$$

for $1 \leq k \leq s$. It follows that

$$f_0 = \int_{K^n} f(\mathbf{X}) d\mathbf{X} \tag{A.15}$$

and that all the summands on the right-hand side of Eq. A.13 are orthogonal,

i.e. for $i_1, ..., i_s \not\equiv j_1, ..., j_l$

$$\int_{K^n} f_{i_1,...,i_s} f_{j_1,...,j_l} d\mathbf{X} = 0. \tag{A.16}$$

In fact, at least one of the indices $i_1, ..., i_s, j_1, ..., j_l$ is not repeated and the integral with respect to that variable is zero because of Eq A.14. The terms if the decomposition can be written in terms of conditional expected values, as follows:

$$\begin{aligned} f_0 &= E(Y) \\ f_i(X_i) &= E(Y|X_i) - f_0 \\ f_{i,j}(X_i, X_j) &= E(Y|X_i, X_j) - f_0 - f_i - f_j. \end{aligned} \tag{A.17}$$

Assuming that $f(\mathbf{X})$ is square-integrable, yields

$$\int_0^1 f^2(\mathbf{X}) d\mathbf{X} - f_0^2 = \sum_{s=1}^{n} \sum_{i_1<...<i_s}^{n} \int f_{i_1,...,i_s} dX_{i_1} ... dX_{i_s}. \tag{A.18}$$

The term on the left is the variance of Y, while the terms on the right are variance terms decomposed with respect to sets of input variables. This leads to

$$Var(Y) = \sum_{i=1}^{n} V_i + \sum_{1\le i<j\le n}^{n} V_{i,j} + ... + V_{1,...,n} \tag{A.19}$$

with

$$\begin{aligned} V_i &= Var(E(Y|X_i)) \\ V_{i,j} &= Var(E(Y|X_i, X_j)) - V_i - V_j. \end{aligned} \tag{A.20}$$

The above decomposition shows that the input variance can be divided into terms attributable to each input, as well as the interactions between each input. Input variances can be converted into proportions, by dividing them by $Var(Y)$, as

follows:

$$1 = \sum_{i=1}^{n} \frac{V_i}{Var(Y)} + \sum_{1 \le i < j \le n}^{n} \frac{V_{i,j}}{Var(Y)} + ... + \frac{V_{1,...,n}}{Var(Y)} = \sum_{i=1}^{n} S_i + \sum_{1 \le i < j \le n}^{n} S_{i,j} + ... + S_{1,...,n}. \tag{A.21}$$

Using main effect S_i, first-order interactions $S_{i,j}$ and higher-order Sobol indices, one can build a picture of the inputs relative importance on the output. With large number of input variables, it requires to evaluate $2^n - 1$ indices. Therefore, another useful quantity, called total effect index can be introduced, to measure the uncertainty remaining in the output, given all inputs, except X_i, as follows

$$S_{Ti} = 1 - \frac{Var(E(Y|X_{\sim i}))}{Var(Y)}. \tag{A.22}$$

The notation $X_{\sim i}$ denotes the set of all input variables, except X_i. In general, $\sum_{i=1}^{n} S_{Ti} \ge 1$, and is equal to 1 only when the model is purely additive.

These sensitivity measures can be computed from the terms of Eq. A.13, in terms of conditional expected values. A great deal of the work in this field is done on efficient and accurate ways for estimating these conditional expectations from data. Sobol indices are estimated using Monte Carlo sampling methods, which are very computationally expensive requiring several thousands of model calls. To overcome this shortcoming, the metamodel approach is frequently used to simulate the behavior of an experimental system or computationally expensive numerical model. A surrogate model, having much lower computational cost, and good prediction capabilities, is fit to a set of initial training samples, and then used to efficiently produce several thousands model calculations.

A.3 Gaussian Process Regression

Gaussian Process Regression, or Kriging as it is known in geostatistics, is a stochastic regression algorithm, used to approximate noise-free data, that has

proven to be very versatile for tasks such as optimization, design space exploration and sensitivity analysis.

Given model response $y(\mathbf{x}) : \mathbb{R} \rightarrow \mathbb{R}^n$, which is a realisation of a Gaussian process, having inputs $\mathbf{x} \in \mathcal{D}_x \subset \mathbb{R}^n$, with n parameter space dimension, the Kriging surrogate model, $\hat{y}(\mathbf{x})$, approximates $y(\mathbf{x})$, through the following equation

$$\hat{y}(\mathbf{x}) = \mathcal{F}(\boldsymbol{\beta}, \mathbf{x}) + \mathcal{Z}(\mathbf{x}). \tag{A.23}$$

The first part of Eq. A.23 is a global regression term or *trend*, $\mathcal{F}(\boldsymbol{\beta}, \mathbf{x}) = \mathbf{f}^T\boldsymbol{\beta} = \sum_{j=1}^{p} \beta_j f_j(\mathbf{x})$, where $\boldsymbol{\beta}$ is the regression parameters vector and $\mathbf{f}^T$ is the vector of basis functions. The second part of Eq. A.23 is a local stochastic Gaussian process, that is normally distributed $\mathcal{Z}(\mathbf{x}) \sim \mathcal{N}(0, \sigma^2)$, with zero mean and variance σ^2. This process is defined by the covariance between any couple of domain inputs,

$$Cov(\mathcal{Z}(\mathbf{x}), \mathcal{Z}(\mathbf{x}')) = \sigma^2 R(\mathbf{x}, \mathbf{x}', \boldsymbol{\theta}) \tag{A.24}$$

The correlation function $R(\mathbf{x}, \mathbf{x}', \boldsymbol{\theta})$ describes the spatial similarity between two samples of the input space, $\mathbf{x}$ and $\mathbf{x}'$ and depends on the choice of hyperparameters $\boldsymbol{\theta}$, that needs to be determined.

Let us suppose that $\hat{y}(\mathbf{x})$ is a predictor of y, which can be obtained as a linear combination of m observations in the design data $\mathbf{S} = [\mathbf{s}_1, ..., \mathbf{s}_m]$ and responses $\mathbf{y}_s = [y_1, ..., y_m]$, as

$$\hat{y}(\mathbf{x}) = \mathbf{c}^T\mathbf{y}_s, \tag{A.25}$$

with $\mathbf{c} = \mathbf{c}(\mathbf{x}) \in \mathbb{R}^m$. The error of the predictor is

$$\begin{aligned} \hat{y}(\mathbf{x}) - y(\mathbf{x}) &= \mathbf{c}^T\mathbf{y}_s - y(\mathbf{x}) \\ &= \mathbf{c}^T(\mathbf{F}\boldsymbol{\beta} + \mathbf{d}) - (\mathbf{f}^T\boldsymbol{\beta} + \mathcal{Z}(\mathbf{x})) \\ &= \mathbf{c}^T\mathbf{d} - \mathcal{Z}(\mathbf{x}) + (\mathbf{F}^T\mathbf{c} - \mathbf{f})^T\boldsymbol{\beta} \end{aligned} \tag{A.26}$$

where $\mathbf{d}$ is the vector of deviations from the regression model at design space

sites. To keep the predictor unbiased, it is required that $\mathbf{F}^T\mathbf{c} - \mathbf{f} = 0$, which means that the regression does not over or understimate the true process. This effectively allows to express the predictor error as $\hat{y}(\mathbf{x}) - y(\mathbf{x}) = \mathbf{c}^T\mathbf{d} - \mathcal{Z}(\mathbf{x})$. From Eq. A.26, it follows that the Mean Squared Error is

$$\begin{aligned} MSE = E[(\hat{y}(\mathbf{x}) - y(\mathbf{x}))^2] &= E[(\mathbf{c}^T\mathbf{d} - \mathcal{Z})^2] \\ &= E[\mathcal{Z}^2 + \mathbf{c}^T\mathbf{d}\mathbf{d}^T\mathbf{c} - 2\mathbf{c}^T\mathbf{d}\mathcal{Z}] \\ &= \sigma^2(1 + \mathbf{c}^T\mathbf{R}\mathbf{c} - 2\mathbf{c}^T\mathbf{r}) \end{aligned} \tag{A.27}$$

with $\mathbf{R}$ the correlation matrix, having components $R_{i,j} = R(\mathbf{s}_i, \mathbf{s}_j)$ and $\mathbf{r}$ correlation vector between the new prediction point and the design space points $r_i = R(\mathbf{s}_i, \mathbf{x})$.

Equation A.27 can be minimised, under the unbiased constraint ($\mathbf{F}^T\mathbf{c} - \mathbf{f} = 0$), using a Lagrangian

$$\mathcal{L}(\mathbf{c}, \boldsymbol{\lambda}) = \sigma^2(1 + \mathbf{c}^T\mathbf{R}\mathbf{c} - 2\mathbf{c}^T\mathbf{r}) - \boldsymbol{\lambda}^T(\mathbf{F}^T\mathbf{c} - \mathbf{f}), \tag{A.28}$$

where $\boldsymbol{\lambda}$ are the Lagrange multipliers. In order to minimise Eq. A.27, we take the gradient of $\mathcal{L}(\mathbf{c}, \boldsymbol{\lambda})$ with respect to $\mathbf{c}$:

$$\nabla_{\mathbf{c}}\mathcal{L}(\mathbf{c}, \boldsymbol{\lambda}) = 2\sigma^2(\mathbf{R}\mathbf{c} - \mathbf{r}) - \mathbf{F}\boldsymbol{\lambda} = 0. \tag{A.29}$$

Then the following system of equations needs to be solved

$$\begin{bmatrix} \mathbf{R} & \mathbf{F} \\ \mathbf{F}^T & \mathbf{0} \end{bmatrix} \begin{bmatrix} \mathbf{c} \\ \tilde{\boldsymbol{\lambda}} \end{bmatrix} = \begin{bmatrix} \mathbf{r} \\ \mathbf{f} \end{bmatrix} \tag{A.30}$$

with $\tilde{\boldsymbol{\lambda}} = \boldsymbol{\lambda}/(2\sigma^2)$. The system has solutions

$$\begin{aligned} \tilde{\boldsymbol{\lambda}} &= (\mathbf{F}^T\mathbf{R}^{-1}\mathbf{F})(\mathbf{F}^T\mathbf{R}^{-1}\mathbf{r} - \mathbf{f}) \\ \mathbf{c} &= \mathbf{R}^{-1}(\mathbf{r} - \mathbf{F}\tilde{\boldsymbol{\lambda}}) \end{aligned} \tag{A.31}$$

and from Eq. A.25

$$\hat{y}(\mathbf{x}) = \mathbf{r}^T\mathbf{R}^{-1}\mathbf{y}_s - (\mathbf{F}^T\mathbf{R}^{-1}\mathbf{r} - \mathbf{f})^T(\mathbf{F}^T\mathbf{R}^{-1}\mathbf{F})^{-1}\mathbf{F}^T\mathbf{R}^{-1}\mathbf{y}_s. \tag{A.32}$$

The predictor can be written as

$$\hat{y}(\mathbf{x}) = \mathbf{f}^T\hat{\boldsymbol{\beta}} + \mathbf{r}^T\mathbf{R}^{-1}(\mathbf{y}_s - \mathbf{F}\hat{\boldsymbol{\beta}}) \tag{A.33}$$

with regression coefficient $\hat{\boldsymbol{\beta}} = (\mathbf{F}^T\mathbf{R}^{-1}\mathbf{F})^{-1}\mathbf{F}^T\mathbf{R}^{-1}\mathbf{y}_s$.

From Eq. A.27 the prediction variance can be simply calculated as

$$\sigma^2_{\hat{y}(\mathbf{x})} = E[(\hat{y}(\mathbf{x}) - y(\mathbf{x}))^2] = \sigma^2(1 - \mathbf{r}^T\mathbf{R}^{-1}\mathbf{r} + \mathbf{u}^T(\mathbf{F}^T\mathbf{R}^{-1}\mathbf{F})^{-1}\mathbf{u}) \tag{A.34}$$

with $\mathbf{u} = \mathbf{F}^T\mathbf{R}^{-1}\mathbf{r} - \mathbf{f}$ and $\sigma = 1/n(\mathbf{y}_s - \mathbf{F}\hat{\boldsymbol{\beta}})^T\mathbf{R}^{-1}(\mathbf{y}_s - \mathbf{F}\hat{\boldsymbol{\beta}})$. Note that since the Kriging predictor is interpolating the data in the experimental design, $\sigma^2_{\hat{y}(\mathbf{x})} = 0$, $\forall \mathbf{x} \in \mathbf{S}$.

The choice of autocorrelation function is crucial to produce an accurate Kriging Model. A commonly used class of stationary correlation functions is

$$R(\mathbf{x}, \mathbf{x}') = exp\left(-\sum_{i=1}^{n} \theta_i |x_i - x_i'|^p\right). \tag{A.35}$$

Note that these functions only depend on the distance between the two points, with higher correlation corresponding to closer points. The parameter p controls the initial drop in correlation as a function of the distance; often a value of 2 is used (equal to a Gaussian correlation function), which assume a smooth,

continuous regression surface. The hyper-parameters θ_i describe the sphere of influence of a point on nearby points in each direction. As already mentioned, the hyper-parameters are unknown and needs to be identified using Maximum Likelihood Estimation (MLE).

While Kriging is useful in many noise-free applications, it might produce undesired results when dealing with stochastic simulations and/or in presence of noise [235]. Stochastic Kriging, also known as Regression Kriging, extends Kriging for approximation instead of interpolation. The noise is modeled as separate Gaussian process, with mean 0 and covariance matrix $\mathbf{\Sigma}$, and the predictor becomes

$$\hat{y}(\mathbf{x}) = \mathbf{f}^T\hat{\boldsymbol{\beta}} + \mathbf{r}^T(\mathbf{R} + \frac{1}{\sigma^2}\mathbf{\Sigma})^{-1}(\mathbf{y}_s - \mathbf{F}\hat{\boldsymbol{\beta}}). \tag{A.36}$$

Assuming that noise is homogenously distributed across the input space, the covariance matrix has non zero values on its diagonal, *i.e.* $\mathbf{\Sigma} = 10^{\lambda}\mathbf{I}_n$, with $\mathbf{I}_n$ $n \times n$ identity matrix. The variable amount of noise due to λ is also estimated as part of the MLE optimization.

For all Kriging surrogate models used in Chapter 5 and 6, *ordinary Kriging* was chosen and the Matlab ooDace toolbox was used to determine the predictor [235]. *Ordinary Kriging* refers to the choice of a constant trend, yet having unknown value, namely $\boldsymbol{\beta}^T\mathbf{f}(\mathbf{x}) = \boldsymbol{\beta}^T$ $(f_i(\mathbf{x}) = 1)$

A.4 Wall Hypoxia

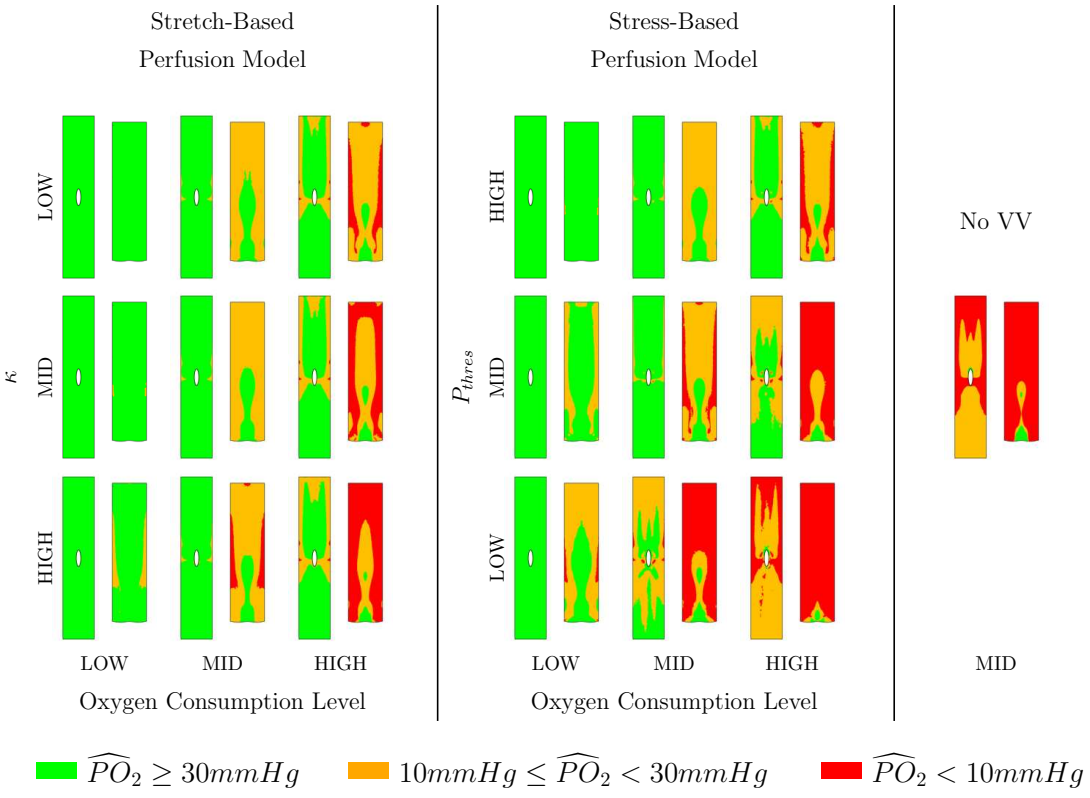

Figure A.1: Tri-color maps of normal (green - $\widehat{O}_2 \geq 30mmHg$), low (orange - $10mmHg \leq \widehat{O}_2 < 30mmHg$) and hypoxic (red - $\widehat{O}_2 < 10mmHg$) oxygen levels for two different perfusion models (Strain, Stress), three perfusion levels and three oxygen consumption rates, in excised and flattened views of depth-integrated average O2. The case with shut-off perfusion (NoVV) is also included in the analysis. The results are presented for a 20-80 flow split.

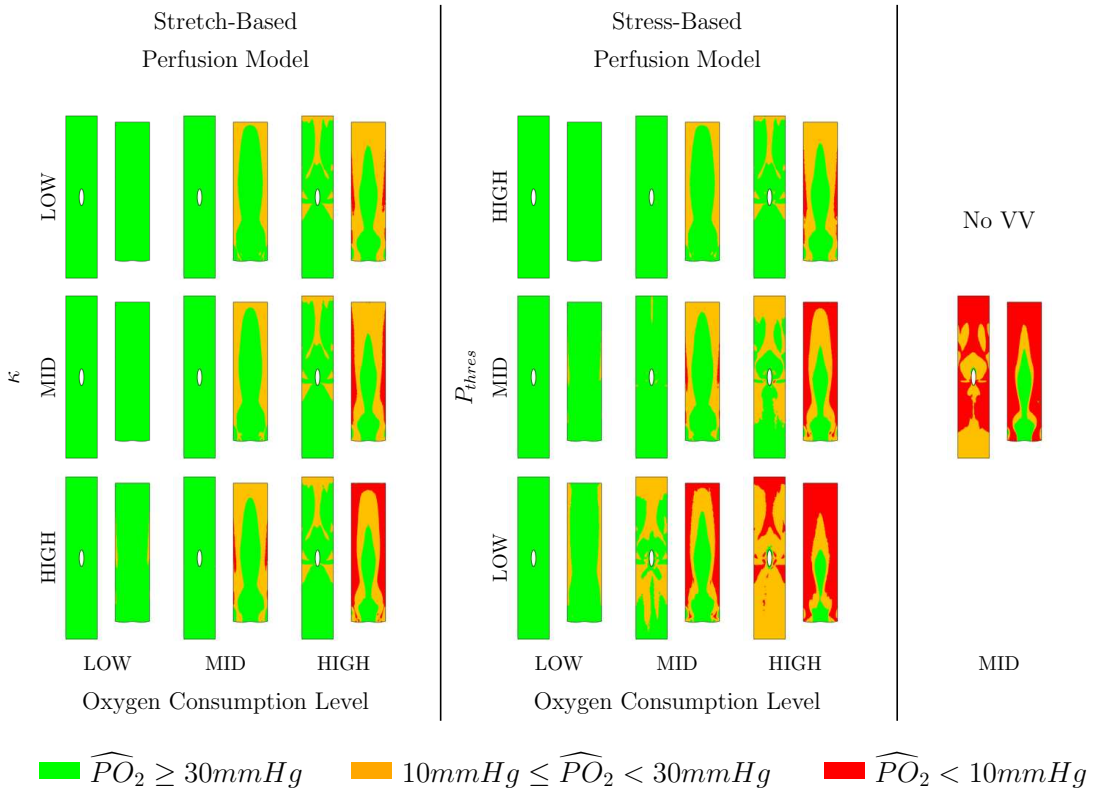

Figure A.2: Tri-color maps of normal (green - $\widehat{O}_2 \geq 30mmHg$), low (orange - $10mmHg \leq \widehat{O}_2 < 30mmHg$) and hypoxic (red - $\widehat{O}_2 < 10mmHg$) oxygen levels for two different perfusion models (Strain, Stress), three perfusion levels and three oxygen consumption rates, in excised and flattened views of depth-integrated average O2. The case with shut-off perfusion (NoVV) is also included in the analysis. The results are presented for a 50-50 flow split.

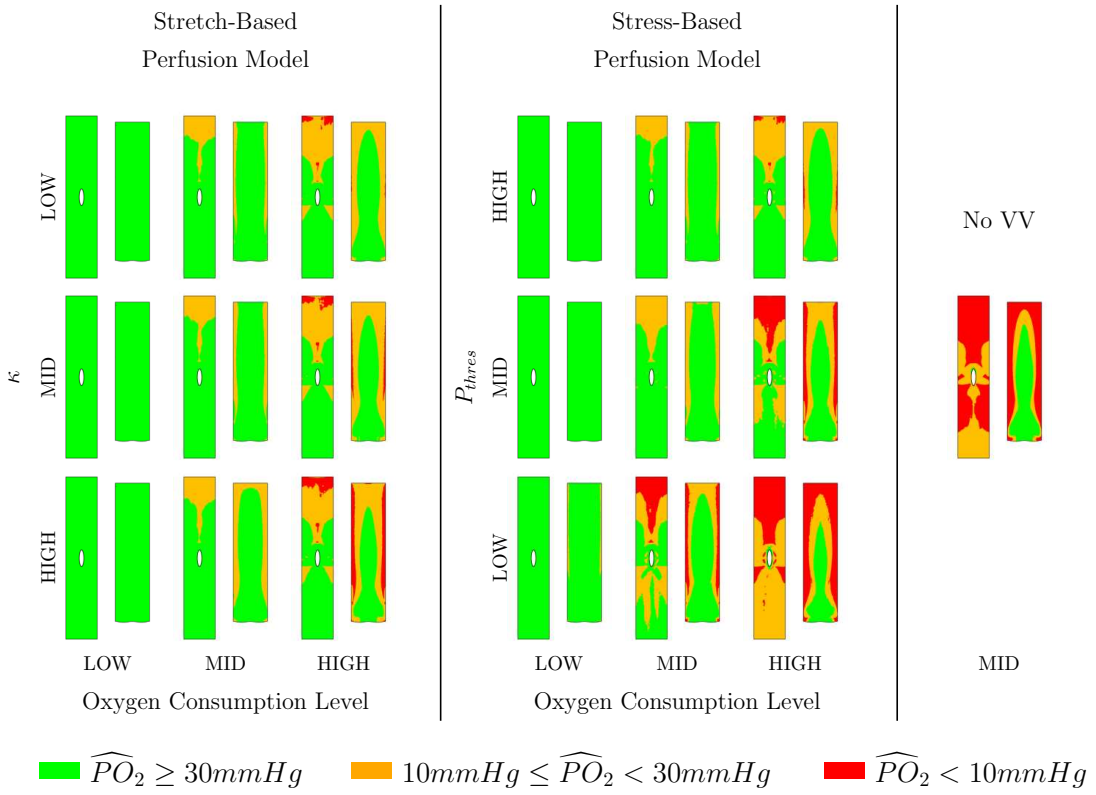

Figure A.3: Tri-color maps of normal (green - $\widehat{O}_2 \geq 30mmHg$), low (orange - $10mmHg \leq \widehat{O}_2 < 30mmHg$) and hypoxic (red - $\widehat{O}_2 < 10mmHg$) oxygen levels for two different perfusion models (Strain, Stress), three perfusion levels and three oxygen consumption rates, in excised and flattened views of depth-integrated average O2. The case with shut-off perfusion (NoVV) is also included in the analysis. The results are presented for a 80-20 flow split.

A.5 AVF Configurations

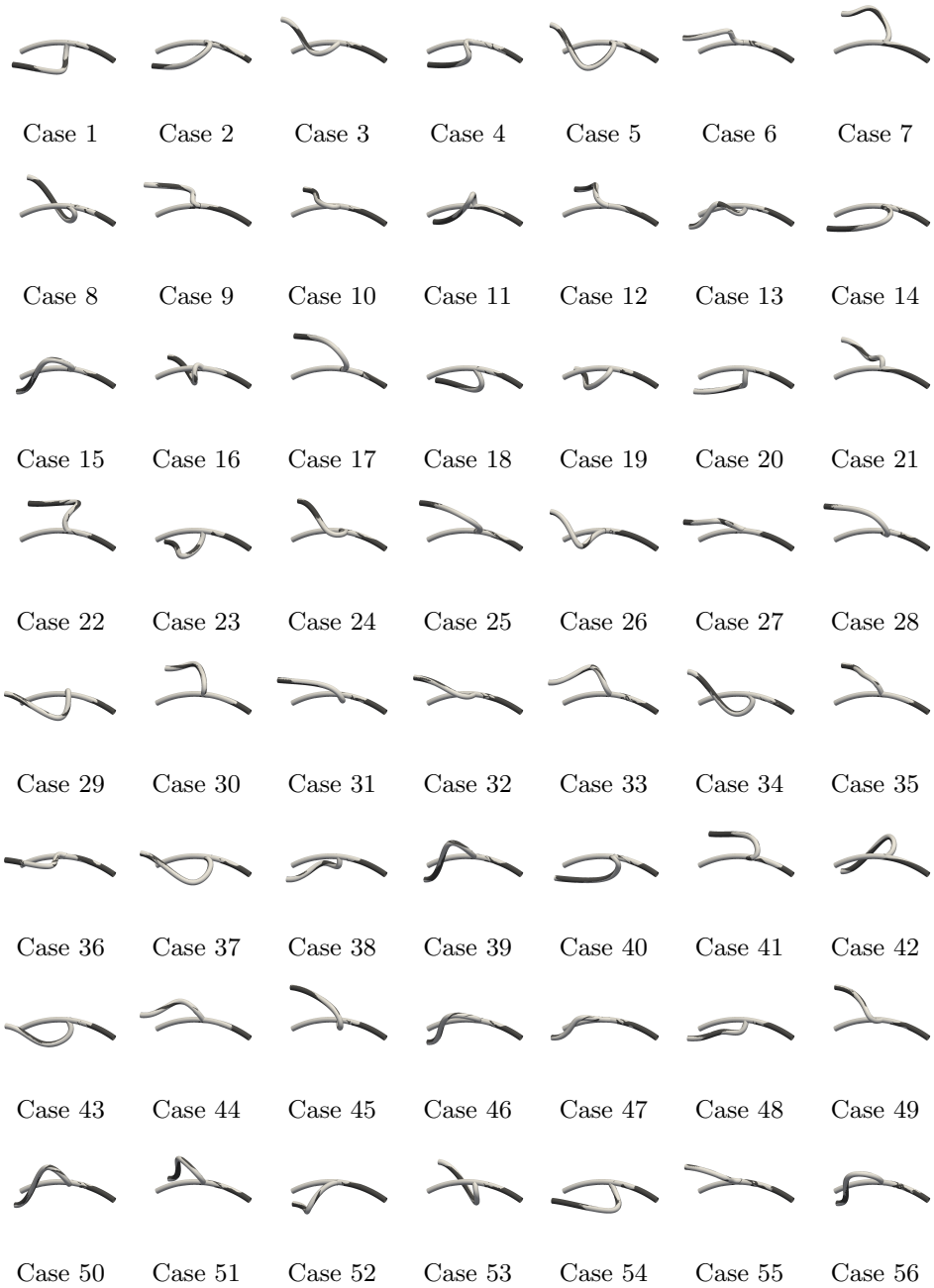

Case 57 Case 58 Case 59 Case 60 Case 61 Case 62 Case 63

Case 64 Case 65 Case 66 Case 67 Case 68 Case 69 Case 70

Case 71 Case 72 Case 73 Case 74 Case 75 Case 76 Case 77

Case 78 Case 79 Case 80 Case 81 Case 82 Case 83 Case 84

Case 85 Case 86 Case 87 Case 88 Case 89 Case 90 Case 91

Case 92 Case 93 Case 94 Case 95 Case 96 Case 97 Case 98

Case 99 Case 100 Case 101 Case 102 Case 103 Case 104 Case 105

Case 106 Case 107 Case 108 Case 109 Case 110 Case 111 Case 112

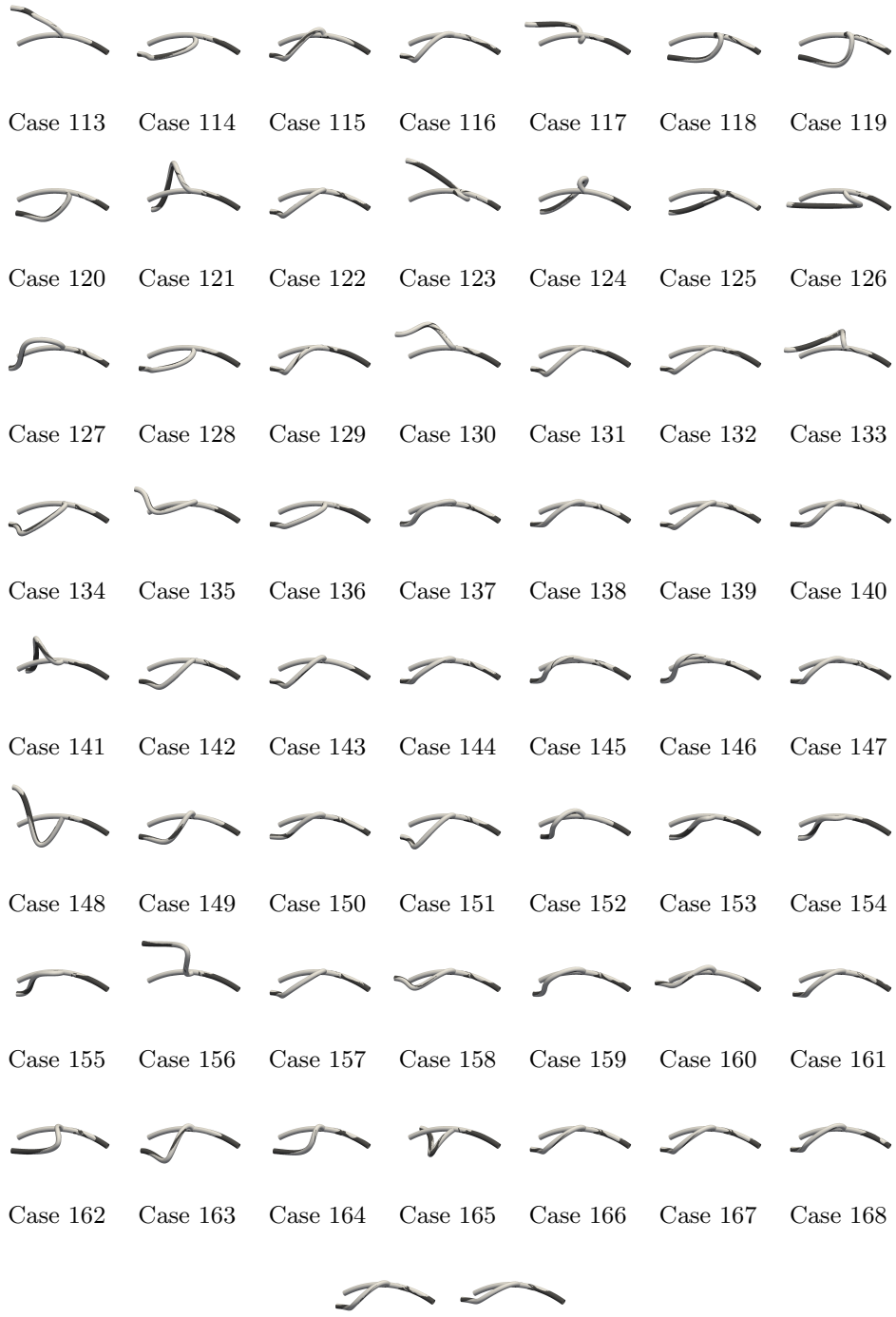

Figure A.4: The complete AVF configuration sample: cases from 1 to 100 were used to seed the Kriging-Based surrogate model; cases from 101 to 170 were tried during the MADS. In dark gray, iso-surfaces of $\psi = 1$ (see Eq. 6.5).